Rendell-Bhatti, Frederic (2022) *Manipulation and exploitation of the dynamic processes of Skyrmions*. PhD thesis.

https://theses.gla.ac.uk/82968/

Copyright and moral rights for this work are retained by the author

A copy can be downloaded for personal non-commercial research or study, without prior permission or charge

This work cannot be reproduced or quoted extensively from without first obtaining permission in writing from the author

The content must not be changed in any way or sold commercially in any format or medium without the formal permission of the author

When referring to this work, full bibliographic details including the author, title, awarding institution and date of the thesis must be given

Enlighten: Theses
https://theses.gla.ac.uk/
research-enlighten@glasgow.ac.uk

Manipulation and Exploitation of the Dynamic Processes of Skyrmions

Frederic Rendell-Bhatti
BSc, PGCE, MSc

Submitted in fulfilment of the requirements for the
Degree of Doctor of Philosophy

Materials and Condensed Matter Physics Group
School of Physics and Astronomy
University of Glasgow

May 2022

Abstract

Magnetic skyrmions are emergent, topological quasiparticles with vortex-like magnetisation profiles, stabilised in magnetic systems hosting the Dzyaloshinskii–Moriya (DM) interaction. Their high physical stability and ease of propagation by electrical currents, means that skyrmions have the potential to act as information carriers in future low-power data storage and transmission devices. However, for skyrmions to be used in such a manner, their stability under non-equilibrium conditions and in a range of magnetic systems must be investigated further. This thesis provides a contribution to such studies, through investigating the dynamics and physical stability of magnetic skyrmions in a range of material systems.

Arrays of skyrmions may be stabilised into a hexagonal skyrmion crystal lattice (SkX), under favourable conditions of magnetic field and temperature. Image analysis was performed on high frame rate Fresnel LTEM video data, showing repeated, spontaneous skyrmion motion across a SkX domain boundary. It was observed that the motion involved the creation and annihilation of skyrmions through splitting and merging of deformed skyrmions. The energy landscape of a SkX domain boundary region was investigated using micromagnetic simulations, with SkX defects found to be dominated by the interplay between exchange and Zeeman energies. Informed by Fresnel LTEM imaging and micromagnetic simulations, a mechanism for skyrmion creation and annihilation involving anti-skyrmions is proposed. This work demonstrates that in regions of high energy density, skyrmions may exhibit such large deformations that they are able to spontaneously split or merge with neighbouring skyrmions. These observations highlight the limits of skyrmion stability when alternative energy pathways involving topological structures are available.

Advanced image processing including total variation (TV) denoising and non-negative matrix factorisation (NMF) was carried out on sub-millisecond Fresnel image frames showing skyrmion dynamics, providing the ability to automatically identify transient skyrmion states. These analysis techniques provide a means of improving signal-to-noise ratio (SNR) and configurational state identification using machine learning. Perturbation of the SkX is carried out through the application of sub-μs perpendicular magnetic field pulses within the TEM. The realisation of such *in-situ* magnetic field pulses was achieved through the design, creation and testing of a bespoke microcoil and current pulser. Realisation of extensive disorder, and the formation of many defect regions within the SkX is demonstrated, where long-range reorientation of the SkX is unable to occur due to the duration of the pulses. Application of precise magnetic field pulses will allow for greater control over skyrmion nucleation and may aid in the study of skyrmion metastability.

Methods for enhancing skyrmion stability in the technologically relevant synthetic antiferromagnetic (SAF) systems are investigated through the utilisation of micromagnetic simulations. Variation in skyrmion stability within multilayer SAF systems is described, through studying the process of offsetting the destabilising dipole interactions with interlayer exchange coupling. SAF systems with 'spinterface' regions are investigated, focusing on the skyrmion stabilising effect of including a C_{60}–metal interface. Non-trivial skyrmion size behaviour is shown when the C_{60} is explicitly simulated as a dilute magnetic layer, due to coupling between three distinct magnetic subsystems. These micromagnetic studies highlight the ability to tune magnetic interactions, and thus skyrmion stability, through the engineering of multilayer condensed matter systems.

Declaration

This thesis is a record of research carried out by myself under supervision of Dr. Damien McGrouther, within the Materials and Condensed Matter Physics group in the School of Physics and Astronomy at the University of Glasgow between 2018-2021. The contents of this dissertation are original and have not been submitted in whole or in part for consideration for any other degree or qualification in this, or any other university. The work described herein is my own, except where specific reference is made to the work of others, summarised below.

- TEM samples used in Chapters 4 and 5 were created from the B20 FeGe single crystal grown by Y. Kousaka and Y. Togawa of Osaka Prefecture University, Japan.
- Raymond Lamb and Damien McGrouther, University of Glasgow, performed the Lorentz Fresnel TEM imaging experiment, filming spontaneous skyrmion motion introduced in Chapter 4. The raw data from this experiment has been used with permission.
- William Legrand, ETH Zürich, wrote the original MuMax3 SAF script, which has been used with permission and modified in Chapter 6.

Furthermore, much of the work contained in Chapter 4 can be found within the following paper:

- Rendell-Bhatti, F., Lamb, R.J., van der Jagt, J.W., Paterson, G.W., Swagten, H.J.M. and McGrouther, D. Spontaneous creation and annihilation dynamics and strain limited stability of magnetic skyrmions. *Nat Commun* **11,** 3536 (2020).

Acknowledgements

I would first like to thank Dr Damien McGrouther for his valuable support throughout my PhD experience. It was in no small part due to his guidance and encouragement that I enjoyed my PhD studies so much. Thank you for providing help when it was needed, whilst allowing me to develop as an independent researcher. I would also like to thank Professor Stephen McVitie for functioning as my secondary supervisor at the University of Glasgow, and for providing me with encouragement and advice, particularly during the yearly progression process.

Both the work in this thesis and my own development as a materials scientist would not have been possible without the excellent instrument training and technical support provided by Dr Sam McFadzean, Colin How and William Smith. Thank you all for working hard on keeping the precious core of the MCMP functioning. I would like to thank Dr Tim Moorsom for his guidance, and for the opportunity to pursue an exciting avenue of study in the final year of my PhD. This was during a particularly low point in motivation due to ongoing COVID restrictions, and it provided much needed re-invigoration through new, exciting problems to solve. A special thanks to both Gary Paterson and Aurelio Rodriguez for providing guidance, advice and feedback during preparation and submission of my first paper. I would also like to thank all other members of the MCMP, particularly my (albeit transient) office mates Hristo and Becky, for enjoyable discussions, both scientific and otherwise!

A special thanks to my family, it's only through their love, inspiration and support that I am able to write these words within this thesis. Mum and Dad, thank you for being such supportive parents. Flora and Harry, I'm lucky to have such amazing siblings, with whom I share so many commonalities. Eva, thank you for your love and companionship... not just during my PhD, but all the years behind and those ahead.

Thanks to Trinket, the best boy.

Lastly, my appreciation to the Natural World for providing tranquillity during difficult times, and the Universe at large for being such a beautiful oddity to study.

Contents

List of Figures vii

1 Introduction **1**

2 Skyrmions in Magnetic Systems **7**
- 2.1 Ferromagnetism and Exchange Interactions 7
- 2.2 Micromagnetic Theory 10
  - 2.2.1 Exchange Energy 10
  - 2.2.2 Demagnetising Energy 11
  - 2.2.3 Magnetocrystalline Anisotropy Energy 12
  - 2.2.4 Zeeman Energy 14
  - 2.2.5 Magnetic Configurations 14
- 2.3 RKKY Interaction 15
- 2.4 Nanoscale Magnetism 16
- 2.5 Magnetic Skyrmions 17
  - 2.5.1 Dzyaloshinkii-Moriya Interaction 18
  - 2.5.2 Skyrmions in Non-Centrosymmetric Magnets 19
  - 2.5.3 Skyrmions in Thin Film Multilayers 21
- 2.6 Micromagnetic Simulation Methods 22

3 Instrumentation and Methodology **29**
- 3.1 Transmission Electron Microscopy 29
  - 3.1.1 Conventional Transmission Electron Microscope 31
  - 3.1.2 Scanning Transmission Electron Microscopy 35
  - 3.1.3 Aberrations and Limitations of the Electron Microscope 37
- 3.2 Direct Electron Detectors 39
- 3.3 Magnetic Imaging 39
  - 3.3.1 Lorentz TEM 41
  - 3.3.2 Fresnel Imaging 43

3.3.3 Differential Phase Contrast Imaging 45
3.4 Focused Ion Beam Microscopy 47
3.4.1 TEM Sample Preparation 49

4 Spontaneous Skyrmion Dynamics 55
4.1 Imaging Skyrmion Lattice and Characterisation of Defects 55
4.2 Analysis of Spontaneous Skyrmion Motion 58
4.2.1 Configurational State Identification 59
4.2.2 Image Analysis of Configurational States 61
4.2.3 Energy Landscape of 5-7 Defects 65
4.2.4 Energetic Stability of Configurational States 69
4.2.5 Skyrmion Creation and Annihilation Mechanisms 73
4.3 Discussion and Conclusions 78

5 Induced Skyrmion Dynamics 85
5.1 Fast-frame Image Analysis Techniques 85
5.1.1 Image Denoising 86
5.1.2 Automated State Identification 88
5.1.3 Implementing Frame Superposition for Fast Dynamics 96
5.1.4 Discussion and Conclusions 99
5.2 Magnetic Field Pulses in the TEM 100
5.2.1 Microcoil Design 101
5.2.2 Current Pulser Design 103
5.2.3 Experimental Device Testing 108
5.3 Discussion and Conclusions 112

6 Skyrmion Stability in Synthetic Antiferromagnetic Systems 121
6.1 Stabilising Skyrmions in SAF Multilayers 121
6.1.1 Unbalanced SAF Systems 124
6.1.2 Simulating Multilayer SAFs 125
6.1.3 Results 129
6.2 Metal-Molecular Interfaces in SAF systems 134
6.2.1 Simulating PMA Enhancement Effects 136
6.2.2 Explicit Simulation of C_{60} 139
6.3 Discussion and Conclusions 143

7 Summary and Outlook 149

List of Figures

1.1 Estimation of skyrmion research output by publication year, using data from www.webofknowledge.com, generated on 06 June 2021. Plot shows the number of individual research records containing the keyword 'skyrmion' for each year, in the range 2006-2020. The trend shows that research involving skyrmions has been rising dramatically since 2010. . . 2

2.1 **a** Interaction of internal magnetic moments (red arrow) with the demagnetising field they create in a simple bar magnet and **b** a flux-closed magnetic configuration, which minimises demagnetising energy through the formation of magnetic domains. 12

2.2 Examples of simple magnetic configurations for a generic ferromagnet with different energies contributing to the total energy and minimum energy configuration. **a** Exchange energy only, **b** Exchange and demagnetising energies, **c** Exchange, demagnetising and MA energies, **d** Exchange, demagnetising, MA and Zeeman energies. The red arrows represent the magnetisation, M, within each domain. 15

2.3 **a** The DM interaction between two ferromagnetic atoms (grey) and a high SOC atom (orange). The $\mathrm{D_{ij}}$ vector points perpendicular to $\mathrm{S_{i,j}}$, favouring clockwise or counterclockwise spin rotation depending on the sign of $\mathrm{D_{ij}}$. **b**,**c** Orientation of $\mathrm{D_{ij}}$ relative to magnetic film, favouring formation of Bloch and Néel skyrmions, respectively. The labels in **c** refer to heavy metal (HM) and ferromagnetic (FM) layers. 19

2.4 Vector plots of a **a** Bloch skyrmion, **b** Neél skyrmion and **c** how their magnetisation can be mapped to a unit sphere, demonstrating their non-trivial topology. Magnetic moments are coloured according to their m_z magnetisation. 19

2.5 A mix of vector and scalar diagrams demonstrating the different magnetic phases in B20 helimagnets, accessed by varying the applied perpendicular magnetic field strength. As field is increased, it is possible to transition between the helical, skyrmion lattice, conical and saturated phases. This is assuming a region of uniform thickness at a constant temperature. 20
2.6 Phase diagram of FeGe showing the stability of the skyrmion lattice (SkX) as a function of magnetic field and temperature for sample varying thickness. Reproduced with permission from Ref. [**Yu2011**], Springer Nature. 21

3.1 **a** Simplified TEM schematic diagram demonstrating CTEM imaging. **b** Image formation process. Mathematical quantities are defined in Eqs. 3.5 - 3.10. 33
3.2 Critical components for describing the reciprocity relationship between **a** STEM and **b** CTEM. Adapted from [**Cowley1969**]. 36
3.3 A series of plots demonstrating the oscillatory nature of the CTF and how the interpretable resolution varies as a function of the defocus. . . 38
3.4 Schematics demonstrating the application of both in-plane and out-of-plane magnetic field components to magnetic samples in the TEM. **a** View from above the tilt and rotate sample holder **b** how this translates to the fields present within the sample for an x-axis rotation of θ. 41
3.5 LTEM Fresnel images of magnetic nanowires and how domain wall motion can be initiated through tilting the sample in a non-zero perpendicular magnetic field. The in-plane magnetic field is calculated through $H_y = \mathbf{H}\sin(\theta)$, where **H** is the out-of-plane field strength. . . . 41
3.6 Schematic showing Fresnel contrast formation due to the deflection of electrons travelling through a magnetic sample. Transmitted electrons are convergent or divergent depending on their interaction with the in-plane magnetisation, this results in alternating bright and dark intensity regions corresponding to the domain walls. 44
3.7 **a** DPC schematic demonstrating how the electron spot is deflected by a magnetic sample with distinctly magnetised domains. **b** Schematic showing how the deflection in **a** leads to different detection on the segmented detector. 46
3.8 Simplified FIB microscope schematics. **a** Showing all key components, **b** set up for material ablation, used in TEM sample preparation and **c** set up for FEBID, to grow magnetic nanostructures. 48

3.9 TEM lamella preparation using 'lift-out' method. 1: Deposition of protective platinum layers to protect sample. 2: Trench milling. 3: Partial undercut of the lamella. 4: Welding of lamella to OmniProbe needle. 5: Lamella cut free from bulk sample. 6: Welding of lamella to OmniProbe grid. 7: Lamella cut free from OmniProbe needle. 8: Successive thinning of lamella to electron transparency. 49

3.10 SEM image showing a thinned FeGe sample using the FIB 'lift-out' process. The bright region is the thinnest section and the fact it is so bright demonstrates the electron transparency. 50

4.1 Fresnel TEM images (top) and Delaunay triangulation plots (bottom) showing (a) regular hexagonal SkX, (b) isolated 5-7 defect within SkX, where the annotations denote the coordination of the indicated skyrmions, (c) SkX with a domain boundary containing three 5-7 defects and three regions (A, B, C) with distinct principle lattice vectors ($\mathbf{q}_{1A}$, $\mathbf{q}_{1B}$, $\mathbf{q}_{1C}$). Delaunay triangulation plots generated from the skyrmions geometric centre of mass are coloured according to the normalised area of the triangles and give an indication of skyrmion density. The red outlines are to provide a guide for the eye in locating the 5-7 defects. 57

4.2 Fresnel image of a skyrmion lattice formed in a FeGe thin plate at a temperature of 243.15 K and a perpendicular magnetic field of approximately 0.2 T. The white spots denote the locations of the individual skyrmions. The dark curves seen in the bottom right of the image are bend contours, diffraction contrast arising from the fact that the sample is not entirely flat. The areas in the coloured boxes correspond to distinct regions as follows, blue: helical phase, red:, regular hexagonal SkX, green: approaching field polarised/conical, yellow: deformed elongated skyrmion. 58

4.3 Fresnel TEM images of SkX and identification of configurational states. **a** Entire region of observed SkX, showing the domain boundary with an average misorientation angle of 14° (black dashed lined) and principle lattice vectors (arrows). The three coloured (blue, red and green) dashed lines demonstrate how the domain boundary shifts during transitions between the P_x states. **b**-**g** Examples of the six observed configurational states, time of each frame given in the bottom left corner of each image. The black arrowheads point along the row of skyrmions in which lateral motion was taking place. Skyrmions with 7- and 5-fold coordination (SkCoH and SkCoP, respectively) are highlighted by the conjoined pentagons and heptagons. **h** A portion of the transition data showing the progression of transitions between states shown in **b**-**g**. The markers (b)-(g) additionally indicate the time of occurrence of the images shown in **b**-**g**. Colour in each panel is associated with the identified configurational states, according to the bottom key. Scale bars, 200 nm. 60

4.4 Transition matrix with probabilities normalised to unity across rows. Colour bar indicates the transition probability of each observed transition. 62

4.5 Spatial analysis of the six observed configurational states. **a** Successive frames showing the variation in structure of the SkCoH in the P_1 state, frame time in the bottom right of each image. **b**,**c** Normalised summed intensity images of each observed state (left) and Delaunay triangulation calculated from the skyrmion geometric centre of mass (right). The colour bar indicates the area of the triangles in nm^2. **d**,**e** Integrated line profile plots of the P_x and T_x states respectively, measured across the dashed rectangles in **b**,**c**. The double inner peak in **d** demonstrates the dumbbell structure of the SkCoH in the P_x states. Scale bars, 100 nm. 63

4.6 Normalised summed intensity image and line profile plot across a stationary (under observation) SkCoH, for comparison. This 5-7 defect is located further down the SkX boundary, just below the right black arrow in Fig. 4.3a. Scale bar, 100 nm. 65

4.7 Total energy density plots (summed over the simulated region) as a function of skyrmion lattice parameter, a_{sk}, for a material thickness of 50 nm. **a** Energy density plot over a large range of a_{sk}. **b** Energy density plot near the minimum energy. The labelled equilibrium (minimum energy) lattice parameter of 91.2 nm in **b** is used in future simulations. 67

4.8 2D total energy density plots of, **a** regular SkX with a_{sk} set to 91 nm and **b** SkX containing a pair of 5-7 defects imposed through skyrmion deletion. Energy density comparison between 5-7 defect and regular skyrmion in **b** is calculated from the regions enclosed by the dashed white lines. Energy densities are given in units of $\frac{A}{D^2}$, shown by the colour bar in **a**. In these plots, skyrmions are centred on the highest energy regions, with the skyrmion-skyrmion distance shown by the label for a_{sk} in **a**. 68

4.9 2D total energy density plots of a SkX region containing two boundaries with three 5-7 defects in each. **a** Total energy density for entire simulated SkX region, energy density comparison between 5-7 defect and regular skyrmion from the regions enclosed by the dashed white lines. **b** Exchange+DM energy density, **c** Zeeman energy density and **d** demagnetising energy density. All subplots are from the left-most SkX boundary in **a**, enclosed by the black dashed box. Energy densities are given in units of $\frac{A}{D^2}$, scale shown by the colour bars accompanying each figure. 69

4.10 Lifetime distributions and associated energy barriers of each state. **a** Scatter plots of observed lifetimes, half the frame time (5 ms) was added to the lower bound uncertainties in T_x and P_3 due to the short-lived nature of these states. **b** Relative energy barriers calculated using the Néel-Arrhenius equation and average lifetimes. Each barrier height is given relative to P_1, which had an energy barrier height of 0.55 ev. . . . 70

4.11 Observed state transitions represented as a Markov chain process, only including transitions observed more than once. Circles(arrows) representing each state(transition) are scaled to the relative lifetimes(transition probabilities). Values next to each arrow show the transition probability. 72

4.12 **a** Initial states of skyrmion merging (top) and splitting (bottom). Dashed ellipses show field-pulse confinement, with the arrow giving the positive to negative field gradient. **b** Topological charge as a function of time during the merging (left) and splitting (right) simulations, labels i-v correspond to the panels in **d** and **e**. **c** Colour wheel for simulations in **d** and **e**. **d**,**e** Scalar plots of magnetisation (top) and vector plots of antiskyrmion (bottom) during the skyrmion merging and creation, respectively. **f** Annihilation of antiskyrmion through a thickness of 10 nm. 74

4.13 Skyrmion creation and annihilation mechanisms. **a**,**b** Proposed mechanisms for skyrmion creation and annihilation via splitting and merging, respectively. N gives the topological charge of each structure involved. **c**,**d** Micromagnetic simulation snapshots of splitting and merging transition states, closely resembling the middle states in **a** and **b**, respectively. Colour bar indicates the out of plane (m_z) component of magnetisation. 77

5.1 **a** The effect of using different weights within the Total Variation (TV) denoising algorithm on a single Fresnel TEM image showing a deformed SkCoH. **b** Plot of SNR against denoising weight, the circled weight value of 0.05 was chosen for future denoising analysis on this dataset. 88

5.2 Schematic demonstrating NMF analysis as performed on a cropped Fresnel video containing 6000 individual Fresnel images with dimensions 60 × 60 pixels. First, each image is flattened into a 1-dimensional array and then combined into an $n \times m$ matrix, V, where the rows give the n pixel values for each image, m. Next NMF is performed on V by factorisation into two matrices, W and H, which contain the basis images and encoding, respectively. Each image in V can then be approximated through linear combinations of the basis images in W through multiplication with the encoding in H. 91

5.3 Non-negative matrix factorisation (NMF) performed on a 6000 individual Fresnel image frames to determine the key features. NMF performed with **a** two basis images, which is sufficient to identify the key states and **b** three basis images, highlighting some higher-order structural variation. 93

5.4 Coefficients from encoding matrix H plot as a function of frame to create a time series-like plot for **a** two basis images **b** three basis images. Each line corresponds to a row in the encoding matrix, and contains the coefficients associated with a particular basis image as noted by the key legend in each plot. 94

5.5 NMF analysis using four basis images. **a** Skyrmion defect images as represented by Basis Images 1 - 4. **b** Time series plots of coefficients from matrix H as associated with each Basis Image after smoothing using a Savitzky–Golay filter. 95

5.6 Example of denoising, subsampling and NMF analysis on Fresnel images displaying fast skyrmion dynamics. Nine frames are shown as an example, with key steps shown by the labelled arrows. The outputs of the three basis images given, with the key states outlined. Basis image 1, 2 and 3 show a 5-7 defect in different locations. Basis Image 3 appears to show a more transient state, with smeared intensity. 98

5.7 Coefficient time-series plot for each of three basis images, with red dotted lines demonstrating individual transitions between Basis Image 1 and Basis Image 2. Note the plot is only showing frame 0 to 600. . . 99

5.8 **a** Simplified schematic of a current carrying, single turn copper microcoil, generating an out-of-plane magnetic field with the direction based on the current direction. The copper coil is embedded in an insulating material with a hole in the centre of the circular region to allow the TEM electron beam to transmit through the sample. **b** HC3500 cooling/heating TEM sample holder with annotations showing where a sample would sit and the circuit connections required to provide the electrical current to the microcoil. An acrylic prototype of the microcoil device is installed to demonstrate the geometry and flexibility required. 101

5.9 **a** Schematic of entire microcoil PCB, red regions are the copper trace. Rigid-flex PCB design has been used here, and each section is labelled accordingly. **b** Schematic of magnetic field generating section of microcoil device, inner and outer radii are labelled accordingly. The copper fin-like sections in this design are to reduce resistive heating effects, through heat distribution. **c** 3D render of the device and how it is able flex to fit into the TEM sample holder. All schematics were created in Altium Designer version 21.0.9. 103

5.10 **a** Professionally manufactured microcoil device. **b** Microcoil device installed within the TEM sample holder, with an actual sample in place. 104

5.11 Initial design of current pulser using a number of distinct components including HV switch, power supply and a TTL pulse generator. The components within the dashed box would be contained in an enclosure for safety reasons, and thus the electrical circuit should be embedded within a PCB. 105

5.12 **a** Workshop prototype of current pulser box for testing different components and current output profiles. Two additional components were added after initial testing, a load resistor (R_L) and buffer capacitor (C_B), labelled accordingly. **b** Circuit diagram schematic of the workshop prototype with the bi-directional switch in a high-side configuration. The pulse direction is given by the pulse shape, where the dotted line represents 0 V, and is determined by the HV terminals. For a $+$HV($-$HV) input a positive(negative) pulse is obtained. 106

5.13 **a** Schematic of the voltage-time signal as defined by the pulse generator, which is used as the input for the HV switch. **b** Schematics of signals measured across the microcoil device when using an additional load resistor (R_L) and a buffer capacitor (C_B). Ideally the output signal should match the TTL pulse, however due to impedance mismatch and an unbuffered HV power supply, there is a significant ringing effect as seen by the sharp signal oscillations. This ringing can be reduced through the use of $C_B = 10\ \mu$F across the $+$HV and $-$HV terminals and by increasing the load resistance using $R_L = 0.5\ \Omega$. **c** Oscilloscope trace of input TTL signal (yellow) and measured voltage across device (red). 107

5.14 Experimental setup for Fresnel TEM imaging with *in-situ* magnetic field pulses, consisting of the bespoke current pulser, HC3500 sample holder with the installed microcoil device and the JEOL ARM 200cF TEM.108

5.15 Magnetic field vs time schematics for preliminary experiments to test the microcoil and current pulser. Note that the pulse heights and durations are not to scale in either schematic. a An experiment to generate significant disorder within a SkX to create lattice defects. The static magnetic field from the objective lens is set below the SkX transition field (H_{SkX}) such that the magnetic field pulse from the microcoil temporarily stabilises the SkX phase. **b** An experiment to create controlled changes within the magnetic system during phase transitions initiated through step-changes in the static magnetic field provided by the objective lens (H_1, H_2, etc). In both experiments, Fresnel images are obtained over time at the points indicated by the red circles. 109

5.16 **a** Fresnel TEM image of a region of SkX containing a high density of 5-7 defects, outlined in white, where deformation of SkCoHs ranges from high (i) to low (j). **b** Fresnel TEM image showing a nontrivial SkX lattice defect involving a pair of 5-fold coordinated skyrmions. This defect represents a state prior to a regular 5-7 defect, which would be reached through merging of the two SkCoP, marked Sk_a and Sk_b. **c**,**d** Line profile plots of image intensity along the paths indicated by the green and blue dashed lines, respectively, in **b**. Fresnel images captured using Orius CCD camera, temperature of 213 K and static magnetic field of 0.137 T. 110

5.17 Fresnel TEM Images captured on Orius CCD camera showing skyrmion phase transitions occurring as the static magnetic field is increased. Images along the same row demonstrate how different metastable states become accessible using the magnetic field pulses generated by the microcoil. Scale bar is 200 nm. Annotations highlight important features, as described in the main text. 115

6.1 **a** Generic synthetic antiferromagnetic (SAF) system consiting of two ferromagnetic (FM) layers coupled antiferromagnetically through nonmagnetic (NM) heavy metal (HM) layers. In this system HM_1 and HM_2 provide desired magnetic interactions such as RKKY, DM and PMA, and the strength of these interactions will depend on the choice of metals and the thickness of the layers. **b** Vector schematic of a SAF skyrmion cross-section, where the skyrmion in the top FM layer has opposite topological charge, and is coupled, to the skyrmion in the bottom FM layer. The combination of these two coupled skyrmions forms the single SAF skyrmion, which has a total topological charge of zero. 123

6.2 Methods for creating unbalanced SAF systems, which exhibit non-zero magnetic contrast during LTEM imaging. In these schematics, the elemental composition of the FM and HM layers are the same as defined in the previous section. **a** SAF system is unbalanced by tuning the thickness ratio of the Co layers. The SAF can be unbalanced by holding t_2 constant whilst varying t_1. **b** Introduction of individual [Pt/Co/HM] subsystem repeat units above and below the Ru layer can create an unbalanced multilayer SAF when N_1 and N_2 are different. 125

6.3 **a** Schematic demonstrating the multilayer SAF geometry simulation configuration. The structure consists of two FM subsystems (red and blue layers), which exhibit FM IEC coupling between neighbouring layers within the subsystem. However, the two innermost layers have AFM coupling between them, enabling the anti-parallel spin alignment (shown by white arrows) between the subsystems. **b** MuMax3 simulation initial state example for $N_1 = 3$, $N_2 = 3$, coloured by m_z magnetisation. 127

6.4 Magnetisation scalar plots coloured by m_z, given by the colour bar, for each layer within the 3-layer unbalanced mSAFs, $N_1 = 1$ $N_2 = 2$ and $N_1 = 2$ $N_2 = 1$. Skyrmion radius is calculated using the contour of $m_z = 0$ in each layer. Annotated arrows highlight the type of IEC present between the corresponding layers, as implemented in the simulation. The BL field is acting in Layer 1, out of the plane of the page. 130

6.5 Magnetisation scalar plots coloured by m_z, given by the colour bar, for each layer within the 4-layer mSAFs, $N_1 = 1$ $N_2 = 3$, $N_1 = 2$ $N_2 = 2$ and $N_1 = 3$ $N_2 = 1$. Skyrmion radius is calculated using the contour of $m_z = 0$ in each layer. Annotated arrows highlight the AFM IEC present between the corresponding layers, the FM IEC is implied between all layers with parallel spin alignment. The BL field is acting in Layer 1, out of the plane of the page. 131

6.6 Magnetisation scalar plots coloured by m_z, given by the colour bar, for each layer within the 5-layer mSAFs, $N_1 = 1$ $N_2 = 4$, $N_1 = 2$ $N_2 = 3$, $N_1 = 3$ $N_2 = 2$ and $N_1 = 4$ $N_2 = 1$. Skyrmion radius is calculated using the contour of $m_z = 0$ in each layer. Annotated arrows highlight the AFM IEC present between the corresponding layers, the FM IEC is implied between all layers with parallel spin alignment. The BL field is acting in Layer 1, out of the plane of the page. 132

6.7 Magnetisation scalar plots coloured by m_z, given by the colour bar for mSAFs with different parameters. Although the scale is different in these figures, the simulation space is the same for all cases. **a** 7-layer mSAF with $J_{RKKY\ AFM} = -2.0\,\mathrm{mJ\,m^{-3}}$ **b** 7-layer mSAF with $J_{RKKY\ AFM} = 0.5\ \mathrm{mJ\ m^{-3}}$ **c** 8-layer mSAF with demagnetising field switched off in MuMax3. 133

6.8 Simulated Fresnel images of the **a** 1-1, **b** 1-2 and **c** 2-3 mSAF systems. Images were simulated using the python fpd package [**fpd**], with simulation parameters: spherical aberration $C_S = 0.5$ mm, defocus $\Delta f = 500\ \mu$m and 200 kV acceleration voltage. 134

6.9 Simulation layer setup for the different methods of investigating the enhanced PMA from a Co/C_{60} within a SAF system. **a** bSAF with effect of C_{60} introduced through modification of magnetic properties. The C_{60} is assumed to be in contact with the top Co layer in this case. **a** bSAF with a C_{60} layer explicitly simulated along with the modification of magnetic properties. The magnetic properties of the C_{60} layer will be defined and discussed in Section 6.2.2. 137

6.10 **a** 2D Scalar plots of the minimum energy magnetic configuration of the top (left) and bottom (right) Co layers in a SAF system that incorporates the effect of a Co/C_{60} interface. Each image corresponds to a simulation with a different value of ΔK_u added to the top Co layer. The panel with the black outline reflects the experimentally measured value of $\Delta K_u = 0.27$ MJ m^{-3} for the PMA enhancing effect. Coloured by m_z magnetisation as given by the colour bar. **b** Plot of skyrmion radius as a function of ΔK_u. The circled data points again reflect the experimentally measured PMA enhancing effect value of $\Delta K_u = 0.27$ MJ m^{-3}. 138

6.11 **a** 2D Scalar plots of the minimum energy magnetic configuration for C_{60} layer, top Co layer and bottom Co layer for some instructive values of ΔK_u. **b** Plot of skyrmion radius as a function of ΔK_u for each layer in the simulation. 141

6.12 Comparison plot of skyrmion radius as a function of ΔK_u when only the Co layers are simulated (No Cages) and when the C_60 layer is explicitly simulated (Cages). 143

Chapter 1

Introduction

Magnetic skyrmions have the potential to be at the forefront of a future paradigm shift in magnetic data transfer and storage technologies. Since their theoretical prediction in 2006 [1], and first real-space observation in 2010 [2], research involving skyrmions has been growing rapidly, as demonstrated in Fig. 1.1. The particle-like nature of skyrmions, and the fact that they can be easily propagated by electrical currents [3], means that skyrmions are an attractive entity for both information storage and transmission. Many of their proposed spintronic applications include: information storage in racetrack memory devices, information computing using so-called skyrmionic logic, and skyrmion neuromorphic devices [4]. However, for skyrmions to be used in such a manner, their dynamical behaviour and physical stability in different magnetic systems must be investigated and understood. This thesis is concerned with investigating and manipulating the stability and dynamic processes of magnetic skyrmions by utilising transmission electron microscopy with a high-speed imaging detector, and micromagnetic simulations. Image analysis techniques will be used to extract important configurational state and lifetime information, utilising a mix of image processing, visual analysis and automated state detection using machine learning techniques. Methods of inducing frustration and observing relaxation in a skyrmion lattice will be demonstrated through the application of *in-situ* high frequency magnetic field pulses. The stability of one of the most technologically promising skyrmion-hosting systems, namely multilayer synthetic antiferromagnets [5], will also be studied. The design of these multilayer systems will be explored through micromagnetic simulations, with a focus on those with metal-molecular interfaces, and how it is possible to tune skyrmion stability through multilayer engineering.

Chapter 2 introduces the main physical theories required for understanding and describing magnetic skyrmions. This begins with a general description of ferromagnetic materials, with considerations for thin-film nanoscale effects. This is followed

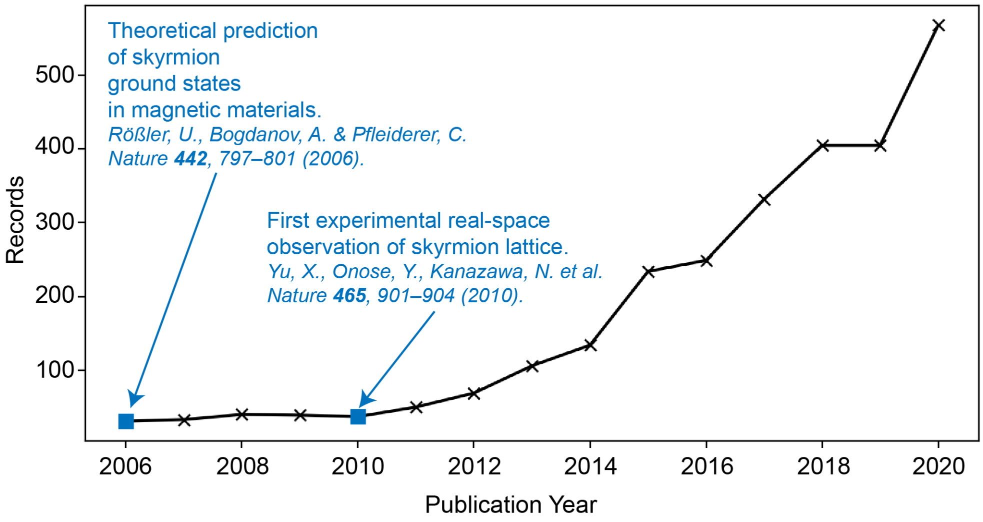

Figure 1.1: Estimation of skyrmion research output by publication year, using data from www.webofknowledge.com, generated on 06 June 2021. Plot shows the number of individual research records containing the keyword 'skyrmion' for each year, in the range 2006-2020. The trend shows that research involving skyrmions has been rising dramatically since 2010.

by a description of micromagnetic theory, the theoretical framework in which the magnetic systems within this thesis are described. Finally, magnetic skyrmions as topological magnetic spin textures are introduced and described in the context of micromagnetic theory.

Chapter 3 is concerned with describing the instrumentation and experimental methodology utilised in the results chapters of this thesis. This is broadly broken down into three aspects: data collection using transmission electron microscopy (TEM), sample preparation using focused ion beam microscopy (FIB) and micromagnetic simulation methods.

Chapter 4 is the first results chapter of the thesis and describes the investigation of spontaneous skyrmion dynamics. In order to understand the organisation of skyrmions within skyrmion crystal lattice (SkX), experimental observations of B20 FeGe using Lorentz TEM imaging methods and micromagnetic simulations of the emergent SkX are undertaken. This includes studies involving both isolated 5-7 defects and those present at SkX domain boundaries. The analysis of observed spontaneous skyrmion motion at a SkX domain boundary follows. Image and statistical analysis methods are used to identify the skyrmion states, the nature of transitions involved and to determine a relative energy landscape. Through image analysis, it is shown that the spontaneous transitions observed correspond to creation and annihilation of skyrmions, raising questions about topological charge conservation and skyrmion deformation. Finally, mechanisms for the creation and annihilation of skyrmions involving antiskyrmions are proposed, aided by micromagnetic simulations.

Chapter 5 presents the investigation of induced skyrmion dynamics. This begins with an extension of the image processing and analysis techniques used in the previous chapter. Methods implemented for detecting transient skyrmion states in the high-speed Fresnel image data include total variation (TV) denoising, frame subsampling and non-negative matrix factorisation (NMF). These methods enable an increase of image signal-to-noise ratio (SNR), and the automatic detection of skyrmion states involved in dynamic processes using machine learning. Next, the design and fabrication of a novel microcoil device and accompanying current pulser, to provide out-of-plane magnetic fields within the TEM, is described. Following this, experimental observations of significantly frustrated skyrmion defect states induced by the microcoil device's *in-situ* magnetic field pulses are presented and analysed.

Chapter 6 presents a series of micromagnetic studies on skyrmions in synthetic antiferromagnetic (SAF) systems, and the effect of including metal-molecular interfaces. This begins with a study on the stabilisation of skyrmions in multilayer SAFs systems, highlighting the destabilising effect of uncompensated dipolar interactions. Next, the inclusion of C_60 molecular layers in SAF systems is presented as a means to stabilise skyrmions through enhancement of perpendicular magnetocrystalline anisotropy (PMA). Finally, the C_{60} layers are explicitly simulated as weak magnetic layers, and a nontrivial behaviour involving skyrmion size is demonstrated.

Chapter 7 acts as a summary of the work undertaken in this thesis and attempts to highlight the promising future of skymionic research.

Bibliography

1. Rößler, U. K., Bogdanov, A. N. & Pfleiderer, C. Spontaneous skyrmion ground states in magnetic metals. *Nature* **442,** 797–801 (2006).
2. Yu, X. Z. *et al.* Real-space observation of a two-dimensional skyrmion crystal. *Nature* **465,** 901–904 (2010).
3. Woo, S. *et al.* Observation of room-temperature magnetic skyrmions and their current-driven dynamics in ultrathin metallic ferromagnets. *Nature Materials* **15,** 501–506 (2016).
4. Zhang, X. *et al.* Skyrmion-electronics: Writing, deleting, reading and processing magnetic skyrmions toward spintronic applications. *Journal of Physics: Condensed Matter* **32** (2020).
5. Zhang, X., Zhou, Y. & Ezawa, M. Magnetic bilayer-skyrmions without skyrmion Hall effect. *Nature Communications* **7** (2016).

Chapter 2

Skyrmions in Magnetic Systems

Introduction

This chapter is dedicated to providing the core theoretical details necessary to understand the ensuing research in this thesis. In order to properly describe magnetic skyrmions and how they emerge in magnetic systems, some general theory on magnetism must first be provided. We begin by introducing the theory of spontaneous magnetism, through exchange interactions in condensed matter systems. This is followed by a description of key energy terms within the micromagnetic framework, a powerful tool in studying micro- and nanoscale magnetic systems. Magnetic skyrmions will then be introduced, highlighting the different magnetic systems that host them. Finally, an overview of micromagnetic simulations will be provided in the context of simulating skyrmion-hosting systems.

2.1 Ferromagnetism and Exchange Interactions

Magnetism in condensed matter systems emerges from the collective behaviour of atomic magnetic moments, arising from the angular momentum of electrons. This can be understood semi-classically by applying Ampère's Law to the Bohr model of the atom, which together describe the magnetic moment associated with an electron's orbit. However, a complete explanation of macroscopic magnetism in solids requires extension to ensembles of localised or delocalised electrons, and depends heavily on the material's electronic band structure [1]. In non-magnetic materials, the number of spin up and spin down electrons are equivalent, and therefore no net magnetic moment arises. However, magnetic materials have an intrinsic imbalance between the number of spin up and spin down electrons, resulting in a non-zero net magnetic moment. Ferromagnetic materials, including iron, cobalt and nickel, are a class of materials that meet the Stoner criterion, which defines a critical point where energy is lowered by having a unequal number of spin up and spin down electrons. According to the Stoner criterion, parallel spin alignment is present in a material when the product of its density of states, which is the number of electrons occupying a particular energy interval per unit volume, and exchange integral is greater than unity [2, 3].

It is possible to define a vector quantity for the magnetisation within a material, $\mathbf{M}$, as the distribution of elementary magnetic moments, $d\mathbf{m}$, within a differential volume, dV:

$$\mathbf{M} = \frac{d\mathbf{m}}{dV} \tag{2.1}$$

Magnetisation may be further defined as a smoothly varying spatial quantity $\mathbf{M}(\mathbf{r})$, within the continuum limit, by ignoring variations arising from the atomic lattice. This assumption is a key constituent of the micromagnetics framework, and will be discussed in more detail in subsequent sections. The maximum magnetisation a material can have is when all of the magnetic moments are pointing in the same direction, and is known as the saturation magnetisation, $\mathrm{M_s}$.

Isolated and collective magnetic moments give rise to six distinct types of magnetic behaviour: paramagnetism, diamagnetism, ferromagnetism, antiferromagnetism, ferrimagnetism and superparamagnetism [4]. Since magnetism is intrinsic to electrons, all materials exhibit at least one of these forms of magnetic behaviours. The magnetic systems in this thesis are primarily dominated by ferromagnetic ordering, and as such it is the focus of this section.

A ferromagnetic material is characterised by spontaneous, nonzero magnetisation below a critical temperature, due to the long-range ordering and alignment of magnetic moments. This type of magnetic behaviour was first described phenomenologically by Pierre Weiss in 1907, through the introduction of a non-physical internal magnetic field, $\mathbf{H_W}$. This field is proportional to magnetisation and acts to align the internal magnetic moments:

$$\mathbf{H_W} = \gamma \mathbf{M} \tag{2.2}$$

where γ is the Weiss molecular field constant, on the order of 100 for strong ferromagnets [5]. The Weiss field, $\mathbf{H_W}$, must therefore take on huge values in order to explain the spontaneous magnetisation observed in some ferromagnets, such as NdFeB. Although no such physical field exists within these magnetic materials, the description remains useful as a classical approximation of magnetic ordering. Indeed, the phenomenological theory is able to accurately explain a wide range of magnetic phenomena including the temperature dependence of magnetisation in ferromagnets.

With the advent of quantum mechanics, Werner Heisenberg provided a full explanation of ferromagnetic behaviour in 1928. The phenomenologically determined Weiss field was found to be the result of strong electron-electron Coloumb interactions and the Pauli exclusion principle, which states that electrons are forbidden from occupying the same quantum state. The energy of two neighboring electron spins is given by the Heisenberg exchange Hamiltonian:

$$H_{ex} = -\sum_{i,j} J_{ij}(\mathbf{S_i} \cdot \mathbf{S_j}) \tag{2.3}$$

where $\mathrm{S_i}$ and $\mathrm{S_j}$ are the spins associated with neighbouring atoms at positions i and j and J_{ij} is the exchange constant. The sign of J_{ij} in Eq. 2.3 determines whether the material exhibits ferromagnetic or antiferromagnetic behaviour. If J_{ij} is positive then neighbouring spins will align parallel, minimising exchange energy. However, if J_{ij} is negative then neighbouring spins will instead align anti-parallel.

Although Eq. 2.3 is defined for localised electrons on adjacent atoms, it can be applied to more complicated long-range exchange mechanisms involving delocalised electrons. An example of this is the Ruderman–Kittel–Kasuya–Yosida (RKKY) interaction, in which the exchange constant, J_{RKKY}, may be oscillatory in nature. This gives rise to alternating ferro- and antiferromagnetic behaviour in magnetic multilayers containing nonmagnetic spacer layers, as a function of the spacer layer thickness [6]. The RKKY interaction will be further discussed in a subsequent section.

Antisymmetric exchange, also known as the Dzyaloshinskii–Moriya (DM) interaction, is another type of exchange interaction present in magnetic systems with strong spin-orbit coupling (SOC) and lacking spatial inversion symmetry [7, 8]. The Hamiltonian for the DM interaction is given by:

$$H_{DM} = -\sum_{i,j} \mathbf{D_{ij}} \cdot (\mathbf{S_i} \times \mathbf{S_j}) \tag{2.4}$$

where $\mathbf{D_{ij}}$ is the DM vector. By inspecting Eq. 2.4, we see that the DM interaction favours a perpendicular alignment of neighbouring spins. Therefore, the DM interaction in a ferromagnet is in direct competition with the Heisenberg exchange interaction (Eq. 2.3), which favours the parallel alignment of neighbouring spins. The DM interaction is a cause of weak ferromagnetic behaviour in antiferromagnets, but may also lead to the formation of chiral magnetic spin-spirals in ferromagnets due to the aforementioned competition with the Heisenberg exchange interaction. The DM interaction is integral to the formation of chiral magnetic skyrmions, and as such it will be discussed in more detail in a subsequent section.

2.2 Micromagnetic Theory

If magnetism in condensed matter systems were only determined by the symmetric exchange interactions (Eq. 2.3), then all spins would be aligned parallel (or antiparallel) to each other and the resulting magnetic configurations would be trivial. However, in most materials, other magnetic interactions are present and these must be taken into account to explain the complexity of observed magnetic configurations. Micromagnetics is a framework concerned with describing magnetic behaviour on the sub-μm length scale, but as a semi-classical approach it does not reach atomic length scales. In this framework, magnetism is represented as a continuously varying vector function, $\mathbf{M}(\mathbf{r})$, and is therefore a continuum approximation. For a particular magnetic material with saturation magnetisation M_s, the magnetisation unit vector is given by:

$$\mathbf{m}(\mathbf{r}) = \mathbf{M}(\mathbf{r})/M_s \tag{2.5}$$

The description of each magnetic interaction that follows is given in terms of either the normalised, $\mathbf{m}(\mathbf{r})$, or unnormalised, $\mathbf{M}(\mathbf{r})$, magnetisation.

For the majority of ferromagnetic materials the key energy terms consist of: magnetostatic (dipolar) energy, magnetocrystalline anisotropy energy, Zeeman energy and exchange energy. Exchange energy encompasses DMI and RKKY interactions in relevant systems that exhibit such phenomena. Summing and minimising these energy terms with respect to $\mathbf{m}(\mathbf{r})$ leads to stable or metastable magnetic configurations. Dynamic behaviour can also be modelled by combining the energy terms into the Landau–Lifshitz–Gilbert (LLG) equation, which will be described in the later section on micromagnetic simulations. Micromagnetic modelling allows for comparison between predicted magnetic configurations and those observed experimentally, and as such it is particularly effective when used in conjunction with experimental observation.

2.2.1 Exchange Energy

Although Eq. 2.3 provides the means to calculate exchange energy between two neighbouring spins, it needs to be extended to incorporate the exchange energy between all nearest neighbours within a magnetic system. In this case, exchange energy in the micromagnetic framework is given by:

$$E_{ex} = A \int_V ((\nabla m_x)^2 + (\nabla m_y)^2 + (\nabla m_z)^2) dV \tag{2.6}$$

where A is the exchange stiffness constant, m_x, m_y and m_z are the components of $\mathbf{m}$ and the integral is taken over the sample volume. The exchange stiffness constant,

A, incorporates the exchange constant, J, and thus the sign of A also determines whether the material exhibits ferro- or antiferromagnetic behaviour.

2.2.2 Demagnetising Energy

Aligned magnetic moments within a material are the source of an internal demagnetising field and external stray field. Inside a uniformly magnetised sample, such as the one shown in Fig. 2.1a, the magnetic moments are necessarily aligned antiparallel to the internal demagnetising field ($\mathbf{H_d}$). This acts to destabilise the magnetic ordering, and is thus a source of increased demagnetising energy. Therefore, the demagnetising field is in direct competition with ferromagnetic exchange, which tends to align magnetic moments. The demagnetising energy of a magnetic sample can be expressed as:

$$E_{demag} = -\frac{\mu_0}{2} \int_V \mathbf{H_d} \cdot \mathbf{M}(\mathbf{r}) \, dV \tag{2.7}$$

where $\mathbf{H_d}$ is the demagnetising field and the integral is taken over the sample volume. The demagnetising energy is the result of long-range dipolar interactions, and is dependent on the exact magnetisation configuration, making it difficult to calculate. To investigate the demagnetising field further, we can express it in terms of the magnetic scalar potential, ϕ_m, as:

$$\mathbf{H_d} = -\nabla \phi_m \tag{2.8}$$

The magnetic scalar potential can then be expressed in terms of volume $(-\nabla \cdot \mathrm{M})$ and surface $(\mathbf{n} \cdot \mathrm{M})$ poles, analogous to their electric counterparts:

$$\phi_m(\mathbf{r}) = -\frac{1}{4\pi} \int_V \frac{\nabla \cdot \mathbf{M}(\mathbf{r}')}{|\mathbf{r} - \mathbf{r}'|} dV + \frac{1}{4\pi} \int_S \frac{\mathbf{n} \cdot \mathbf{M}(\mathbf{r}')}{|\mathbf{r} - \mathbf{r}'|} dS \tag{2.9}$$

where $\mathbf{r}'$ is the variable to be integrated over the volume and surface, respectively. Equation 2.9 demonstrates that regions of converging and diverging magnetisation (left-most integral) as well as normal components of M at the surface (right-most integral) act as a source of the scalar potential, and therefore the demagnetising field. In the absence of an external magnetic field, minimising the sources of these magnetic poles will often lead to the most favourable magnetic configurations.

Figure 2.1a demonstrates how the internal demagnetising field interacts with the magnetic moments within a simple bar magnet. For certain geometries such as that shown in Fig. 2.1b, the direct competition between ferromagnetic exchange energy and demagnetising energy results in flux-closed magnetic configurations. These configurations consist of multiple regions of constant magnetisation, known as magnetic domains, which through their formation minimise magnetostatic energy. The domains are separated by regions of rotating magnetisation, known as domain walls (DWs). DWs are extremely well researched magnetic objects since they have an inherent stability and may even be manipulated by using electrical currents [9], making them technologically relevant magnetic structures in the field of spintronics. The situation of going from a single domain to two domains roughly halves the demagnetising energy due to the reduction in the stray field, however it is not possible to add domains indefinitely. There is an energy cost associated with DWs, due to the rotating magnetisation across the DW costing exchange energy. Thus, a real magnetic system will balance the total number of domains with the cost of each resulting DW.

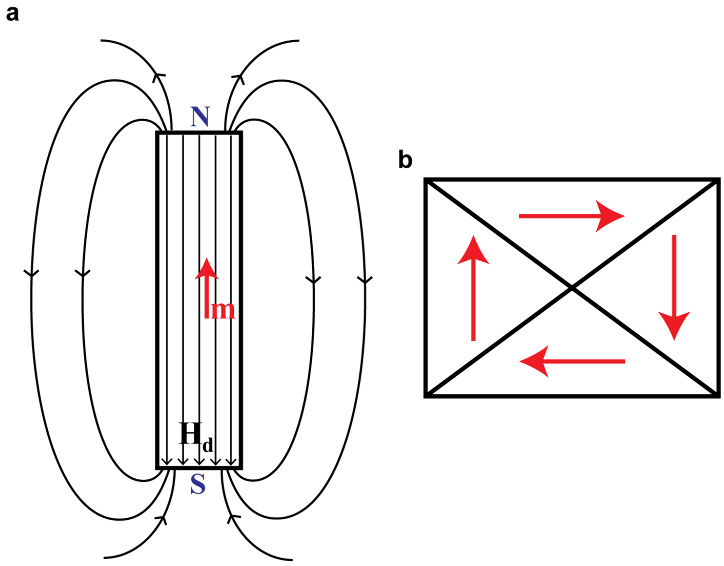

Figure 2.1: a Interaction of internal magnetic moments (red arrow) with the demagnetising field they create in a simple bar magnet and **b** a flux-closed magnetic configuration, which minimises demagnetising energy through the formation of magnetic domains.

2.2.3 Magnetocrystalline Anisotropy Energy

As the name suggests, magnetocrystalline anisotropy (MA) is a material property describing magnetisation variation due to crystal structure. The primary source of MA is from SOC, which is present in all atomic systems due to the relativistic interaction of electron spin with orbital motion. An isolated magnetic atom has spherical symmetry and so it can magnetise in any direction equally. However, once atoms are placed into a crystal structure, certain orbitals are electrostatically stabilised over others due to the electrostatic potential of the crystal. In this case, the electrons are now influenced by the nature of the lattice geometry and magnetic moments will tend to align along certain crystallographic directions. This leads to easy and hard axes, where lowest MA energy is associated with magnetisation aligned with easy axes. The symmetry of the crystal structure determines how many hard or easy axes are present, and their directions. The magnetocrystalline anisotropy energy for the uniaxial case, with a single easy axis, is given by:

$$E_{anis} = VK_u \sin^2\theta \tag{2.10}$$

where θ is the angle $\mathrm{M}(\mathbf{r})$ makes with the easy axis, V is the sample volume and K_u is a material specific constant with units of J m^{-3}. It is possible to reformulate Eq. 2.10 in terms of the easy axis and magnetisation vectors:

$$E_{anis} = -\int_V K_u(\mathbf{u} \cdot \mathbf{M}(\mathbf{r}))^2 dV \tag{2.11}$$

where $\mathbf{u}$ is the easy axis vector and the integral is taken over the sample volume.

Because MA is a spin-orbit effect, it is modified at surfaces or interfaces, where discontinuity in crystal structure occurs. For ultrathin films, it is important to decompose the total anisotropy into separate volume and surface terms:

$$K_u = K_v + \frac{K_s}{t} \tag{2.12}$$

where K_v is the volume anisotropy constant and t is the thickness. Clearly, as t is reduced the surface term starts to dominate, and can explain why a rotation from in-plane to out-of-plane magnetisation is seen as film thickness is reduced [10].

Shape anisotropy is an effect that arises from the aforementioned demagnetising field due to dipolar interactions and unlike MA is not determined by the crystal structure. However, shape anisotropy is often included into the MA energy term by using a geometry dependent demagnetising factor, N_d. The demagnetising factor is determined by the aspect ratio (shape) of the sample and is therefore particularly important when studying structures that have one or more dimensions on the nanoscale. For ultrathin films, with t on the order of 1 nm, these dipolar effects can be combined with the MA effects by defining an effective anisotropy constant, K_{eff}, which is given by [11]:

$$K_{eff} = K_u - \frac{\mu_0}{2} N_{dz} M_s^2 \tag{2.13}$$

where N_{dz} is the demagnetising factor in the z-direction and is equal to unity for ultrathin films and zero for a perfectly symmetrical sample. This allows us to rewrite Eq. 2.11 in terms of the film surface normal unit vector, $\mathbf{n}$, and effective anisotropy constant, K_{eff}, as:

$$E_{anis} = -\int_V K_{eff}(\mathbf{n} \cdot \mathbf{M}(\mathbf{r}))^2 dV \tag{2.14}$$

where a $K_{eff} < 0$ corresponds to in-plane easy axis and $K_{eff} > 0$ corresponds to an out-of-plane easy axis. This is another example of magnetic competition, where demagnetising effects arising from the sample shape are interacting with the MA effects. The implication of Eq. 2.14 is that it is, in principle, possible to achieve a desired anisotropy effect by tuning the thickness of thin films.

2.2.4 Zeeman Energy

The final interaction discussed here is the energy associated with placing a magnetic material within an external magnetic field. Magnetic moments will tend to align parallel to a magnetic field, provided that it is strong enough to disrupt the SOC of electrons. This is known as the Zeeman effect, and magnetic moments will minimise their Zeeman energy, E_Z, according to:

$$E_Z = -\mu_0 \mathbf{m} \cdot \mathbf{H_{ext}} \tag{2.15}$$

which can be extended to be given in terms of the magnetisation of the sample:

$$E_Z = -\mu_0 \int_V \mathbf{M}(\mathbf{r}) \cdot \mathbf{H_{ext}} \, dV \tag{2.16}$$

where $\mathbf{H_{ext}}$ is the applied external magnetic field and the integral is taken over the sample volume.

2.2.5 Magnetic Configurations

The interplay between each of the magnetic energy terms described above can be investigated through their effect on the resulting magnetic ground states of a simple idealised system. Figure 2.2a-d demonstrates how the ground state magnetic configuration might change depending on the different energies contributing to the total energy. If only E_{exch} is considered, the resulting magnetic configuration would be like that of Fig. 2.2a, with all magnetic moments aligned parallel. Including E_{demag} initiates the formation of domains, specifically flux-closed structures such as 2.2b. By considering uniaxial MA with an easy y-axis, magnetisation will tend to lie along this axis in order to minimise E_{anis}, as in Fig. 2.2c. Finally, by providing an external magnetic field and the addition of E_Z, domains will grow or shrink depending on whether their magnetisation is aligned parallel or antiparallel to the applied field, as shown in Fig. 2.2d.

Ultimately, the relative strengths of the magnetic interactions will dictate the interplay of these energy terms and thus the ground state magnetic configurations. A wealth of complexity in magnetic structures and textures can be found by considering only these four interactions, especially when competing terms are relatively close in energy. Domain walls, vortices, helices and magnetic skyrmions are examples of magnetic configurations that can be found in systems with competing magnetic interactions.

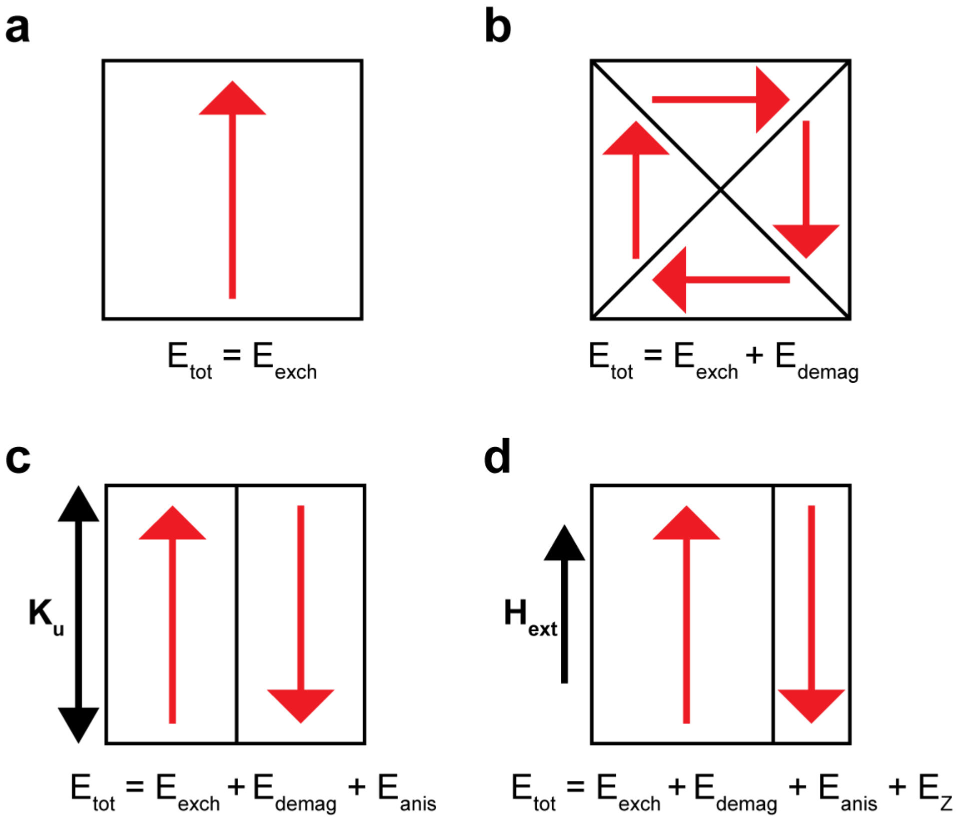
a
$E_{tot} = E_{exch}$
b
$E_{tot} = E_{exch} + E_{demag}$
c
K_u
$E_{tot} = E_{exch} + E_{demag} + E_{anis}$
d
H_{ext}
$E_{tot} = E_{exch} + E_{demag} + E_{anis} + E_Z$

Figure 2.2: Examples of simple magnetic configurations for a generic ferromagnet with different energies contributing to the total energy and minimum energy configuration. **a** Exchange energy only, **b** Exchange and demagnetising energies, **c** Exchange, demagnetising and MA energies, **d** Exchange, demagnetising, MA and Zeeman energies. The red arrows represent the magnetisation, M, within each domain.

2.3 RKKY Interaction

The Ruderman–Kittel–Kasuya–Yosida (RKKY) interaction is an example of an indirect exchange interaction between spatially separated magnetic moments. This interaction was first proposed by Ruderman and Kittel in 1954 [12], and later expanded upon by Kasuya and Yosida [13, 14]. Unlike symmetric and antisymmetric exchange, which are short-range interactions, RKKY acts over extended distances. These interactions involve the coupling of magnetic moments, separated by a distance r, via the conduction electrons in a non-magnetic material. The mechanism involves localised magnetic moments creating oscillatory magnetisation of the conduction electrons, which in turn interact with other, spatially separated, magnetic moments. The sign and approximate magnitude of the RKKY interaction is given in Ref. [4] as:

$$J_{RKKY}(r) \propto \frac{\cos(2rk_F)}{r^3} \tag{2.17}$$

where k_F is the Fermi sphere radius and $J_{RKKY}(r)$ is the separation dependent RKKY exchange constant. The derivation of Eq. 2.17 assumes a large r, when compared with atomic separation, and a spherical Fermi surface. RKKY is often included into the micromagnetic framework through scaling of existing exchange interactions.

As seen by Eq. 2.17, the exchange constant for this type of interaction is oscillatory in nature, depending on the separation distance of the two interacting magnetic subsystems. Varying the separation distance, r, enables one to favour either ferromagnetic (FM) or antiferromagnetic (AFM) coupling between the subsystems. For example, it has been shown that in Co/Ru/Co multilayers, the non-magnetic Ru layer provides RKKY-type interlayer exchange coupling (IEC) between the FM Co layers, with an AFM coupling peak at around 0.8 nm Ru thickness as given in Ref. [6]. This type of coupling allows for significant multilayer engineering and the development of systems with desirable magnetic properties. Chapter 6 will demonstrate how both FM and AFM IEC is fundamental to both the existence and stabilisation of skyrmions in multilayer synthetic antiferromagnetic (SAF) systems.

2.4 Nanoscale Magnetism

Nanoscale magnetism is the study of magnetic systems that have at least one object dimension less than 100 nm. This includes magnetic thin films (2D), nanowires (1D) and nanoparticles (0D) where the dimensionality, nD, describes the number of dimensions, n, which have lengths greater than 100 nm. As the size of dimensions are reduced, they may become comparable to characteristic length scales which can result in sharp transitions of magnetic behaviour. An example of such a transition is the superparamagnetic limit, whereby ferromagnetic nanoparticles become paramagnetic below a critical size, at which point it is no longer energetically favourable to contain DWs. Another such example is the aforementioned effective anisotropy transition, where magnetisation switches from in-plane to out-of-plane below a critical film thickness. These types of size-effects are not limited to magnetic systems, but are widespread across nanoscale condensed matter systems. For example, quantum dots are semiconducting nanoparticles that exhibit interesting optical phenomena only once their characteristic dimensions reach sub-100 nm due to quantum confinement effects [15]. When studying sufficiently small systems, step changes in behaviour may occur, and it becomes necessary to investigate the associated length scales.

An important characteristic length scale in magnetism is the exchange length, which describes the competition between the exchange interaction and the dipolar interactions. The exchange length is given by:

$$l_{ex} = \sqrt{\frac{A}{\mu_0 M_s^2}} \tag{2.18}$$

and typically has a magnitude in the range of 2-5 nm for many ferromagnets, as given in Ref. [1]. The exchange length is a particularly informative parameter, especially in micromagnetic theory, as it defines the length scale associated with uniform magnetisation in a ferromagnet.

Another characteristic length scale, which is of particular importance for systems involving DM interactions, is the helical length, L_D, given by:

$$L_D = 4\pi \frac{A}{|D|} \tag{2.19}$$

This describes the competition between exchange and DM interactions, and L_D is the length over which spins sweep 2π radians, for the helimagnet B20 FeGe, L_D is approximately 70 nm [16].

2.5 Magnetic Skyrmions

Skyrmions are topologically robust, particle-like solutions of nonlinear field theories [17], namely topological solitons. Originally proposed as a model of the nucleon by Tony Skyrme in 1962 [18], skyrmions have since been discovered as emergent structures across a range of condensed matter systems. These include superconductors [19], liquid crystals [20], and magnetic thin films [21]. Although the specific microscopic mechanisms governing the formation of skyrmions is different in each system, the emergent topological structures bear many similarities and skyrmions are therefore of a fundamental interest.

Magnetic skyrmions, henceforth referred to as skyrmions, are examples of such topological quasi-particles, arising in magnetic systems due to competing magnetic interactions [22–25]. It is possible to stabilise chiral skyrmions in multilayer systems containing ferromagnetic (FM)/heavy metal (HM) layers [26, 27] and bulk crystals with broken inversion symmetry [28], due to the aforementioned Dzyaloshinkii-Moriya (DM) interaction. These spin textures have a defined chirality (right- or left-handedness), as determined by the sign of the DM vector, $\mathbf{D_{ij}}$, as given in Eq. 2.4. Non-chiral skyrmions have also been stabilised in systems without the DM interaction, where the competition between other energy terms instead gives rise to skyrmion-like spin textures, such as bubble skyrmions [29]. These bubble skyrmions can be stabilised with either right- or left-handed spin rotation, and are often larger and less stable than skyrmions stabilised by the DM interaction [30]. The non-trivial topology of skyrmions can be characterised in terms of topological charge, or winding number, which takes on integer values according to:

$$N = \frac{1}{4\pi} \iint \mathbf{m} \cdot \left(\frac{\delta \mathbf{m}}{\delta x} \times \frac{\delta \mathbf{m}}{\delta y} \right) dxdy \tag{2.20}$$

where $\mathbf{m}$ is the local magnetisation unit vector. Equation 2.20 counts the number of times, given by N, that the magnetisation wraps a unit sphere (as demonstrated in Fig. 2.4c). The topological nature of skyrmions gives them high physical stability [31], and the ability to be propagated at low current densities [32]. Furthermore, the discrete nature of topological charge means that it is possible to determine a simple set of topological charge conservation rules, whereby changes to and interactions between topological structures will occur in the same discrete steps [33]. These properties position skyrmions as robust and versatile information carriers, especially in low-power spintronic devices [34].

2.5.1 Dzyaloshinkii-Moriya Interaction

Magnetic systems lacking spatial inversion symmetry and with strong SOC may host the relativistic DM interaction, an antisymmetric exchange interaction as defined by Dzyaloshinskii and Moriya in Refs. [7] and [8]. Competition between the DM interaction and the Heisenberg exchange interaction leads to spin canting, and the emergence of skyrmion structures under favourable conditions of temperature and magnetic field [35].

The Hamiltonian for the DM interaction was given in Eq. 2.4 and relates to the spin geometry shown schematically in Fig. 2.3a. This schematic demonstrates the DM interaction between spins $\mathbf{S_i}$ and $\mathbf{S_j}$, mediated by a third non-magnetic atom with high SOC (orange circle). The DM vector, $\mathbf{D_{ij}}$, is oriented perpendicular to the triangle formed by these three atoms. When translated to real material systems, $\mathbf{D_{ij}}$ may point perpendicular to the plane of the system as in Fig. 2.3b, stabilising Bloch-type skyrmions, or parallel to the plane as in Fig. 2.3c, stabilising Néel-type skyrmions. For a particular system, the sign of $\mathbf{D_{ij}}$ determines the chirality of the magnetic texture, namely a clockwise (CW) or counterclockwise (CCW) rotation of spins. The relative strength, sign and direction of the DM interaction determines whether it is possible to stabilise chiral skyrmions in a particular system, and also determines their type and size [30, 36].

Vector plots of Bloch and Neél-type skyrmions are shown in Fig. 2.4a,b respectively, where the difference between the distribution of spins is immediately evident. However, Fig. 2.4c shows how the spins on both of these skyrmion structures may be exactly mapped to a unit sphere, as described mathematically in Eq. 2.20, highlighting their topological equivalence.

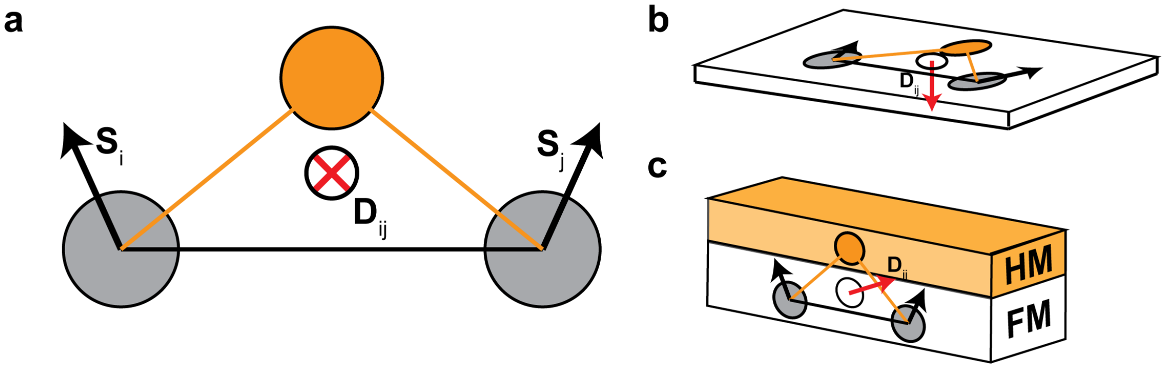

Figure 2.3: **a** The DM interaction between two ferromagnetic atoms (grey) and a high SOC atom (orange). The $\mathbf{D_{ij}}$ vector points perpendicular to $\mathbf{S_{i,j}}$, favouring clockwise or counterclockwise spin rotation depending on the sign of $\mathbf{D_{ij}}$. **b**,**c** Orientation of $\mathbf{D_{ij}}$ relative to magnetic film, favouring formation of Bloch and Néel skyrmions, respectively. The labels in **c** refer to heavy metal (HM) and ferromagnetic (FM) layers.

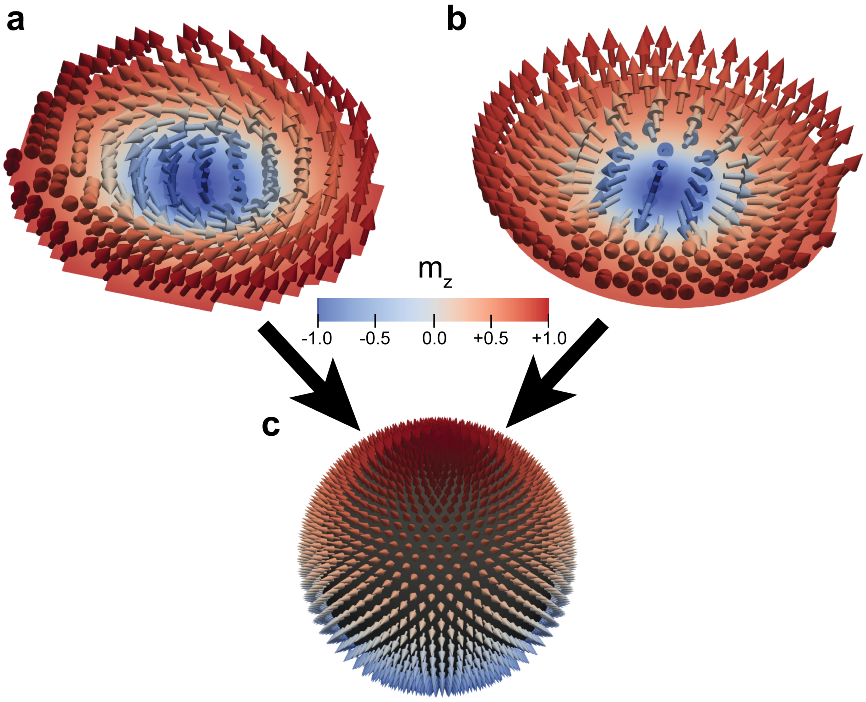

Figure 2.4: Vector plots of a **a** Bloch skyrmion, **b** Neél skyrmion and **c** how their magnetisation can be mapped to a unit sphere, demonstrating their non-trivial topology. Magnetic moments are coloured according to their m_z magnetisation.

2.5.2 Skyrmions in Non-Centrosymmetric Magnets

Common skyrmion-hosting materials include non-centrosymmetric magnets with the B20 crystal structure, including iron germanium (FeGe) and manganese monosilicide (MnSi) [37]. The lack of spatial inversion symmetry inherent to the crystal structure, and presence of heavy metals with large SOC results in a significant DM interaction [38]. Competition with the Heisenberg exchange interaction leads to a noncollinear arrangement of spins into a helical ground state with wave-vector, **q**, pointing along the axis of spin rotation. This type magnetic ordering is known as helimagnetism, and materials that display this type of ordering are known as helimagnets. The chirality of the B20 crystal structure determines whether CW or CCW helimagnetism is present, which in turn is translated to the chirality of any emerging skyrmions. In the B20 helimagnets, skyrmions exist within a distinct region of field-temperature-thickness phase space, and before skyrmions were definitively discovered this anomalous phase was simply referred to as the A-phase [39]. It is possible to navigate between a number of different magnetic phases through varying the magnetic field, for samples of a constant thickness at a constant temperature as demonstrated in Fig. 2.5.

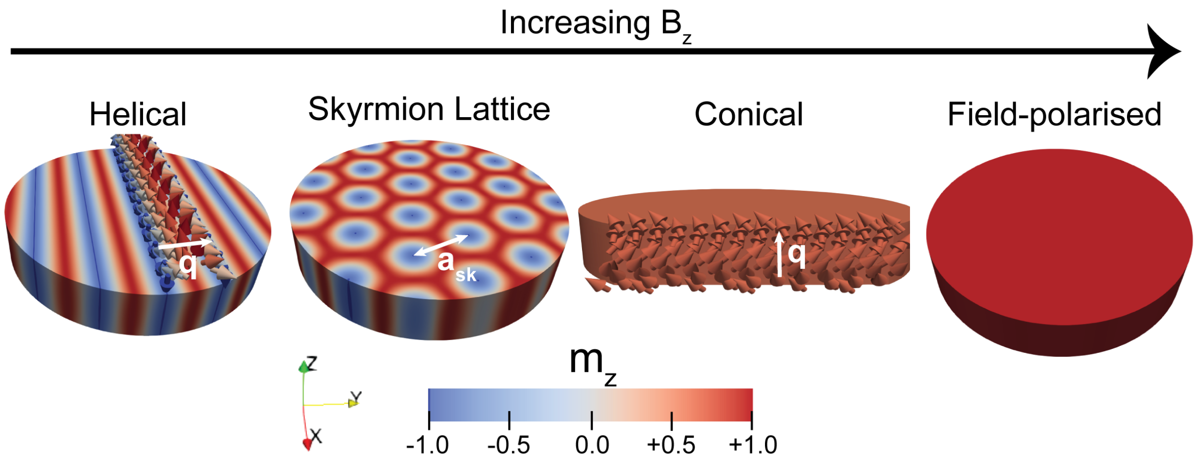

Figure 2.5: A mix of vector and scalar diagrams demonstrating the different magnetic phases in B20 helimagnets, accessed by varying the applied perpendicular magnetic field strength. As field is increased, it is possible to transition between the helical, skyrmion lattice, conical and saturated phases. This is assuming a region of uniform thickness at a constant temperature.

The hexagonal skyrmion lattice (SkX) phase, as shown in Fig. 2.5, can be reached by a phase transition from the helical phase on application of a perpendicular external magnetic field, at temperatures below the material's Curie temperature, and thicknesses on the order of L_D. On further increase of the external magnetic field, the system will transition first to a conical, and finally field-polarised state. The field-temperature-thickness phase space was explored in Ref. [35], and can be seen in Figure 2.6. The SkX is stable in a relatively small region of the phase space, but this can be expanded by decreasing the thickness of the sample. This behaviour has been attributed to the presence of stabilising surface twist states, which occupy a larger fraction of the total z-thickness for thinner samples [40]. Furthermore, it has been demonstrated that individual skyrmions inherit a hexagonal symmetry from the SkX, with the SkX lattice parameter a_{Sk} (as defined in Fig. 2.5) being dependent on the magnetic field strength used to stabilise the SkX [41].

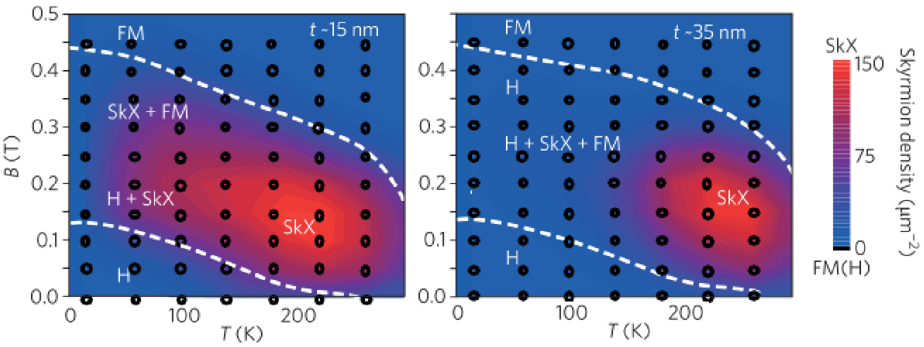

Figure 2.6: Phase diagram of FeGe showing the stability of the skyrmion lattice (SkX) as a function of magnetic field and temperature for sample varying thickness. Reproduced with permission from Ref. [35], Springer Nature.

2.5.3 Skyrmions in Thin Film Multilayers

Néel skyrmions, as previously shown in Fig. 2.4b, can be stabilised at the interface between FM and HM layers, due to the interfacial DM interaction. At these FM/HM interfaces, inversion symmetry is broken and significant SOC provided by the HM layer leads to a non-vanishing DMI. Because this DM interaction arises due to the interfacial effects, the layers must be thin (on the order of the exchange length), otherwise the strength of the effect will be diminished, as described in Ref. [27].

The sign and amplitude of D_{ij} in these multilayer systems is determined by the heavy metal at the interface and the order and size of the layers [42]. Because of this, it is possible to enhance and tune the net interfacial DM interaction by creating HM_1-FM-HM_2 multilayer systems. In such systems, HM_1 and HM_2 provide D_{ij} of opposite signs, which combine additively due to the stacking order [43, 44]. Furthermore, these magnetic multilayer systems typically demonstrate significant PMA, due to the fact that the thickness of the layers are on the order of 1 nm. This can provide additional means of creating skyrmion-hosting multilayer systems, since PMA has been shown to have a skyrmion stabilising effect [45]. However, because the resulting magnetic interactions are so sensitive to the exact details (thickness, roughness, composition) of all layers, any inhomogeneity arising from synthesis can be expected to result in deviations from the expected magnetic behaviour.

The ability to tune different magnetic interactions in multilayer systems give access to a range of key skyrmion properties, such as size and stability. For example, it has recently been demonstrated that it is possible to stabilise synthetic antiferromagnetic (SAF) skyrmions in carefully engineered magnetic multilayers [46], highlighting the versatility that these multilayer systems provide.

2.6 Micromagnetic Simulation Methods

A significant portion of the work in this thesis utilises micromagnetic simulations, specifically using the GPU-accelerated software MuMax3 [47]. As such, the following section provides the general principles and theory associated with simulating magnetic materials, with specific reference to MuMax3 where necessary.

The four magnetic interactions described in the micromagnetic framework: exchange, demagnetising, magnetocrystalline anisotropy and Zeeman energies can be combined to describe an arbitrary number of magnetic systems using numerical techniques. The total energy of a magnetic system in the presence of a magnetic field can be given by:

$$E_{tot} = E_{ex} + E_{demag} + E_{anis} + E_{Zeeman} \tag{2.21}$$

where E_{ex} includes any additional exchange effects such as the DM and RKKY interactions.

The basis of the finite difference simulation approach is to treat the magnetic moments within a sample as a continuously varying vector, $\mathbf{m} = \mathbf{m}(x, y, z)$, and then discretising into cuboidal simulation cells, the sides of which are larger than the relevant atomic distances. The total energy, E_{tot}, of a magnetic state can then be found by summing the energy calculated for each cell.

The choice of cell size is usually informed by the relevant length scales on which magnetisation can be assumed to be uniform, for example the exchange length as defined previously in Eq. 2.18. In fact, the exchange length is often used as an upper limit for discretisation of the simulation space [48]. However, when simulating helimagnetic materials with a non-zero DM interaction, the helical length (Eq. 2.19) gives a better indication for simulation discretisation. This is due to the fact that in such systems there is significant spin canting, compared to systems without the DM interaction. In order to ensure the validity of simulation results, the cell size must be chosen appropriately, particularly when calculating exchange energies as described in Ref. [47]. Furthermore, because the simulation cells are always cuboids, it can be difficult to simulate curved structures. For these types of geometries it is often more appropriate to use finite element simulation methods, which discretise the simulation space into a mesh of tetrahedra [49].

Spin dynamics can be introduced to the micromagnetic simulations by using the Landau-Lifshitz-Gilbert (LLG) equation given by:

$$\frac{d\mathbf{M}}{dt} = -\frac{\gamma}{1+\alpha^2}\mathbf{m} \times \mathbf{H_{eff}} - \frac{\alpha\gamma}{1+\alpha^2}\mathbf{m} \times (\mathbf{m} \times \mathbf{H_{eff}}) \tag{2.22}$$

where γ is the gyromagnetic ratio, α is the damping constant and $\mathbf{H_{eff}}$ is the effective field felt by the local magnetisation. The effective field can be calculated by summing the relevant energy terms, as in Eq. 2.21, and taking the derivative with respect to the direction of the magnetisation vector:

$$\mathbf{H_{eff}} = -\frac{1}{\mu_0 M_s}\frac{dE_{tot}}{d\mathbf{m}} \tag{2.23}$$

Dynamical effects can then be modelled by advancing the LLG equation (Eq. 2.22), which in MuMax3 can be performed by a range of different solvers. Minimum energy configuration states may also be found by disabling the precessional term (first term in Eq. 2.22) such that $\mathbf{H_{eff}}$ points in the direction of decreasing energy and advancing time until the total energy reaches the numerical noise floor.

Although MuMax3 has functionality to combine all of the energy terms described in Eq. 2.21, it can also include user defined custom energy terms. This is particularly important when simulating more complex multilayer systems containing non-magnetic spacer layers and interlayer exchange coupling. Such systems are studied using MuMax3 in Chapter 6, and as such custom energy terms are required to model the systems with sufficient validity.

The robustness of micromagnetic code is typically verified using a series of micromagnetic standard problems, however these do not typically contain systems hosting the DM interactions. Recently, standard problems were proposed for such DM interaction hosting materials, and demonstrated the validity micromagnetic simulation codes, including MuMax3, when simulating such systems [50].

Bibliography

1. Coey, J. M. *Magnetism and magnetic materials* (Cambridge University Press, 2010).
2. Stoner, E. C. Collective Electron Ferromagnetism. *Proceedings of the Royal Society of London. Series A. Mathematical and Physical Sciences* **165,** 372–414 (1938).
3. Stoner, E. C. Collective Electron Ferromagnetism II. Energy and specific heat. *Proceedings of the Royal Society of London. Series A. Mathematical and Physical Sciences* **169,** 339–371 (Feb. 1939).
4. Blundell, S. & Thouless, D. Magnetism in Condensed Matter. *American Journal of Physics* (2003).
5. Spaldin, N. A. *Magnetic materials: Fundamentals and applications* (Cambridge University Press, 2010).
6. Bloemen, P. J., Van Kesteren, H. W., Swagten, H. J. & De Jonge, W. J. Oscillatory interlayer exchange coupling in Co/Ru multilayers and bilayers. *Physical Review B* **50,** 13505–13514 (1994).
7. Dzyaloshinsky, I. A thermodynamic theory of "weak" ferromagnetism of antiferromagnetics. *Journal of Physics and Chemistry of Solids* **4,** 241–255 (Jan. 1958).
8. Moriya, T. Anisotropic superexchange interaction and weak ferromagnetism. *Physical Review* (1960).
9. Tatara, G. & Kohno, H. Theory of Current-Driven Domain Wall Motion: Spin Transfer versus Momentum Transfer. *Physical Review Letters* **92** (2004).
10. Hashimoto, S., Ochiai, Y. & Aso, K. Perpendicular magnetic anisotropy and magnetostriction of sputtered Co/Pd and Co/Pt multilayered films. *Journal of Applied Physics* **66,** 4909–4916 (Aug. 1989).

11. Lim, S. T., Tran, M., Chenchen, J. W., Ying, J. F. & Han, G. Effect of different seed layers with varying Co and Pt thicknesses on the magnetic properties of Co/Pt multilayers. *Journal of Applied Physics* **117,** 17–731 (2015).
12. Ruderman, M. A. & Kittel, C. Indirect exchange coupling of nuclear magnetic moments by conduction electrons. *Physical Review* **96,** 99–102 (Oct. 1954).
13. Kasuya, T. A Theory of Metallic Ferro- and Antiferromagnetism on Zener's Model. *Progress of Theoretical Physics* **16,** 45–57 (July 1956).
14. Yosida, K. Magnetic properties of Cu-Mn alloys. *Physical Review* **106,** 893–898 (June 1957).
15. Protesescu, L. *et al.* Nanocrystals of Cesium Lead Halide Perovskites (CsPbX3, X = Cl, Br, and I): Novel Optoelectronic Materials Showing Bright Emission with Wide Color Gamut. *Nano Letters* **15,** 3692–3696 (June 2015).
16. Beg, M. *et al.* Ground state search, hysteretic behaviour, and reversal mechanism of skyrmionic textures in confined helimagnetic nanostructures. *Scientific Reports* **5** (2015).
17. Manton, N. & Sutcliffe, P. *Topological solitons* (Cambridge University Press, 2004).
18. Skyrme, T. H. A unified field theory of mesons and baryons. *Nuclear Physics* **31** (1962).
19. Garaud, J. & Babaev, E. Skyrmionic state and stable half-quantum vortices in chiral p -wave superconductors. *Physical Review B* **86,** 060514 (Aug. 2012).
20. Fukuda, J. I. & Žumer, S. Quasi-two-dimensional Skyrmion lattices in a chiral nematic liquid crystal. *Nature Communications* **2** (2011).
21. Kiselev, N. S., Bogdanov, A. N., Schäfer, R. & Röler, U. K. Chiral skyrmions in thin magnetic films: New objects for magnetic storage technologies? *Journal of Physics D: Applied Physics* **44,** 392001 (Oct. 2011).
22. Lin, Y. S., Grundy, P. J. & Giess, E. A. Bubble domains in magnetostatically coupled garnet films. *Applied Physics Letters* **23,** 485–487 (Oct. 1973).
23. Rößler, U. K., Bogdanov, A. N. & Pfleiderer, C. Spontaneous skyrmion ground states in magnetic metals. *Nature* **442,** 797–801 (2006).
24. Heinze, S. *et al.* Spontaneous atomic-scale magnetic skyrmion lattice in two dimensions. *Nature Physics* **7,** 713–718 (2011).
25. Okubo, T., Chung, S. & Kawamura, H. Multiple-q states and the Skyrmion lattice of the triangular-lattice Heisenberg antiferromagnet under magnetic fields. *Physical Review Letters* **108** (2012).

26. Dupé, B., Hoffmann, M., Paillard, C. & Heinze, S. Tailoring magnetic skyrmions in ultra-thin transition metal films. *Nature Communications* **5** (2014).
27. Yang, H., Thiaville, A., Rohart, S., Fert, A. & Chshiev, M. Anatomy of Dzyaloshinskii-Moriya Interaction at Co/Pt Interfaces. *Physical Review Letters* **115** (2015).
28. Mühlbauer, S. *et al.* Skyrmion lattice in a chiral magnet. *Science* **323,** 915–919 (2009).
29. Liu, T. *et al.* Reproducible formation of single magnetic bubbles in an array of patterned dots. *Journal of Physics D: Applied Physics* **49,** 245002 (May 2016).
30. Wang, X. S., Yuan, H. Y. & Wang, X. R. A theory on skyrmion size. *Communications Physics* **1,** 1–7 (Dec. 2018).
31. Karube, K. *et al.* Robust metastable skyrmions and their triangular-square lattice structural transition in a high-temperature chiral magnet. *Nature Materials* **15,** 1237–1242 (Dec. 2016).
32. Jonietz, F. *et al.* Spin transfer torques in MnSi at ultralow current densities. *Science* **330** (2010).
33. Garanin, D. A., Chudnovsky, E. M. & Zhang, X. Skyrmion clusters from Bloch lines in ferromagnetic films. *Epl* **120** (2017).
34. Fert, A., Reyren, N. & Cros, V. Magnetic skyrmions: Advances in physics and potential applications. *Nature Reviews Materials* **2** (2017).
35. Yu, X. Z. *et al.* Near room-temperature formation of a skyrmion crystal in thin-films of the helimagnet FeGe. *Nature Materials* **10,** 106–109 (2011).
36. Nagaosa, N. & Tokura, Y. Topological properties and dynamics of magnetic skyrmions. *Nature Nanotechnology* **8,** 899–911 (2013).
37. Bak, P. & Jensen, M. H. Theory of helical magnetic structures and phase transitions in MnSi and FeGe. *Journal of Physics C: Solid State Physics* **13** (1980).
38. Rößler, U. K., Leonov, A. A. & Bogdanov, A. N. Chiral skyrmionic matter in non-centrosymmetric magnets. *Journal of Physics: Conference Series* **303** (2011).
39. Ishikawa, Y. & Arai, M. Magnetic Phase Diagram of MnSi near Critical Temperature Studied by Neutron Small Angle Scattering. *Journal of the Physical Society of Japan* **53,** 2726–2733 (1984).
40. McGrouther, D. *et al.* Internal structure of hexagonal skyrmion lattices in cubic helimagnets. *New Journal of Physics* **18** (2016).
41. Shibata, K. *et al.* Temperature and Magnetic Field Dependence of the Internal and Lattice Structures of Skyrmions by Off-Axis Electron Holography. *Physical Review Letters* **118** (2017).

42. Yamamoto, K. *et al.* Interfacial Dzyaloshinskii-Moriya interaction and orbital magnetic moments of metallic multilayer films. *AIP Advances* **7,** 056302 (2017).
43. Hrabec, A. *et al.* Measuring and tailoring the Dzyaloshinskii-Moriya interaction in perpendicularly magnetized thin films. *Physical Review B - Condensed Matter and Materials Physics* **90,** 20402 (2014).
44. Moreau-Luchaire, C. *et al.* Additive interfacial chiral interaction in multilayers for stabilization of small individual skyrmions at room temperature. *Nature Nanotechnology* **11,** 444–448 (2016).
45. Guslienko, K. Y. Skyrmion State Stability in Magnetic Nanodots With Perpendicular Anisotropy. *IEEE Magnetics Letters* **6** (2015).
46. Legrand, W. *et al.* Room-temperature stabilization of magnetic skyrmions in synthetic antiferromagnets. *Nature Materials,* 1–23 (Sept. 2018).
47. Vansteenkiste, A. *et al.* The design and verification of MuMax3. *AIP Advances* **4,** 107133 (2014).
48. Donahue, M. J. & Porter, D. G. Exchange energy formulations for 3D micromagnetics. *Physica B: Condensed Matter* **343,** 177–183 (2004).
49. Fischbacher, T., Franchin, M., Bordignon, G. & Fangohr, H. A systematic approach to multiphysics extensions of finite-element-based micromagnetic simulations: Nmag. *IEEE Transactions on Magnetics* **43,** 2896–2898 (2007).
50. Cortés-Ortuño, D. *et al.* Proposal for a micromagnetic standard problem for materials with Dzyaloshinskii-Moriya interaction. *New Journal of Physics* **20,** 113015 (2018).

Chapter 3

Instrumentation and Methodology

Introduction

In this chapter, the different instruments and methodologies used within the thesis will be described. Firstly, the basic history and construction of the transmission electron microscope (TEM) will be outlined. This will include a description of the image formation process in the TEM, with comparison to the scanning transmission electron microscope (STEM). The use of direct electron detectors in the TEM, with a focus on high-speed imaging will follow. Magnetic imaging in the TEM will then be introduced, and the main magnetic imaging methods used in this thesis will be outlined. Finally, TEM sample preparation using focused ion beam (FIB) milling will be described.

All TEM work in this thesis was carried out on the JEOL ARM 200cF with either the Orius CCD camera or the Merlin direct electron detector. Sample preparation was carried out on the FEI Nova 200 Ga^+ dual beam FIB. Magnetic nanostructures were grown using the FEI Helios Xe dual beam PFIB. All instruments are located in the Materials and Condensed Matter Physics (MCMP) group at the University of Glasgow.

3.1 Transmission Electron Microscopy

In its most basic construction, a microscope consists of a series of aligned lenses (often made of glass or plastic) that act to refract light and thereby generate magnified images of objects. The term microscope was coined by German botanist Giovanni Faber in 1625 to describe the compound microscope designed by Galileo Galilei. Almost 400 years later, the visible light microscope (VLM) is still used by scientists of all disciplines to gain insight into details otherwise obscured from experimental observation. One major drawback with the VLM however, is that it utilises visible light, which has a fundamental resolution limit of around 200 nm. This is given by the Abbe diffraction limit, which approximates to:

$$\delta = \frac{0.61\lambda}{\mu \sin\beta} \tag{3.1}$$

where δ is the smallest distance between individually distinguishable features, λ is the wavelength of electromagnetic radiation, and the quantity $\mu \sin\beta$ is known as the numerical aperture (NA) of the optical system and takes on values of approximately unity [1]. What this means practically, is that features separated by less than 200 nm would not be observable as distinct objects in a VLM image. By inspecting Eq. 3.1, it follows that by reducing the wavelength of radiation, one may improve the imaging resolution.

The advent of quantum mechanics and conception of the wave–particle duality provided the means of harnessing such low-wavelength radiation. In 1924 Louis de Broglie proposed that all matter may be described as having wave-like properties, and this relationship is given by de Broglie's surprisingly simple equation:

$$\lambda = \frac{h}{p} \tag{3.2}$$

where λ is the de Broglie wavelength, h is Planck's constant and p is the particle's momentum. By 1928, the wave–particle duality hypothesis had been confirmed in two separate experiments [2, 3], the second of which was carried out by Davisson and Germer and involved the scattering of electrons from a nickel surface and formation a diffraction pattern. Thus, the natural duality between particles and waves was confirmed, and with it a means to assign any quantum entity a corresponding momentum and wavelength. The consequence of this duality for electron imaging is that electrons can be described as waves with a defined wavelength, and these electron waves may interact with matter through diffraction effects.

By incorporating Einsteins theory of special relativity, to account for the relativistic effects of the electrons, it can be shown that the wavelength of an electron accelerated by a voltage V is given by:

$$\lambda = \frac{h}{\left[2m_0 eV(1 + \frac{eV}{2m_0 c^2})\right]^{\frac{1}{2}}} \tag{3.3}$$

where m_0 is the rest mass of the electron, e is the electronic charge of the electron and c is the speed of light in a vacuum. Inserting a common accelerating voltage of 200 kV for a traditional transmission electron microscope (TEM), we can see that the corresponding electron wavelength is 0.002 nm, which is an order of magnitude less than the radius of the carbon atom (0.070 nm [4]). Therefore, under appropriate imaging conditions, it should be possible to resolve individual atoms using electron radiation. Furthermore, the Davisson–Germer experiment demonstrated that electrons scattered from a specimen contained information regarding its atomic structure, via the resulting diffraction pattern. These diffraction patterns can be understood as constructive interference of the electron radiation at the Bragg condition:

$$n\lambda = 2d\sin(\theta) \tag{3.4}$$

where n is an integer termed the diffraction order, λ is the electron wavelength and d is the atomic plane spacing. θ is defined as the angle of incident radiation (and scattered radiation), with respect to the atomic plane. The diffraction condition defined when Eq. 3.4 is satisfied generates maximum constructive interference, and is the basis of both bright field (BF) and dark field (DF) structural imaging in the TEM.

By 1933, only five years after experimental confirmation of the wave nature of electrons, physicist Ernst Ruska and electrical engineer Max Knoll had built the first electron microscope, which exceeded the resolution limit of the VLM [5]. It did not however, reach the resolution limit of electrons described for diffraction above. Almost a century later, and modern TEMs bear many similarities with Ruska's original design, through focusing electron waves using electromagnetic lenses. However, there have been many improvements, modifications and additions to the original TEM design, primarily in the form of lens aberration corrector systems, which have drastically improved electron optics within the TEM. Unlike the VLM, image resolution in the TEM is primarily limited by aberrations caused by the imperfect electromagnetic lenses. By utilising complex corrector systems, consisting of multipole lenses, it has been possible to reach sub-nm resolution [6]. The TEM therefore lends itself to investigation of condensed matter systems, by providing resolutions on the order of atomic separation, allowing the detailed observational study of physical phenomena on the nm and sub-nm scale.

3.1.1 Conventional Transmission Electron Microscope

With the intention of expanding the description of electron microscopy to include magnetic imaging, that which has been introduced as transmission electron microscopy will henceforth be referred to as conventional transmission electron microscopy (CTEM) within this chapter. CTEM involves obtaining information about a specimen's microscopic structure as electron waves are transmitted through the specimen, interacting with its projected electrostatic potential. The fundamentals of the TEM do not differ between magnetic and non-magnetic imaging, only the ways in which the components are utilised and how the images are interpreted. As such, the general construction of the TEM and the main steps in CTEM imaging will be discussed here and then modified to include magnetic imaging later.

In CTEM, the fundamental imaging process can be broken down into the following steps. Firstly, within the electron gun at the top of the TEM column, electrons are produced by a source, accelerated and then focused into an initial beam. Two main classes of electron gun exist: thermionic and field-emission guns, where field-emission guns (FEGs) tend to produce much more coherent electron beams. Note, the experimental work in this thesis was performed on the JEOL ARM 200cF, which hosts a FEG and therefore benefits from the increased electron coherency and brightness that FEGs provide. Next, the electron beam is focused further using a series of electromagnetic lenses, apertures and coils, before being transmitted through the specimen. At this point, the phase and amplitude of the transmitted electron wave is modified by the specimen's electrostatic potential. During this process the electrons obtain information about the structure and composition of the specimen through elastic and inelastic interactions. Finally, the transmitted electron beam is focused and magnified before being imaged, often by a phosphorescent screen coupled to a charge-coupled device (CCD) camera.

A simplified schematic of a CTEM system can be seen in Figure 3.1a, a few of the main components will be discussed. The condenser (C1 and C2) lenses are involved in probe formation, eg illuminating the sample. The beam shift and tilt coils provide small adjustments to the electron beam, through magnetic fields in the x- and y-directions. The shift and tilt coils allow the electron beam to travel along the optic axis of the different electromagnetic lenses, even if those are physically misaligned. The objective lens is arguably the most important lens as it serves to magnify and form the first image plane of the sample. The projector system involves a series of lenses to further magnify the image and the detection system is what allows the user to observe and record the image data. The user may (directly or indirectly) exert control over all of the components shown in the schematic in order to illuminate the sample, focus the image and set the desired magnification. In order to obtain clear, in-focus images with the desired resolution however, the user must go through a series of preliminary alignment steps. Amongst other things, this ensures the maximum number of electrons are travelling down the column along the optic axis and corrects for some lens aberrations, such as condenser and objective lens astigmatism.

It is possible to mathematically describe the TEM imaging process using Abbe's theory of image formation. Within this framework, imaging in the TEM can be understood as the process by which radiation transfers information from a specimen to an image. In general, the amplitude and phase of the incident radiation will be modulated when transmitted through the specimen. However, in this case we will assume that the specimen is thin enough such that only the phase is modified on emergence

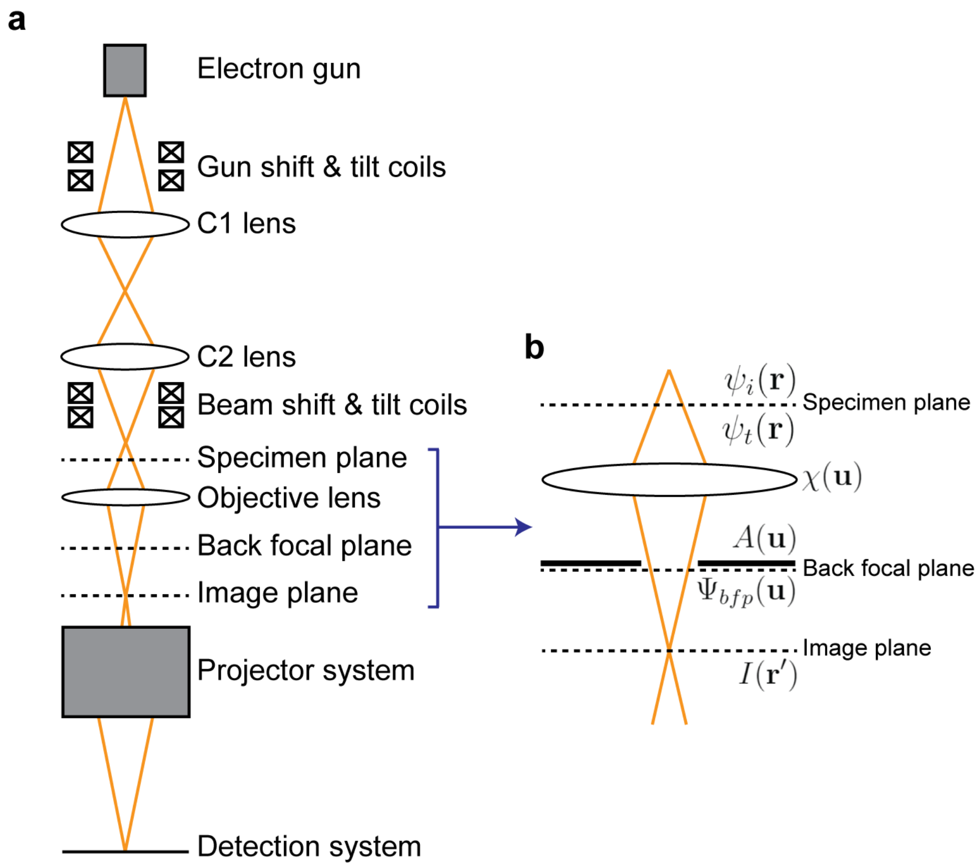
a
Electron gun
Gun shift & tilt coils
C1 lens
C2 lens
Beam shift & tilt coils
Specimen plane
Objective lens
Back focal plane
Image plane
Projector system
Detection system
b
$\psi_i(\mathbf{r})$
Specimen plane
$\psi_t(\mathbf{r})$
$\chi(\mathbf{u})$
$A(\mathbf{u})$
Back focal plane
$\Psi_{bfp}(\mathbf{u})$
Image plane
$I(\mathbf{r}')$

Figure 3.1: **a** Simplified TEM schematic diagram demonstrating CTEM imaging. **b** Image formation process. Mathematical quantities are defined in Eqs. 3.5 - 3.10.

from the specimen, namely invoking the phase object approximation (POA). The reason for this decision is that when we shift our description to magnetic imaging, the magnetic samples will also be treated as phase objects, where the origin of magnetic contrast is due to phase variations. Thus, the following description is valid within the context of high resolution TEM (HRTEM), where specimens are thin enough to be considered pure phase objects. Although HRTEM is not a focus of this thesis, it provides a useful starting point for understanding phase contrast in the TEM, which is integral to magnetic imaging.

We start by invoking the wave–particle duality in order to model the electrons as coherent plane waves, and describe how they interact with the specimen, apertures and lenses of the TEM [7]. Electrons are incident on the specimen as coherent plane waves of the form:

$$\psi_i(\mathbf{r}) = e^{2\pi ikz} \tag{3.5}$$

where the wave is travelling in the positive z-direction (defined as down the microscope column, from gun to detector), $k = \frac{1}{\lambda}$ is the wavenumber and $\boldsymbol{r}$ is a real-space vector describing a point in the xy-plane. As the electron wave passes through the specimen, its phase is modified through interaction with the specimen's electrostatic potential. The wave emerges with a phase difference:

$$\psi_t(\mathbf{r}) = \psi_i(\mathbf{r}) \cdot e^{i\phi(x)} \tag{3.6}$$

where $\phi(x)$ is the phase. The wave then passes through the objective lens and enters the back focal plane (BFP) of the objective lens, where the electron wave distribution may be expressed as a Fourier transform of the transmitted wave, $\Psi_t(\mathbf{u}) = FT(\psi_t(\mathbf{r}))$:

$$\Psi_t(\mathbf{u}) = \iint e^{i\phi(x)} \cdot e^{-2\pi i(\mathbf{u}\cdot\mathbf{r})}\, dx\, dy \tag{3.7}$$

Note that the electron wave entering the BFP of the objective lens is now a function of $\boldsymbol{u} = (k_x, k_y)$, a reciprocal-lattice vector. The components k_x and k_y are therefore spatial frequencies, which are proportional to the real-space displacements (x, y) in the BFP. The electron wave subsequently emerging from the back focal plane experiences a further phase difference inflicted by the aberrations present in the objective lens. The aberration function is given approximately by:

$$\chi(\mathbf{u}) = \pi\Delta f\lambda u^2 + \frac{1}{2}\pi C_s\lambda^3 u^4 \tag{3.8}$$

assuming no astigmatism and where C_s is the spherical aberration coefficient of the objective lens and Δf is the defocus. This is combined with an aperture function $A(\boldsymbol{u})$, which is unity within the objective aperture and zero elsewhere, to give the transfer function:

$$t(\mathbf{u}) = A(\mathbf{u}) \cdot e^{-i(\chi(\mathbf{u}))} \tag{3.9}$$

The transfer function, $t(\mathbf{u})$, is multiplied by the transmitted wave function, $\psi_t(\mathbf{r})$, to give the final form of the electron wave in the back focal plane:

$$\Psi_{bfp}(\mathbf{u}) = \Psi_t(\mathbf{u}) \cdot t(\mathbf{u}) \tag{3.10}$$

The electron wave arriving at the image plane and incident on the detector can be described by Fourier transformation of $\Psi_{bfp}(\boldsymbol{u})$, with the observed intensity being the modulus squared of this wave function:

$$I(\mathbf{r}') = \left| \iint \Psi_{bfp}(\mathbf{u}) \cdot e^{-2\pi i(\mathbf{u}\cdot\mathbf{r}')}\, dk_x\, dk_y \right|^2 \tag{3.11}$$

A key property of this result is that if the transfer function (Eq. 3.9) was unity at all points then the intensity (Eq. 3.11) would be constant and there would be no observable contrast in the image. This means that in order to obtain contrast from phase variations in the specimen, some aberrations are required such that these variations become perceptible intensity variations in the image [7]. The enhancement of magnetic phase contrast through the introduction of non-zero defocus (Δf) is an example of this fact, and will be discussed in more detail in a later section.

This treatment of electron waves demonstrates an important aspect of CTEM imaging, namely that the image formation process can be thought of as a succession of Fourier transforms. Firstly, from real space (specimen plane) to reciprocal space (back focal plane) and then to real space (image plane). This gives additional insight into the nature of the information that can be obtained by placing detectors at different locations within the TEM, be it real space or reciprocal space. Figure 3.1b highlights the image formation process schematically, demonstrating how the electron wave changes form as it propagates through the sample and key components of the TEM.

3.1.2 Scanning Transmission Electron Microscopy

Scanning transmission electron microscopy (STEM) imaging involves the formation of a small, focused electron spot (also known as a probe) at the specimen plane and sequential scanning of this probe across the specimen. In this imaging mode, the electron beam reaching the sample is highly focused and passes through the C2 aperture, defining the semi-convergence angle that determines the size of the probe and the resolution of the final image. In order to form an image, a diffraction pattern for every point in the scan is formed and recorded by a detector in the BFP of the objective lens. Most commonly these detectors consist of an annular dark-field (ADF) detector and a solid BF detector, which obtain information about scattered and unscattered electrons, respectively. This information can then be used to form BF and DF images of the specimen, using the Bragg scattered electrons (BF) or unscattered electrons (DF). Additionally, a high-angle annular dark-field (HAADF) detector can be used to obtain elemental information using electrons inelastically scattered at high angles, where the intensity observed is proportional to Z^2, where Z is atomic number.

Through the use of a FEG and aberration corrector systems, it is possible to obtain a sub-nanometer or even sub-angstrom probe [8], which is subsequently rastered across the specimen . This not only enables atomic scale image resolution, but also site-specific spectroscopic, diffraction or magnetic information of the same resolution to be obtained. Therefore, depending on the detectors available, it is possible to obtain a wealth of information about the specimen at each point in the scan. Some techniques enabled by STEM include electron energy loss spectroscopy (EELS), energy dispersive x-ray spectroscopy (EDS) and differential phase contrast (DPC) imaging.

Although the specific electron-optical components and operating procedures differ between STEM and CTEM, the two methods of electron imaging can be related through the principle of reciprocity. Originally described in 1968 for electronic microscopes [9], and expanded upon in 1969 [10], reciprocity relates the appearance of phase-contrast from a broad incoherent source (CTEM) with that of a scanning probe (STEM) [11]. The value of relating the two techniques this way is that it allows the technique of STEM to be understood using theory from the relatively well understood CTEM imaging process.

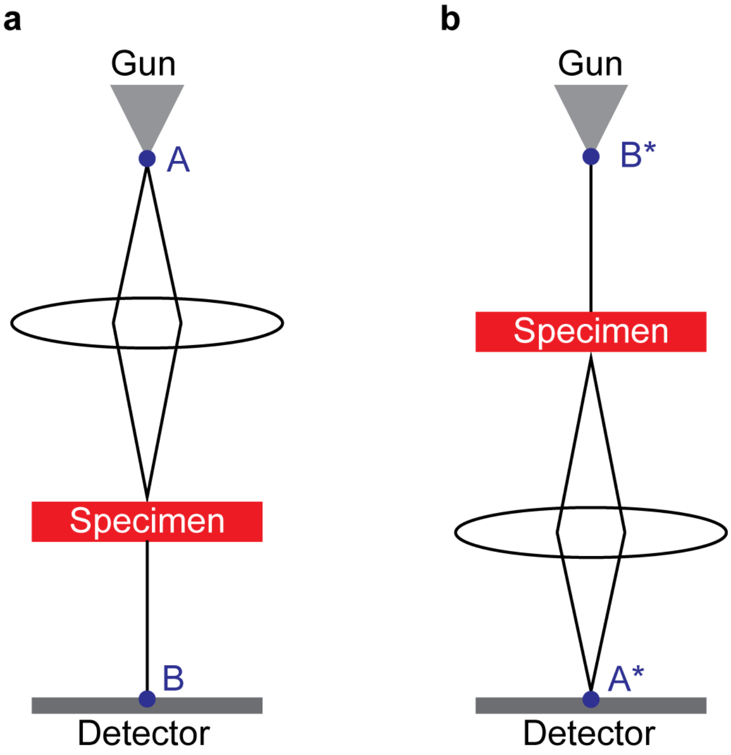

Figure 3.2: Critical components for describing the reciprocity relationship between **a** STEM and **b** CTEM. Adapted from [10].

Figure 3.2 demonstrates the reciprocity relationship between STEM (Fig. 3.2a) and CTEM (Fig. 3.2b), with only a single lens included for simplicity. In STEM, electrons emitted from a source at point A are focused into a small probe at the specimen, and the resulting intensity is measured at a distance from the specimen at point B on the detector. Conversely in CTEM, electrons emitted from a source at point B* hit the specimen, are scattered and subsequently focused at point A* on the detector. Thus, by the principle of reciprocity, the intensity of point B due to the source point A in the STEM system will be the same as the intensity at A* due to the source point B* in the CTEM system. This equivalence means that the effects of all aberrations and microscope limitations will have exactly the same effect in both STEM and CTEM imaging. Other insights into STEM imaging can also be gained from this principle, such as the effect of resolution. Since points A and A* are related through reciprocity, modifying the size of the source in STEM is the same as modifying the size of the detector in CTEM, which will affect the resulting resolution. The upshot of reciprocity in transmission electron microscopy is that image contrast in STEM is fundamentally related to image contrast in CTEM [10].

3.1.3 Aberrations and Limitations of the Electron Microscope

As mentioned previously, the electromagnetic lenses used to focus electrons within the TEM column are not perfect. In this context, an imperfect lens is one in which the focusing power of the lens is unable to generate a perfect image of an object. The lens imperfections are known as aberrations, and there are a range of such aberrations which ultimately degrade the maximum achievable resolution. Probably the easiest aberration to spot and correct for is astigmatism, which occurs due to the non-uniformity of the magnetic field produced by the lenses. This form of aberration is usually corrected using stigmator coils, which provide compensating fields to counter the astigmatism introduced by the electromagnetic lenses. However, in order to reach atomic or sub-atomic resolution (high-resolution TEM or HRTEM), the relationship between spherical aberration and defocus must be understood. With astigmatism fixed, we're left with the two terms in the aberration function, which was given in Eq. 3.8, involving defocus Δf and spherical aberration C_s. Spherical aberration is introduced because electrons travelling along the central axis of the lens are refracted less than those travelling at the periphery of the lens. This results in points in the object plane being represented as finite discs in the plane of "least confusion", limiting resolution. The defocus can be changed by the microscope user by adjusting the excitation of the objective lens, however the spherical aberration is intrinsic in lenses with spherical symmetries and must be compensated for by the microscope's C_s corrector.

It is possible to investigate how defocus and spherical aberration affect the maximum obtainable resolution in the TEM by treating the specimen as a weak-phase object. In this case, the contrast obtained in the image is determined by the contrast transfer function (CTF), given by:

$$T(\mathbf{u}) = 2A(\mathbf{u})\,\mathrm{sin}\chi(\mathbf{u}) \tag{3.12}$$

where $\chi(\mathbf{u})$ is the aberration function defined in Eq. 3.8 and $A(\mathbf{u})$ is the aperture function. Equation 3.12 demonstrates the oscillatory nature of phase contrast transfer, which results in difficulty interpreting images especially at high spatial frequencies. Its possible to optimise the CTF such that all spatial frequencies up to a critical value, corresponding to the maximum interpretable resolution, are transferred with similar phase to the final image intensity. In 1949 Scherzer showed that for a particular value of C_s, it is possible to find an optimum defocus value to maximise the interpretable resolution. A later modification of this work led to the relationship between C_s and defocus given by:

$$\Delta f_{Sch} = -1.2(C_s\lambda)^{\frac{1}{2}} \tag{3.13}$$

where Δf_{Sch} is the Scherzer defocus and λ is the relativistic electron wavelength [12]. This relation calculates the optimum defocus for a particular microscope and operating voltage, maximising the interpretable resolution.

This can be investigated by plotting the CTF as a function of spatial frequency, a series of such plots are shown in Fig. 3.3. Each plot is calculated using Eqs. 3.3 and 3.8 for 200 keV electrons and $C_S = 0.5$ mm, for three defocus values including the Schezer defocus. The second zero (first x-axis intercept) in each plot defines the minimum interpretable distance, and maximum interpretable resolution. It is evident that the maximum interpretable resolution degrades either side of the Schezer defocus, since $\mathbf{u_1}$ and $\mathbf{u_2}$ are both less than $\mathbf{u_{Sch}}$. The minimum interpretable distance is given by $\frac{1}{\mathbf{u_{Sch}}}$, and therefore at the Schezer defocus and for the parameters given, would be approximately 0.21 nm. This demonstrates the severity of lens imperfections within electron imaging systems and importance of obtaining images at focus. Even with sophisticated corrector systems, such as those in the JEOL ARM 200cF, the minimum interpretable distance is still two orders of magnitude larger than that imposed by the theoretical diffraction limit of electrons.

The majority of the TEM work in this thesis will be carried out in Fresnel mode, which will be described shortly. In Fresnel imaging, magnetic contrast is generated through intentional defocusing of the electron beam, away from the Scherzer defocus. As such, it is not possible to obtain the maximum interpretable resolution described here when using Fresnel TEM imaging due to this intentional defocussing. As such, the resolution in Fresnel mode is approximately an order of magnitude worse than is achievable using in-focus modes.

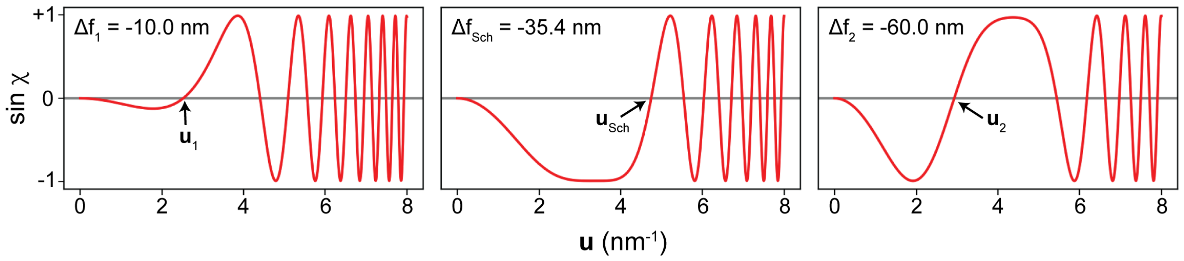

Figure 3.3: A series of plots demonstrating the oscillatory nature of the CTF and how the interpretable resolution varies as a function of the defocus.

3.2 Direct Electron Detectors

In order to achieve increased resolution and a higher signal-to-noise ratio, direct electron detectors can replace the charge-coupled device (CCD) cameras present in many TEM systems [13]. Direct electron detectors, as the name suggests, are able to directly detect the electrons emerging from the sample. This is in contrast to the CCD camera, which cannot detect electrons directly, due to the amount of energy deposited by incident electrons, reducing dynamic range and cause risk of damage [14]. CCD cameras must therefore be fibre-optically coupled to a phosphorescent screen, which leads to a loss of resolution due to scattering effects [15]. Semiconductor detectors, such as those in the Medipix3 family, are able to detect single electron hit events. These detectors utilise a semiconductor chip, often made of silicon, which is pixelated using electronics and the material-specific electron interaction volume. The Medipix3, which is the electron detector used within this thesis, is capable of imaging at extremely high frame rates (sub 1 ms) and even in a continuous mode, where frame duration can be determined in post processing. The Medipix3 chip consists of a 256×256 pixel matrix and periphery electronics, which handle the energy threshold and counting processes [16]. This is made possible because the devices are capable of recording a timestamp of each electron hit, allowing them to capture high-throughput image data. This means that the direct electron detectors are only subject to the fundamental shot noise associated with the stochastic process of electron arrival. As such, this method of detecting electrons makes the summing of data more effective as you are not also summing excessive random noise. Higher temporal resolution is also possible using the Timepix3 device, which has a theoretical limit of its time-of-arrival (TOA) data of 1.56 ns [17].

The use of direct electron detectors opens up the opportunity to perform fast time-resolved electron microscopy in the traditional TEM [18], [19]. This is extremely valuable in condensed matter physics, enabling the possibility of studying dynamic processes such as phase transitions and structural dynamics [20], [21]. As such, the Merlin Medipix3 detector installed on the JEOL ARM 200cF was used to obtain high spatial and temporal resolution data of dynamic processes. Specifically, the high signal-to-noise and frame rates enabled advanced image processing techniques, described in detail in Chapters 4 and 5.

3.3 Magnetic Imaging

Thus far, the description of electron imaging has been limited to the generation of structural contrast arising from the interaction between electrons and generic samples. In CTEM operation, the sample sits within a strong magnetic field produced by the objective lens pole pieces. This magnetic field effectively saturates any magnetic textures present in a sample, severely limiting the obtainable information. Therefore, a prerequisite for magnetic imaging is switching off the objective lens and creating a field-free region at the sample location. A series of other lenses, condenser mini and objective mini, are used instead of the objective lens to focus the electrons for imaging. However, when using these lenses, even with the corrector systems in place on the JEOL ARM 200cf, the maximum resolution obtainable is around 1 nm (in field-free 200 kV STEM mode) [22]. This is approximately an order of magnitude worse than the resolution obtained when the objective lens is switched on, due to the large C_S associated with using the mini-lenses and the fact that these lenses are purposefully located further from the sample, reducing the convergence angle, probe size and therefore resolution in STEM imaging. This type of imaging is typically referred to as Lorentz TEM (LTEM) imaging, due to the nature of how magnetic contrast is formed, which will be discussed further below. LTEM encompasses a collection of different techniques for generating magnetic contrast, two of which will be introduced and described in the following sections.

The objective lens does provide a function in magnetic imaging however, as it allows for the application of out-of-plane magnetic fields to the sample. In-plane magnetic fields can also be produced through tilting of the sample, however an out-of-plane component will always be present as well. Figure 3.4 demonstrates how one can provide both in-plane and out-of-plane magnetic fields to a sample within the TEM using the tilt and rotate sample holder. The relative strengths of the in-plane and out-of-plane magnetic fields applied to the sample are given by:

$$H_{out-of-plane} = \mathbf{H}\cos(\theta) \tag{3.14}$$

$$H_{in-plane} = \mathbf{H}\sin(\theta) \tag{3.15}$$

where **H** is determined by the objective lens excitation and θ is the sample tilt about the x-axis (defined in Fig. 3.4). Rotation of the sample about the z-axis allows alignment of the magnetic field with a particular axis of the magnetic sample. This is particularly important for elongated magnetic structures, such as wires. In such samples, the propagation of magnetic domain walls may be initiated through tilting of the sample, following the alignment of the wire's long axis with the tilt direction.

This effect is demonstrated experimentally in Fig. 3.5, where the Fresnel contrast highlights movement of magnetic domain walls (bright and dark regions) on application of a magnetic field in the y-direction. Here, tilting through angles $\theta = 0$ to $\theta = 10$ increases the in-plane magnetic field applied according to Eq. 3.15 and causes the domain walls to move in the direction of the applied field. In these images, the

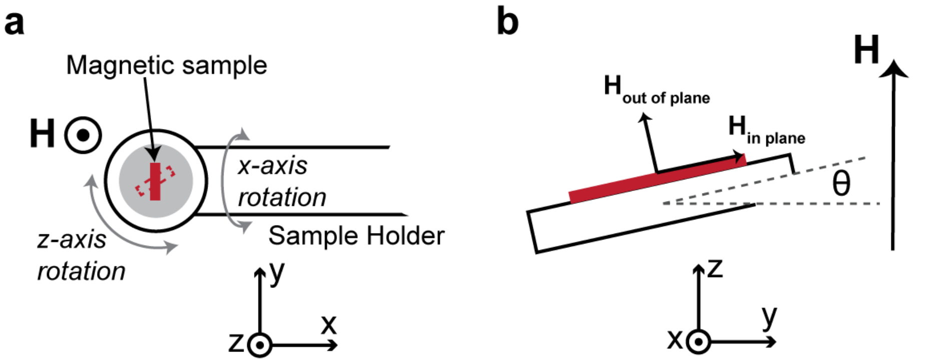
a
Magnetic sample
H
x-axis rotation
z-axis rotation
Sample Holder
y
x
z
b
H
H out of plane
H in plane
θ
z
x
y

Figure 3.4: Schematics demonstrating the application of both in-plane and out-of-plane magnetic field components to magnetic samples in the TEM. **a** View from above the tilt and rotate sample holder **b** how this translates to the fields present within the sample for an x-axis rotation of θ.

contrast is primarily magnetic in nature and is particularly sensitive to the domain walls. Explanation on how this contrast is formed and the different types of magnetic imaging follows.

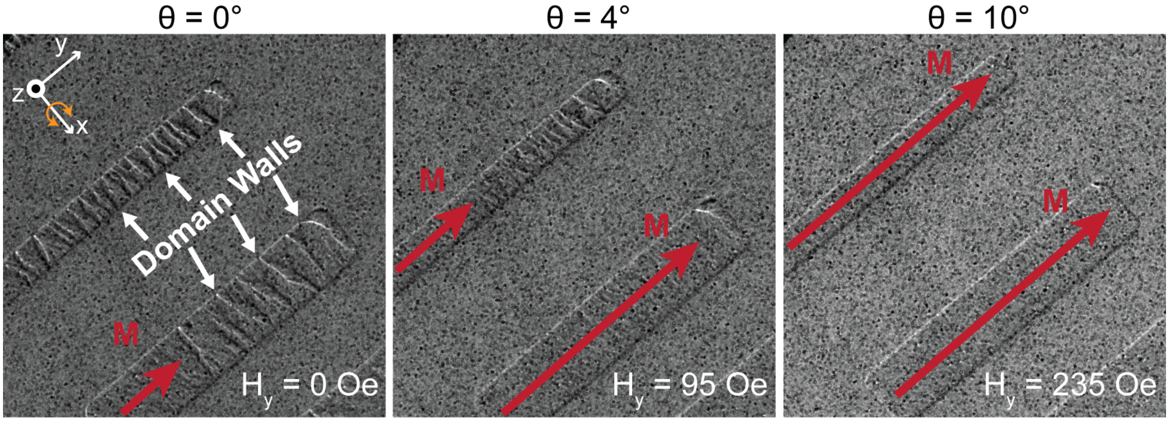
θ = 0°
θ = 4°
θ = 10°
y
z
x
Domain Walls
M
H$_y$ = 0 Oe
M
M
H$_y$ = 95 Oe
M
M
H$_y$ = 235 Oe

Figure 3.5: LTEM Fresnel images of magnetic nanowires and how domain wall motion can be initiated through tilting the sample in a non-zero perpendicular magnetic field. The in-plane magnetic field is calculated through $H_y = \mathbf{H}\sin(\theta)$, where $\mathbf{H}$ is the out-of-plane field strength.

3.3.1 Lorentz TEM

We begin this section by describing the interaction of electrons with magnetic samples using a classical framework, and later expand the description to include the full quantum mechanical effects. Electrons transmitted through a sample are not only influenced by the sample's electrostatic potential, as described in Section 3.1.1, but also any magnetic potential generated by the sample. Classically, the magnetic force acting on an electron travelling in a magnetic field, is given by the Lorentz force:

$$\mathbf{F}_{\mathbf{magnetic}} = -q(\mathbf{v} \times \mathbf{B}) \tag{3.16}$$

where q is the magnitude of the electron charge, $\mathbf{v}$ is the electron velocity and $\mathbf{B}$ is the magnetic field, which can be defined as:

$$\mathbf{B} = \mu_0(\mathbf{M} + \mathbf{H}) \tag{3.17}$$

$$\mathbf{B} = \nabla \times \mathbf{A} \tag{3.18}$$

where $\mathbf{A}$ is the magnetic vector potential. Thus, according to Eq. 3.16, an electron travelling in a magnetic field, or within a material with non-zero magnetisation, will have its trajectory modified by the Lorentz force. However, if the electron is travelling parallel to $\mathbf{B}$ it experiences no Lorentz force, since the quantity $\mathbf{v} \times \mathbf{B}$ is zero. This directional lack of sensitivity limits the amount of information that can be obtained using LTEM techniques for out-of-plane magnetic textures.

The consequence of the Lorentz force in the TEM is that an electron will be deflected as it passes through a magnetic sample. The magnitude of this Lorentz deflection, β, for an electron travelling through a uniformly magnetised sample is given by:

$$\beta = \frac{qB_0\lambda}{h} \tag{3.19}$$

where B_0 is the z-averaged saturation induction and t is the thickness of the sample. This deflection is typically on the order of μrad, which is multiple orders of magnitude smaller than the Bragg deflections associated with structural imaging. The consequence of this large difference in deflection angles means that it is, in principle, possible to separate the structural and magnetic signals. It is worth noting that if quantitative magnetic information about the sample is desired, this classical description of electron deflection is not sufficient. Therefore, before describing the detection of magnetic signals we must first investigate how the electron wave behaves when interacting with a magnetic sample. The Lorentz imaging process can be treated using a quantum mechanical wave model, which leads to a quantitative description of magnetic contrast formation.

The interaction between an electron wave and a magnetic potential is described through the Aharonov-Bohm effect. This phenomenon arises from the coupling of a magnetic potential to the complex phase of the electron's wave function, as such it is an entirely quantum-mechanical effect. Electrons travelling different paths from the same point will pick up a relative phase difference, $\Delta\phi$, when they rejoin if their paths enclose magnetic flux:

$$\Delta\phi = \frac{2\pi q}{h} \oint_C \mathbf{A} \cdot d\mathbf{l} \tag{3.20}$$

where the line integral is around the closed path C traced by the electron trajectories

[23]. Equation 3.20 can be reformulated in terms of the magnetic field, B, using Eq. 3.18 and invoking Stokes' theorem. This essentially converts the line integral to a surface integral, describing the flux of magnetic potential through the surface, S, traced out by the electron trajectories:

$$\Delta\phi = \frac{2\pi q}{h}\int \mathbf{B}\cdot\, d\mathbf{S} \tag{3.21}$$

Assuming constant B in the z-direction and that the sample is wholly within the path traced by the electrons, evaluating the integral gives:

$$\Delta\phi = \frac{2\pi q}{h} B_0 t x \tag{3.22}$$

where the integrated surface is found by the product of sample thickness, t, and width, x. This can be generalised to a situation where the enclosed magnetic induction varies between two x-coordinates:

$$\Delta\phi(x) = \frac{2\pi q t}{h}\int_{x1}^{x2} B_y(x)\, dx \tag{3.23}$$

Finally, we can link this quantum mechanical description back to the classical description using the Lorentz deflection earlier. Taking the gradient of Eq. 3.22 and comparing it directly with Eq. 3.19 yields:

$$\frac{d(\Delta\phi)}{dx} = \frac{2\pi q}{h} B_0 t = \frac{2\pi\beta}{\lambda} \tag{3.24}$$

Thus, the differential phase difference is proportional to the local magnetic induction, which is in turn proportional to the Lorentz deflection angle, β [24]. Equation 3.23 additionally demonstrates the fact that magnetic samples act as pure phase objects in relation to the electron beam. This hearkens back to the image formation treatment in Section 3.1.1, where image intensity was related to phase variations imposed by ultra-thin samples. Furthermore, Eq. 3.24 provides a way to calculate the local magnetic induction from the phase difference, two ways of experimentally measuring such a phase difference are given in the following sections.

3.3.2 Fresnel Imaging

As was stated previously, in order for electron phase variations to result in perceptible contrast differences in the image, some aberrations are required. Because the Lorentz deflection angle (electron phase difference) is so small, the intrinsic aberrations are not sufficient to generate observable magnetic contrast in the image. Therefore, in order to observe the kind of magnetic contrast shown in Fig. 3.5, a non-zero value of defocus, Δf, must be introduced. This method of forming magnetic contrast is known as Fresnel imaging, and the intensity seen in the image is given by the equation:

$$I(\mathbf{r}, \Delta f) = 1 - \frac{\Delta f \lambda}{2\pi} \nabla^2[\phi(\mathbf{r})] \tag{3.25}$$

where the Laplacian ($\nabla^2[\phi(\mathbf{r})]$) relates only to in-plane sample coordinates, $\mathbf{r}$, as (x, y) [25]. This demonstrates why only the domain walls in Fig. 3.5 are clearly visible, Fresnel imaging is only sensitive to the Laplacian of the phase, and therefore regions of constant magnetisation generate zero Fresnel contrast.

The method by which the Lorentz deflection of electrons generates magnetic contrast in Fresnel imaging is shown for a series of 180° domains in Fig. 3.6. Electrons travelling in the positive z-direction through the sample are deflected in opposite directions, depending on the direction of in-plane magnetisation that they experience. This leads to alternating bright and dark regions in the observed intensity, corresponding to the domain wall locations. Although Fresnel imaging is typically used to provide qualitative information, it is possible to retrieve phase information and therefore quantitative information on sample magnetisation. This is done by taking a series of in-focus, over and under focus images, and using the transport of intensity equation (TIE) method [25].

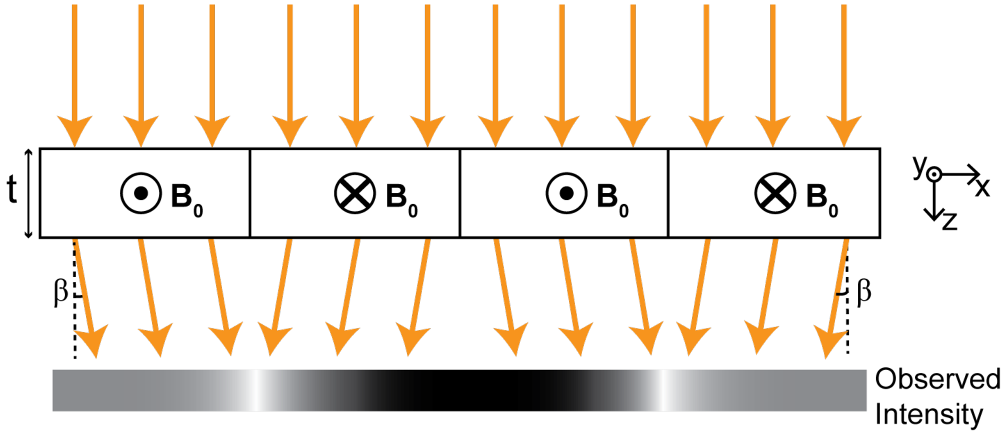

Figure 3.6: Schematic showing Fresnel contrast formation due to the deflection of electrons travelling through a magnetic sample. Transmitted electrons are convergent or divergent depending on their interaction with the in-plane magnetisation, this results in alternating bright and dark intensity regions corresponding to the domain walls.

As a parallel illumination method, Fresnel imaging benefits from the high temporal resolutions provided by using direct electron detectors, such as the Merlin Medipix3 detector installed on the JEOL ARM 200cF. As such, Fresnel TEM is particularly suited to studying magnetic phase transitions and skyrmion dynamics in the B20 helimagnets, which host distinct magnetic phases namely helical, SkX and field-polarised/conical phases [26]. These phases each generate distinct Fresnel contrast, and transitions between them can be initiated through the application of external perpendicular magnetic fields. The majority of experimental work in this thesis is concerned with the dynamics and deformation of individual skyrmions, collective phase transitions and breaking of long-range order through defects. As such, much of the magnetic imaging performed utilises LTEM techniques. However, a significant downside of Fresnel imaging is the relatively poor resolution due to the microscope being operated in a defocused state. Fresnel imaging therefore cannot typically be solely relied upon to detect intricate nanoscale variations in magnetisation. Therefore, in order to obtain a more detailed description of magnetic textures, a complementary imaging method can be used in STEM mode, namely differential phase contrast imaging.

3.3.3 Differential Phase Contrast Imaging

The intrinsically quantitative mode of Lorentz imaging is known as differential phase contrast (DPC) imaging, and requires STEM mode operation. In DPC-STEM, the magnetic sample is rastered with a small electron probe, and can be related back to Fresnel imaging through the principle of reciprocity as previously described. As such, the general principles of Lorentz imaging in CTEM, can be translated over to DPC-STEM. Unlike Fresnel imaging however, which generates contrast from the Laplacian of the electron phase ($\nabla^2[\phi(\mathbf{r})]$), DPC imaging generates contrast from the gradient of the electron phase, ($\nabla[\phi(\mathbf{r})]$). Equation 3.24 gives the direct relationship between the gradient of the electron phase, the Lorentz deflection of electrons, and the local integrated magnetic induction. Therefore, by measuring the deflection of the electron probe at every point in the scan, it is possible to retrieve a detailed quantitative map of the magnetic induction across the sample [27].

Figure 3.7a demonstrates schematically, how a probe with a semi-convergence angle, α, is deflected by the magnetisation of the domains within a sample. The sensitivity of DPC is directly linked to spatial resolution in STEM imaging, where both are determined by the semi-convergence angle. The Lorentz deflection, β, translates the disc, which is formed at the detector plane, by an amount proportional to the deflection. The magnetic domains that are magnetised in the positive and negative y-directions deflect the disc in the positive and negative y-directions, respectively. However, for the magnetic domain which is magnetised in the negative z-direction, there is no Lorentz deflection and the disc remains centralised. The deflection of the electron disc is typically measured by segmented annular detectors as difference signals [24], as shown in Fig. 3.7b, where the deflection in the x and y-directions, β_x and β_y, can be calculated according to:

$$\beta_x = \alpha \frac{\pi}{4} \frac{(A+D)-(B+C)}{(A+B)+(C+D)} \tag{3.26}$$

$$\beta_y = \alpha \frac{\pi}{4} \frac{(A+B)-(C+D)}{(A+B)+(C+D)} \tag{3.27}$$

Equations 3.26 and 3.27 can be used with Eq. 3.24 to determine the two orthogonal magnetisation components at each point in the scan. The formation of magnetic contrast in DPC can be improved further by using a direct electron detector instead of the annular segmented detectors, which has been shown to minimise the effect of diffraction contrast [28]. This type of detection is known as 4D-STEM DPC due to the fact that, at each point in the two-dimensional scan of the specimen, a two-dimensional image of the electron probe is obtained. As such, 4D datasets are very large in size, and require significant data processing to obtain an image when compared to segmented detector DPC [29, 30].

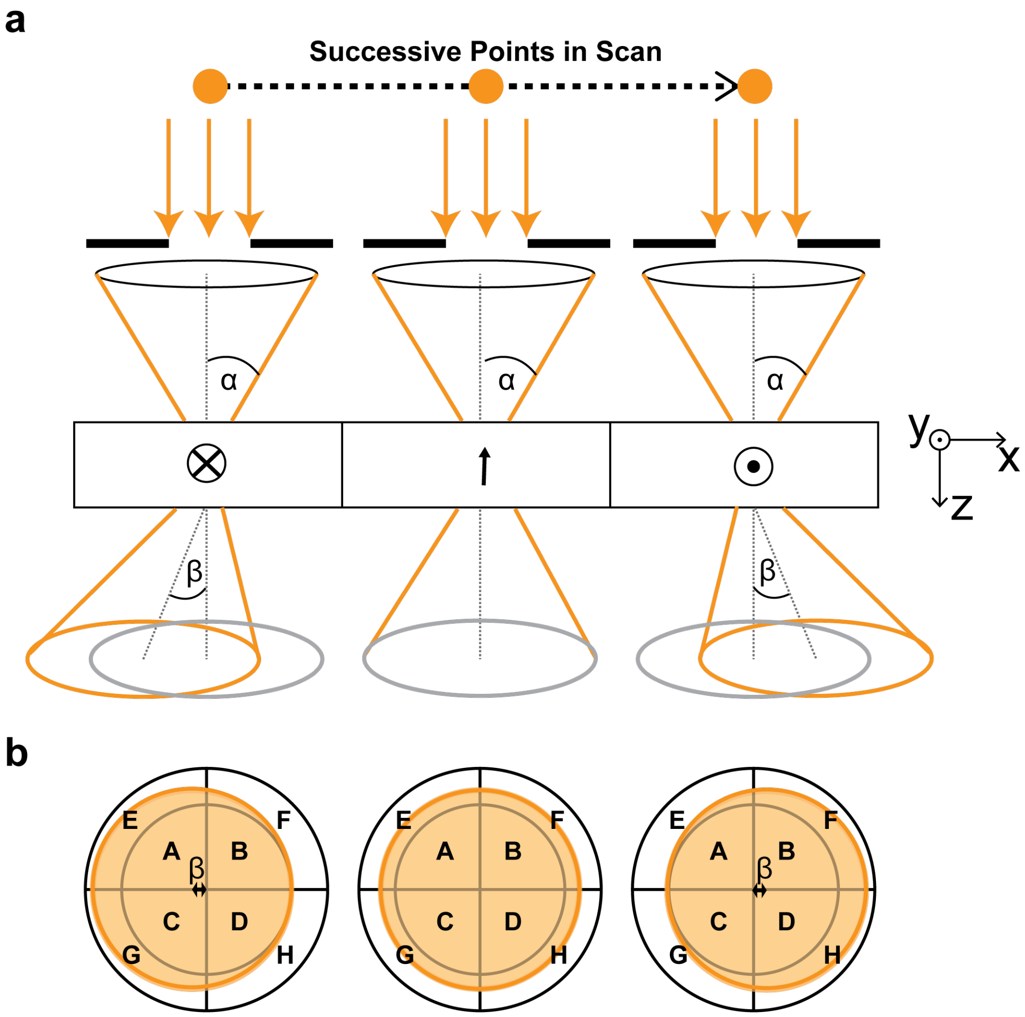

Figure 3.7: **a** DPC schematic demonstrating how the electron spot is deflected by a magnetic sample with distinctly magnetised domains. **b** Schematic showing how the deflection in **a** leads to different detection on the segmented detector.

Since DPC imaging is an in focus method, it benefits from increased spatial resolution over Fresnel imaging through increased sensitivity. Indeed, DPC can produce magnetic induction maps of permalloy with spatial resolutions as low as 1 nm, as shown in Ref. [22]. Unlike Fresnel imaging however, which can utilise the high-temporal resolution of direct electron detectors, DPC imaging is fundamentally limited in this regard. This is because of the non-zero time it takes to raster the sample to create each image frame. As such, DPC imaging is typically only used to investigate static magnetic structures and is therefore of limited use for the investigation of skyrmion dynamics presented in this thesis.

3.4 Focused Ion Beam Microscopy

The focused ion beam (FIB) microscope is a powerful complementary tool for use in experimental condensed matter physics. This is particularly true for dual beam FIB instruments, which incorporate both ion and electron beams to facilitate a wide range of functions [31]. These include the generation and study of material cross-sections, preparation of samples for other experimental techniques, 3-dimensional structural data acquisition and both bottom-up and top-down nanofabrication [32]. Both of the FIBs used in this thesis are dual beam instruments, however the ions used in each instrument differ. The FEI Nova 200 FIB utilises gallium ions (Ga^+), whereas the FEI Helios plasma FIB (PFIB) has a plasma source of xenon ions (Xe^+). The choice of which FIB to use is situational, Ga^+ FIBs allow small probe sizes and high current densities whereas Xe^+ PFIBs generate much higher maximum current. PFIBs using Xe^+ additionally benefit from the fact that xenon is a noble element, and as such minimises contamination [33].

For the experimental work in this thesis, the Nova Ga^+ FIB was used to mill bulk samples to prepare electron transparent specimens for use in the TEM. This is because the milling using Xe^+ ions was too aggressive on the FeGe samples used within this thesis. Since many functions and components are shared between both FIBs and PFIBs, these will be discussed first before delving into the details of the two different instruments and their accompanying methods. Figure 3.8a highlights the key components in both the FIB and PFIB, with Fig. 3.8b demonstrating the FIB operation for milling and Fig. 3.8c showing the setup for focused electron beam-induced-deposition (FEBID). Although not specifically utilised within the work in this thesis, FEBID enables the bottom-up growing of magnetic nanostructures [34–36], and highlights the versatility of FIBs.

By inspecting Fig. 3.8a, it can be seen that the electron and ion columns are oriented at an angle of 52° to each other. This allows both beams to be coincident on a specimen in the eucentric plane. Furthermore, only a single secondary electron (SE) detector is required for imaging, since both electron-sample and ion-sample interactions generate secondary electrons. Much like scanning electron microscopy (SEM), this means that the image contrast formation in FIB is topographic in nature [37]. The sample holder and accompanying stage is able to rotate, tilt and move in the x, y and z-directions, as shown in Fig. 3.8b, in order to access all areas of the sample with both beams. Finally, the gas injection system (GIS) is used to deposit material onto a substrate or sample, this includes welding and complex structure growth. This deposition process proceeds via the use of local chemical vapour deposition through the interaction between an organometallic precursor and the high energy electron or ion beam [35].

An important aspect not easily visualised in the FIB schematics is the need for sophisticated vacuum systems. Poor vacuums will impede both the electron and ion beams by decreasing the mean free path of the charged particles, resulting in decreased effective beam current. Additionally, unwanted elements such as carbon and oxygen present on the sample or within the instrument can contaminate the sample if a sufficiently high vacuum isn't maintained. As such, all regions of the FIB and PFIB instruments are under high vacuum conditions, facilitated by a range of auxiliary pumps, valves and gauges.

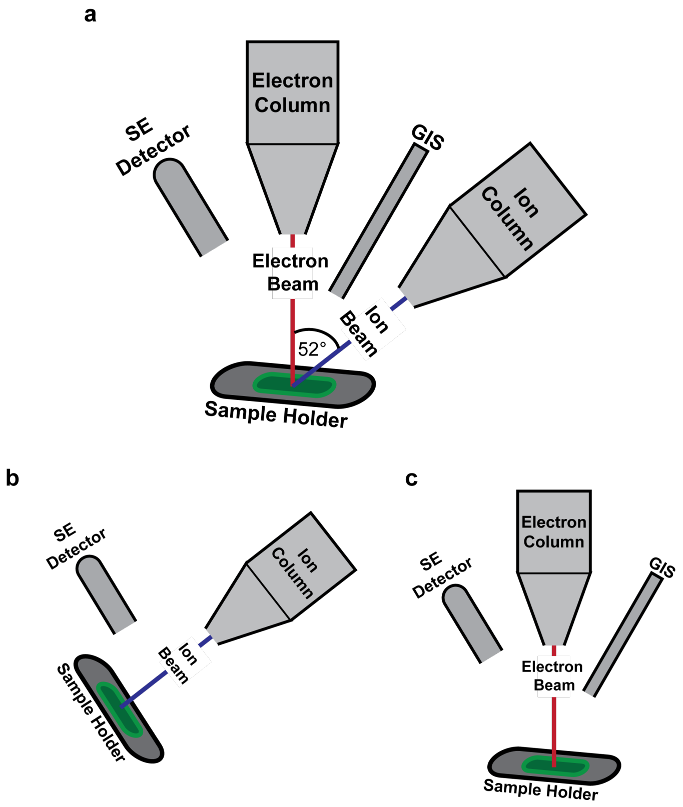
a
Electron Column
SE Detector
GIS
Ion Column
Electron Beam
Ion Beam
52°
Sample Holder
b
SE Detector
Ion Column
Ion Beam
Sample Holder
c
Electron Column
SE Detector
GIS
Electron Beam
Sample Holder

Figure 3.8: Simplified FIB microscope schematics. **a** Showing all key components, **b** set up for material ablation, used in TEM sample preparation and **c** set up for FEBID, to grow magnetic nanostructures.

3.4.1 TEM Sample Preparation

No amount of TEM imaging enhancements will compensate for a poorly prepared sample. Most importantly, if electrons are not able to transmit through the specimen, then zero material information can be obtained. One of the most revolutionary uses of the FIB is TEM sample preparation, as it brings increased accuracy and throughput compared to alternative methods such as mechanical polishing [38]. TEM sample preparation in the FIB involves gradual milling of a bulk sample via controlled etching, utilising the high kinetic energy of the ions. Although both the Nova Ga^+ FIB and Helios Xe^+ PFIB can be used for TEM sample preparation, the work in this thesis used the Ga^+ FIB.

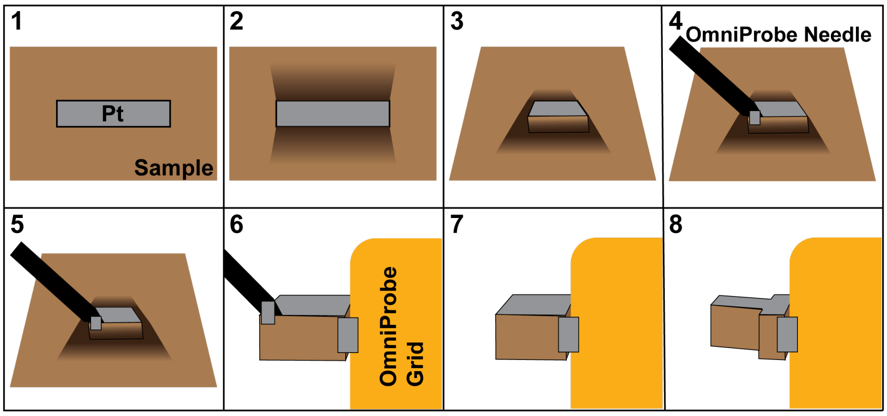

Figure 3.9: TEM lamella preparation using 'lift-out' method. 1: Deposition of protective platinum layers to protect sample. 2: Trench milling. 3: Partial undercut of the lamella. 4: Welding of lamella to OmniProbe needle. 5: Lamella cut free from bulk sample. 6: Welding of lamella to OmniProbe grid. 7: Lamella cut free from OmniProbe needle. 8: Successive thinning of lamella to electron transparency.

The basic principles of FIB milling involve the energetic interactions between Ga^+ ions and atoms near the surface of the sample. The Ga^+ ions are accelerated and focused onto the sample surface, where transfer of momentum and kinetic energy sputters atoms from the sample. This milling process can be applied to creating electron transparent TEM lamellae, in a 'lift-out' process [39]. This process is partially automated on the Nova FIB, but essentially involves a number of discrete steps, shown schematically in Fig. 3.9. First, a small region (8×2 μm) of the sample is coated with a 500 nm thick platinum layer in order to protect the lamella from excessive ion irradiation during imaging and thinning. The next few steps involve milling to first create a trench on either side of the lamella, partially cutting the lamella from the bulk sample and attaching it to an OmniProbe needle. The lamella is then cut free from the bulk sample, attached to an OmniProbe grid and the OmniProbe needle is subsequently cut free. Finally, the lamella is thinned through an iterative process of tilting the lamella and reducing the beam current. Once the sample is thinned to electron transparency (< 100 nm), the OmniProbe grid can be placed in the TEM. The 'lift-out' steps above are carried out with an ion beam acceleration voltage of 30 kV and currents between 48 pA and 0.28 nA.

An example of a thinned FeGe sample can be seen in Fig. 3.10, where the electron transparent region is the bright section of the lamella. This is an example of a sample which has been thinned too aggressively, where the protective platinum layer has been milled away, causing the leading edge to thin much more quickly. This typically occurs if using a high beam current or tilting the sample too much, and results in an uneven thickness and potentially high sample damage and/or Ga$^+$ ion implantation.

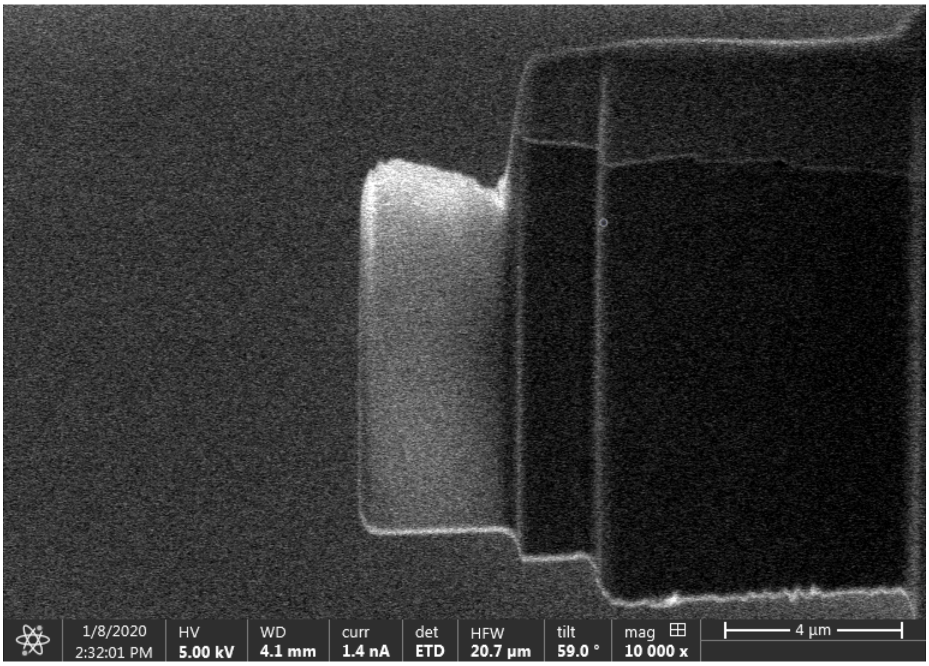

Figure 3.10: SEM image showing a thinned FeGe sample using the FIB 'lift-out' process. The bright region is the thinnest section and the fact it is so bright demonstrates the electron transparency.

Bibliography

1. Williams, D. & Carter, C. B. *The Transmission Electron Microscope* (1996).
2. Thomson, G. P. & Reid, A. Diffraction of cathode rays by a thin film. *Nature* **119,** 890 (1927).
3. Davisson, C. J. & Germer, L. H. Reflection of Electrons by a Crystal of Nickel. *Proceedings of the National Academy of Sciences* **14,** 317–322 (Apr. 1928).
4. Slater, J. C. Atomic radii in crystals. *The Journal of Chemical Physics* **41,** 3199–3204 (1964).
5. Hawkes, P. W. Ernst ruska. *Physics Today* **43,** 84–85 (Jan. 1990).
6. Haider, M. *et al.* A spherical-aberration-corrected 200 kV transmission electron microscope. *Ultramicroscopy* **75,** 53–60 (Oct. 1998).
7. Chapman, J. N. The investigation of magnetic domain structures in thin foils by electron microscopy. *Journal of Physics D: Applied Physics* **17,** 623–647 (1984).
8. Dellby, N., Krivaneka, L., Nellist, D., Batson, E. & Lupini, R. Progress in aberration-corrected scanning transmission electron microscopy. *Journal of Electron Microscopy* **50,** 177–185 (2001).
9. Pogany, A. P. & Turner, P. S. Reciprocity in electron diffraction and microscopy. *Acta Crystallographica Section A* **24,** 103–109 (Jan. 1968).
10. Cowley, J. M. Image Contrast in a Transmission Scanning Electron Microscope. *Applied Physics Letters* **15,** 58–59 (1969).
11. Krause, F. F. & Rosenauer, A. Reciprocity relations in transmission electron microscopy: A rigorous derivation. *Micron* **92,** 1–5 (Jan. 2017).
12. Scherzer, O. The theoretical resolution limit of the electron microscope. *Journal of Applied Physics* **20,** 20–29 (1949).
13. Deptuch, G. *et al.* Direct electron imaging in electron microscopy with monolithic active pixel sensors. *Ultramicroscopy* **107,** 674–684 (2007).

14. Faruqi, A. R. & McMullan, G. Direct imaging detectors for electron microscopy. *Nuclear Instruments and Methods in Physics Research, Section A: Accelerators, Spectrometers, Detectors and Associated Equipment* **878,** 180–190 (2018).

15. Faruqi, A. R. & Andrews, H. N. Cooled CCD camera with tapered fibre optics for electron microscopy. *Nuclear Instruments and Methods in Physics Research, Section A: Accelerators, Spectrometers, Detectors and Associated Equipment* (1997).

16. Ballabriga, R., Campbell, M., Heijne, E. H. M., Llopart, X. & Tlustos, L. The Medipix3 prototype, a pixel readout chip working in single photon counting mode with improved spectrometric performance. *IEEE Transactions on Nuclear Science* **54,** 1824–1829 (2007).

17. De Gaspari, M. *et al.* Design of the analog front-end for the Timepix3 and Smallpix hybrid pixel detectors in 130 nm CMOS technology. *Journal of Instrumentation* **9** (2014).

18. Lee, Y. M., Kim, Y. J., Kim, Y. J. & Kwon, O. H. Ultrafast electron microscopy integrated with a direct electron detection camera. *Structural Dynamics* **4** (2017).

19. Vecchione, T. *et al.* A direct electron detector for time-resolved MeV electron microscopy. *Review of Scientific Instruments* **88** (2017).

20. Kirkland, A. I. *et al.* Observing Structural Dynamics and Measuring Chemical Kinetics in Low Dimensional Materials Using High Speed Imaging. *Microscopy and Microanalysis* **25,** 1682–1683 (Aug. 2019).

21. Shimizu, T. *et al.* Real-time Video Imaging of Mechanical Motions of a Single Molecular Shuttle with Sub-millisecond Sub-angstrom Precision. *Bulletin of the Chemical Society of Japan* (2020).

22. McVitie, S. *et al.* Aberration corrected Lorentz scanning transmission electron microscopy. *Ultramicroscopy* **152,** 57–62 (May 2015).

23. Aharonov, Y. & Bohm, D. Significance of electromagnetic potentials in the quantum theory. *Physical Review* **115,** 485–491 (Aug. 1959).

24. Chapman, J. N., McFadyen, I. R. & McVitie, S. Modified Differential Phase Contrast Lorentz Microscopy for Improved Imaging of Magnetic Structures. *IEEE Transactions on Magnetics* **26,** 1506–1511 (1990).

25. McVitie, S. & Cushley, M. Quantitative Fresnel Lorentz microscopy and the transport of intensity equation. *Ultramicroscopy* **106,** 423–431 (2006).

26. Rajeswari, J. *et al.* Filming the formation and fluctuation of skyrmion domains by cryo-Lorentz transmission electron microscopy. *Proceedings of the National Academy of Sciences of the United States of America* **112,** 14212–14217 (2015).

27. McGrouther, D. *et al.* Internal structure of hexagonal skyrmion lattices in cubic helimagnets. *New Journal of Physics* **18** (2016).

28. Krajnak, M., McGrouther, D., Maneuski, D., O'Shea, V. & McVitie, S. Pixelated detectors and improved efficiency for magnetic imaging in STEM differential phase contrast. *Ultramicroscopy* **165,** 42–50 (2016).

29. Nord, M. *et al.* Fast Pixelated Detectors in Scanning Transmission Electron Microscopy. Part I: Data Acquisition, Live Processing, and Storage. *Microscopy and Microanalysis* **26,** 653–666 (2020).

30. Paterson, G. W. *et al.* Fast Pixelated Detectors in Scanning Transmission Electron Microscopy. Part II: Post-Acquisition Data Processing, Visualization, and Structural Characterization. *Microscopy and Microanalysis* **26,** 944–963 (2020).

31. Volkert, C. A. & Minor, A. M. *Focused ion beam microscopy and micromachining* 2007.

32. Munroe, P. R. *The application of focused ion beam microscopy in the material sciences* Jan. 2009.

33. Dutka, M. *A New Generation of Multiple Ion Plasma FIB Technology | Helios Hydra* 2019.

34. Fernndez-Pacheco, A., De Teresa, J. M., Córdoba, R. & Ibarra, M. R. Magnetotransport properties of high-quality cobalt nanowires grown by focused-electron-beam-induced deposition. *Journal of Physics D: Applied Physics* **42,** 055005 (Feb. 2009).

35. Fernández-Pacheco, A. *et al.* Three dimensional magnetic nanowires grown by focused electron-beam induced deposition. *Scientific Reports* **3,** 1–5 (Mar. 2013).

36. De Teresa, J. M. *et al.* Review of magnetic nanostructures grown by focused electron beam induced deposition (FEBID). *Journal of Physics D: Applied Physics* **49** (2016).

37. Sheng, G. T. *et al.* Tin whiskers studied by focused ion beam imaging and transmission electron microscopy. *Journal of Applied Physics* **92,** 64–69 (June 2002).

38. Klepeis, S. J., Benedict, J. P. & Anderson, R. M. A Grinding/Polishing Tool for TEM Sample Preparation. *MRS Proceedings* **115** (1987).

39. Li, J., Malis, T. & Dionne, S. Recent advances in FIB-TEM specimen preparation techniques. *Materials Characterization* **57,** 64–70 (July 2006).

Chapter 4

Spontaneous Skyrmion Dynamics

Introduction

This chapter presents the analysis of spontaneous skyrmion motion across a skyrmion crystal lattice (SkX) domain boundary, and provides mechanistic insight into the skyrmion creation and annihilation processes involved. First, preliminary Fresnel TEM imaging experiments are used to demonstrate how different magnetic phases in B20 FeGe may be differentiated, and how to identify SkX defects. The observation of spontaneous skyrmion motion across a SkX domain boundary is then presented, and the high-speed image data is analysed using a variety of techniques to determine the configurational states involved. Next, micromagnetic simulations are performed in order to determine the key energy terms related to the formation of SkX defects and deformed skyrmions. Finally, by combining Fresnel TEM images and dynamic micromagnetic simulations, mechanisms for the observed skyrmion creation and annihilation processes are proposed.

Much of the work within this chapter can be found within the following published journal article: 'Rendell-Bhatti, F., Lamb, R.J., van der Jagt, J.W., Paterson, G.W., Swagten, H.J.M. and McGrouther, D. Spontaneous creation and annihilation dynamics and strain limited stability of magnetic skyrmions. *Nat Commun* **11,** 3536 (2020)'.

4.1 Imaging Skyrmion Lattice and Characterisation of Defects

Emergence of a hexagonal skyrmion lattice crystal (SkX) in B20 helimagnets can be described as a magnetic phase transition, involving nucleation of skyrmion quasi-particles from the helical ground state. This particle-like description of skyrmions is supported by experimental observations that indicate their high physical stability

[1], and ability to organise themselves into lattice domains within the SkX [2]. The SkX organisational structure is thus analogous to hexagonal close-packed atomic lattices, and two-dimensional honeycomb lattices such as graphene [3]. In such atomic systems, defects and domain boundaries exist to minimise lattice strain due to atomic vacancies and grain misorientation, respectively [4]. Analogously, the SkX may contain pairs of 5-fold and 7-fold coordinated skyrmions within $\Sigma 7$ domain boundaries, so called 5-7 defects as defined by coincidence lattice site (CSL) theory [5]. As in atomic systems, these domain boundaries separate regions of the SkX with distinct principle lattice vectors [6]. Interestingly however, and quite unlike atoms, the skyrmions involved in these regions are able to deform, accommodating local coordination changes through changing their structure.

Details of the SkX and its defects can be investigated using Fresnel TEM imaging, particularly in FeGe where the inter-skyrmion distance is on the order of 80 - 100 nm. The high-contrast variation of the skyrmions and inter-skyrmion regions in the SkX allows for the identification of defects [6], and the tracking of skyrmion positions [7], with relative ease. Figure 4.1 provides an example of a regular SkX (Fig. 4.1a), an isolated 5-7 defect (Fig. 4.1b) and a domain boundary (Fig. 4.1c). These Fresnel images were obtained on the JEOL ARM 200cF TEM, using the Orius CCD camera and were subsequently processed using ImageJ's 'Rolling Ball' algorithm to remove unwanted background contrast variation. The top panel of each figure shows the processed Fresnel TEM image, and the bottom panel is a Delaunay triangulation plot generated from the geometric centre of mass of the skyrmions in the Fresnel image.

Within the regular hexagonal SkX shown in Fig. 4.1a, each skyrmion has 6-fold coordination as demonstrated in the accompanying Delaunay triangulation, in which colour denotes the normalised triangular area, as given by the colour bar at the bottom of Fig. 4.1. In this regular section of SkX, skyrmions are separated by the equilibrium skyrmion lattice parameter, shown by the near uniform colour across the Delaunay Triangulation plot. The presence of an isolated 5-7 defect can be seen in Fig. 4.1b, where the skyrmions with 5- and 7-fold coordination are labelled accordingly. The Fresnel image demonstrates how the skyrmion with 7-fold coordination is spatially extended, whilst the skyrmion with 5-fold coordination is spatially compressed. As such, there is a variation in skyrmion lattice parameter around 5-7 defects, shown by the yellow and dark green regions in the Delaunay triangulation. Such deformations do not alter the topology of the skyrmions since they are continuous in nature, and thus the topological charge, N, remains constant during these deformations.

Finally, Fig. 4.1c shows a SkX containing a chain of 5-7 defects between two SkX regions (A and B), with principle lattice vectors (q_{1A} and q_{1B}). The presence of these 5-7 defects, like in atomic systems, reduces the lattice strain due to the misorientation of the domains. In this SkX, the domain boundary misorientation angle is reducing from right to left, and as such the boundary does not extend across the entire SkX. Therefore, a third SkX region (C) exists on the left of the SkX, with its own principal lattice vector, q_{1C}.

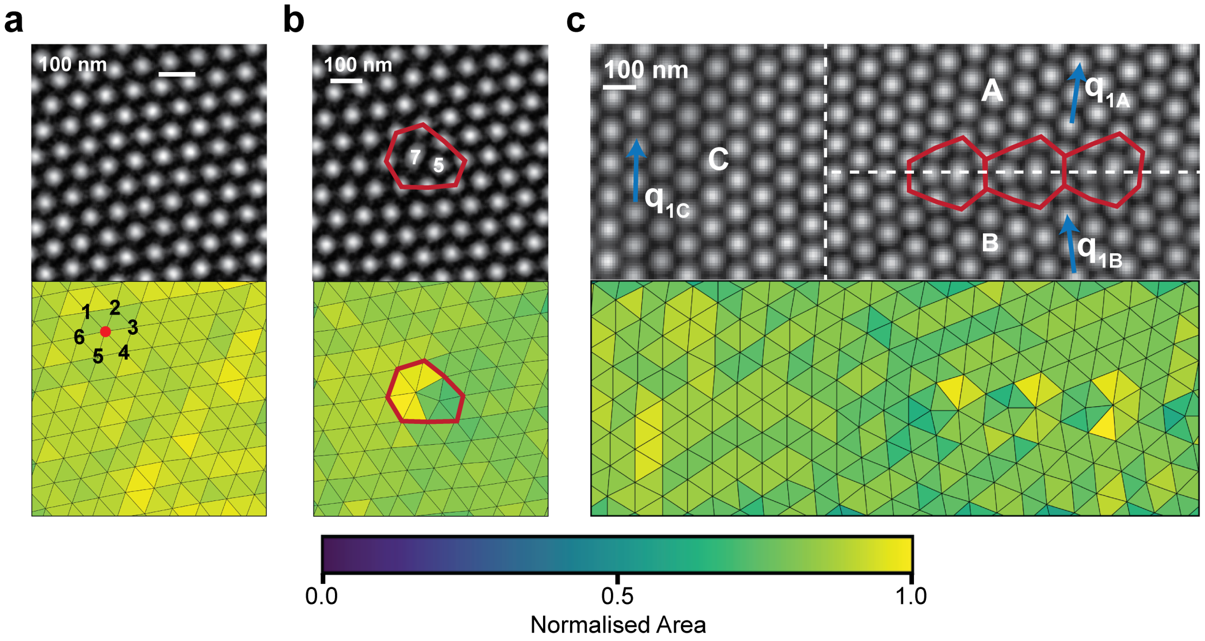

Figure 4.1: Fresnel TEM images (top) and Delaunay triangulation plots (bottom) showing (a) regular hexagonal SkX, (b) isolated 5-7 defect within SkX, where the annotations denote the coordination of the indicated skyrmions, (c) SkX with a domain boundary containing three 5-7 defects and three regions (A, B, C) with distinct principle lattice vectors (q_{1A}, q_{1B}, q_{1C}). Delaunay triangulation plots generated from the skyrmions geometric centre of mass are coloured according to the normalised area of the triangles and give an indication of skyrmion density. The red outlines are to provide a guide for the eye in locating the 5-7 defects.

The Fresnel image of a thin (<60 nm) FeGe plate is shown in Fig 4.2, prepared using FIB thinning techniques. Using the variations of magnetic structure indicated by the magnetic contrast, it is possible to deduce that the sample does not have a uniform thickness. Slight thickness variations across the sample mean that different regions have their own magnetic field–temperature phase space. For example, a region in the SkX phase is shown in the red box, the blue box highlights a region in the helical phase and a section approaching the field-polarised phase is shown in the green box. This suggests that the region in the blue box is too thick to stabilise skyrmions whereas the region in the green box is too thin to stabilise skyrmions. All three of these magnetic configurations are present at the same temperature and applied magnetic field value due to this sample thickness variation. Furthermore, the curved dark lines seen in the image are due to bending contours, indicating sample curvature. This non-magnetic contrast can often obfuscate magnetic detail, but the effect may be minimised through sample tilting.

The fact that SkX formation is dependent on thickness, magnetic field and temperature means that it is crucial to characterise phase change behaviour in individual samples. This is particularly important when investigating temperature or field dependence on dynamic processes, since changing these parameters may also induce magnetic phase transitions. It is possible to influence the formation of SkX domain boundaries and lattice defects, such as the extended skyrmion structure shown in the yellow box in Fig. 4.2, by quickly modulating the applied external magnetic field in the TEM by changing the excitation of the objective lens rapidly. Furthermore, it is often possible to eliminate these frustrated states, including defects and SkX domain boundaries, by increasing the temperature or applied magnetic field, analogous to annealing defects in atomic crystals.

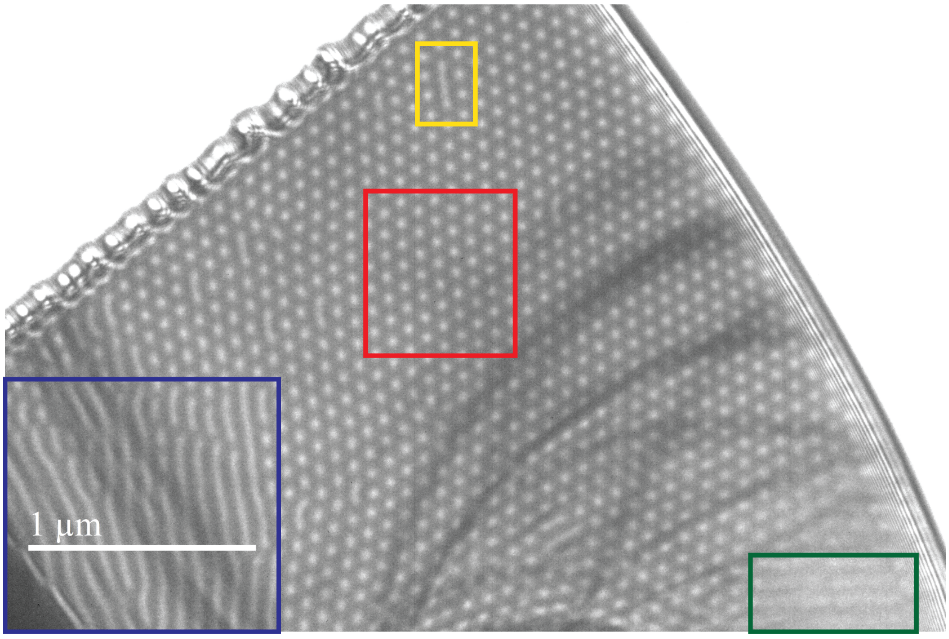

Figure 4.2: Fresnel image of a skyrmion lattice formed in a FeGe thin plate at a temperature of 243.15 K and a perpendicular magnetic field of approximately 0.2 T. The white spots denote the locations of the individual skyrmions. The dark curves seen in the bottom right of the image are bend contours, diffraction contrast arising from the fact that the sample is not entirely flat. The areas in the coloured boxes correspond to distinct regions as follows, blue: helical phase, red:, regular hexagonal SkX, green: approaching field polarised/conical, yellow: deformed elongated skyrmion.

4.2 Analysis of Spontaneous Skyrmion Motion

The raw Lorentz Fresnel image data of skyrmion dynamics across a domain boundary, which will be presented within this section, was previously acquired by Raymond Lamb and Damien McGrouther at the University of Glasgow. This raw data has been used with permission, and all analysis presented within this chapter is original work. The method to generate the aforementioned skyrmion dynamics is outlined below, before moving onto the analysis.

A SkX with two distinct domains, and therefore a domain boundary, was induced by application of a 510 Oe perpendicular magnetic field to a disordered helical state in a thin plate of FeGe at a temperature of 253 K. Filming of the skyrmion dynamics occurring across a SkX boundary was captured with the JEOL ARM 200cF transmission electron microscope (TEM), using the high-speed Merlin detector in continuous read/write mode with an exposure time of 10 ms. A total of 1000 frames displaying the dynamic skyrmion behaviour were acquired, and analysis of these Fresnel images follows.

4.2.1 Configurational State Identification

Spontaneous transitions between six unique configurational states (Fig. 4.3b-g) were observed within a region of SkX defined by the dashed box in Fig. 4.3a. These states were further categorised into three primary P_x states, namely, P_1, P_2 and P_3 (Fig. 4.3b–d), and three transition T_x states, namely, T_1, T_2 and T_3 (Fig. 4.3e–g). Each of the identified states featured a 5-7 defect, highlighted in Fig. 4.3b by the conjoined pentagon and heptagon. The skyrmions at the centre of the pentagons and heptagons are herein denoted as SkCoP and SkCoH, respectively. As previously mentioned, SkCoP are spatially compressed whereas the SkCoH are spatially expanded, due to the ability for skyrmions to continuously deform to account for local variations in coordination. Categorisation into the P_x or T_x states was defined by the relative position of the 5-7 defect and the number of skyrmions present along the row of skyrmions in which the lateral motion was taking place, highlighted by the black triangles in Fig. 4.3b–g. Within the field of view shown, T_x states contain eight skyrmions whereas P_x states contain seven skyrmions along the indicated row. This fact initially suggests that the repeated, spontaneous motion involves both creation and annihilation of individual skyrmions. Furthermore, during transitions between the six states, motion of the 5–7 defects alters the position of the domain boundary (shown by the blue/red/green dotted lines in Fig. 4.3a) and is accompanied by very slight shifts in the regular lattice skyrmions in the immediate vicinity as they accommodate the change.

In order to analyse the order of occurrence of the six states, each of the 1000 frames was assigned to one of the observed P_x or T_x states, through a combination of visual inspection and Delaunay triangulation. The system was observed to transition reversibly between P_x states via T_x states, and a portion of the recorded sequence data can be seen in Fig. 4.3h. An example highlighting the reversibility of the transitions is shown in section J of Fig. 4.3h, where the system begins in the P_1 state, goes through a series of transitions and ends up back in the P_1 state. However, some P_x–P_x transitions observed did not visibly appear to proceed via a T_x state, for example section K in Fig. 4.3h demonstrates an apparent P_1-P_2 transition. In these cases, it is assumed that, owing to the short-lived nature of the T_x states when compared to the frame acquisition time, occupation of the T_x state simply comprised a small fraction of the duration of an individual frame. Evidence for such an assumption comes from observations in which some smearing of intensity suggested multiple states (P_x and T_x) being captured in a single frame. Furthermore, the system did not always transition between different P_x states, as recorded in section L of Fig. 4.3h. This pattern suggests that, once the system is in a T_x state it can lower its energy by transitioning to a neighbouring P_x state, or back to its starting P_x state.

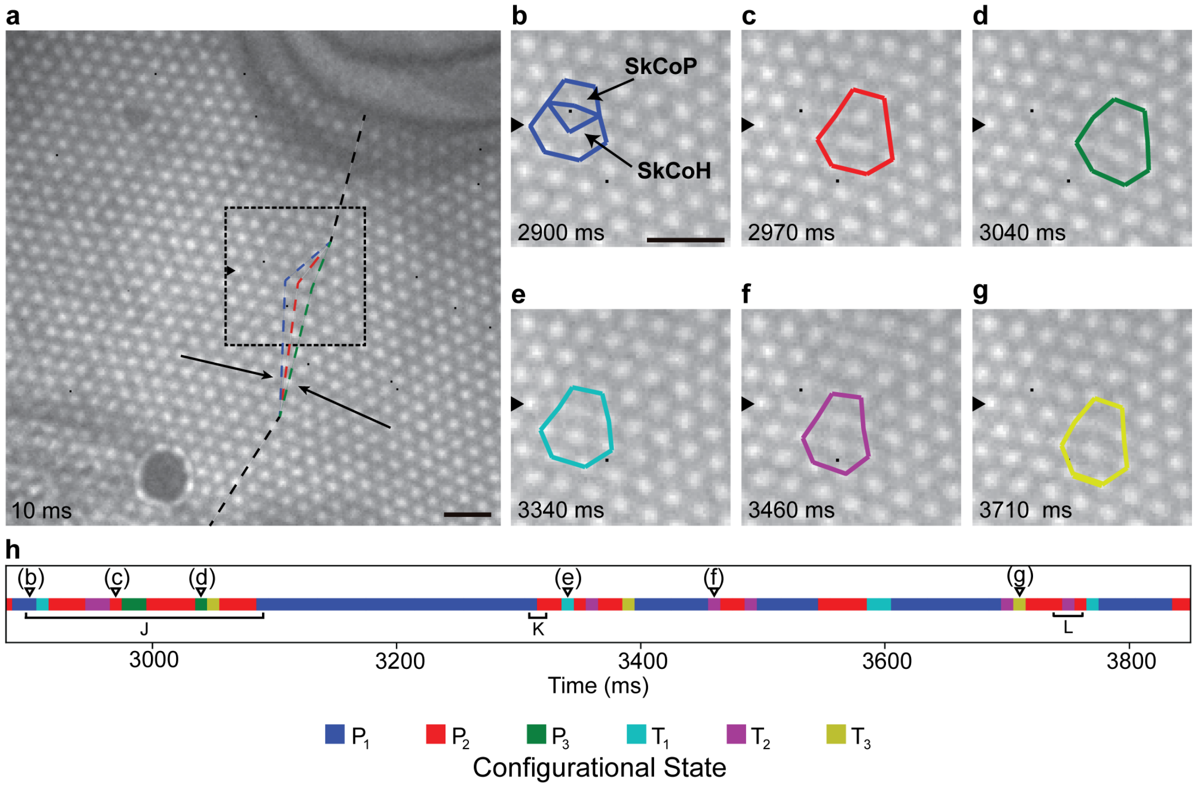

Figure 4.3: Fresnel TEM images of SkX and identification of configurational states. **a** Entire region of observed SkX, showing the domain boundary with an average misorientation angle of 14° (black dashed lined) and principle lattice vectors (arrows). The three coloured (blue, red and green) dashed lines demonstrate how the domain boundary shifts during transitions between the P_x states. **b-g** Examples of the six observed configurational states, time of each frame given in the bottom left corner of each image. The black arrowheads point along the row of skyrmions in which lateral motion was taking place. Skyrmions with 7- and 5-fold coordination (SkCoH and SkCoP, respectively) are highlighted by the conjoined pentagons and heptagons. **h** A portion of the transition data showing the progression of transitions between states shown in **b-g**. The markers (b)-(g) additionally indicate the time of occurrence of the images shown in **b-g**. Colour in each panel is associated with the identified configurational states, according to the bottom key. Scale bars, 200 nm.

Additionally, its possible to determine whether successive transitions are random in nature or follow a pattern by inspecting the transition probabilities shown in the matrix in Fig. 4.4. This demonstrates that successive transitions most commonly hop between spatially adjacent P_x states via the appropriate T_x state. For example, the probability of a P_1 to T_1 transition is higher than that of a P_1 to T_2 or P_1 to T_3 transition. Furthermore, the transition matrix shows that some transitions simply did not occur under observation, for example once the system was in the P_1 state it never transitioned to the T_3 state. This can be understood by the fact that the change in the lattice configuration from a P_1 to T_3 state is much greater than that of a P_1 to T_1/T_2 state. Therefore, it is assumed that the energy barrier associated with the 'neighbouring' transitions is much lower than that of the more spatially separated transitions, resulting in a much higher likelihood to occur.

Finally, the transitions may be described in terms of skyrmion creation and annihilation. During P_x to T_x transitions, the number of skyrmions present along the row involved in the lateral motion increases from seven to eight. During this process a SkCoP is created, appearing to be formed by the division of the expanded SkCoH in the original P_x state. Thus, through the SkCoH splitting, a skyrmion has been created and the local average skyrmion density should correspondingly increase. Conversely, during a T_x to P_x transition, the newly created SkCoP is annihilated by merging with a nearest-neighbour skyrmion, reducing local skyrmion density. Thus, skyrmion creation is associated with P_x to T_x transitions, and skyrmion annihilation is associated with T_x to P_x transitions. The higher local skyrmion density in T_x states than P_x implies a reduction of the mean inter-skyrmion distance, and a corresponding modification of local energy density. The portion of transition data given previously in Fig. 4.3h highlights the relatively transient nature of the T_x states when compared with the P_x states. This suggests that the energy cost of having an extra skyrmion in T_x states outweighs that of having one fewer in the P_x states. However, since the transitions are occurring spontaneously it shows that the thermal energy of the system is sufficient to initiate passage between these different configurations. The precise structure of the SkCoH and SkCoP within the 5–7 defects is elucidated through further image analysis of the six observed states.

4.2.2 Image Analysis of Configurational States

With the definition of the six configurational states, it is now possible to gain further insight into the microscopic details of the key skyrmions (SkCoH in P_x states and SkCoP in T_x states) involved in the spontaneous dynamics. First, the characteristics of P_x states will be described, followed by analysis of the more transient T_x states. In order to improve contrast in the images, each frame in the following analysis has had a background subtraction using ImageJ's 'Rolling Ball' algorithm, which is inspired by the algorithm presented in Ref. [8].

A series of four successive frames of the P_1 state is given in Fig. 4.5a, where the

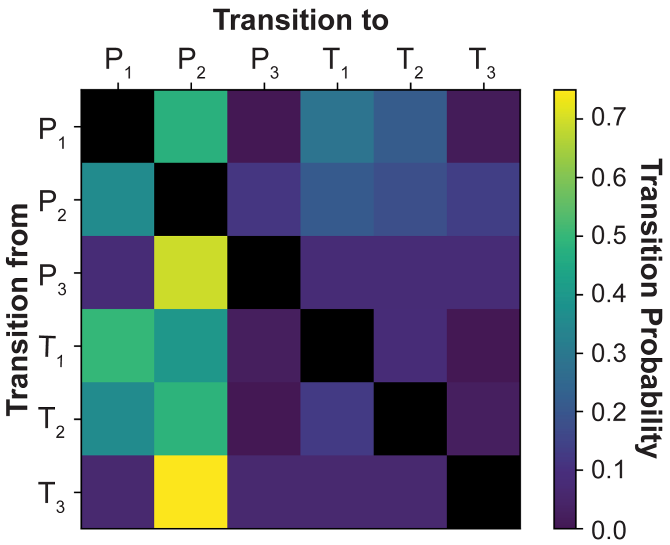

Figure 4.4: Transition matrix with probabilities normalised to unity across rows. Colour bar indicates the transition probability of each observed transition.

time of frame acquisition is given in the top left of each image. These series of images demonstrate that the SkCoH appears to have distinct curvature around its centre, and that the curvature increases as the sequence progresses. This behaviour demonstrates the dynamic nature of the SkCoH structure, in which the skyrmion appears to be deforming between elongated and dumbbell structures. Such structures represent a significant deformation from the regular 6-fold coordinated lattice skyrmions, and hints at the instability of such deformed SkCoH structures. However, it should be noted that as long as the deformations are continuous in nature, the topological charge of the deformed skyrmion remains unchanged. In other words, even though the skyrmion structure appears to be changing, it remains topologically stable across the four image frames. However, to be sure that there are no discontinuous breaks in the structure, quantitative information about the spin profile is required. This can be obtained on static structures using DPC imaging, however this method cannot be used in dynamic processes due to the finite scanning time to generate an image. It is therefore assumed that no such discontinuities are present and that, at least for P_1 states, lifetimes are on average greater than that of the frame time $(10\ \text{ms})$. A more detailed discussion of the method by which skyrmions are created and destroyed during the observed transitions will be given later in Section 4.2.5. Furthermore the observation of the P_1 state over successive frames indicates that lifetimes of all six states may be calculated from the order of occurrence data to determine relative energy barriers for transitions. This analysis will be performed in Section 4.2.4.

In order to obtain an average image for each of the six states, every frame of the one thousand total frames was assigned a state based on the analysis in Section 4.2.1. The individual frames of each state were then summed together and intensity normalised, to obtain six resulting average images, constructed from the corresponding frames. Each pair of images in Fig. 4.5b,c, consists of a normalised summed intensity image (left) and a Delaunay triangulation of the average skyrmion positions (right). Again, the Delaunay Triangulation plots are coloured according the triangular area, as defined by the colour bar. In Fig. 4.5d,e, integrated intensity profiles extracted from the dotted box in each summed intensity image in Fig. 4.5b,c are plotted. They record the intensity values along a path joining two skyrmions of regular 6-fold coordination, passing through a SkCoH in the case of P_x states (Fig. 4.5d) or through a SkCoP in the case of T_x states (Fig. 4.5e).

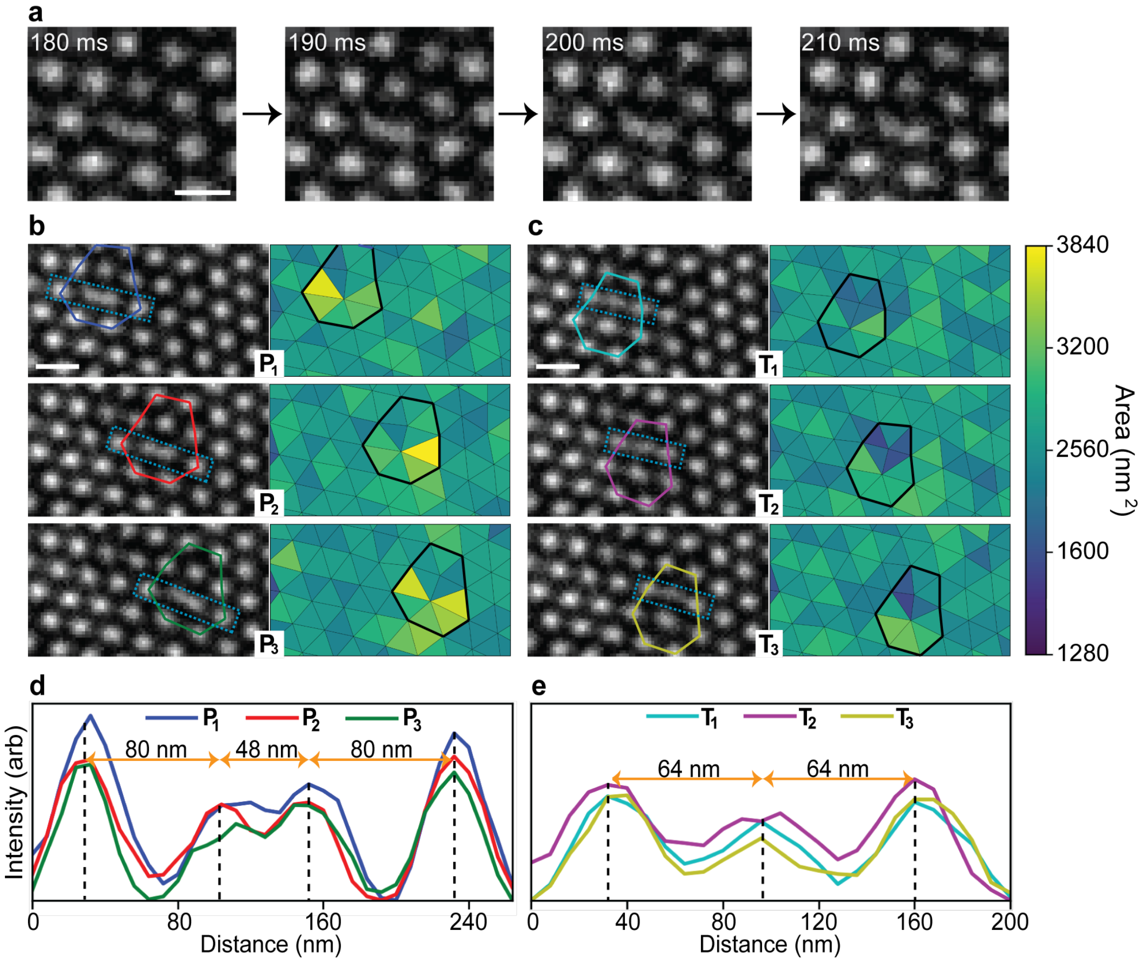

Figure 4.5: Spatial analysis of the six observed configurational states. **a** Successive frames showing the variation in structure of the SkCoH in the P_1 state, frame time in the bottom right of each image. **b**,**c** Normalised summed intensity images of each observed state (left) and Delaunay triangulation calculated from the skyrmion geometric centre of mass (right). The colour bar indicates the area of the triangles in nm^2. **d**,**e** Integrated line profile plots of the P_x and T_x states respectively, measured across the dashed rectangles in **b**,**c**. The double inner peak in **d** demonstrates the dumbbell structure of the SkCoH in the P_x states. Scale bars, 100 nm.

A key feature of the P_x states appears to be the relatively deformed structure of the SkCoH, as shown in Fig. 4.5b. From the summed intensity images, the SkCoH structure appears to possess the aforementioned dumbbell shape on average. This observation is supported by the intensity profiles in Fig. 4.5d, which further confirms that the SkCoH in each of the distinct P_x states have a highly similar form. These intensity profiles are characterised by two clearly defined central intensity peaks of approximately equal height, with an intensity 60%–70% lower than the regular neighbouring skyrmions of 6-fold coordination. These two central peaks correspond to the dumbbell shape of the SkCoH within the images. Structure of the P_x states is elucidated further through the Delaunay triangulation plots, where the 5-7 defect has a relatively low skyrmion density, as shown by the larger area yellow-coloured triangles. Figure 4.5d also shows that the same-row nearest-neighbour distances (i.e., from the intensity peaks of the SkCoH dumbbell to the intensity peaks of the adjacent regular 6-fold coordinated skyrmions) approximately match those of the bulk lattice of 80 nm. This suggests that the singular SkCoH is in fact deforming into an extended structure with two ‘lobes’, each at approximately the equilibrium distance from the regular lattice skyrmions. By comparing the SkCoH structure of the two most common states (P_1 and P_2), it was observed that 41% (205 of 499 frames showing P_1) and 87% (328 of 376 frames showing P_2) were characterised by a SkCoH skyrmion possessing an intensity central double peak, as described for the summed intensity images in Fig. 4.5b. This observation suggests that the precise structure of the SkCoH fluctuates, but a common state (indeed the most common state for the less stable P_2 state) is the dumbbell-like form.

Following a similar set of analyses for the T_x states in Fig. 4.5c, the SkCoP appears to be less well defined in the summed intensity images, appearing somewhat smeared. This highlights the transient nature of the T_x states, specifically the fact that the lifetime of these states appears to be on the order of the frame time (10 ms). The intensity profiles in Fig. 4.5e reflect this fact, where the inter-skyrmion intensity decreases to only around 58%–68% of the central peak values. This indicates that between the skyrmion positions, magnetic contrast does not fall to zero, likely due to change in structure on timescales less than the frame time. The line profile shows three defined intensity peaks, with a spatial extent of 128 nm, compared to the line profile of the P_x states with a spatial extent of 208 nm. This is further evidence of the creation of a skyrmion on transition from a P_x state to a T_x state, as the elongated SkCoH splits. The compressed nature of the SkCoP in the T_x state can also be observed in both the Delaunay triangulation map of Fig. 4.5c and in the intensity profile of Fig. 4.5e, in which same-row nearest-neighbour distance is measured to be 64 nm, 20% closer than in the bulk lattice.

A non-time varying 5–7 defect (from a different location along the same SkX domain boundary) is shown in Fig. 4.6, with the intensity across the SkCoH shown in the integrated line profile. Again, the SkCoH is more spatially extended than regular hexagonally coordinated lattice skyrmions. However, instead of the two distinct central intensity peaks that were observed for the dynamic SkCoHs in Fig. 4.5b, there is a single offset peak. This suggests that the stationary SkCoH in Fig. 4.6 likely possesses a single elongated core, displaced toward one side. The distance between the two intensity peaks belonging to regular skyrmions in Fig. 4.6 is approximately 192 nm, whereas this same distance is around 208 nm in the P_x states in Fig. 4.5d. This indicates that the SkCoHs in the P_x states have a greater lateral spatial extent than static 5-7 defects. This may be a contributing factor causing additional deformation that yields the dumbbell structure, and eventual skyrmion splitting. This suggests that a very deformed SkCoH structure may be a requirement for the skyrmion creation process, through modification of the energy landscape. Finally, comparing the dynamic and stationary SkCoH integrated intensity line profiles (Fig. 4.5d and Fig. 4.6, respectively), the lower relative central peak intensity further implies a higher structural variance in the dynamic SkCoH structures in the P_x states.

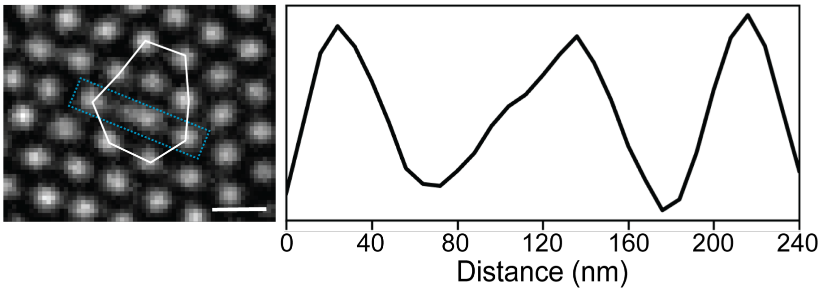

Figure 4.6: Normalised summed intensity image and line profile plot across a stationary (under observation) SkCoH, for comparison. This 5-7 defect is located further down the SkX boundary, just below the right black arrow in Fig. 4.3a. Scale bar, 100 nm.

By comparing the Delaunay triangulation images in Fig. 4.5b,c, it is clear that the triangular cells joining each skyrmion location have a lower area in the T_x states, making the overall nearest-neighbour distances shorter than in the P_x states (shown by the colour scale). This difference reinforces the fact that skyrmion creation causes regions of higher skyrmion density (T_x states) that reduce local energetic stability, leading to later relaxation to a P_x states through annihilation of a skyrmion. The fact that these transitions occur spontaneously suggests that the relative energies of the six states are close, and that the thermal energy fluctuations of the system are sufficient to overcome the potential energy barriers separating them.

4.2.3 Energy Landscape of 5-7 Defects

In order to gain insight into the energy terms that might govern the skyrmion creation and annihilation processes, we performed a series of micromagnetic simulations (using MuMax3) of both isolated 5–7 defects and those within a SkX boundary.

The damping, DM constant, exchange stiffness, saturation magnetisation and external magnetic field in these simulations were set as follows: Landau-Lifshitz damping constant $\alpha = 0.1$, bulk DM constant $D_{bulk} = 1.58$ mJ m^{-2}, exchange stiffness $A_{ex} = 8.78$ pJ m^{-1}, saturation magnetisation $M_s = 384$ kA m^{-1} and applied perpendicular magnetic field $B_z = 0.2$ T. All simulations were performed at 0 K and the material parameters were chosen in order to represent that of FeGe [9].

In order to compare the relative energy densities of a 5-7 defect and regular 6-fold coordinated skyrmions, the appropriate equilibrium lattice parameter first needed to be determined. This was found by varying the dimensions of a SkX triangular unit cell and minimising the energy with an external field of 0.2 T applied out-of-plane, as in Ref. [10]. Figure 4.7a shows the relationship between total energy density, η_{tot}, and skyrmion lattice parameter, a_{sk}, over a large range of lattice parameters. The overall shape of this graph resembles that of a Lennard-Jones potential for two interacting particles, again highlighting the particle-like nature of skyrmions. The minimum in the energy density plot can be seen more clearly in Fig. 4.7b, and corresponds to the equilibrium skyrmion lattice parameter of approximately 91 nm. This lattice parameter was implemented into the future simulations by constraining the simulation dimensions. This is an important step to ensure that the variations in energy density across the SkX are due to the presence or absence of 5-7 defects, rather than the relaxation towards the equilibrium value of a_{sk}.

The 2D energy density plots in Fig. 4.8a,b were obtained by simulating a 50 nm thick film of FeGe using periodic boundary conditions in the xy-plane, averaging the energy density through the thickness. The simulation in Fig. 4.8a involves a repeating array of 64 skyrmions, with simulation dimensions 632 nm $\times$ 730 nm $\times$ 50 nm and a cell volume of 1 nm^3. The skyrmions are located at the regions of high energy density (yellow regions in the figure) and the definition of a_{sk} is given through annotations. In order to obtain isolated 5-7 defects, a single skyrmion was deleted from the array of 64 skyrmions, using a strong localised field. This modified simulation state was then allowed to relax to reach the minimum energy configuration state shown in Fig. 4.8b. The deformed SkCoHs show up clearly as regions of high energy density, due to the large central skyrmion region, where the spins are oriented anti-parallel to the applied magnetic field. This increases the total Zeeman energy of a SkCoH when compared to a regular hexagonal skyrmion. A comparison between the energy densities of a 5-7 defect and regular skyrmion can be seen through the annotations in Fig. 4.8b, showing that there is an energy cost associated with the formation of a 5-7 defect within a SkX.

Although the simulations presented in Fig. 4.8 provide some insight into the energy cost of SkCoHs within 5-7 defects, they do not precisely represent the 5-7 defects located within domain boundaries observed in the dynamic processes. Thus,

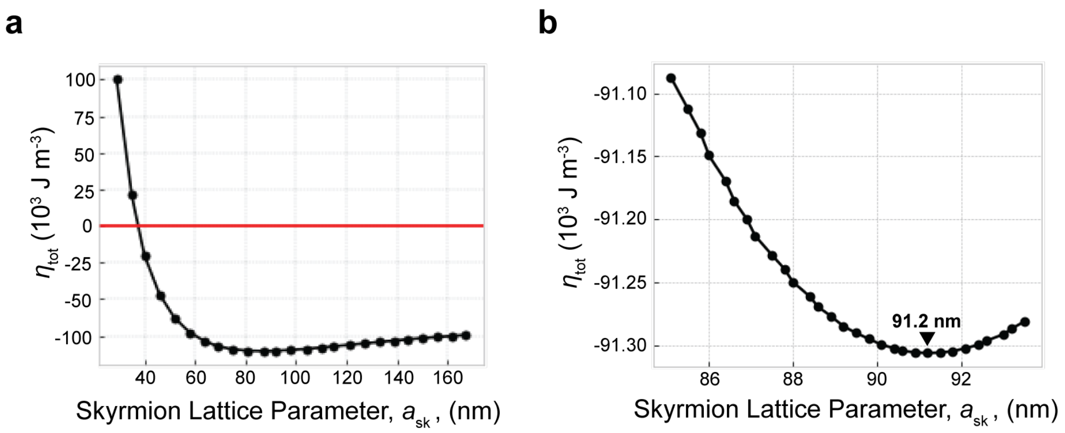

Figure 4.7: Total energy density plots (summed over the simulated region) as a function of skyrmion lattice parameter, a_{sk}, for a material thickness of 50 nm. **a** Energy density plot over a large range of a_{sk}. **b** Energy density plot near the minimum energy. The labelled equilibrium (minimum energy) lattice parameter of 91.2 nm in **b** is used in future simulations.

the formation of domain boundaries within a simulated SkX was pursued to investigate each of the energy contributions (Zeeman, Exchange+DM and demagnetising) in domain boundary 5-7 defects. In order to achieve the bi-domain state shown in Fig. 4.9a, the system was initialised in a randomly magnetised state and subsequently allowed to relax into a disordered helical lattice at zero applied magnetic field ($B_z = 0.0$ T). A perpendicular magnetic field of 0.4 T was subsequently applied in order to nucleate skyrmions, and allowed to evolve for a total simulation time of 1 μs. This length of time was required for the randomly distributed skyrmions to arrange themselves into a multi-domain skyrmion lattice. The external magnetic field was subsequently reduced to 0.2 T and the system relaxed, allowing the SkX to adopt the previously calculated skyrmion lattice parameter. Simulation dimensions were 1670 nm $\times$ 980 $\times$ 50 nm, with a cell volume of 1 nm^3.

As with isolated 5-7 defects, the SkCoHs within the SkX boundaries in Fig. 4.9a can be identified through their elongated cores. These elongated skyrmions have high integrated Zeeman energy density, as exemplified by the circled region in the Zeeman energy density plot (Fig. 4.9c). Additionally, the exchange+DM energy density plot (Fig. 4.9b) highlights an increased exchange energy density in the inter-skyrmion regions, particularly around the compressed SkCoPs (circled). Importantly, this suggests that regions of higher skyrmion density have an exchange energy cost, whilst regions of lower skyrmion density have a Zeeman energy cost. This is reflected in the lattice parameter plot of Fig. 4.7b, where deviating from the equilibrium lattice parameter in either direction leads to a higher total energy density. Furthermore, this helps to explain why increasing the external magnetic field acts to eliminate defects from a SkX (analogous to annealing), as it drastically increases the Zeeman energy cost of deformed SkCoHs with extended central regions. Finally, the demagnestising

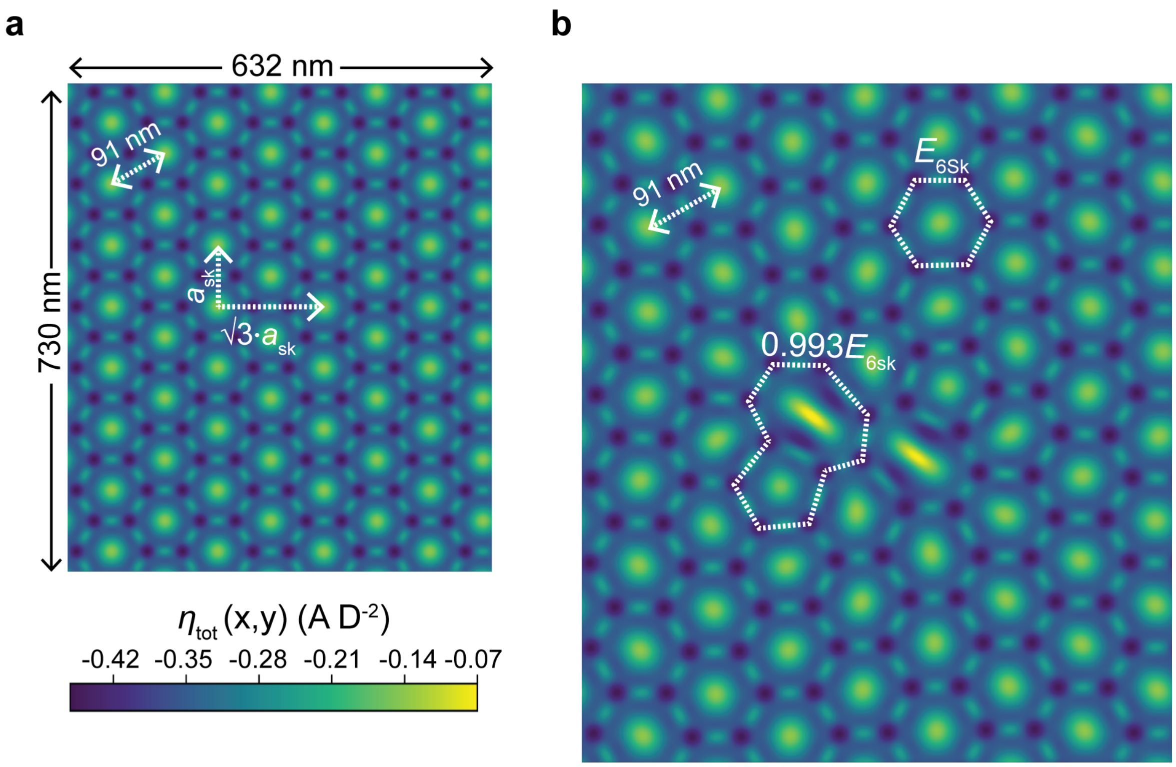

Figure 4.8: 2D total energy density plots of, **a** regular SkX with a_{sk} set to 91 nm and **b** SkX containing a pair of 5-7 defects imposed through skyrmion deletion. Energy density comparison between 5-7 defect and regular skyrmion in **b** is calculated from the regions enclosed by the dashed white lines. Energy densities are given in units of $\frac{A}{D^2}$, shown by the colour bar in **a**. In these plots, skyrmions are centred on the highest energy regions, with the skyrmion-skyrmion distance shown by the label for a_{sk} in **a**.

energy density plot can be seen in Fig. 4.9c, but this does not show any significant long-range effects across the lattice, and so does not appear to contribute as much to the formation of 5-7 defects as the short-ranged interactions.

Although these simulations are non-dynamic and performed at zero temperature, they provide some key insights into the minimum energy configuration of a SkX containing 5-7 defects within a domain boundary. Furthermore, they provide hints into the key magnetic interactions involved in the observed dynamic processes. Since the observed transitions between the six configurational states are accompanied by skyrmion creation and annihilation, the local skyrmion density is in constant flux. These transitions proceed via the splitting of an expanded SkCoH (P$_x$ to T$_x$ transition), which lowers the Zeeman energy but in creating an extra skyrmion, leads to regions of high skyrmion density (T$_x$ states), increasing the local exchange energy. Therefore, these states quickly collapse back into one of the P$_x$ states via skyrmion annihilation (T$_x$ to P$_x$ transition), lowering the skyrmion density but resulting in significantly expanded SkCoHs with a high Zeeman energy cost. These micromagnetic studies suggest that the interplay and balance of these two energy configurations results in the observed repeated, spontaneous transitions involving skyrmion creation

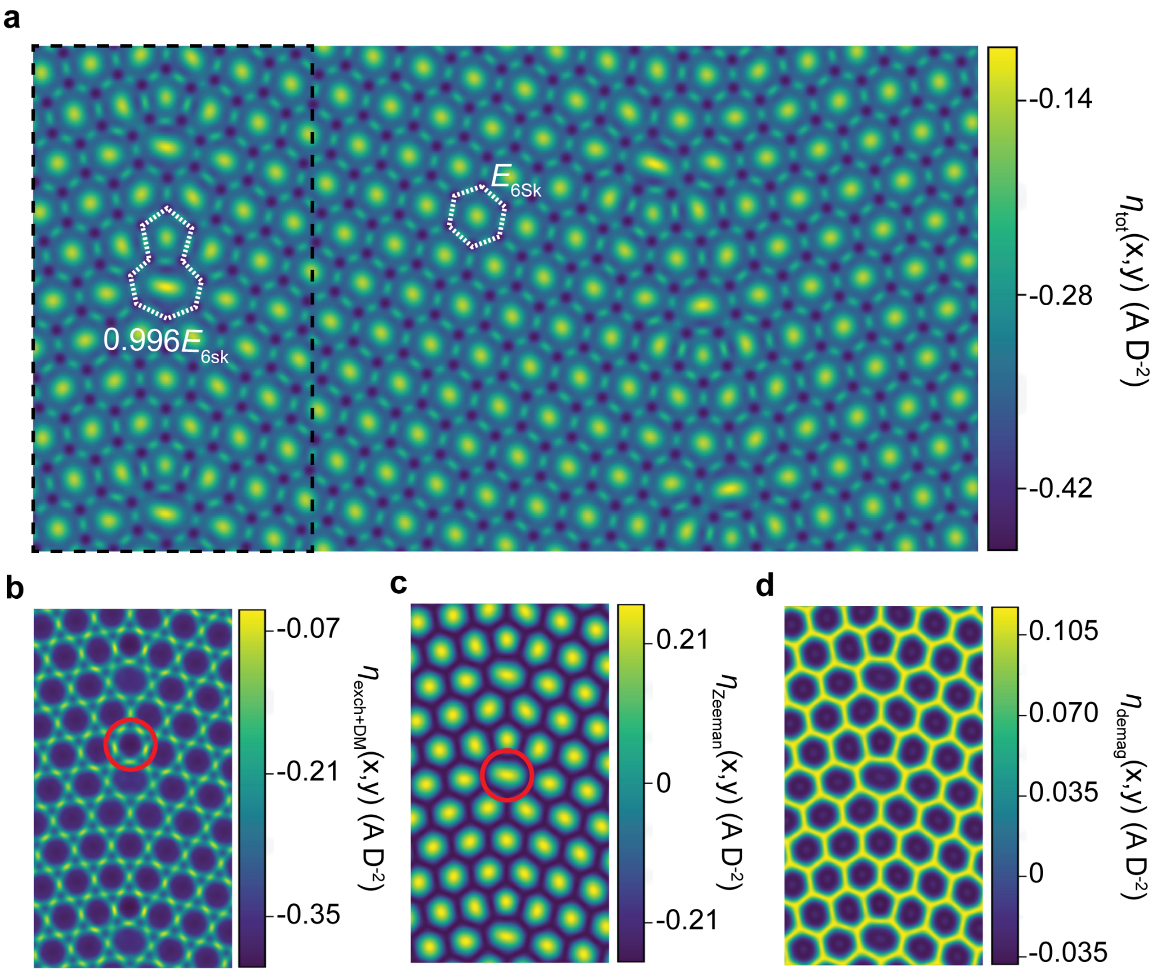

Figure 4.9: 2D total energy density plots of a SkX region containing two boundaries with three 5-7 defects in each. **a** Total energy density for entire simulated SkX region, energy density comparison between 5-7 defect and regular skyrmion from the regions enclosed by the dashed white lines. **b** Exchange+DM energy density, **c** Zeeman energy density and **d** demagnetising energy density. All subplots are from the left-most SkX boundary in **a**, enclosed by the black dashed box. Energy densities are given in units of $\frac{A}{D^2}$, scale shown by the colour bars accompanying each figure.

and annihilation.

4.2.4 Energetic Stability of Configurational States

In order to investigate the energetic stability of the six configurational states, lifetimes of each state over the one thousand frames were measured. This was carried out by counting the number of successive frames of a particular state and multiplying this number by the frame time (10 ms). Figure 4.10a shows the lifetime distributions along with the total number of observations of each of the six states. This shows that the P_1/T_1 and P_2/T_2 states were the most commonly observed. Owing to the short-lived nature of the T_x and P_3 states, these transitions may not always be captured individually, but may instead be averaged across the frame duration as previously mentioned. This explanation also suggests why T_x states were not always observed during transitions, since (for example) state lifetimes of 1 ms would contribute only 10 % intensity to the final 10 ms frame. This also suggests that use of a shorter frame time may help to elucidate the structure of these more transient states. It has been established that the system can transition to or from the same P_x state (P_1–T_1–P_1 for example). However, if the T_x state was very short-lived, then it is possible that the system would appear to have remained in the P_x state (for example P_1–P_1). This summing effect might explain some observations of very long lifetimes of around 400 ms for the P_1 state.

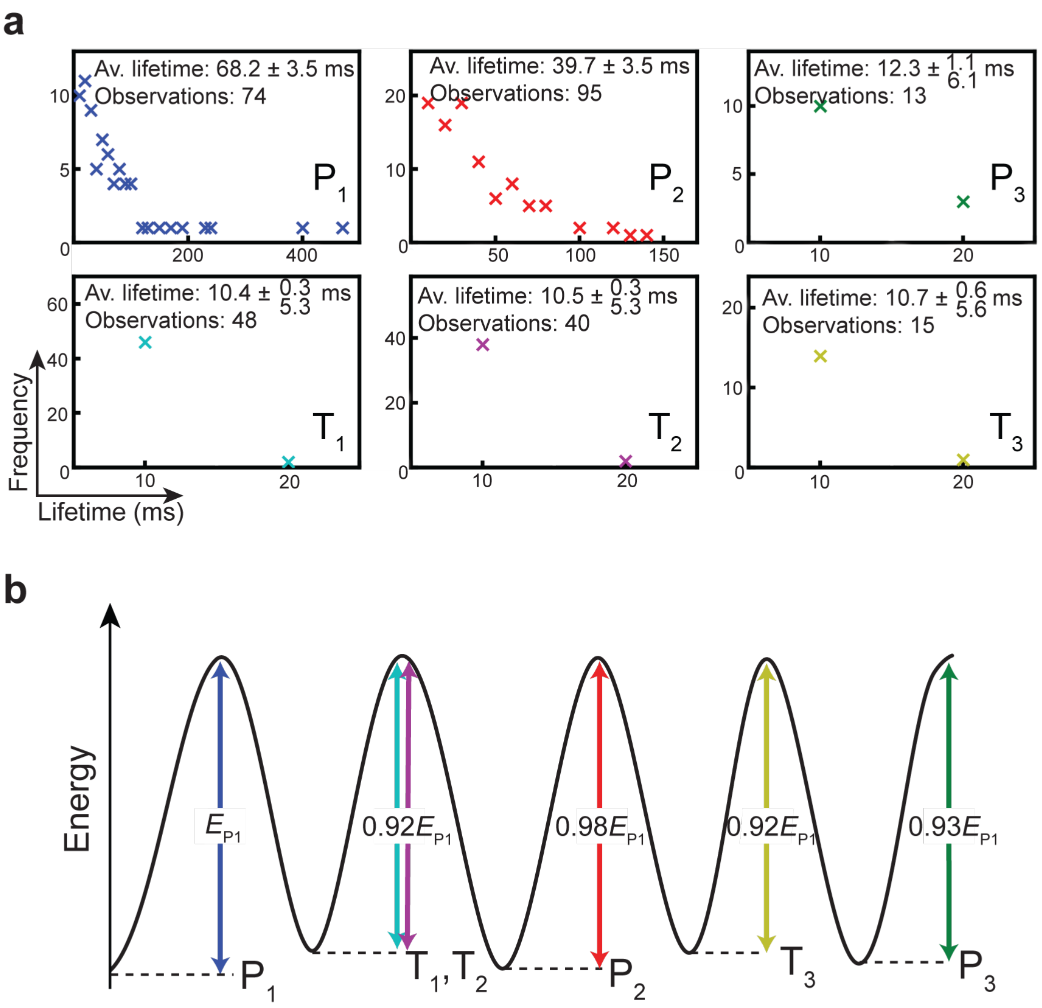

Figure 4.10: Lifetime distributions and associated energy barriers of each state. **a** Scatter plots of observed lifetimes, half the frame time (5 ms) was added to the lower bound uncertainties in T_x and P_3 due to the short-lived nature of these states. **b** Relative energy barriers calculated using the Néel-Arrhenius equation and average lifetimes. Each barrier height is given relative to P_1, which had an energy barrier height of 0.55 ev.

The timescale of a thermally activated magnetic transition between two states, separated by a potential energy barrier can be deduced from the Néel–Arrhenius equation:

$$\frac{1}{\tau} = \nu_0(T)e^{-\frac{\Delta E}{kT}} \tag{4.1}$$

where the lifetime, τ, of a particular state is the product of the temperature dependent attempt frequency $\nu_0(T)$ and an exponential term containing the Boltzmann factor, which gives the probability of a transition with energy barrier ΔE to occur at temperature T. The precise form of $\nu_0(T)$ can only be determined from detailed information about the minimum energy path taken during transitions. However, it has been reported that the attempt frequency for magnetic skyrmion annihilation in thin films is around 10^9 – 10^{10} Hz [11], which is in the range typically reported for other magnetic systems [12]. Conversely, theoretical studies into the minimum energy pathway of isolated skyrmion collapse report strong entropy-compensation effects, particularly for metastable skyrmions far from equilibrium conditions. These compensation effects lead to reported variations in $\nu_0(T)$ of up to five orders of magnitude [13–15]. However, the use of an attempt frequency of 10^9 Hz is justified here since only relative barrier heights are required. Therefore, any error in the estimated value of $\nu_0(T)$ will simply shift the entire energy landscape vertically, leaving the relative barrier heights unchanged.

With the assumption that the observed transitions obey Eq. 4.1 to a first approximation, and using an attempt frequency of 10^9 Hz and kT of 0.022 eV, relative energy barriers for the skyrmion creation and annihilation processes were thus calculated. These can be seen in the barrier heights of Fig. 4.10b, where each of the states are compared to the most energetically stable state, P_1, which had an absolute calculated barrier height of 0.55 ev. Note again that this absolute value was calculated using the approximate $\nu_0(T)$, which may vastly differ from the true value, and as such confidence in the absolute barrier height is low. Figure 4.10 additionally shows that the less stable P_2 state has 28 % more observations than the P_1 state. This disparity can be understood by the fact that the P_2 state is both energetically and spatially positioned between the P_1 and P_3 states. This suggests that there may be entropy-compensation effects involved due to the increased number of possible transition state configurations accessible from the P_2 state, thereby decreasing its observed lifetime.

By assuming that any individual transition is not affected by past transitions, the state transitions can be modelled using a Markov chain [16]. The observed transition probabilities and average lifetimes of each state were combined to give the Markov chain schematic in Fig. 4.11. In this diagram only transitions that occurred more than once are included, and the arrows(circles) are scaled to the relative transition probabilities(state lifetimes). By inspecting Fig. 4.11 it can be seen that during a transition from P_1 to P_3, it is more probable for the system to proceed in multiple lower energy steps via the P_2 state instead of a single step. Evidence for this multistep process is demonstrated by the individual transition probabilities given in Fig. 4.11, where zero transitions are observed between the P_1 and either T_3 or P_3 states. Instead, every state has a connection both to and from the P_2 state (red circle). This provides further evidence for the short lifetime and higher frequency of the P_2 state, being at the nexus of the transitions.

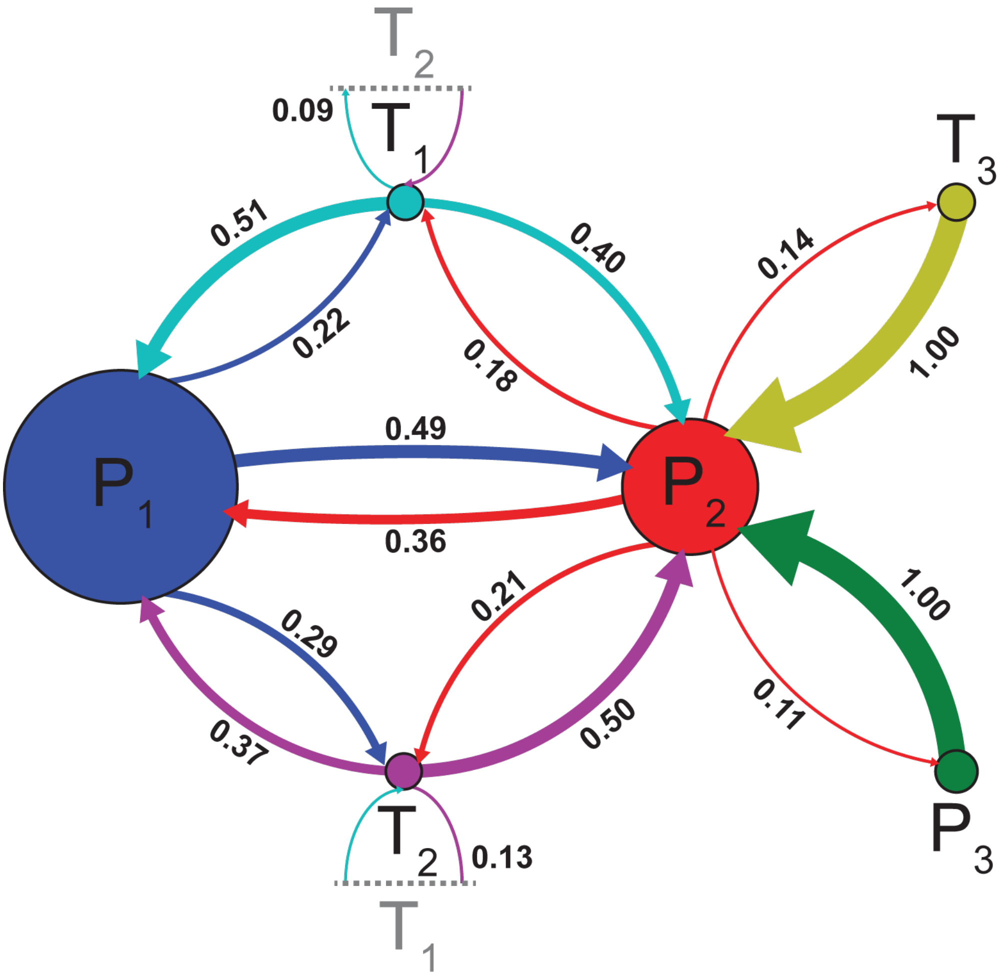

Figure 4.11: Observed state transitions represented as a Markov chain process, only including transitions observed more than once. Circles(arrows) representing each state(transition) are scaled to the relative lifetimes(transition probabilities). Values next to each arrow show the transition probability.

It should be noted that the T_1 and T_2 states were labelled at the same position in the energy landscape (Fig. 4.10b). This is because although they are spatially distinct (as was demonstrated in Fig. 4.5c), they differ only by a small shift in the skyrmion positions local to the SkCoP and therefore were approximately equally likely to occur. However, Fig. 4.11 and Fig. 4.4 both demonstrate that there is a small probability bias when transitioning from a T_x state to the corresponding P_x state. For example, T_2 to P_2 is more likely to occur than T_2 to P_1 because it requires a smaller overall shift in skyrmion positions.

4.2.5 Skyrmion Creation and Annihilation Mechanisms

Due to limitations in the spatial and temporal resolution of LTEM measurements, the fine details of the transition mechanisms are not yet accessible experimentally. However, it is possible to gain mechanistic insight into the skyrmion creation and annihilation process through micromagnetic simulations. By using spatially confined, short-duration magnetic field gradients, it was possible to initiate the merging of two neighbouring skyrmions (Fig. 4.12a top panel) and the splitting of an elongated skyrmion (Fig. 4.12a bottom panel). Figure 4.12d,e shows a series of magnetisation snapshots of skyrmion merging and splitting, respectively. The simulation parameters were chosen to represent FeGe and were as follows: $D_{bulk} = 1.58$ mJ m^{-2}, $A_{ex} = 8.78$ pJ m^{-1} and $M_s = 384$ kA m^{-1}. A damping parameter of α = 0.02 was used in order to investigate the dynamical aspects of the simulation under study here. A cell size of 1 nm was used, and the sample dimensions were 484 nm $\times$ 560 nm $\times$ 2 nm for the merging case and 512 nm $\times$ 256 nm $\times$ 2 nm for the splitting case. The merging process was also separately carried out with a 10 nm thick sample (484 nm $\times$ 560 nm $\times$ 10 nm) in order to investigate the details of antiskyrmion destruction through the thickness, shown in Fig. 4.12f. Figure 4.12b tracks the topological charge during the simulations for merging (left panel) and splitting (right panel).

The merging simulation is shown in Fig. 4.12d, where a very short-pulsed (0.7 ns) magnetic field gradient (25 MT m^{-1}) was localised around a skyrmion within a SkX. The field pulse is confined within a two-dimensional Gaussian distribution, with a standard deviation of 50 nm in the x-direction and 35 nm in the y-direction, shown by the dashed ellipse in Fig. 4.12a (top panel). This causes the skyrmion localised under the field gradient to move towards a neighbouring skyrmion, and eventually merge. The merging of the two skyrmions results in continuous rotation of magnetisation surrounding the two skyrmions, as demonstrated by the black circular arrow in Fig. 4.12d (left-most panel). This structure gives the appearance of an elongated skyrmion, with an antiskyrmion superimposed at the centre, indicated by the trapped out-of-plane magnetised region in the dashed box. This antiskyrmion subsequently reduces in size, as shown in the bottom set of vector plot panels in Fig. 4.12d. Once the antiskyrmion is at the minimum size allowed by the simulation, the central spin rotates in plane and the antiskyrmion topology is immediately destroyed. This is because the rotation of the central spin represents a discontinuous change in the structure. This is accompanied by a step-change in the topological charge (left panel in Fig. 4.12b), which accounts for the removal of the $N = -1$ associated with the antiskyrmion.

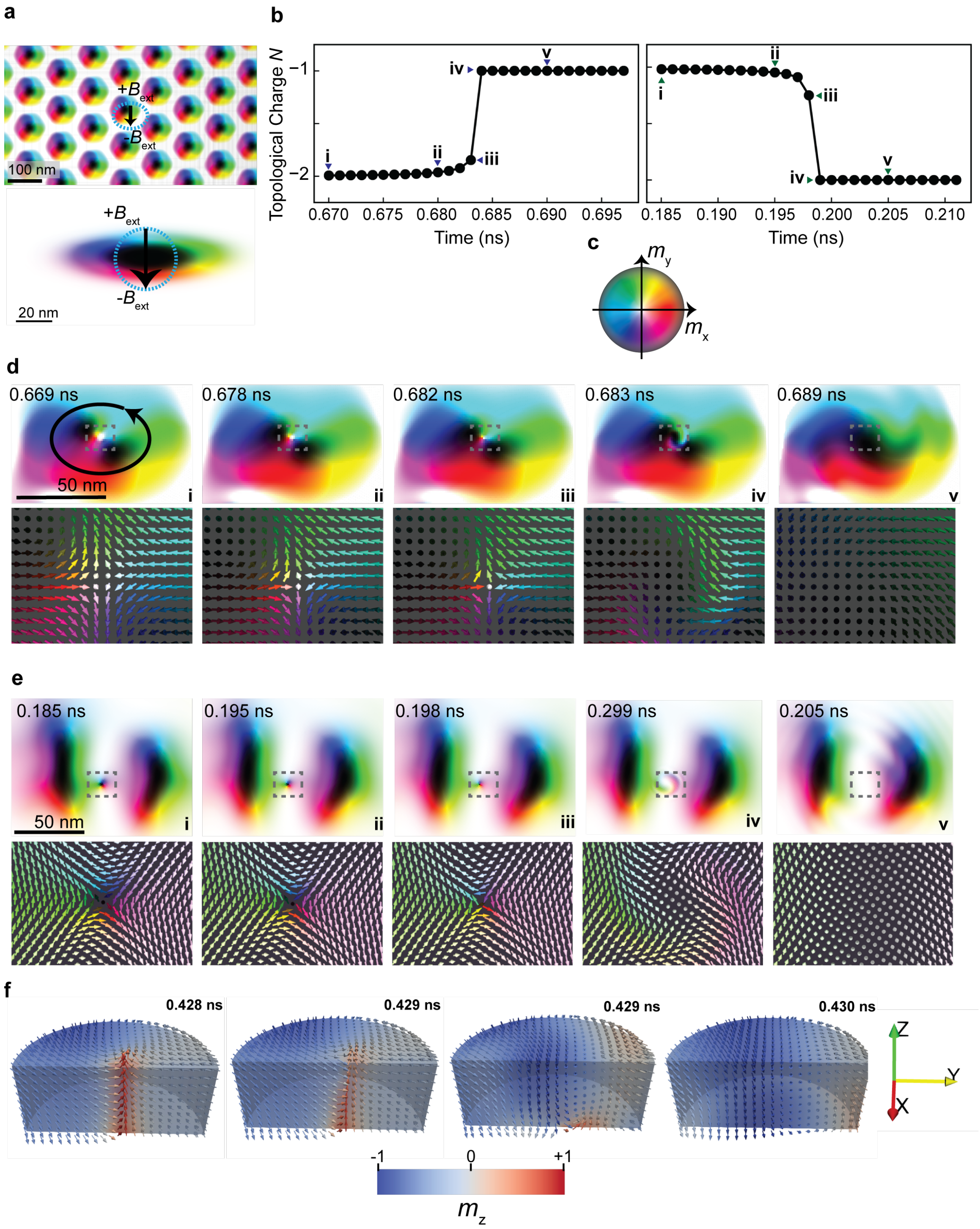

Figure 4.12: **a** Initial states of skyrmion merging (top) and splitting (bottom). Dashed ellipses show field-pulse confinement, with the arrow giving the positive to negative field gradient. **b** Topological charge as a function of time during the merging (left) and splitting (right) simulations, labels i-v correspond to the panels in **d** and **e**. **c** Colour wheel for simulations in **d** and **e**. **d**,**e** Scalar plots of magnetisation (top) and vector plots of antiskyrmion (bottom) during the skyrmion merging and creation, respectively. **f** Annihilation of antiskyrmion through a thickness of 10 nm.

The splitting simulation is shown in Fig. 4.12e, again a short-pulsed (0.15 ns) magnetic field gradient was localised around the centre of an elongated skyrmion.

The standard deviation of the gaussian in this case was 25 nm in both the x and y-directions, shown in the bottom panel of Fig. 4.12a. In this case, the elongated skyrmion quickly separates into two skyrmions each with $N = -1$, and a central antiskyrmion with $N = +1$. This conserves the initial topological charge of $N = -1$ of the single skyrmion. As before, the antiskyrmion first reduces in size and is then destroyed when the central spin rotates in plane. This is accompanied by a discontinuous change in topological charge (right panel in Fig. 4.12b) corresponding to the removal of the $N = +1$ associated with the antiskyrmion. Note the antiskyrmion in the merging case has opposite polarity to the antiskyrmion in the splitting case, which is why they have N of opposite signs.

Figure 4.12f shows how the antiskyrmion structure is eliminated in three dimensions, when a 10 nm thick sample is simulated. Here it can be seen that the central spin on the top surface first rotates in-plane, and then progresses down through the sample over a duration of 0.002 ns. This demonstrates the existence of antiskyrmion structures terminating mid-sample in a similar fashion to skyrmion bobbers [17], where the antiskyrmion structure only exists in half of the sample thickness (second panel in 4.12f) during its elimination.

Using information obtained from the micromagnetic simulations of skyrmion merging and separating, it is now possible to take account of the topological changes associated with skyrmion merging and splitting. This information has led to the proposal of mechanisms that explain how the experimentally observed spontaneous dynamic processes may be accomplished. Fig. 4.13a shows how a significantly deformed SkCoH with a topological charge of $N = -1$ may split into two separate skyrmions, corresponding to an experimentally observed P_x to T_x transition. This first occurs through stretching of the SkCoH, from an elongated structure to a dumbbell structure (as was shown experimentally in Fig. 4.5a). Such a deformation is continuous, and as such there is no associated change in topological charge. However, at the centre of the dumbbell-like SkCoH structure, significant magnetisation gradients and curvature occur, creating a region of locally high energy density and low energetic stability. This leads to formation of two skyrmion structures with a total topological charge of $N = -2$, connected by a central region containing an antiskyrmion with $N = +1$ (positive topological charge since it has the same core polarity as the two formed skyrmions). Thus, the antiskyrmion fulfils topological charge conservation during the SkCoH splitting into two skyrmions. The middle state in Fig. 4.13a corresponds to the states observed in the dynamical micromagnetic simulations. This micromagnetic transition state can be seen reproduced in Fig. 4.13c, where two individual skyrmions are joined by an antiskyrmion. The final step involves the unstable antiskyrmion reducing in size, until eventually the central spin rotates in-plane and the antiskyrmion topology is destroyed, accompanied by a step-change in total topological charge of $N = -1$ to $N = -2$. This antiskyrmion collapse mechanism has been proposed theoretically in Ref [14], where the saddle point configuration corresponds to the state preceding the central spin flipping (Fig. 4.13c right panel).

Figure 4.13b demonstrates the case for skyrmion merging (corresponding to a T_x to P_x transition). It is proposed that the reverse mechanism is followed, such that a reduction in proximity of two neighbouring skyrmions, with a total topological charge of $N = -2$, leads to a singled elongated skyrmion with $N = -1$. During merging of these neighbouring skyrmions, a region of out-of-plane magnetisation is necessarily trapped between the two merging skyrmions (middle panel in Fig. 4.13b). This structure is an antiskyrmion of opposite polarity to the previous splitting case, and thus has an associated topological charge of $N = -1$. Therefore, the antiskyrmion again fulfils the role of topological charge conservation during skyrmion merging. The resulting transition state and antiskyrmion corresponding to the middle state in Fig. 4.13b can be seen in Fig. 4.13d. Again, the antiskyrmion reduces in size until it is eventually destroyed when the central spin flips, resulting in a step change in topological charge from $N = -2$ to $N = -1$. This merging mechanism is similar to one suggested for skyrmion lattice inversion during polarity switching of an applied external magnetic field, whereby antiskyrmions are formed at the point of skyrmion core merging [18].

The notion of antiskyrmions conserving topological charge during creation or annihilation events has also been studied in dipolar magnets, in which antiskyrmions have a higher stability than that in chiral magnets [19]. The thickness of our sample (on the order of the FeGe helical length, 70 nm) implies that variation in magnetisation through the thickness will be minimal. This leads us to believe that the mechanism involves the creation and annihilation of antiskyrmions rather than the involvement of Bloch point zippers as discussed in Ref. [20], which studied a bulk sample. However, both of these mechanisms involve topological structures that are created and eventually destroyed to fulfil topological charge conservation during transitions. The mechanisms involving antiskyrmions demonstrated in Fig. 4.13 also bear resemblance to the proposed mechanisms of magnetic vortex core reversal, whereby anti-vortices are created and subsequently destroyed [21].

Recently, a theoretical study using a saddle point search method was used to determine saddle point configurations of skyrmions undergoing duplication and collapse [22]. These configurations bear many similarities with the dumbbell-like structures observed here, and are suggestive of the proposed transition state configurations involving antiskyrmions. It has been shown that, using a 360° domain wall model, skyrmion deformation does not significantly lower the universal skyrmion energy (the energy required to reduce skyrmion radius to zero) [23]. The energy barrier should be sufficient to prevent spontaneous skyrmion annihilation through reduction in radius, at the temperatures studied here. However, it is proposed that thermal fluctuations combined with extreme skyrmion deformation leads to the formation of the antiskyrmions as described. Thereby providing new energy pathways and providing a form of entropy-compensation for skyrmion creation and annihilation that are much lower than the calculated universal skyrmion energy.

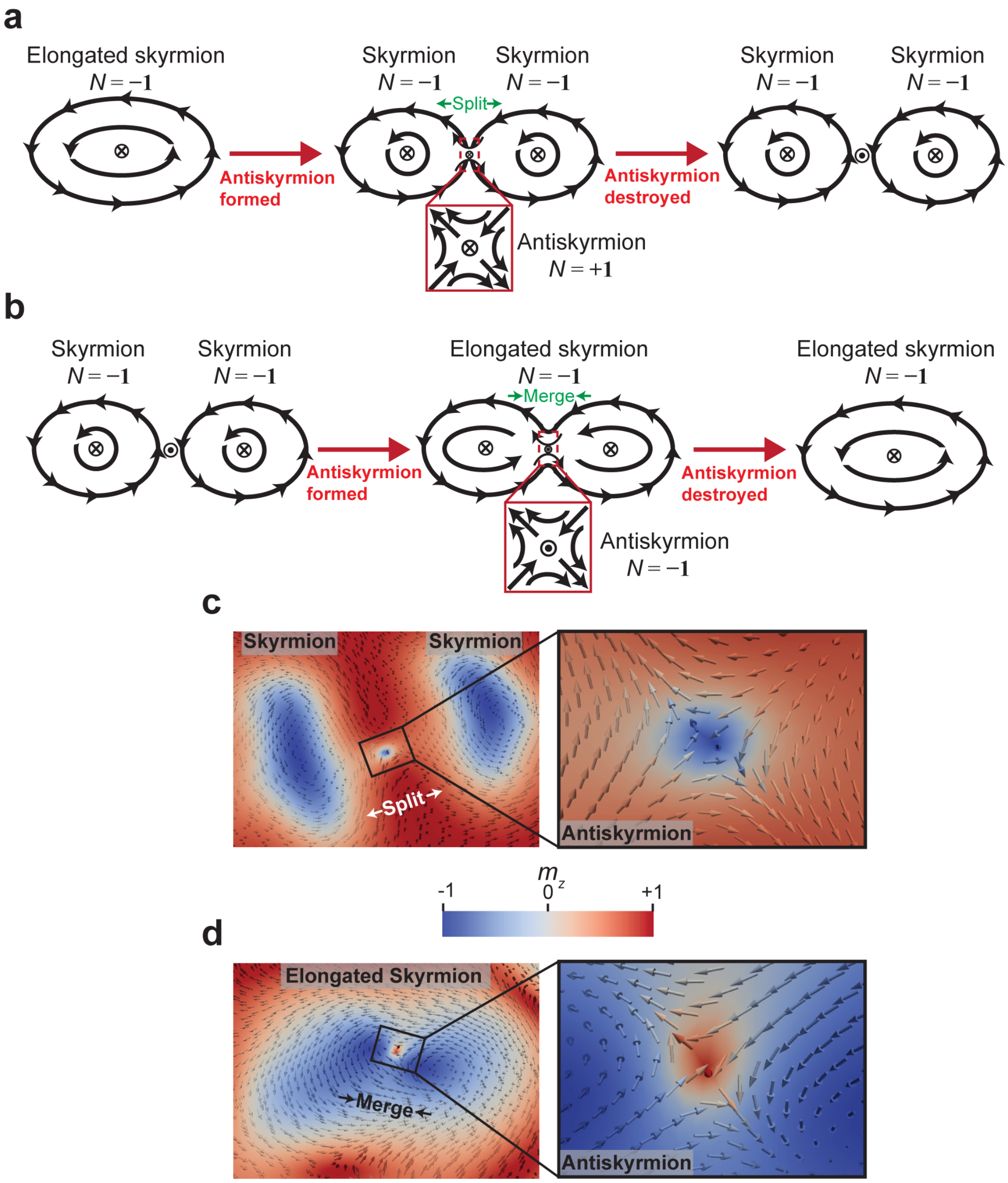
a
Elongated skyrmion
N = −1
Antiskyrmion formed
Skyrmion
N = −1
Split
Skyrmion
N = −1
Antiskyrmion destroyed
Skyrmion
N = −1
Skyrmion
N = −1
Antiskyrmion
N = +1
b
Skyrmion
N = −1
Skyrmion
N = −1
Antiskyrmion formed
Elongated skyrmion
N = −1
Merge
Antiskyrmion destroyed
Elongated skyrmion
N = −1
Antiskyrmion
N = −1
c
Skyrmion
Skyrmion
Split
Antiskyrmion
m z
-1
0
+1
d
Elongated Skyrmion
Merge
Antiskyrmion

Figure 4.13: Skyrmion creation and annihilation mechanisms. **a**,**b** Proposed mechanisms for skyrmion creation and annihilation via splitting and merging, respectively. N gives the topological charge of each structure involved. **c**,**d** Micromagnetic simulation snapshots of splitting and merging transition states, closely resembling the middle states in **a** and **b**, respectively. Colour bar indicates the out of plane (m_z) component of magnetisation.

4.3 Discussion and Conclusions

This chapter presents the analysis of spontaneous dynamic processes involving the creation and annihilation of individual skyrmions involved in 5-7 defects within a SkX domain boundary. Section 4.1 first introduced methods for imaging and identifying different magnetic configurations in skyrmion-hosting B20 helimagnets using Fresnel TEM imaging. The observed spontaneous dynamic motion of skyrmions was then introduced in Section 4.2. Next, in Section 4.2.1, frame-based analysis enabled the identification of key configurational states, and Section 4.2.2 presented the variations of structure within SkCoH and SkCoP that lead to skyrmion creation and annihilation through splitting and merging. Investigation into the key energy terms and the energy landscape of 5-7 defects was carried out using micromagnetic simulations in Section 4.2.3. This demonstrated the importance of both the Zeeman and exchange interactions within the deformed SkCoH and SkCoP in explaining the repeated spontaneous motion. It was determined that the primary P_x states, with their spatially extended SkCoH, had a significant Zeeman energy cost, whilst the T_x states with their higher skyrmion density had a significant exchange energy cost. Naturally, the observed transitions between these states are governed by thermal fluctuations, and induced exploration of a relative potential energy landscape in Section 4.2.4. These transitions appeared at first sight not to fulfil the concept of topological charge conservation, however, aided by micromagnetic simulations in Section 4.2.5, it is proposed that skyrmions can exhibit extreme deformation, leading to the formation of antiskyrmions. Through subsequent random local magnetisation fluctuations, the unstable antiskyrmions are destroyed. The appearance and subsequent destruction of these antiskyrmions may provide lower energy pathways for skyrmion creation and annihilation, in which topological charge is conserved.

These observations provide evidence of magnetic strain-limited skyrmion energetic stability in lattices, based on Zeeman and exchange interaction energies. This finding is contrary to many reports of high energetic stability, arising from topological protection for both isolated skyrmions and those in lattices [23–26]. Furthermore, the observations provide the potential for a new method of controlling skyrmion creation and annihilation through engineering SkX boundaries with high magnetic strain, induced via the intentional patterning of magnetic/non-magnetic defects with key dimensions comparable to SkX periodicity. Although the present study was limited to investigating a single SkX boundary, general observations are that 5-7 defect density and the rate of skyrmion dynamic events increase as a function of SkX misorientation angle [27]. A very recent high-resolution DPC study involving skyrmion creation processes [28], similar to those observed here, demonstrates that antiskyrmion structures are indeed involved in skyrmion creation as the proposed mechanism in Section 4.2.5 and Ref. [18] suggest. To summarise, the work presented here provides new insights into the dynamic transformation processes of topological structures within condensed matter systems. These observations strengthen theoretical predictions involving skyrmion and antiskyrmion duplication and annihilation made previously in Refs. [14, 18, 19, 22, 29, 30].

Although the image analysis presented in this chapter lead to the discovery of non-trivial skyrmion states during dynamic processes, it was limited to 10 ms frame times and a fairly low number of total frames (1000). In order to go faster, reaching the sub-ms frame time limit on the Merlin detector, and obtain larger datasets (6000 frames or more) more sophisticated automated methods for extracting skyrmion states are required. The following chapter highlights how such automated image detection algorithms may be combined with visual inspection to analyse dynamic processes involving skyrmions.

Bibliography

1. Karube, K. *et al.* Robust metastable skyrmions and their triangular-square lattice structural transition in a high-temperature chiral magnet. *Nature Materials* **15,** 1237–1242 (Dec. 2016).
2. Pöllath, S. *et al.* Dynamical Defects in Rotating Magnetic Skyrmion Lattices. *Physical Review Letters* **118** (2017).
3. Skowron, S. T., Lebedeva, I. V., Popov, A. M. & Bichoutskaia, E. Energetics of atomic scale structure changes in graphene. *Chemical Society Reviews* **44,** 3143–3176 (2015).
4. Randle, V. The coincidence site lattice and the ’sigma enigma’. *Materials Characterization* **47,** 411–416 (2001).
5. Brandon, D. G. The structure of high-angle grain boundaries. *Acta Metallurgica* **14,** 1479–1484 (Nov. 1966).
6. Matsumoto, T. *et al.* Quantum Physics: Direct observation of 7 domain boundary core structure in magnetic skyrmion lattice. *Science Advances* **2** (2016).
7. Huang, P. *et al.* Melting of a skyrmion lattice to a skyrmion liquid via a hexatic phase. *Nature Nanotechnology,* 1–7 (2020).
8. Sternberg, S. R. Biomedical Image Processing. *Computer* **16,** 22–34 (1983).
9. Beg, M. *et al.* Ground state search, hysteretic behaviour, and reversal mechanism of skyrmionic textures in confined helimagnetic nanostructures. *Scientific Reports* **5** (2015).
10. Shibata, K. *et al.* Temperature and Magnetic Field Dependence of the Internal and Lattice Structures of Skyrmions by Off-Axis Electron Holography. *Physical Review Letters* **118** (2017).
11. Rohart, S., Miltat, J. & Thiaville, A. Path to collapse for an isolated Néel skyrmion. *Physical Review B* **93,** 214412 (Jan. 2016).

12. Weller, D. & Moser, A. Thermal effect limits in ultrahigh-density magnetic recording. *IEEE Transactions on Magnetics* **35** (1999).
13. Wild, J. *et al.* Entropy-limited topological protection of skyrmions. *Science Advances* **3** (2017).
14. Desplat, L., Suess, D., Kim, J. V. & Stamps, R. L. Thermal stability of metastable magnetic skyrmions: Entropic narrowing and significance of internal eigenmodes. *Physical Review B* **98,** 134407 (2018).
15. Desplat, L., Vogler, C., Kim, J. V., Stamps, R. L. & Suess, D. Path sampling for lifetimes of metastable magnetic skyrmions and direct comparison with Kramers' method. *Physical Review B* **101,** 060403 (Feb. 2020).
16. Rabiner, L. R. & Juang, B. H. An Introduction to Hidden Markov Models. *IEEE ASSP Magazine* **3,** 4–16 (1986).
17. Zheng, F. *et al.* Experimental observation of chiral magnetic bobbers in B20-type FeGe. *Nature Nanotechnology* **13,** 451–455 (June 2018).
18. Pierobon, L., Moutafis, C., Li, Y., Löffler, J. F. & Charilaou, M. Collective antiskyrmion-mediated phase transition and defect-induced melting in chiral magnetic films. *Scientific Reports* **8,** 16675 (Dec. 2018).
19. Koshibae, W. & Nagaosa, N. Theory of antiskyrmions in magnets. *Nature Communications* **7,** 10542 (Apr. 2016).
20. Milde, P. *et al.* Unwinding of a skyrmion lattice by magnetic monopoles. *Science* **340,** 1076–1080 (May 2013).
21. Van Waeyenberge, B. *et al.* Magnetic vortex core reversal by excitation with short bursts of an alternating field. *Nature* **444,** 461–464 (2006).
22. Müller, G. P. *et al.* Duplication, Collapse, and Escape of Magnetic Skyrmions Revealed Using a Systematic Saddle Point Search Method. *Physical Review Letters* **121** (July 2018).
23. Büttner, F., Lemesh, I. & Beach, G. S. Theory of isolated magnetic skyrmions: From fundamentals to room temperature applications. *Scientific Reports* **8,** 1–12 (2018).
24. Sampaio, J., Cros, V., Rohart, S., Thiaville, A. & Fert, A. Nucleation, stability and current-induced motion of isolated magnetic skyrmions in nanostructures. *Nature Nanotechnology* **8,** 839–844 (2013).
25. Leonov, A. O. *et al.* Chiral Surface Twists and Skyrmion Stability in Nanolayers of Cubic Helimagnets. *Physical Review Letters* **117** (2016).
26. Oike, H. *et al.* Interplay between topological and thermodynamic stability in a metastable magnetic skyrmion lattice. *Nature Physics* **12,** 62–66 (2016).

27. Rajeswari, J. *et al.* Filming the formation and fluctuation of skyrmion domains by cryo-Lorentz transmission electron microscopy. *Proceedings of the National Academy of Sciences of the United States of America* **112,** 14212–14217 (2015).

28. Matsumoto, T., So, Y. G., Ikuhara, Y. & Shibata, N. Direct visualization of nucleation intermediate state of magnetic skyrmion from helical stripes assisted by artificial surface pits. *Journal of Magnetism and Magnetic Materials* **531,** 167976 (2021).

29. Garanin, D. A., Chudnovsky, E. M. & Zhang, X. Skyrmion clusters from Bloch lines in ferromagnetic films. *Epl* **120** (2017).

30. Desplat, L., Kim, J. .-V. & Stamps, R. L. Paths to annihilation of first- and second-order (anti)skyrmions via (anti)meron nucleation on the frustrated square lattice. *Physical Review B* **99** (Feb. 2019).

Chapter 5

Induced Skyrmion Dynamics

Introduction

This chapter presents further studies involving the analysis and creation of skyrmion dynamics processes. First, the utilisation of advanced image processing techniques are introduced and demonstrated, through investigation of transient skyrmion states involved in dynamic processes. This includes the implementation of image denoising algorithms and subsequent parts-based analysis of images via non-negative matrix factorisation. This combination of techniques leads to automated skyrmion state identification, using sub-ms Fresnel image frames. Next, the design and construction of a bespoke microcoil device for generating out-of-plane magnetic field pulses within the TEM is presented. Through the use of the microcoil and accompanying current pulser, highly disordered SkX states and controlled phase transitions are achieved.

5.1 Fast-frame Image Analysis Techniques

When acquiring high-speed Fresnel TEM video data of complex dynamical processes, it can be difficult to rely on visual inspection to characterise magnetic structure in the constituent image frames. A fast acquisition time often leads to noisy individual frames with low average intensity and contrast, due to fewer electron counts per frame. This presents a problem to both human visual inspection and automated identification methods such as ImageJ's Analyse Particles algorithm, both of which depend on relatively high-contrast images. Within the published work associated with imaging spontaneous skyrmion dynamics in Chapter 4 [1], this was overcome through the use of 10 ms frame acquisition times. With a frame time that is over ten times higher than the 0.822 ms supported by the Merlin detector readout system used in the work, it provided high average intensity within image frames. A downside to using a relatively long frame acquisition time, as demonstrated in Ref. [1], is that dynamic events with characteristic timescales less than the frame time are not always captured in individual frames. The result is an averaging of structure across multiple frames, making both visual analysis and automated techniques less effective. In order to confidently identify key configurational states involved in a dynamic process, the individual image frames should ideally contain a single distinct configuration. This promotes the use of fast frame acquisition times, resulting in the aforementioned issues with average image intensity and contrast.

A further challenge associated with high-speed Fresnel imaging, is the sheer quantity of images contained within large video datasets. By using a fast acquisition time, a larger number of total frames are required to capture dynamics occurring within the same time. For example, 1000 frames with a frame acquisition time of 10 ms results in a total video time of 10 s. To obtain this same video time with a 0.822 ms acquisition time, requires $12,165$ frames. This presents a serious challenge when attempting to identify and extract key configurational details from each constituent frame, and more statistical tools are required. Methods to overcome these challenges include Total Variation (TV) denoising algorithms with frame subsampling [2] and machine learning techniques involving neural networks [3–5]. This section presents a combination of these techniques in the form of TV denoising, frame subsampling and machine learning parts-based analysis. It is shown that it is possible to automatically identify skyrmion states from large (6000 frame) datasets, captured with sub-ms frame-times.

5.1.1 Image Denoising

A significant benefit of using the Merlin detector during Fresnel TEM imaging is the ability to acquire high-speed image data in the continuous read/write mode. The speed of this mode is limited by the data readout time, which is 0.822 ms for the default 120 MHz clock rate of the readout system, corresponding to frame times of 0.822 ms per frame (1216.5 FPS) [6]. However, as previously mentioned, when recording at these speeds a significant limiting factor becomes the number of electrons hitting the detector per second, thus reducing contrast and signal-to-noise ratio (SNR) in the resulting image frames. However, SNR may be improved post-acquisition through the use of image processing techniques such as Total Variation (TV) denoising algorithms [7]. TV denoising reduces the total variation of a signal, with the assumption that noise is a source of unwanted high variation. Thus, through the implementation of TV denoising, image noise can be reduced whilst preserving important details within the image. The TV denoising algorithm used within this thesis is part of the python skimage restoration module, and was originally proposed in

Ref. [8] for use with image data. Because of the low electron count in the original high-speed image frames, details in the denoised images can often still be difficult to interpret due to low image contrast. However, superposition of multiple denoised frames can be used to further increase contrast and SNR within the superposed images at the cost of frame time [2]. Here, it will be shown that by implementing these methods it is possible to obtain Fresnel TEM videos of skyrmion dynamic processes with frame rates of 400 FPS, four times higher than those employed in the previous chapter.

Figure 5.1a highlights the effect of the TV denoising algorithm on a Fresnel image of a SkX, demonstrating the variation in image detail as the weight parameter is increased. The images contain the familiar 5-7 lattice defect, as shown by the conjoined heptagon (red outline) and pentagon (blue outline). The SkX within the image was stabilised at a temperature of 240 K and a perpendicular magnetic field strength of 85 mT. The Fresnel image is of a cropped region of a SkX, where the original 256×256 pixel image frame has been reduced to 60×60 pixels, to centre the field of view around the 5-7 defect. This single image frame is one of six thousand, captured using the Merlin detector with a frame acquisition time of 0.822 ms. The full multi-frame dataset shows dynamic processes involving the aforementioned 5-7 defect, and will be treated further using NMF in the following section. The red arrow highlights the deformed 7-fold coordinated skyrmion at the centre of the heptagon, abbreviated to SkCoH in the previous chapter, as a visual guide to the effect of TV denoising.

When implementing the TV denoising algorithm, weight measures the strength of the resulting denoising effect, with a higher weight corresponding to a stronger effect. To determine the effectiveness of the TV denoising algorithm at different weights, the SNR was calculated in each image according to:

$$SNR = \frac{\mu_{sig}}{\sigma_{sig}} \tag{5.1}$$

where μ_{sig} is the mean signal value and σ_{sig} is the standard deviation of the signal. In this case, for images, the signal is the pixel intensity values. By inspecting the images in Fig. 5.1a and the SNR plot in Fig. 5.1b, it is clear that as the weight is increased, the denoising effect is also increased. Details within the image become obfuscated as the denoising starts to mask features within the images. There is a corresponding overall increase to SNR as well, however there is an initial drop in SNR for low weight values (0.00 to 0.02). The reason for this initial drop is due to the fact that for low weight values there is a slight reduction in μ_{sig} accompanying the reduction in σ_{sig}. This observed behaviour informed the chosen weight value for future implementations of the TV denoising algorithm. Overall, it was determined that a compromise between image fidelity and SNR should be used, and as such a weight of 0.05 (circled value in Fig. 5.1b) was chosen for future TV denoising processing on this dataset. It should be noted that the effect of TV denoising weight depends on the signal, and as such different weights may be required for different image datasets. The choice of weight value should preserves some high spatial frequency detail whilst increasing the SNR, thus improving the effectiveness of future image analysis techniques.

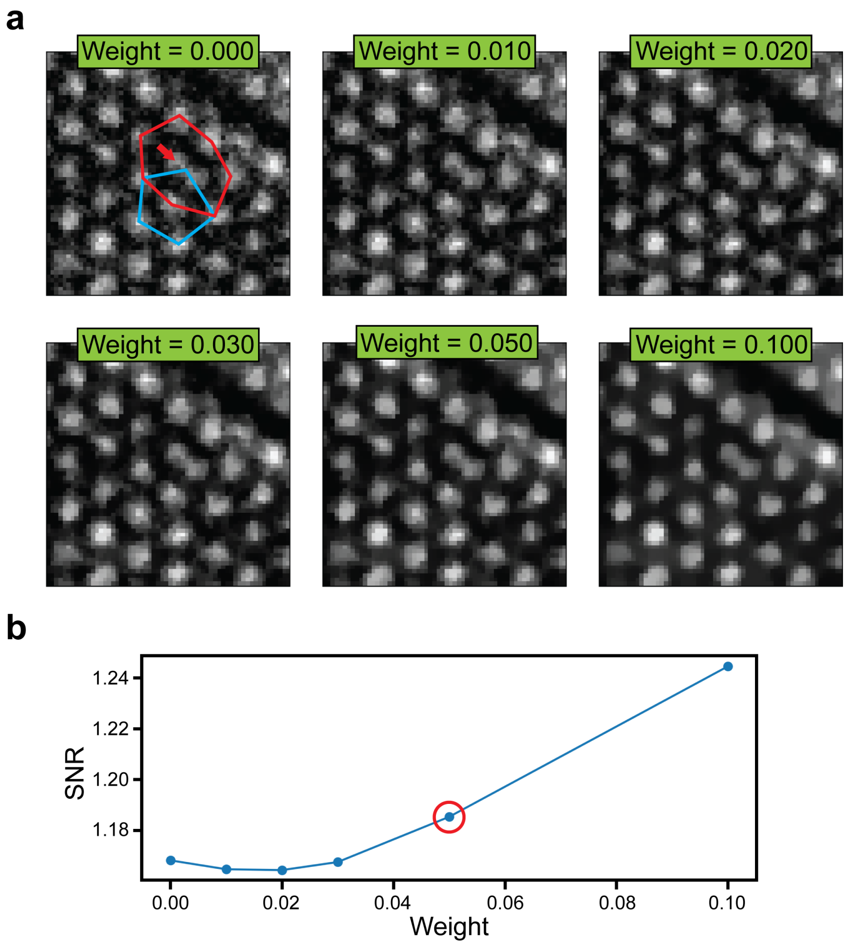

Figure 5.1: a The effect of using different weights within the Total Variation (TV) denoising algorithm on a single Fresnel TEM image showing a deformed SkCoH. **b** Plot of SNR against denoising weight, the circled weight value of 0.05 was chosen for future denoising analysis on this dataset.

5.1.2 Automated State Identification

As previously mentioned, when analysing large Fresnel video datasets it becomes difficult and time-consuming to rely on visual inspection to identify distinct magnetic states. Therefore, it is beneficial to employ other automated methods and although image processing techniques such as particle detection and edge finding algorithms may be implemented, these can often fail with low-contrast images or when features of interest are not sharply defined. An alternative method is to treat the multi-frame image data with parts-based analysis techniques such as non-negative matrix factorisation (NMF). NMF is a machine learning technique whereby a multi-dimensional dataset is approximated as a linear combination of basis elements and coefficients, through matrix factorisation. NMF is an unsupervised machine learning technique because it does not require training data, and instead learns to represent the large dataset by parts, using an iterative process. The power of this technique is that the generated basis elements represent key features within the original dataset, thus automatically extracting important information from arbitrarily large datasets. The non-negative constraint in this method dictates that the basis elements can only be combined additively when approximating an object within the original dataset. This is in contrast to other components-based analysis techniques, such as principle component analysis (PCA). Therefore, NMF is particularly well suited to analysing image data containing a range of configurational states, since images are intrinsically non-negative.

It has been shown that, by utilising NMF, it is possible to decompose a series of images depicting human faces, into a number of basis images and an encoding matrix [9]. The generated basis images contain key features extracted from the original images, such as noses, mouths, eyes, etc. It is then possible to approximate any original face image, using a linear combination of the basis images as determined by coefficients contained within the encoding matrix. By varying the number of basis images used in the analysis, it is possible to tune the quality of the approximation and therefore extract both low-order (few basis images) and high-order (many basis images) structural variations from the original dataset. As such, this NMF represents a robust, automated method of extracting distinct skyrmion states from a sequence of Fresnel images (i.e. a Fresnel video) showing skyrmion dynamics. NMF has been used within the context of electron microscopy previously to treat spectroscopic data [10], diffraction data [11], individual TEM images [12], and more recently large 4D STEM datasets [13]. In each case, NMF was employed to automatically treat large datasets and retrieve and interpret key features within the corresponding data types. Within this work, NMF was chosen to treat Fresnel video data, which is also four dimensional in nature and thus proves difficult for human interpretation alone. The NMF module used within this work was from the Scikit-learn python library [14], developed according to the work in Refs. [15, 16].

The process of performing NMF on Fresnel images will be now exemplified by using the image data from the previous section, shown in Fig. 5.1. The raw data consisted of six thousand 256×256 pixel Fresnel image frames, captured with a 0.822 ms frame acquisition time on the Merlin detector. The image stack was subsequently cropped to 60×60 pixel frames, such that the region of interest (skyrmion dynamics involving a 5-7 defect) was centred in the image. Subsequently, TV denoising was applied to each image with a weight of 0.05. To properly prepare the data for NMF, it is important that the desired features fill the field of view, and that the images have uniform, non time-varying contrast. If this is not the case then the NMF may pick up these variations as potentially important features. This justifies why the original 256×256 pixel images were intensity normalised, background subtracted and cropped to 60×60 pixels, centred around the region exhibiting the dynamics of interest.

The NMF process related to this dataset is demonstrated schematically in Fig. 5.2, where a cropped Fresnel video consisting of 6000 frames is factorised into a series of basis images and encodings in order to find key skyrmion states within the original image sequence. First, each image within the 6000 frames is converted to a one-dimensional column vector and combined into the $n \times m$ matrix V, where the m images are represented by the columns containing n pixels values in the rows. In this case, the dimensions of V are 3600×6000, since each of the 6000 images contained 3600 pixels (60×60 pixels). The goal of the NMF algorithm is then to approximate V through:

$$V \approx WH \tag{5.2}$$

where each column in the matrix W contains pixel values for a basis image, and each corresponding column in the matrix H contains encoding coefficients. The dimensions of W and H are $n \times r$ and $m \times r$, respectively, where r is the rank of the factorisation and gives the number basis images chosen to decompose the original data into. Thus, an image in the original dataset (a column in V) may be approximated through matrix multiplication between W and the corresponding encoding (column) in H. As an example, Image 1 in V (dimensions 3600×1) may be reconstructed through the matrix multiplication of W (dimensions 3600×2) with Encoding 1 in H (dimensions 2×1), resulting in an element in the new matrix WH (dimensions 3600×1). Note that V and WH will necessarily have the same dimensionality as they represent the same information in an original and approximated form, respectively.

In the example shown in Fig. 5.2, the number of basis images is two, which means that every original image in V will be represented as some linear combination of two basis images, with weights (coefficients) given by the encoding matrix, H. The number of basis images is a user-defined parameter, and as previous stated, the larger the number of basis images, the better the $V \approx WH$ approximation will be. However, the goal of using NMF on the Fresnel images is to determine the key skyrmion states, and its therefore possible disregard the high-order variations in the images contained in V. As such, it is advantageous to set the number of basis images to a low value and slowly increase it, whilst inspecting the generated basis images. By using this iterative method, it is possible to find the key states involved in skyrmion motion, since

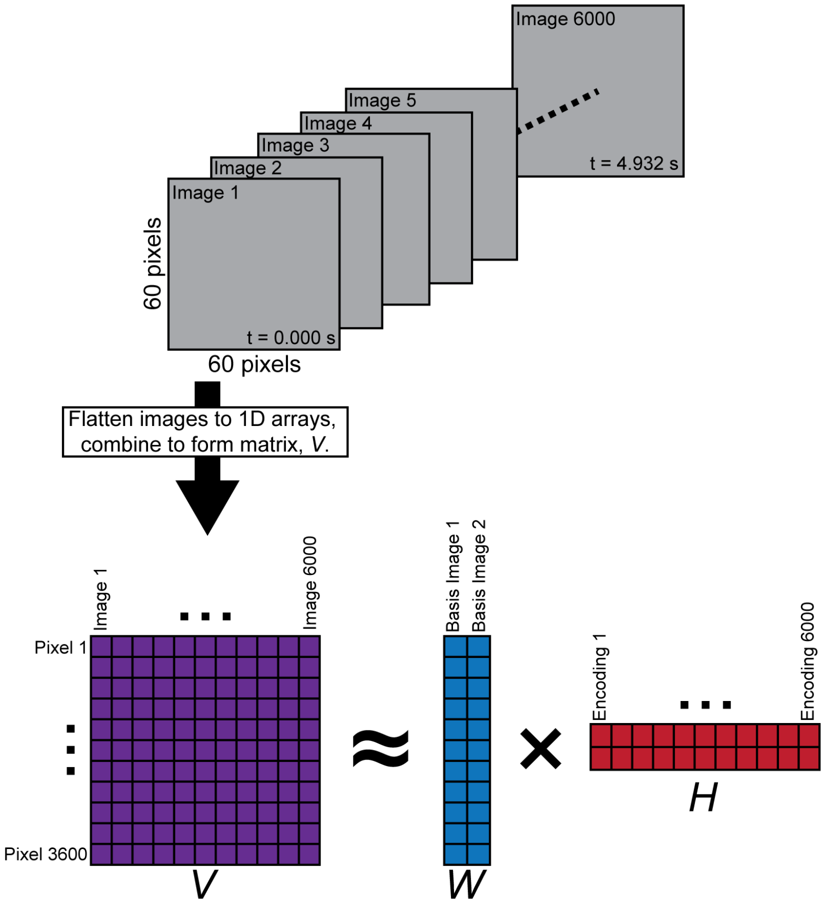
Image 6000
t = 4.932 s
Image 5
Image 4
Image 3
Image 2
Image 1
60 pixels
t = 0.000 s
60 pixels
Flatten images to 1D arrays, combine to form matrix, V.
Image 1
Image 6000
Pixel 1
Pixel 3600
V
Basis Image 1
Basis Image 2
W
Encoding 1
Encoding 6000
H

Figure 5.2: Schematic demonstrating NMF analysis as performed on a cropped Fresnel video containing 6000 individual Fresnel images with dimensions 60 × 60 pixels. First, each image is flattened into a 1-dimensional array and then combined into an $n \times m$ matrix, V, where the rows give the n pixel values for each image, m. Next NMF is performed on V by factorisation into two matrices, W and H, which contain the basis images and encoding, respectively. Each image in V can then be approximated through linear combinations of the basis images in W through multiplication with the encoding in H.

those that are most common over time should be the basis images generated by the NMF algorithm. Further structural complexity can then be found by increasing the number of basis images, thus accounting for higher-order variations within the original images.

Figure 5.3 shows the reconstructed basis images, contained in W, after NMF has been performed on the 6000 frames. The process was first carried out with two basis images, which can be seen reconstructed in Fig. 5.3a, whereas Fig. 5.3b shows the case for three basis images. First, inspecting Fig. 5.3a, we can immediately see that the NMF algorithm has identified two skyrmion 5-7 defect states (denoted Defect 1 and Defect 2) as the basis images. This suggests that to a first order approximation, every image in the original 6000 frames can be represented as some linear combination of these two basis images. It is therefore highly likely that these are two key skyrmion states involved the dynamics. To determine whether any further unique states are present within the dataset, the number of basis images can be increased by one before rerunning the NMF analysis on the original dataset. By increasing the number of basis images to three, as shown in Fig. 5.3b, it is apparent that Basis Image 1 and Basis Image 2 remain qualitatively similar to those in Fig. 5.3a. However, the defect in Basis Image 3 appears to have a highly similar form to the one in Basis Image 2, as shown by the outline around the 5-7 defect. Defect 2' in Basis Image 3 is demonstrating some higher-order structural variation, namely increased intensity (as shown by the red arrow) between the two skyrmions involved in the dynamic process. The fact that both Basis Image 2 and 3 appear to be representing the same 5-7 defect, suggests that Defect 2 is perhaps less stable and exhibits more structural variations than Defect 1, represented solely by Basis Image 1. Note that an arbitrary number of basis images may be chosen, and in this case prior knowledge of the video data was used to make the choice of the number of basis images. When extending to four basis images, it will be shown below how more dynamic complexity may be extracted but it is up to the user to determine at what point the basis images cease to be physically meaningful or useful.

It is possible to use the coefficients held within the encoding matrix, H, to obtain further information about the configurational skyrmion states, represented by the basis images. Since the encoding matrix H contains the coefficients required to approximate the original dataset V using the basis images W, each row in H can be plot concurrently to produce a time series-like plot for the transitions between basis images. In these plots, the higher the coefficient, the larger contribution that particular basis image has when estimating the original image frame in V. Note that in this case, the time increments will be determined by the frame acquisition time, so the frame number is a proxy for the time, t, assuming the detector is functioning in the continuous read/write mode. This temporal information can then be used to determine the order of occurrence and approximate lifetimes of the states as determined by the basis images.

The time series plots for two and three basis images can be seen in Fig. 5.4. Within these plots, a coefficient of zero means that the basis image is not required for representing the original image frame, and a high coefficient means that the basis image is a good representation of the original image frame. In the case of two basis images, in Fig. 5.4a, there are very clear transition points between the different defect states represented by Basis Image 1 and 2. These discontinuous transitions are thus exhibiting clear first-order transition behaviour between the two states. This plot demonstrates three such transitions within the 6000 frames, and it is apparent that the lifetimes of these states are on the order of thousands of milliseconds. Due to this relatively long lifetime, there is not sufficient data to estimate lifetimes of the two states. However, qualitatively it appears that Defect 2 (as represented by Basis Image 2) has a shorter

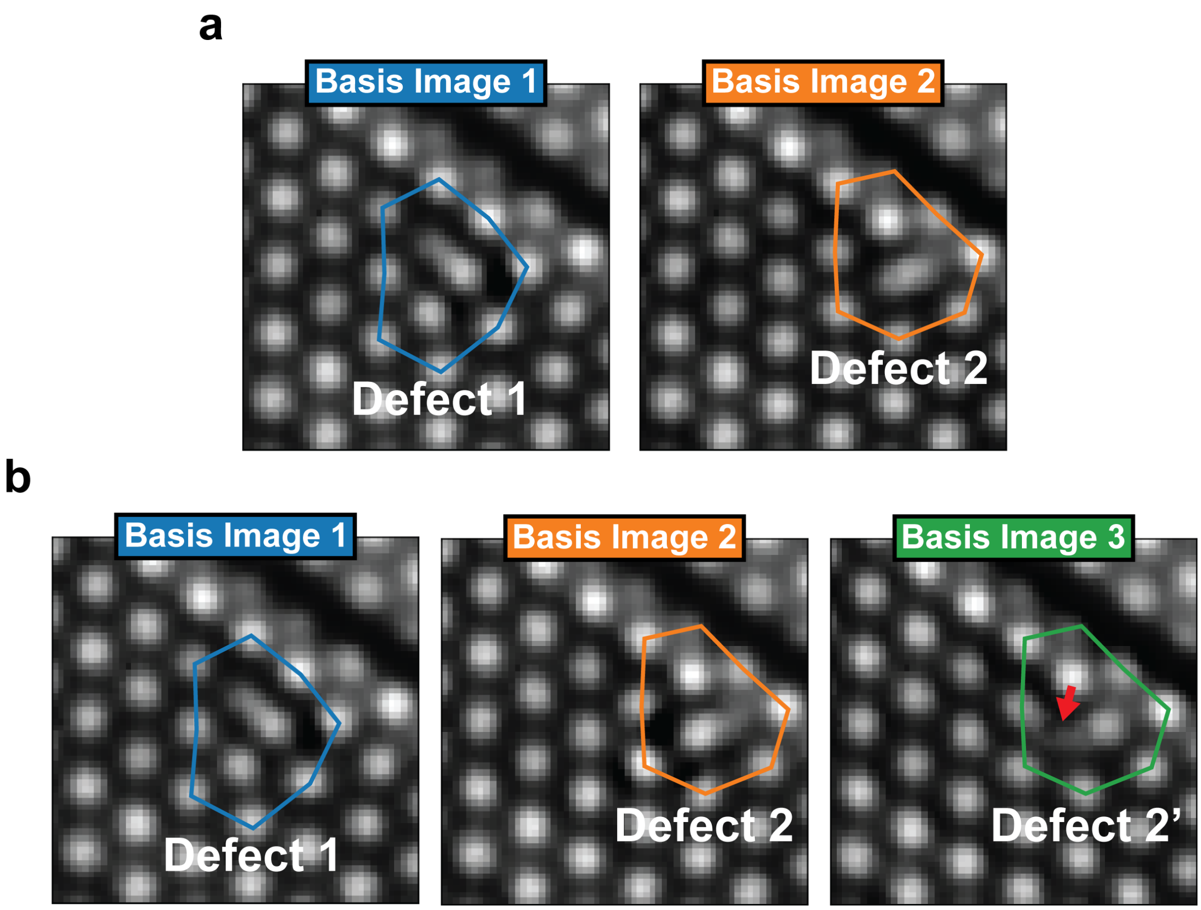

Figure 5.3: Non-negative matrix factorisation (NMF) performed on a 6000 individual Fresnel image frames to determine the key features. NMF performed with **a** two basis images, which is sufficient to identify the key states and **b** three basis images, highlighting some higher-order structural variation.

lifetime than Defect 1 (as represented by Basis Image 1). Increasing the basis images to three, in Fig. 5.4b, the previous first-order transition behaviour between Defect 1 and Defect 2 is still present. However, higher-order structural variations as represented by Basis Image 3 is is present throughout, and specifically within the first 2800 frames. The plot of Basis Image 3 reflects continuous structural variations occurring, as the curve varies smoothly rather than discontinuously (as in Basis Image 1 and 2). These two plots highlight the fact that, to a first-order approximation, the dynamic behaviour of skyrmions within the Fresnel video can be represented as a series of discontinuous transitions between two distinct configurational states, represented by Basis Image 1 and 2. However, higher-order variations of a continuous nature are extracted on addition of a third basis image, and the discontinuous structural change is superposed with continuous variations associated with Basis Image 3. Given the topological nature of skyrmions, it is likely that the continuous variations within Basis Images coefficients are associated with topologically conserved structure variation, whereas the discontinuous variations represent change in topology.

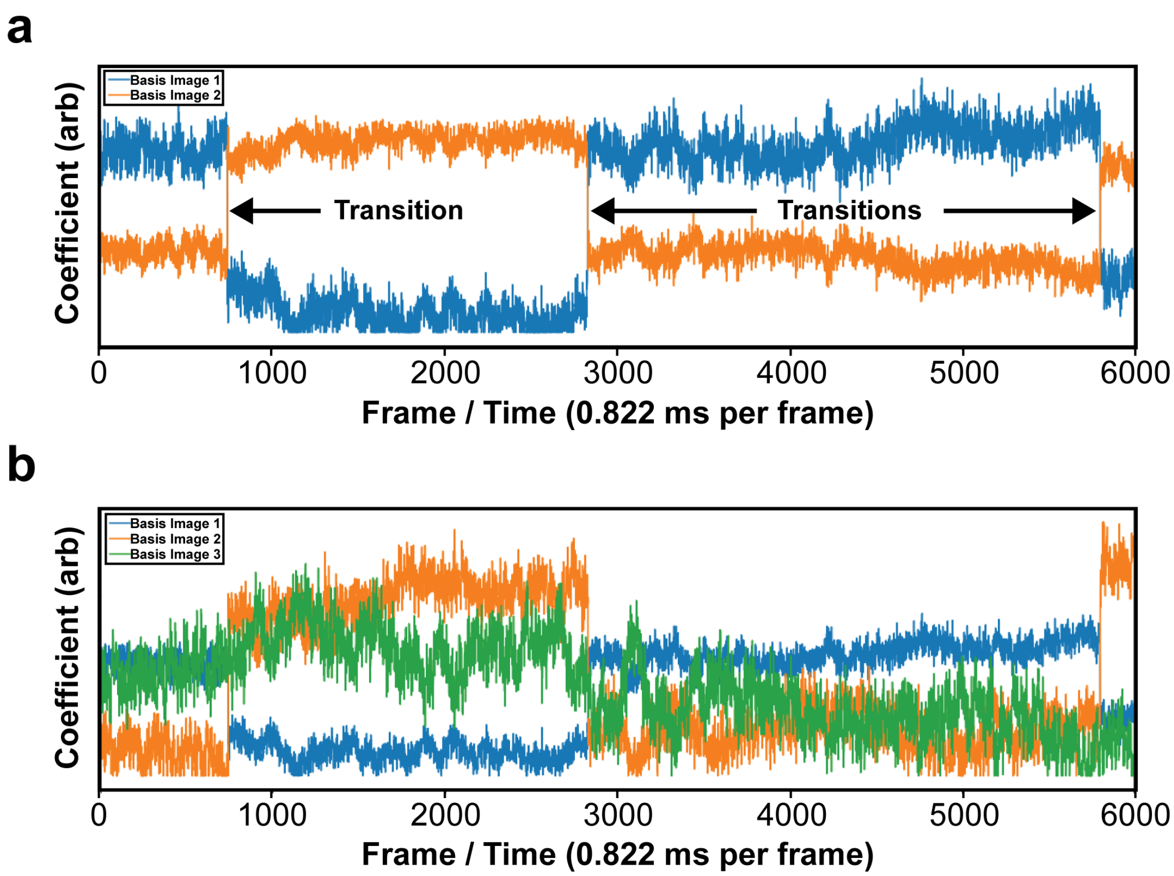

Figure 5.4: Coefficients from encoding matrix H plot as a function of frame to create a time series-like plot for **a** two basis images **b** three basis images. Each line corresponds to a row in the encoding matrix, and contains the coefficients associated with a particular basis image as noted by the key legend in each plot.

Indeed, the transition between Basis Image 1 and Basis Image 2 closely resembles the transitions observed in Chapter 4 involving discontinuous changes in topology as facilitated by antiskyrmions, and it is highly likely that a similar mechanism is involved here as well.

This analysis can be extended further through NMF utilising four basis images, as shown in Fig. 5.5a. Although there is some variation in intensity distribution, Basis Image 1 and 2 still represent Defect 1 and 2, respectively. Basis Image 3 again corresponds to Defect 2' and Basis Image 4 shows the same 5-7 defect configuration as Basis Image 1, and is thus given the label Defect 1'. It is now apparent that the main difference between Defect 1(Defect2) and Defect 1'(Defect 2') is in the intensity variations associated with the elongated 7-coordinated skyrmion, SkCoH. In both Defect 1' and Defect 2', there is a circular region of intensity associated with the SkCoH and a tail of lower intensity to the right and left respectively, as indicated by the pairs of arrows in each panel. This indicates that the majority of structural variations within the Fresnel video can be represented by basis images containing a pair of 5-7 defects, whereby higher-order structural variations represent structural changes of a continuous nature.

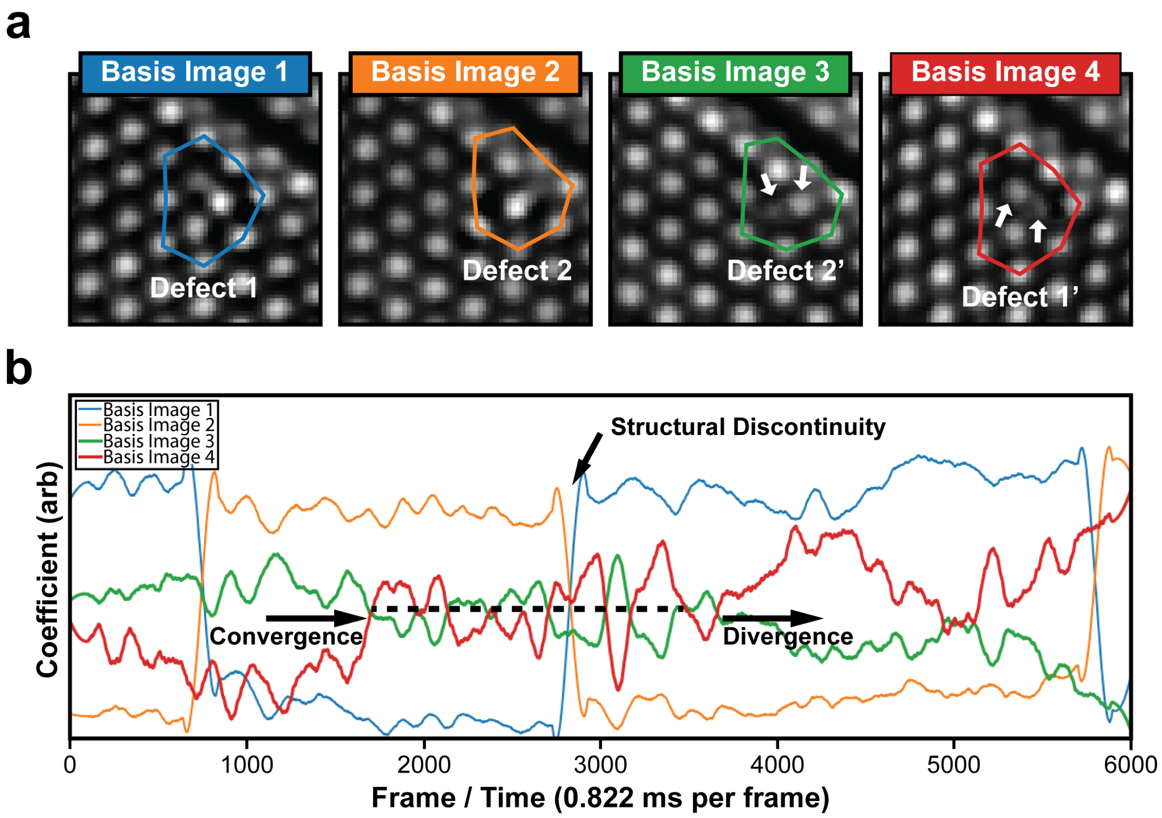

Figure 5.5: NMF analysis using four basis images. **a** Skyrmion defect images as represented by Basis Images 1 - 4. **b** Time series plots of coefficients from matrix H as associated with each Basis Image after smoothing using a Savitzky–Golay filter.

Inspecting the time series plots in Fig.5.5b, the coefficient data has been smoothed using a Savitzky–Golay filter to minimise the effects of the highest frequency coefficient variations. This averaging was done to improve the readability of the plot due to the noise of the four individual plots. The original discontinuous transition behaviour is still clearly apparent between Basis Image 1 and 2, and the smoothing has revealed some further interesting behaviour involving Basis Image 3 and 4. Again, both Basis Image 3 and 4 demonstrate smoothly varying behaviour signifying continuous change in structure. Furthermore, either side of the structural discontinuity around Frame 2800, there appears to be a series of fluctuations of Basis Image 3 and 4 around a central average coefficient value (approximately given by the dotted line). This suggests that at some moments there is more Defect 1' character, whilst at other moments there is more Defect 2' character. However, in the frames preceding the labelled convergence point there is more overall Defect 2' character, whereas in the frames following the labelled divergence point there is more overall Defect 1' character. Furthermore, there appears to be high-frequency (with periods on the order of 150 ms) coefficient oscillations superimposed onto the behaviour of every basis image. With respect to Basis Image 3 and 4, these oscillations appear to be anti-correlated in nature, suggesting that these choice of basis images are appropriate for characterising the dynamic behaviour. Overall, the plots in Fig.5.5b demonstrate that along with the first-order structural transitions between Defect 1 and Defect 2, there are accompanying higher-frequency continuous fluctuations between Defect 1' and Defect 2'. These continuous fluctuations may be similar in nature to the SkCoH deformations observed in Chapter 4 involving the transitions between elongated and dumbbell structures. Furthermore, skyrmion fluctuations have reported around a first-order phase transition from a helical state to a skyrmion lattice[17], which bears similarity to the first-order transitions observed here between Defect 1 and 2. This suggests that since skyrmions can deform, first-order transitions involving skyrmions are also accompanied by continuous, second-order structural variations.

By using these coefficient time series-like plots, in combination with the reconstructed basis images, it has been demonstrated that new insight may be obtained into fluctuations (both continuous and discontinuous) involved in dynamic processes. Instead of tracking skyrmions on an individual level, NMF provides an automated statistical way to treat the entire dataset and find key features therein. Furthermore, NMF is particularly useful for treating video data, as it decouples spatial (basis images from W) and temporal (coefficient plots from H) components, providing a way to inspect both independently. The fact that the skyrmion dynamic processes analysed in this section had relatively few (two) distinct configurational states meant that a small number of basis images were sufficient to probe the behaviour. However, the appropriate number of basis images used within NMF analysis will depend on the dataset, and will ultimately have an upper-bound associated with the loss of discernable structure in both the basis image and coefficient plots.

5.1.3 Implementing Frame Superposition for Fast Dynamics

A final demonstration of the denoising and NMF method will be given for a dataset that contained much faster dynamic events than in the previously analysed dataset. These dynamics were induced by manually oscillating the magnetic field above and below the SkX nucleation field within the TEM using the objective lens at 250 K. This was done by visually observing the transition between SkX and helical pattern as the objective lens excitation was varied manually until sufficient disorder was introduced and repeated skyrmion dynamics were observed under static field. This method initiates rapid transitions between magnetic phases, and causes rapid reorientation of the SkX/helical lines. As disorder is induced, it becomes increasingly likely that domain boundaries within the SkX will form when the SkX nucleation field is reached. However, there is a limit on the rate at which the magnetic field can be oscillated using this method, and therefore a corresponding limitation on the level of frustration. This limitation was a contributing factor to the development of a magnetic field pulse-generating microcoil, the development of which will be described in Section 5.2.

After data acquisition, the subsequent analysis process is shown in Fig. 5.6, showing only the first 9 frames as an example, and the NMF output when using three basis images. The images were recorded with a frame time of 0.822 ms, and a total of 6000 frames were acquired (for a total recording time of 4.932 s, at 1216 FPS). The dynamics were obtained at a temperature of 238 K and a final static magnetic field of 87 mT. Each frame was denoised using the TV denoising algorithm, and then subsampled by superposition of three successive frames, giving a new frame time of 2.467 ms/frame. The purpose of the subsampling is to to increase the SNR and contrast of the images, and is performed here for illustrative purposes. Indeed, when obtaining data with even faster frame-acquisition times it may be a requirement to subsample fast-frames to obtain images with clear features as in Ref. [2]. In this case, TV denoising and frame subsampling increases the SNR from 1.24 to 1.33, as shown by the annotations. These 2000 subsampled frames were then analysed using NMF to find the key skyrmion states involved in the dynamics.

Inspecting the reconstructed basis images, the first two depict a 5-7 defect located within the same row of skyrmions within the SkX. The third basis image also contains a 5-7 defect, however the SkCoP (shown by the white arrow) has smeared intensity and appears to have formed from skyrmion separation. This suggests that the dynamics involve skyrmion motion between two 5-7 defect states, and the formation of a third transient skyrmion, much like that seen in the dynamics analysed in Chapter 4.

The coefficient time series plot for this data can be seen in Fig. 5.7, where only frame 0 to 600 is shown for visual clarity, and the data has undergone smoothing. Transitions are indicated by the red dotted lines, as determined by the cross-over points for Basis Image 1 and Basis Image 2. Immediately apparent is the decreased lifetimes of the states represented by Basis Image 1 and 2, compared to the previous dataset. Furthermore, Basis Image 3 displays some peaks of coefficient values, some of which are located at the points of transitions. This is as expected, since Basis Image 3 appears to represent a transition-like state between the defect in Basis Image 1 and Basis Image 2. This analysis demonstrates that it is possible to extract dynamical and configurational state information from fast-frame Fresnel video data, through a combination of TV denoising, frame subsampling and NMF. Finally, it should be noted that if dynamics are occurring on a similar timescale to the frame time (2.467 ms in this case), then smoothing the data is not appropriate as it necessarily causes a loss of high frequency information. However, since the state lifetimes associated

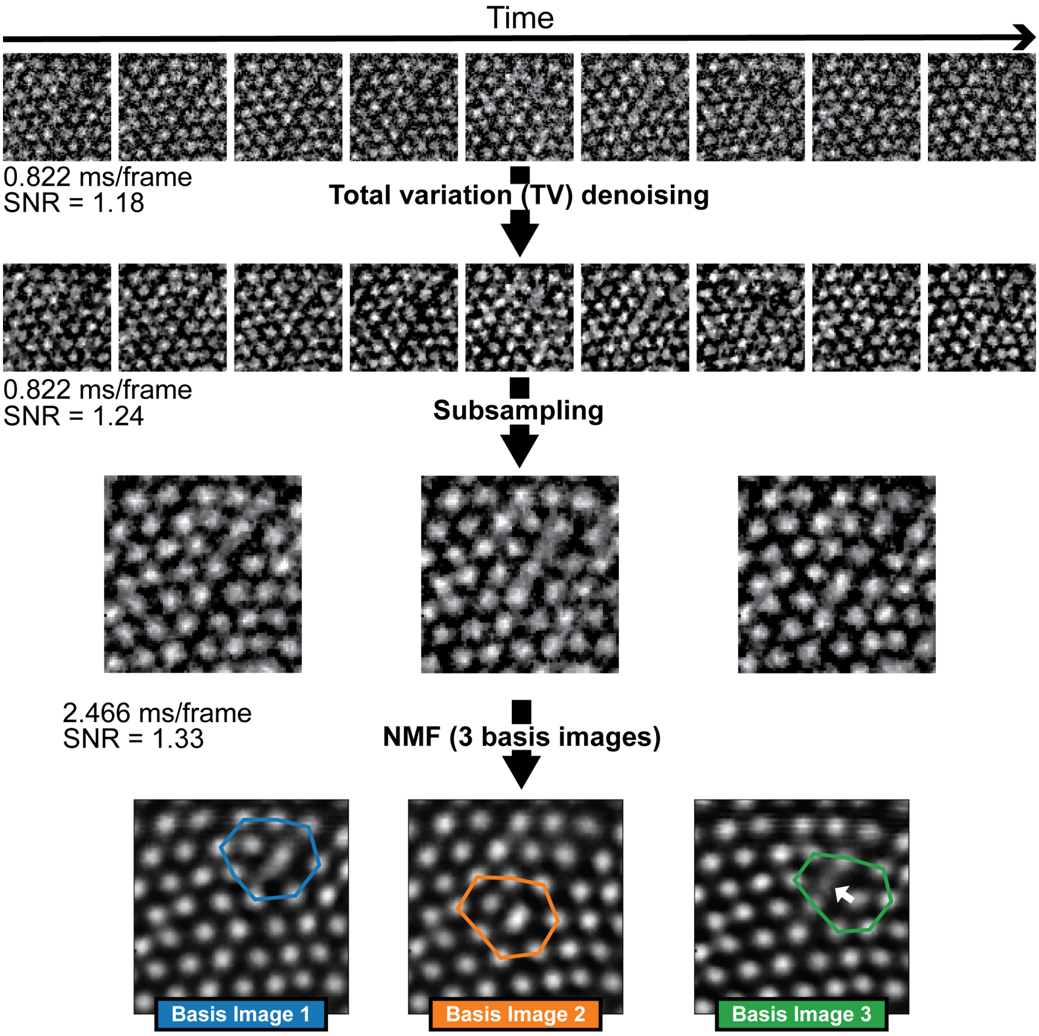
Time
0.822 ms/frame
SNR = 1.18
Total variation (TV) denoising
0.822 ms/frame
SNR = 1.24
Subsampling
2.466 ms/frame
SNR = 1.33
NMF (3 basis images)
Basis Image 1
Basis Image 2
Basis Image 3

Figure 5.6: Example of denoising, subsampling and NMF analysis on Fresnel images displaying fast skyrmion dynamics. Nine frames are shown as an example, with key steps shown by the labelled arrows. The outputs of the three basis images given, with the key states outlined. Basis image 1, 2 and 3 show a 5-7 defect in different locations. Basis Image 3 appears to show a more transient state, with smeared intensity.

with the dynamics in this dataset appear to be on the order of 10s to 100s of ms, the smoothing is justified.

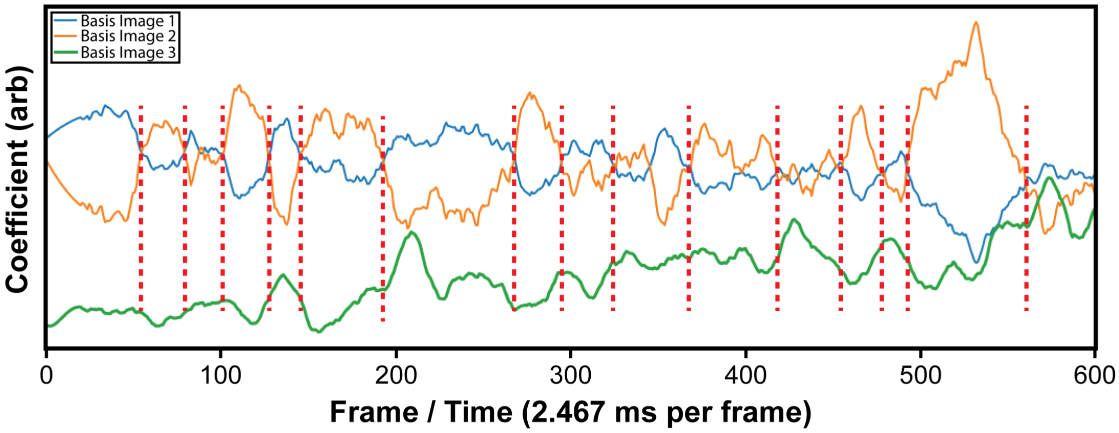

Figure 5.7: Coefficient time-series plot for each of three basis images, with red dotted lines demonstrating individual transitions between Basis Image 1 and Basis Image 2. Note the plot is only showing frame 0 to 600.

5.1.4 Discussion and Conclusions

The image analysis techniques presented within this section have demonstrated that it is possible to use machine-learning algorithms in the form of NMF to both automatically identify key skyrmion states and extract information related to low-order and higher-order structural variations as a function of time. The basis images contained within the matrix W represent key features within the original dataset, which in the case of Fresnel videos of skyrmion motion corresponds to configurational states. Furthermore, the coefficient data contained within the encoding matrix H is sufficient to extract lifetime information assuming that the Fresnel images are captured in a continuous read/write mode.

This work demonstrates that through a series of image analysis techniques, it is possible to obtain skyrmion structural information from image data obtained at the highest rate possible from the Merlin detector. Indeed, it should be possible to obtain useful information from images with even lower frame times than 0.822 ms/frame, through a combination of TV denoising and subsampling. After obtaining these processed images, NMF can be implemented to automatically identify key features involved in skyrmion dynamics. This adds an additional tool to aid visual inspection of image sequences (videos), particularly for large datasets obtained at high frame aquisitions. These techniques may be combined with other analysis techniques, such as Delaunay triangulation, to further elucidate the key skyrmion states involved in dynamic processes.

5.2 Magnetic Field Pulses in the TEM

The application of out-of-plane magnetic fields is integral to the formation of skyrmions in the types of magnetic systems under study here. Although the objective lens is able to provide such out-of-plane magnetic fields required to nucleate and image skyrmions in the TEM, it does have certain limitations. These include the fact that the TEM's electromagnetic lenses were not suitable for generating bi-directional magnetic fields or high frequency magnetic field pulses at the time of performing this work. In order to increase the level of control over SkX nucleation, and to investigate dynamic processes induced through SkX frustration, a means of generating magnetic fields with varying strength, direction and duration is required.

Devices capable of generating in-plane magnetic fields at the sample's location within the TEM have been developed previously [18–20]. Although the construction and operation of these devices differ, they are all able to provide *in-situ* magnetic fields with varying strengths during TEM operation. As an example, the device described in Ref. [18] consists of a pair of current-carrying parallel gold wires, embedded in an insulating material, placed just below the specimen plane. On application of an electrical current through the gold wires, a magnetic field is generated in the specimen plane, perpendicular to the axis containing the gold wires. This device is able to provide magnetic fields with strengths of 0.002 T A^{-1}. If similar strengths can be obtained with devices creating out-of-plane magnetic fields, then currents of under 100 A would be sufficient to study dynamics in the SkX, by providing a range of magnetic fields between 0.0 T and 0.2 T.

Simple, single-turn copper microcoils provide a means of generating out-of-plane magnetic fields when current is passed around them, as described by the Biot–Savart law. Such microcoils have previously been developed and used for the study of magnetic systems [21–23], and in combination with current pulsers are able to generate fast, bi-directional perpendicular magnetic field pulses [24]. In order to generate such magnetic fields within the TEM however, the microcoil device must meet a number of key criteria. First, the device needs to be able to fit into the TEM sample holder within a circular region, approximately 3 mm in diameter. The device then needs to be able to connect to a circuit on the external side of the TEM, utilising the wiring through the sample holder. Furthermore, the magnetic field generating part of the device must be in contact with the sample, as close as possible to increase the magnetic field at the sample location. Finally, the device must be designed such that the electron beam is still able to pass through the sample. These criteria can be met through the design and fabrication of a bespoke, compact, rigid-flex printed circuit board (PCB) microcoil design. This device then needs to be connected to a current pulser on the external side of the TEM, capable of outputting sub-microsecond current pulses. Furthermore, these pulses must be of sufficient amplitude to generate magnetic fields capable of perturbing the magnetic systems under study.

5.2.1 Microcoil Design

A simplified schematic of the required microcoil geometry can be seen in Fig. 5.8a, consisting of a single turn copper coil, embedded in an insulating material. Furthermore, the insulating material contains a through-hole at the centre of the circular coil, allowing transmission of the electron beam through the sample. The direction of the magnetic field can be reversed by the current direction, as shown in the top and bottom panels. Figure 5.8b shows a section of the HC3500 cooling/heating TEM sample holder, with annotations for the sample location and the circuit connections required to provide current to the microcoil. In this image, an acrylic prototype is installed in the sample holder, demonstrating the size and flexibility required of the microcoil device. In order to determine the appropriate geometry and dimensions of the microcoil, some constraints need to be defined. Firstly, in order to reduce resistive heating, increase component longevity and improve safety, the device should require no more than around 100 A pulses during operation. Furthermore, the microcoil size and geometry is limited by the sample location within the HC3500 TEM sample holder, which has a 3.25 mm diameter. Finally, the microcoil should be able to provide a magnetic field strength of at least 0.1 T, which would be sufficient to nucleate skyrmions from the helical ground state without the need for the TEM objective lens.

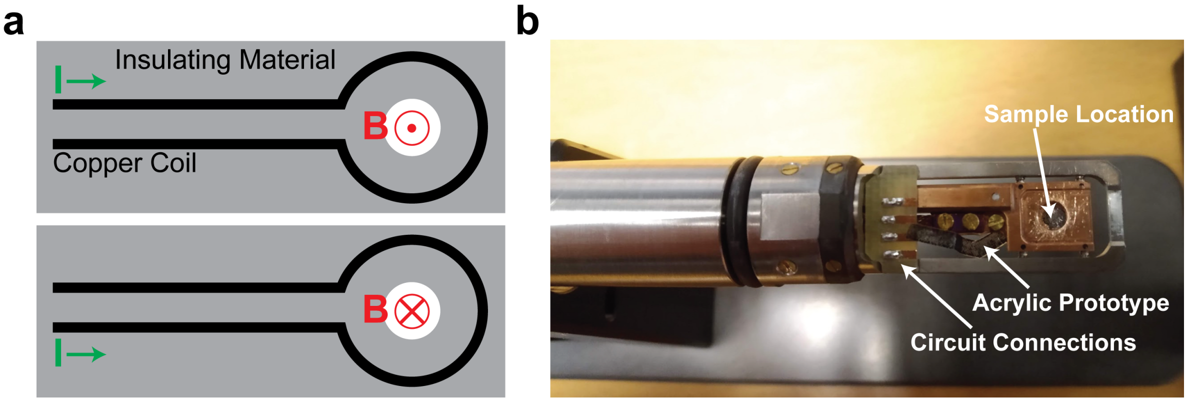

Figure 5.8: a Simplified schematic of a current carrying, single turn copper microcoil, generating an out-of-plane magnetic field with the direction based on the current direction. The copper coil is embedded in an insulating material with a hole in the centre of the circular region to allow the TEM electron beam to transmit through the sample. **b** HC3500 cooling/heating TEM sample holder with annotations showing where a sample would sit and the circuit connections required to provide the electrical current to the microcoil. An acrylic prototype of the microcoil device is installed to demonstrate the geometry and flexibility required.

For a coil carrying a uniform current distribution, the magnetic field generated at the centre of the coil is given in Ref. [21] as:

$$B = \frac{\mu_0 I}{r_i} \frac{F(\alpha, \beta)}{2(\alpha - 1)\beta} \tag{5.3}$$

where $\alpha = \frac{r_o}{r_i}$ and $\beta = \frac{d}{2r_i}$. d is the coil thickness, r_i and r_o are the inner and outer radii of the coil respectively. $F(\alpha, \beta)$ is known as a 'field factor' [25], which is a geometrical function of the coil given by:

$$F(\alpha, \beta) = \beta \ln \frac{\alpha^2 + \sqrt{\alpha^2 + \beta^2}}{1 + \sqrt{1 + \beta^2}} \tag{5.4}$$

Equations 5.3 and 5.4 are sufficient to determine a range of coil geometries, given a magnetic field and current of 0.1 T and 100 A, respectively. Furthermore, given that the standard width of copper trace in PCB manufacturing is 0.254 mm, r_o will be further constrained through $r_o = r_i + 0.254 \times 10^{-3}$.

Figure 5.9a shows a schematic for the final microcoil device geometry, with annotations highlighting the scale of the device. It was necessary to design the device as a rigid-flex PCB to ensure it would fit into the TEM sample holder and connect to its internal wiring. The rigid and flexible sections can be seen through the annotations in Fig. 5.9a. The magnetic field generating section of the microcoil device is shown in Fig. 5.9b, with the inner and outer radii labelled respectively. The fin-like regions are introduced to reduce resistive heating effects, through improved heat distribution. Inserting the values of $r_i = 0.35 \times 10^{-3}$m, $r_o = 0.60 \times 10^{-3}$m and the thickness of the copper trace of $d = 3.6 \times 10^{-5}$m into Eq. 5.4 and Eq. 5.3 gives a magnetic field strength of 0.002 T A^{-1}, which means that approximately 50 A should be sufficient to generate a magnetic field of 0.1 T. However, this calculation is for the magnetic field at the centre of the coil, and the magnetic flux density will diminish away from the coil, where the sample is located. This means that currents greater than 50 A may be required in practice, and calibration experiments will be required to determine the magnetic field generated at the sample location. Nonetheless, this provides indication that the proposed microcoil geometry (shown in Fig. 5.9a) is sufficient to generate the magnetic fields required. Finally, a 3D rendered version of the device is shown in Fig. 5.9c, where the two panels demonstrate how the device can bend to fit into the TEM sample holder.

Once designs were finalised, the PCB was subsequently professionally manufactured, and the physical microcoil device can be seen in Fig. 5.10a. Figure 5.10b shows the microcoil device installed into the HC3500 TEM sample holder, with the connections soldered and a TEM sample on an omniprobe grid in the sample location.

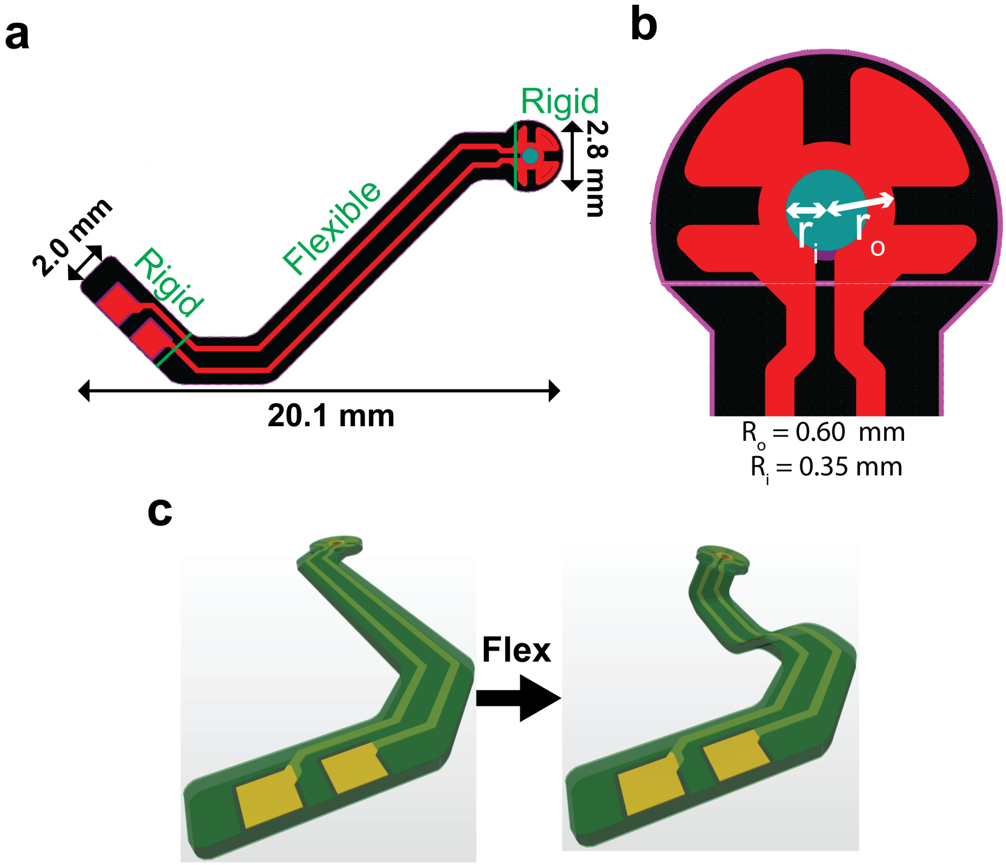

Figure 5.9: **a** Schematic of entire microcoil PCB, red regions are the copper trace. Rigid-flex PCB design has been used here, and each section is labelled accordingly. **b** Schematic of magnetic field generating section of microcoil device, inner and outer radii are labelled accordingly. The copper fin-like sections in this design are to reduce resistive heating effects, through heat distribution. **c** 3D render of the device and how it is able flex to fit into the TEM sample holder. All schematics were created in Altium Designer version 21.0.9.

5.2.2 Current Pulser Design

The purpose of the current pulser is to provide well-defined, user controlled current pulses of microsecond duration to the microcoil device. The chosen method of providing such current pulses was through the combination of a high-voltage (HV) switch, power supply and pulse generator. A prototype circuit layout with these distinct components can be seen in Fig. 5.11, where everything in the dotted box was to be isolated within an acrylic enclosure for both safety and ease of use. Each of the connections outside the dotted box would therefore require a corresponding socket to interface with each of the inputs. The left side of the schematic is the low-voltage side, which consists of the pulse generator transistor-transistor logic (TTL) input, a $+5$ V DC input for powering the HV switch, and a ground (GND) connection. The right side corresponds to the high-voltage side, which consists of the positive (+) and negative (−) terminals on the power supply and the resistive load (TEM sample holder and microcoil device). Note that the polarity of the generated magnetic field

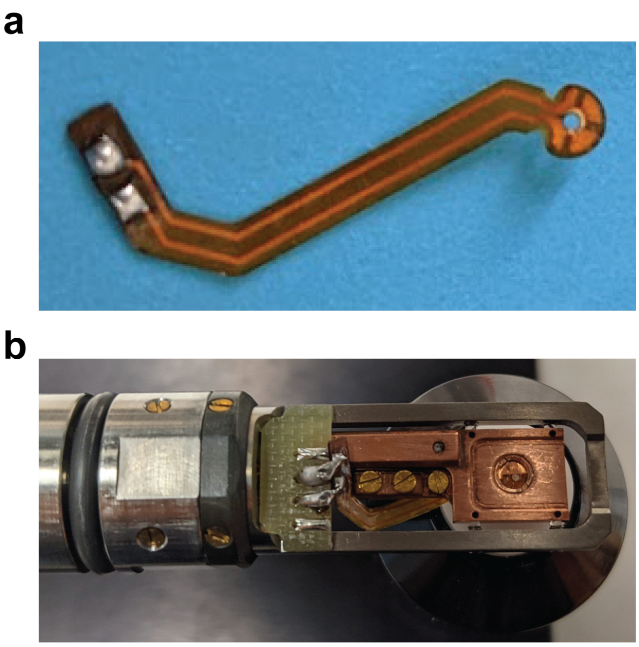

Figure 5.10: **a** Professionally manufactured microcoil device. **b** Microcoil device installed within the TEM sample holder, with an actual sample in place.

pulse within the microcoil can be reversed by switching $+$HV and $-$HV, assuming that the HV switch is bi-directional.

The central component of the proposed circuit is the HV switch, which acts to modulate the current pulse in the microcoil. By supplying either a positive or negative voltage ($+/-$HV in Fig. 5.11), the bi-directional HV switch is capable of generating positive or negative current pulses in the microcoil, as determined by the pulse generator. The chosen bi-directional switch was the BEHLKE HTS 31-23 AC-SiC-C, which has a maximum voltage of 3 kV, a variable on-time (100 ns to infinity) and a maximum current of 230 A. Given that the microcoil resistance was approximately $0.5\ \Omega$, a silicon carbide (SiC) switch was chosen with an extremely low on-resistance (less than $1\ \Omega$). The purpose for this choice was to reduce the required supply voltage and impedance mismatch within the circuit.

In order to investigate the suitability of components, and to test the viability of a current pulser design as proposed in Fig. 5.11, a workshop prototype device was constructed. This meant that both the JEOL ARM 200cF TEM and HC3500 sample holder were not required within the preliminary test circuits. This enabled a relatively low-risk iterative design process, without the chance of damaging the TEM or sample holder. To realise the current pulser device, a PCB was designed and professionally fabricated to provide an embedded circuit with connection pads for installing input sockets. The PCB was subsequently installed into an acrylic enclosure, and this prototype device can be seen in Fig. 5.12a. Each of the labelled sockets was installed into the walls of the enclosure and subsequently soldered via wires to the PCB. Once de-

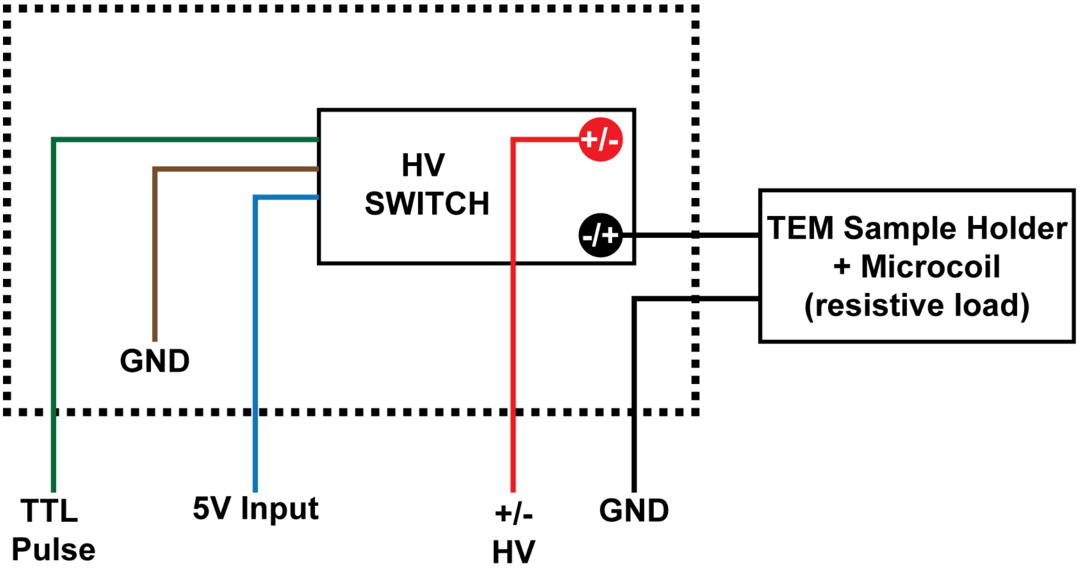

Figure 5.11: Initial design of current pulser using a number of distinct components including HV switch, power supply and a TTL pulse generator. The components within the dashed box would be contained in an enclosure for safety reasons, and thus the electrical circuit should be embedded within a PCB.

sign and initial testing was completed, the microcoil and TEM sample holder would be introduced to the circuit via the labelled 9-pin D-sub connector socket.

The physical setup of the current pulser is translated to a circuit diagram schematic in Fig. 5.12b. In this schematic, it can be seen that a high-side switch configuration was chosen, such that the resistive load is on the ground side of the switch, as in the initial design (Fig. 5.11). Therefore, since the switch is bi-directional, simply switching the $+$HV and $-$HV inputs from the power supply produces positive and negative current pulses as depicted in the schematic (where the dotted line represents 0 V). Note that the pulse shapes given in Fig. 5.12b are idealised, and do not take into account the real measured voltages across the microcoil.

The two additional components shown in Fig. 5.11a,b are the load resistor and buffer capacitor, labelled R_L and C_B respectively. The purpose of adding these components was to improve the quality of the current pulse in the microcoil device, such that it more closely resembles the input TTL pulse. An example of a square wave input pulse provided to the HV switch is shown schematically in Fig. 5.13a. This signal is then amplified and reproduced via the power supply and HV switch, generating a current pulse of the same form within the microcoil. The output (post-switch) voltage signal was measured across the microcoil and load resistor using an oscilloscope, and schematic examples of these signals are shown in Fig. 5.13b. It is clear that without the use of a buffer capacitor or load resistor, the voltage signal deviates significantly from the original input TTL pulse signal, specifically exhibiting oscillatory behaviour. This 'ringing' effect can be caused both by parasitic ca-

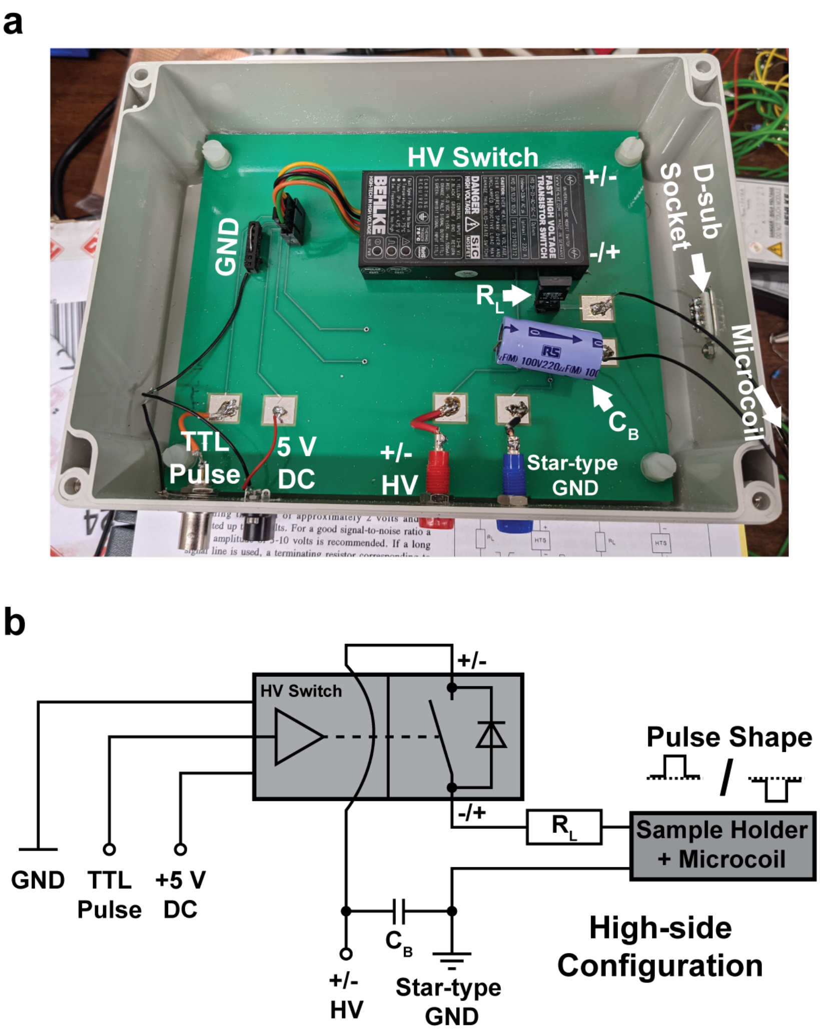
a
HV Switch
+/-
-/+
GND
D-sub Socket
Microcoil
R_L
C_B
TTL Pulse
5 V DC
+/- HV
Star-type GND
b
HV Switch
+/-
-/+
Pulse Shape
R_L
Sample Holder + Microcoil
GND
TTL Pulse
+5 V DC
C_B
+/- HV
Star-type GND
High-side Configuration

Figure 5.12: a Workshop prototype of current pulser box for testing different components and current output profiles. Two additional components were added after initial testing, a load resistor (R_L) and buffer capacitor (C_B), labelled accordingly. **b** Circuit diagram schematic of the workshop prototype with the bi-directional switch in a high-side configuration. The pulse direction is given by the pulse shape, where the dotted line represents 0 V, and is determined by the HV terminals. For a +HV(−HV) input a positive(negative) pulse is obtained.

pacitances/inductances and impedance mismatch reflections caused by a current or voltage pulse. Thus, it should be possible to minimise the ringing effect by isolating the high-voltage circuit from parasitic capacitors and impedance matching where possible.

By incorporating a buffer capacitor with a capacitance of $C_B = 10\ \mu$F, the signal shape is dramatically improved, specifically the oscillations in the high-voltage part of the signal are eliminated. This is due to the isolation of the circuit from the power supply, a likely source of parasitic capacitance and inductance. However, there is still significant ringing present at the end of the pulse, which is likely due to signal reflections arising from impedance mismatch in the circuit. It was found that this ringing effect could be reduced by introducing an additional load resistor in series

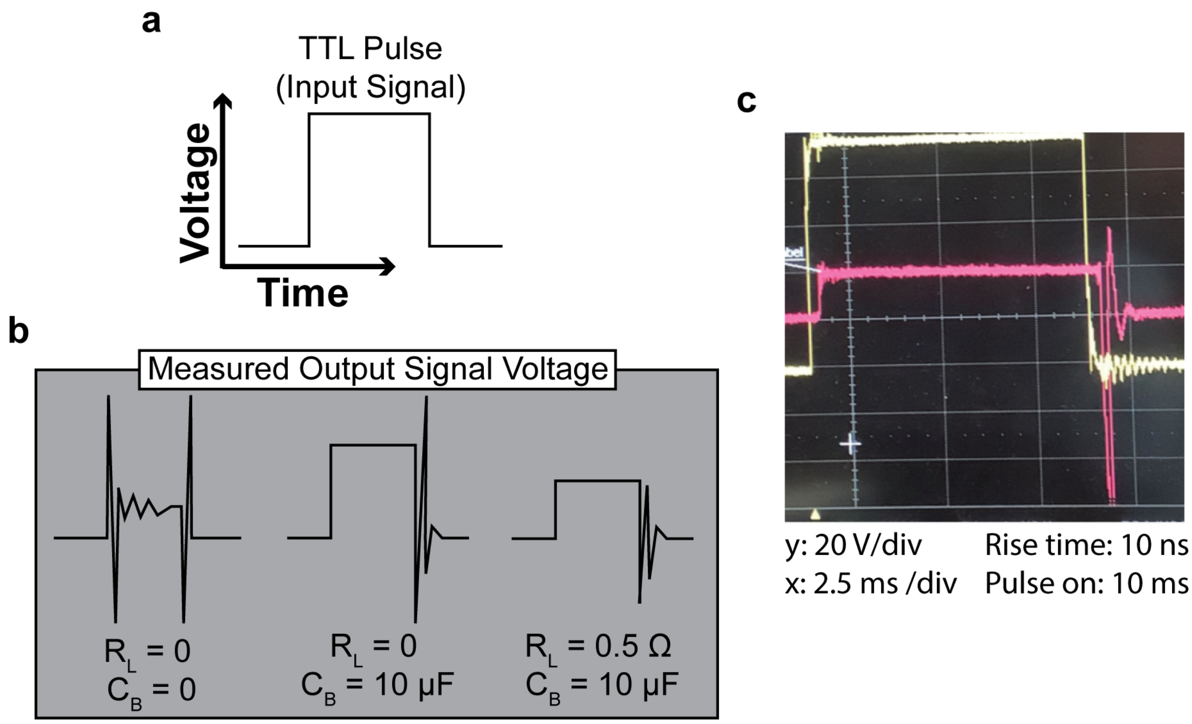

Figure 5.13: a Schematic of the voltage-time signal as defined by the pulse generator, which is used as the input for the HV switch. **b** Schematics of signals measured across the microcoil device when using an additional load resistor (R_L) and a buffer capacitor (C_B). Ideally the output signal should match the TTL pulse, however due to impedance mismatch and an unbuffered HV power supply, there is a significant ringing effect as seen by the sharp signal oscillations. This ringing can be reduced through the use of $C_B = 10\ \mu$F across the $+$HV and $-$HV terminals and by increasing the load resistance using $R_L = 0.5\ \Omega$. **c** Oscilloscope trace of input TTL signal (yellow) and measured voltage across device (red).

with the microcoil. A range of different load resistors were tested, and it was found that the ringing effect was drastically reduced for high resistances. Unfortunately, due to Ohm's law, this increased the required voltage to generate the same current through the microcoil, and with access only to a 150 V power supply, high resistances were not an option. A load resistance of $R_L = 0.5\ \Omega$ was finally chosen, as a compromise between signal fidelity and amplitude, and ensured that sufficient current would still pass through the microcoil. An oscilloscope trace of the input TTL signal and measured voltage across the microcoil device with the chosen load resistance can be seen in yellow and red respectively within Fig. 5.13c.

Once the buffer capacitor and load resistor were installed and the circuit was optimised, the microcoil device was soldered to the TEM sample holder and connected to the current pulser. The final measured resistance of the resistive load was $2.3\ \Omega$, meaning that a voltage of 150 V could generate currents of approximately 65 A. Therefore, it should be possible to generate magnetic field pulses within the microcoil device of up to 0.13 T, given the value of 0.002 T A^{-1} calculated in Section 5.2.1 using the microcoil geometry.

5.2.3 Experimental Device Testing

To determine the real-world functionality of both the current pulser and microcoil device, a series of experiments involving Fresnel imaging of a SkX were performed. An annotated image of the current pulser and microcoil during use on the JEOL ARM 200cF TEM can be seen in Fig. 5.14. With this setup, pulse shape and duration is defined and supplied to the microcoil by triggering the pulse generator, thus providing user-defined magnetic field pulses to magnetic samples within the TEM. Two Fresnel imaging experiments were chosen to investigate the capability of the microcoil to both induce frustrated states in the SkX and also improve the level of control over SkX phase transitions.

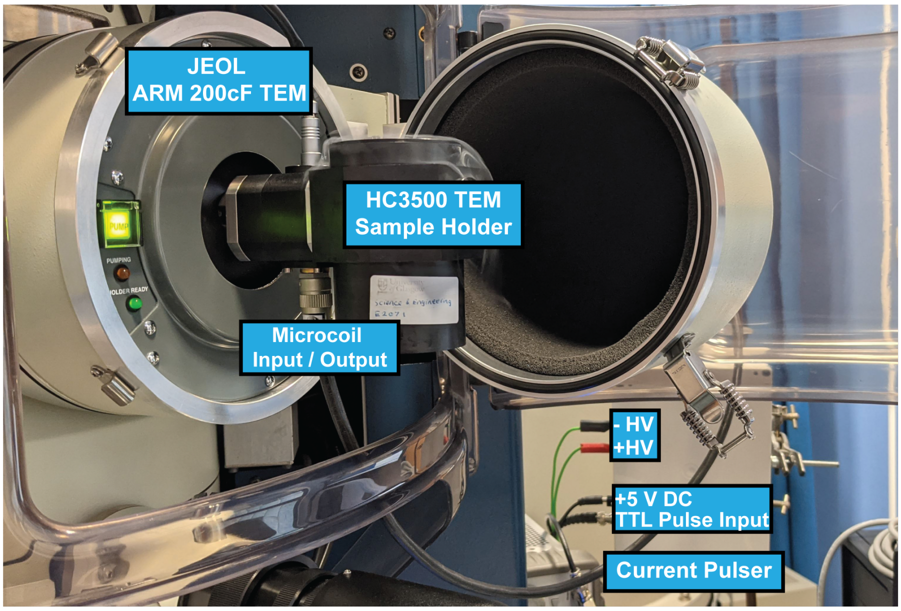

Figure 5.14: Experimental setup for Fresnel TEM imaging with *in-situ* magnetic field pulses, consisting of the bespoke current pulser, HC3500 sample holder with the installed microcoil device and the JEOL ARM 200cF TEM.

The first experiment involved generating significant frustration within the SkX to initiate defect formation by oscillating the applied magnetic field around the SkX transition field, H_{SkX}. A schematic showing the approximate magnetic field profile as a function of time at the sample location during this experiment can be seen in Fig. 5.15a. In order to achieve the proposed magnetic field profile, a static out-of-plane magnetic field was first applied using the TEM objective lens, below the SkX transition field. To generate the magnetic field pulse, a voltage of 143 V was used to generate a $3\ \mu$s current pulse through the microcoil, with total resistance 2.3 Ω, giving a calculated amplitude of 62 A. This corresponds to an approximate magnetic field of 0.12 T, according to the geometry of the microcoil as defined in Section 5.2.1. The magnetic pulse was applied in an iterative process of triggering the pulse generator and acquiring a Fresnel TEM image once the pulse had ended. With each magnetic field pulse, the system momentarily transitions to a region of the SkX phase space, stabilising the hexagonal SkX. Once the pulse ends however, the system undergoes a phase transition back towards the helical state, and disorder is thus introduced as some metastable regions of the SkX reorient. This iterative process introduces significant disorder through SkX domain boundaries and isolated defects, and results in a number of Fresnel images depicting different levels of SkX frustration.

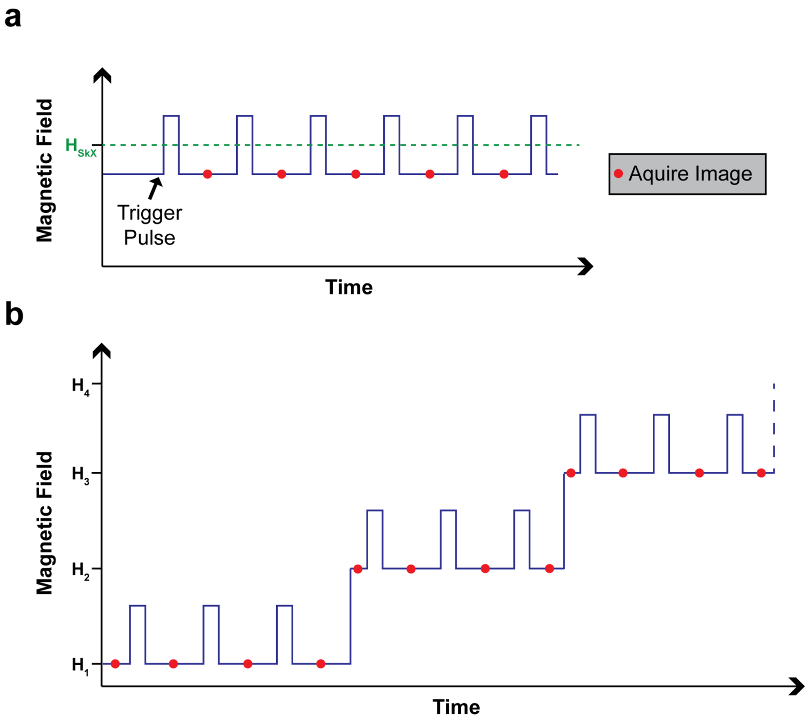

Figure 5.15: Magnetic field vs time schematics for preliminary experiments to test the microcoil and current pulser. Note that the pulse heights and durations are not to scale in either schematic. a An experiment to generate significant disorder within a SkX to create lattice defects. The static magnetic field from the objective lens is set below the SkX transition field (H_{SkX}) such that the magnetic field pulse from the microcoil temporarily stabilises the SkX phase. **b** An experiment to create controlled changes within the magnetic system during phase transitions initiated through step-changes in the static magnetic field provided by the objective lens (H_1, H_2, etc). In both experiments, Fresnel images are obtained over time at the points indicated by the red circles.

The outcome of the first experiment can be seen in the Fresnel TEM images in Fig. 5.16a,b. Both of these images are of the same SkX at different locations and were captured using the Orius CCD camera at 213 K and with a static magnetic field from the objective lens of 0.137 T. Immediately apparent in Fig. 5.16a is the high density of 5-7 defects, including a connected defect chain on the right side of the image. Furthermore, there is a variation to the extent of deformation present in the SkCoHs, from extremely elongated and dumbbell-like (marked i) to relatively compressed (marked j). It has not been possible to create this density of 5-7 defects before, especially as they are not involved in a clearly defined SkX domain boundary. However, although the density of these 5-7 defects is high, their individual geometry is not unlike those already formed before in other experiments.

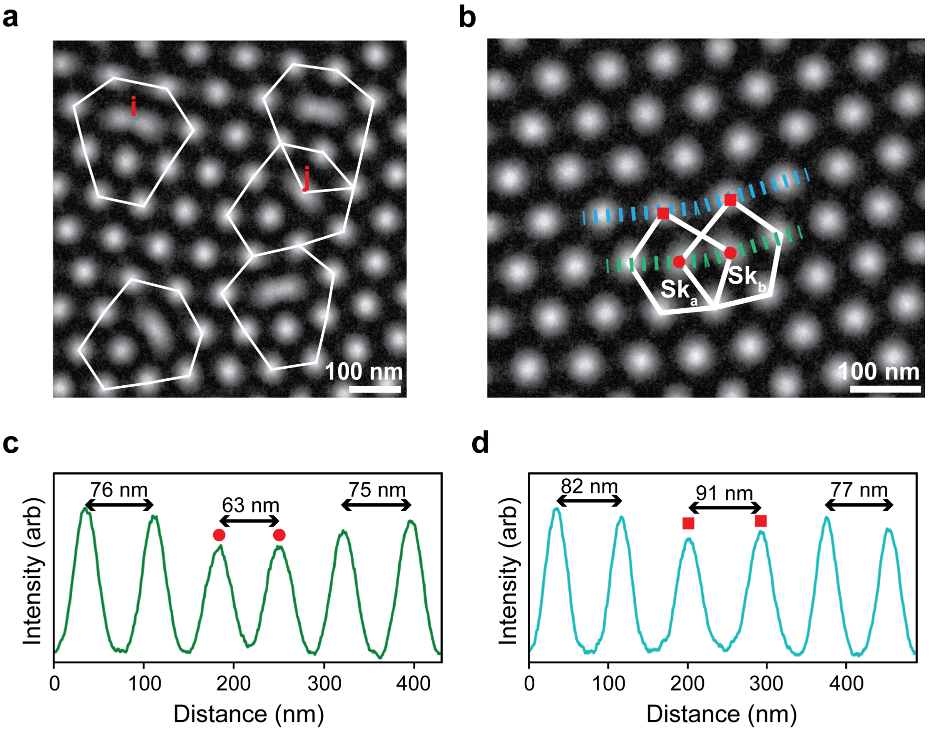

Figure 5.16: a Fresnel TEM image of a region of SkX containing a high density of 5-7 defects, outlined in white, where deformation of SkCoHs ranges from high (i) to low (j). **b** Fresnel TEM image showing a nontrivial SkX lattice defect involving a pair of 5-fold coordinated skyrmions. This defect represents a state prior to a regular 5-7 defect, which would be reached through merging of the two SkCoP, marked Sk$_a$ and Sk$_b$. **c**,**d** Line profile plots of image intensity along the paths indicated by the green and blue dashed lines, respectively, in **b**. Fresnel images captured using Orius CCD camera, temperature of 213 K and static magnetic field of 0.137 T.

The defect state shown in Fig. 5.16b however, is unlike those created previously, and represents an interesting, highly symmetrical (compared to 5-7 defects) configurational motif within the SkX. This defect consists of a neighbouring pair of 5-fold coordinated skyrmions (SkCoP) without a corresponding 7-fold coordinated skyrmion (SkCoH). This pair of defects results in two skyrmions further than than the equilibrium distance (marked with red squares), and two closer than the equilibrium distance (marked red circles). This behaviour is elucidated further through the integrated intensity line profiles taken from the blue and green dashed lines, shown in the plots within Fig. 5.16c,d, respectively. In Fig. 5.16c it can be seen that the skyrmions marked with red circles are 22 % closer than the measured regular skyrmion lattice parameter of 81 nm. Furthermore, Fig. 5.16d shows that the skyrmions marked with red squares are 12 % further apart than the equilibrium lattice parameter. From this information and the geometry of the defect it is assumed that this state is a precursor for a regular 5-7 defect, which may form on the merging of the close skyrmions marked Sk_a and Sk_b in Fig. 5.16b. The creation of these defects highlights the ability of the pulsed magnetic fields to purposefully introduce significant frustration to the SkX, thereby generating interesting and nontrivial isolated SkX defects.

The second experiment involved initiating helimagnetic phase transitions using static magnetic fields from the objective lens, and subsequently inducing disorder and mixed states using magnetic field pulses. The schematic showing the magnetic field vs time profile for this experiment was given in Fig. 5.15b. Here, the static magnetic field is increased in a step-wise fashion, with each increase separated by three magnetic field pulses each with a $10\ \mu$s duration. For this experiment, an initial Fresnel image was obtained at each of five static magnetic field values, and again after each of three magnetic field pulses, generating a total of twenty Fresnel images. These images (captured using the Orius CCD camera) can be seen in Fig. 5.17, where horizontal images belong to the same static field value, obtained after successive magnetic field pulses. Each set of four images has been assigned a coloured label denoting the magnetic phase, with annotations of matching colour highlighting key features. These images and features will be described sequentially, in order of increasing pulse number, as the static field is increased.

Starting at a magnetic field of 0.077 T, the system is in the helical state, as seen by the characteristic white and black stripes in the Fresnel image. As the system is subjected to magnetic field pulses, discontinuities in the helical pattern are introduced (shown by the dark orange arrows). The feature marked i is of particular interest, showing a section of helical line with contrast variations towards the terminating end. These intensity variations are due to magnetic moments with in-plane components, and suggest that additional helical discontinuities may form. In fact, this particular feature bears many similarities with a defect-pinned helical line, imaged in Ref. [26] using differential phase contrast (DPC) TEM imaging, whereby a skyrmion was nucleated. In this case however, after the third magnetic field pulse, although significant disorder has been introduced to the top left of t=he image, no skyrmion appears to have been nucleated. Overall, the magnetic system remains in the helical state through pulses 1 - 3, however significant disorder is introduced in the form of discontinuities, even though the static magnetic field remains unchanged.

Increasing the static field to 0.097 T, we immediately see the formation of a single isolated skyrmion (as marked by the orange arrow). As the magnetic field pulses are sequentially applied, the region of disorder that was previously introduced begins to extend (shown by the growing orange boxes). The magnetic field pulses appear to nucleate small clusters of skyrmions within the helical pattern, particularly localised in regions where discontinuities were previously located. These images provide clearer examples of the states generated in Ref. [27], and demonstrates the effectiveness of fast magnetic field pulses in forming these highly frustrated mixed states.

After reaching a static magnetic field of 0.116 T, skyrmions can be seen to have nucleated in a much larger region of the sample. There is still significant disorder present, but short-range hexagonal symmetry is emerging (as shown by the green hexagons). After two magnetic field pulses, the first 5-7 defect is formed, along with more complex defects involving significantly deformed skyrmions (within the green box). After the final magnetic field pulse, two distinct regions of SkX can be seen with their own principle lattice vectors (green arrows), and a series of 5-7 defects separating them. Note however, that helical lines are still present, which suggests that this SkX may be metastable only.

At a static magnetic field of 0.126 T, the system still appears to contain a mix of helical and SkX regions. Upon application of the magnetic field pulses, the helical lines disappear and a SkX domain boundary is formed, and then shifts (as shown by the dotted green lines). This demonstrates the ability for fast magnetic field pulses to initiate subtle orientational changes within the SkX. Finally, after reaching a static magnetic field of 0.137 T, the system is in a mostly uniform SkX state. A SkX domain boundary is present in the bottom of the image, and this boundary shifts location on application of the magnetic field pulses. Furthermore, isolated 5-7 defects (blue outlines) are introduced and then eliminated, as small re-orientations in the SkX shift the energy landscape.

To summarise, both Fig. 5.16 and Fig. 5.17 demonstrate the functionality of the bespoke microcoil and current pulser devices in inducing non-trivial, frustrated skyrmion states. Through repeated application of a pulsed magnetic fields near a phase transition, significant disorder is introduced, leading to the formation of non-trivial defects. Furthermore, by providing pulsed magnetic fields at different points within the magnetic phase space, it is possible to generate metastable skyrmion states through a combination of temporary (magnetic field pulses) and permanent (static field increases) navigation of the phase space. This allows for the precise creation of highly frustrated, mixed skyrmion states that have many interesting structural features. It is expected that the creation of these states is due to the fact that, during the fast magnetic field pulses, short-range magnetic reorientation is possible whereas long-range lattice reorientation is not. This is evidenced in Fig. 5.17 through the formation of distinct regions of mixed skyrmion/helical states, helical discontinuities and the formation and movement of isolated skyrmion defects and domain boundaries on application of successive magnetic field pulses.

5.3 Discussion and Conclusions

The work within this chapter presented methods for both investigating, and inducing high-speed skyrmion dynamic processes using Fresnel TEM imaging. Within section 5.1, Total Variation (TV) denoising and the machine learning technique of non-negative matrix factorisation (NMF) were used to analyse large Fresnel image datasets. It was shown that the implementation of TV denoising algorithms and subsequent superposition of image frames increased signal-to-noise ratio (SNR) of Fresnel images with sub-ms frame times, captured using the Merlin Medipix3 detector. Subsequently, these denoised image sequences, displaying skyrmion dynamics, were analysed with NMF and this enabled the automated detection of distinct skyrmion states in the form of basis images. It was shown that the NMF method provides user-defined control over the ability to generate an arbitrary number of basis images, and thus detected structural variations, from the original 4D dataset. For few basis images, the method generates key states based on low-spatial frequency variations. However, by increasing the number of basis images, NMF takes into account higher-spatial frequency variations within the original data. This provides flexibility in searching for key configurational states within a large dataset of images, whereby both low- and high-order variations of magnetic structure may be identified. Furthermore, plotting the basis image coefficients held within the encoding matrix generated by NMF, was shown to generate a time series-like plot whereby transitional information, such as state lifetimes may be extracted. Thus, NMF is able to provide both spatial information, in the form of key features represented by the basis images, and temporal information, in the form of the coefficient time series plots. The combination of presented image processing techniques here provide additional tools for analysing large, high-speed TEM image data generated by direct electron detectors such as the Merlin detector.

Although NMF has been used previously to treat electron microscopy datasets as reported in Refs. [10–13], this work demonstrates the ability to treat Fresnel video data of dynamic skyrmion events and extract both spatial and temporal information in a novel fashion. Furthermore, it adds to an increasing number of uses of machine learning more widely in condensed matter physics studies [16].

In Section 5.2, experimental methods for inducing skyrmion dynamic processes and controlling skyrmion phase transitions were achieved through the use of a bespoke magnetic field pulse device. This consisted of firstly designing and fabricating a magnetic field-generating microcoil in Section 5.2.1, whilst designing a current pulser was the focus of Section 5.2.2. In Section 5.2.3 the two devices were designed, constructed and experimentally tested, confirming their ability to provide *in-situ*, sub-ms perpendicular magnetic field pulses to a sample within the TEM. Experiments involving the field pulse device led to the generation of significantly frustrated SkX configurations, including a non-trivial lattice defect involving a neighbouring pair of SkCoPs. This defect was determined to be the precursor to a 5-7 defect, whereby subsequent merging of the two SkCoPs would lead to a 5-7 defect. Furthermore, by combining both static magnetic field increases provided by the TEM objective lens and the magnetic field pulses, it was possible to navigate the helimagnetic phase space and form a number of frustrated, mixed skyrmion states containing a wealth of interesting structural and topological defects.

The types of skyrmion states observed during application of the pulsed magnetic field are similar to those previously observed in Ref. [27], and more recently using DPC in Ref [26]. Specifically, the Fresnel images obtained in this work provide a clearer example of the range of metastable skyrmion clusters and isolated skyrmions within helical lines than previously reported. Furthermore, this work highlights a reproducible way of generating a wide range of these observed and predicted skyrmion states.

The work contained within this chapter demonstrates the ability to perturb magnetic systems with pulsed perpendicular magnetic fields within the TEM. In contrast to the usual method of providing magnetic fields using the objective lens, the presented method demonstrates a much finer level of control of the applied magnetic fields. Furthermore, in combination with high-speed TEM detectors and the machine learning-based analysis techniques, these methods present new avenues of investigating dynamic processes within condensed matter systems.

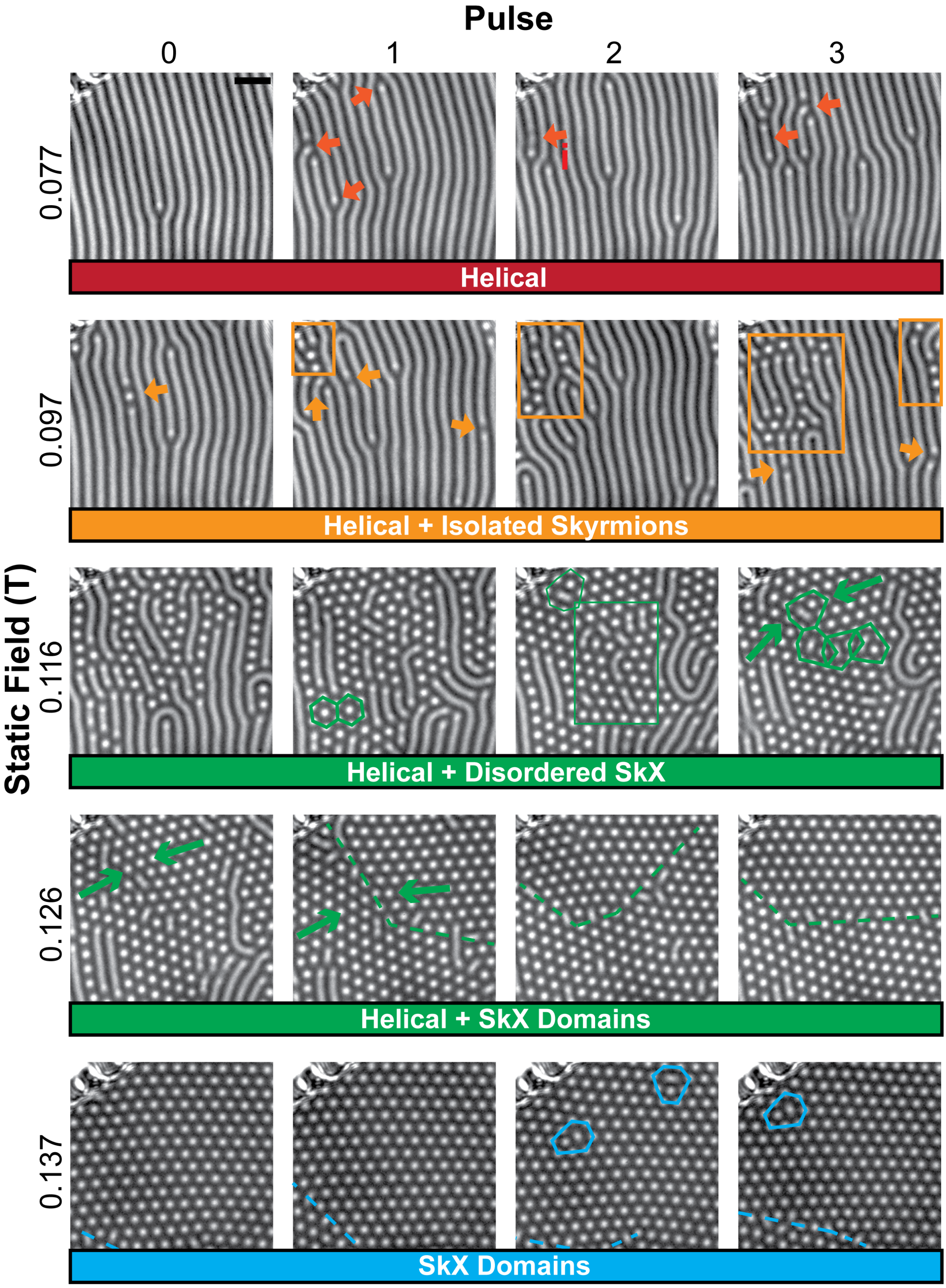
Pulse
0
1
2
3
Static Field (T)
0.077
0.097
0.116
0.126
0.137
Helical
Helical + Isolated Skyrmions
Helical + Disordered SkX
Helical + SkX Domains
SkX Domains

Figure 5.17: Fresnel TEM Images captured on Orius CCD camera showing skyrmion phase transitions occurring as the static magnetic field is increased. Images along the same row demonstrate how different metastable states become accessible using the magnetic field pulses generated by the microcoil. Scale bar is 200 nm. Annotations highlight important features, as described in the main text.

Bibliography

1. Rendell-Bhatti, F. *et al.* Spontaneous creation and annihilation dynamics and strain-limited stability of magnetic skyrmions. *Nature Communications* **11,** 3536 (Dec. 2020).
2. Shimizu, T. *et al.* Real-time Video Imaging of Mechanical Motions of a Single Molecular Shuttle with Sub-millisecond Sub-angstrom Precision. *Bulletin of the Chemical Society of Japan* (2020).
3. Iakovlev, I. A., Sotnikov, O. M. & Mazurenko, V. V. Supervised learning approach for recognizing magnetic skyrmion phases. *Physical Review B* **98,** 174411 (Nov. 2018).
4. Deviatov, A. Y., Iakovlev, I. A. & Mazurenko, V. V. Recurrent Network Classifier for Ultrafast Skyrmion Dynamics. *Physical Review Applied* **12,** 54026 (2019).
5. Wang, W., Wang, Z., Zhang, Y., Sun, B. & Xia, K. Learning Order Parameters from Videos of Skyrmion Dynamical Phases with Neural Networks. *Physical Review Applied* **16,** 14005 (2021).
6. Nord, M. *et al.* Fast Pixelated Detectors in Scanning Transmission Electron Microscopy. Part I: Data Acquisition, Live Processing, and Storage. *Microscopy and Microanalysis* **26,** 653–666 (2020).
7. Rudin, L. I., Osher, S. & Fatemi, E. Nonlinear total variation based noise removal algorithms. *Physica D: Nonlinear Phenomena* **60,** 259–268 (Nov. 1992).
8. Chambolle, A. An Algorithm for Total Variation Minimization and Applications. *Journal of Mathematical Imaging and Vision* **20,** 89–97 (2004).
9. Lee, D. D. & Seung, H. S. Learning the parts of objects by non-negative matrix factorization. *Nature* **401,** 788–791 (Oct. 1999).
10. Shiga, M. *et al.* Sparse modeling of EELS and EDX spectral imaging data by non-negative matrix factorization. *Ultramicroscopy* **170,** 43–59 (Nov. 2016).

11. Kiss, Á. K. & Lábár, J. L. Determining Projections of Grain Boundaries from Diffraction Data in Transmission Electron Microscope. *Microscopy and Microanalysis* **22,** 551–564 (Feb. 2016).
12. Jany, B. R., Janas, A. & Krok, F. Automatic microscopic image analysis by moving window local Fourier Transform and Machine Learning. *Micron* **130,** 102800 (Mar. 2020).
13. Uesugi, F. *et al.* Non-negative matrix factorization for mining big data obtained using four-dimensional scanning transmission electron microscopy. *Ultramicroscopy* **221,** 113168 (Feb. 2021).
14. Pedregosa, F. *et al.* Scikit-learn: Machine Learning in Python. *Journal of Machine Learning Research* **12,** 2825–2830 (2011).
15. Sun, D. L. & Févotte, C. *Alternating direction method of multipliers for non-negative matrix factorization with the beta-divergence* in *ICASSP, IEEE International Conference on Acoustics, Speech and Signal Processing - Proceedings* (2014), 6201–6205.
16. Carleo, G. *et al.* Machine learning and the physical sciences. *Reviews of Modern Physics* **91,** 045002 (Dec. 2019).
17. Esposito, V. *et al.* Skyrmion fluctuations at a first-order phase transition boundary. *Applied Physics Letters* **116,** 181901 (May 2020).
18. Yi, G. *et al.* A new design of specimen stage for in situ magnetising experiments in the transmission electron microscope. *Ultramicroscopy* **99,** 65–72 (Feb. 2004).
19. Arita, M., Tokuda, R., Hamada, K. & Takahashi, Y. Development of TEM holder generating in-plane magnetic field used for in-situ TEM observation. *Materials Transactions* **55,** 403–409 (2014).
20. Sugawara, A. *et al.* A 0.5-T pure-in-plane-field magnetizing holder for in-situ Lorentz microscopy. *Ultramicroscopy* **197,** 105–111 (Feb. 2019).
21. Mackay, K., Bonfim, M., Givord, D. & Fontaine, A. 50 T pulsed magnetic fields in microcoils. *Journal of Applied Physics* **87,** 1996–2002 (Feb. 2000).
22. Grainys, A. & Novickij, J. Investigation of microcoils for high magnetic field generation. *Elektronika ir Elektrotechnika* **109,** 63–66 (Mar. 2011).
23. Kadonosawa, K., Kikuchi, N., Goto, R., Okamoto, S. & Kitakami, O. Magnetization Reversal of Nd-Fe-B Thin Film under a Nanosecond Pulse Magnetic Field. *Electrical Engineering in Japan (English translation of Denki Gakkai Ronbunshi)* **203,** 3–8 (Apr. 2018).

24. Takamasu, T., Sato, K., Imanaka, Y. & Takehana, K. Fabrication of a micro-coil pulsed magnet system and its application for solid state physics. *Journal of Physics: Conference Series* **51,** 591–594 (Nov. 2006).

25. Montgomery, D. B. The generation of high magnetic fields. *Reports on Progress in Physics* **26,** 69–104 (Jan. 1963).

26. Matsumoto, T., So, Y. G., Ikuhara, Y. & Shibata, N. Direct visualization of nucleation intermediate state of magnetic skyrmion from helical stripes assisted by artificial surface pits. *Journal of Magnetism and Magnetic Materials* **531,** 167976 (2021).

27. Müller, J. *et al.* Magnetic Skyrmions and Skyrmion Clusters in the Helical Phase of Cu2OSeO3. *Physical Review Letters* **119,** 137201 (2017).

Chapter 6

Skyrmion Stability in Synthetic Antiferromagnetic Systems

Introduction

This chapter is concerned with investigating the stability of skyrmions within synthetic antiferromagnetic (SAF) systems, and magnetic systems with metal-molecular interfaces. These studies will be presented through a series of micromagnetic simulations using MuMax3. First, some context and motivation will be provided relating to SAF systems, particularly related to unbalanced SAFs. This will be followed by a study into how skyrmion stability in a multilayer SAF (mSAF) may be influenced by uncompensated dipolar interactions, and how these may be compensated for through the introduction of ferromagnetic (FM) interlayer exchange coupling (IEC). Next, a skyrmion stabilising effect will be presented through the introduction of metal-molecular interfaces in bilayer SAF (bSAF) systems. The focus will be on C_{60} and Co layers, where the stabilising effects are due to anisotropy enhancement effects at the Co/C_{60} interface. Finally, non-trivial variations in skyrmion radius are found when the C_{60} layers are explicitly included in micromagnetic simulations, suggesting interesting future experiments involving these types of metal-molecular SAF systems.

The original MuMax3 script for simulating SAF systems was written by William Legrand, ETH Zürich. This script was subsequently modified for use within this chapter.

6.1 Stabilising Skyrmions in SAF Multilayers

A number of challenges still exist for skyrmions to be realised as information carriers within future data transmission and storage devices. These include improving zero-field stability, achieving small skyrmion radii and enhancing current-induced motion. Due to the long-range dipolar interactions present in most skyrmion-hosting magnetic systems, skyrmion stability relies on the application of external magnetic fields and furthermore, skrymions are prevented from reaching ultra-small sizes ($<$ 10 nm) [1]. Methods of reducing the effects of the dipolar interactions include either decreasing the thickness or the saturation magnetisation ($\mathrm{M_s}$) of the ferromagnetic (FM) layers within skyrmion-hosting systems. However, materials of a finite thickness and non-zero $\mathrm{M_s}$ will always generate a non-vanishing stray-field, which destabilises small skyrmions. Furthermore, skyrmion deflection during current-induced motion, due to the skyrmion Hall effect (SHE), must be minimised or eliminated to enable the desirable linear propagation of skyrmions [2]. The consequence of the SHE is that skyrmions will be deflected with a component of their velocity perpendicular to the current direction that drives their motion, and therefore poses significant real-world challenges when designing skyrmion race-track devices. Therefore, minimising both dipolar interactions and the SHE is of paramount importance for future skyrmion-based devices.

Synthetic antiferromagnets (SAF) are an excellent candidate system for providing solutions to the challenges posed above, through their ability to stabilise pairs of antiferromagnetically coupled skyrmions with opposite topological charge ($\pm N$). In its simplest construction, a SAF consists of two antiferromagnetically coupled FM layers, separated by a non-magnetic (NM) heavy metal (HM) spacer layer. The HM layer facilitates antiferromagnetic exchange coupling between the two FM layers through a Ruderman–Kittel–Kasuya–Yosida (RKKY)-type interaction. Thus, SAF systems aim to replicate the antiparallel spin configuration present in regular antiferromagnets, between the two coupled FM layers. An example of a general SAF system is shown in Fig. 6.1a, where the two FM layers are coupled antiferromagnetically due to the thickness and elemental choice of the $\mathrm{HM_1}$ layer. In these SAF systems, skyrmions of opposite polarity may exist in the FM layers as shown in Fig. 6.1b, coupled together to form a single SAF skyrmion. This type of long-range exchange coupling between distinct magnetic layers can have both FM and antiferromagnetic (AFM) character, and will henceforth be refereed to generally, as interlayer exchange coupling (IEC) for the purposes of this thesis.

It is possible to carefully tune the magnetic interactions present within the SAF system through multilayer engineering, for example the composition and thicknesses of the $\mathrm{HM_1}$, $\mathrm{HM_2}$ and FM layers in Fig. 6.1a. Thus, the SAF system as a whole will determine the nature and strength of important magnetic interactions for stabilising skyrmions, including the Dzyaloshinskii–Moriya (DM) interaction and perpendicular magnetocrystalline anisotropy (PMA) [3]. Recently, SAF skyrmions have been stabilised in (Pt/Co/Ru)-based multilayers, and experimentally detected using mag-

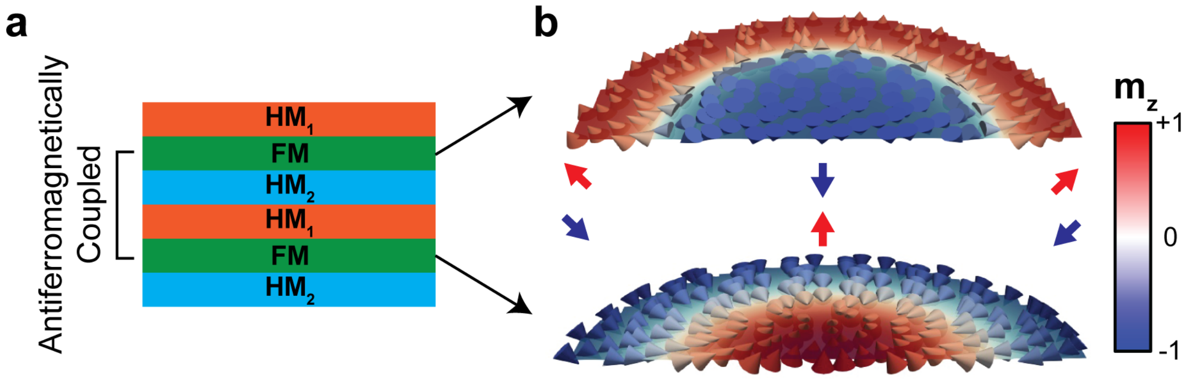

Figure 6.1: **a** Generic synthetic antiferromagnetic (SAF) system consiting of two ferromagnetic (FM) layers coupled antiferromagnetically through non-magnetic (NM) heavy metal (HM) layers. In this system HM$_1$ and HM$_2$ provide desired magnetic interactions such as RKKY, DM and PMA, and the strength of these interactions will depend on the choice of metals and the thickness of the layers. **b** Vector schematic of a SAF skyrmion cross-section, where the skyrmion in the top FM layer has opposite topological charge, and is coupled, to the skyrmion in the bottom FM layer. The combination of these two coupled skyrmions forms the single SAF skyrmion, which has a total topological charge of zero.

netic force microscopy (MFM) as described in Ref. [3]. In this case, HM$_1$ $=$ Pt, HM$_2$ $=$ Ru and FM $=$ Co, and the thickness of each layer was carefully chosen to reach an optimum balance of DM interaction for skyrmion formation, RKKY for AFM coupling and PMA to obtain zero effective anisotropy ($K_{eff} = 0$) in the FM layers.

In SAF systems, the aforementioned dipolar interactions are minimised due to the proximity of the antiferromagnetically coupled FM layers. The stray fields generated by each of the FM layers compensate for each other due to their opposing magnetisation and close proximity, theoretically allowing for small skyrmion sizes. Additionally, the SAF skyrmion has a net zero topological charge, which eliminates the deflection caused by the Magnus force during current induced motion due to the SHE [4, 5]. However, although the FM layers may be close (<1 nm) there is still a non-zero separation between them. Therefore the dipolar effects will not be fully compensated, and a finite stray-field will still be present. This should create a lower-bound for the minimum achievable skyrmion radius, and furthermore may impose a requirement some form of stabilising field for the smallest skyrmion sizes. Indeed, the experimental observation of SAF skyrmions in Ref. [3] reported that although no global magnetic field was required to stabilise the SAF skyrmions, coupling of the SAF to a FM biasing layer (BL) was required to nucleate skyrmions. A BL is chosen over an external magnetic field because of the asymmetric effect that a global magnetic field would have on the individual skyrmions in a SAF system. For example, a magnetic field applied in the $+z$-direction (perpendicular to the SAF surface) would cause the skyrmion in one FM layer to grow in size and the skyrmion in the other layer to shrink, thus destabilising the coupled SAF skyrmion. Note that in the remainder of this thesis the term 'SAF skyrmion' refers to the extended skyrmion structure with a net $N = 0$, which may consist of two or more individual skyrmions coupled via IEC.

6.1.1 Unbalanced SAF Systems

Imaging a SAF skyrmion using Lorentz TEM (LTEM) is not a straight-forward process like it is for the SkX within a B20 helimagnet, as described in Chapter 4 and 5. In LTEM, electrons are transmitted through the entire specimen and therefore in a perfectly balanced SAF, any Lorentz deflection caused by one FM layer would be cancelled out by an equal and opposite deflection from the other FM layer. This would have the effect of generating zero or near-zero magnetic contrast in both Fresnel and DPC imaging. Note that any technologically relevant SAF system should be balanced to ensure a net-zero SHE and maximum cancellation of dipolar interactions, however it is not straight forward to investigate such a system using LTEM imaging methods. It is therefore a useful endeavour to create unbalanced SAF systems for LTEM imaging purposes, such that the two vertically separated FM layers do not precisely compensate for each others stray fields, and a net magnetic induction in the z-direction may be thus detected. This is not an issue for surface techniques such as MFM, because asymmetry is introduced from the MFM probe being closer to one FM layer than the other, thereby detecting uncompensated local stray-fields. Two methods for creating unbalanced SAFs are summarised schematically in Fig. 6.2, achieved by either tuning the FM layer thickness (Fig. 6.2a) or number of FM subsystem repeat units (Fig. 6.2b).

The first method described here involves varying the thickness of one FM layer, whilst the thickness of the other FM layer is held constant. In Fig. 6.2a this is shown through the variation of the Co layer thicknesses, namely holding t_2 constant and increasing t_1. The result of this variation in FM layer thickness will be an increased integrated magnetic induction in the top Co layer when compared to the bottom Co layer, resulting in non-zero magnetic contrast during LTEM imaging. A problem with this method is that by modifying the thickness of the Co layer, any magnetic interactions with a thickness dependence will also be modified. Examples include the effective anisotropy (K_{eff}) and the interfacial DM interaction (D_{ind}), both of which will have an impact on the properties of any skyrmion structures formed. Thus, a FM thickness variation would result in differences in the skyrmion-forming properties between the top and bottom FM layers, which may not be desirable.

An alternative method for creating an unbalanced SAF is to introduce repeat units of FM/HM above and/or below the RKKY-providing Ru layer. In Fig. 6.2b this is represented by the [Pt/Co/HM] repeat unit ($\mathrm{N_{Rep}}$), where the HM is chosen to optimise

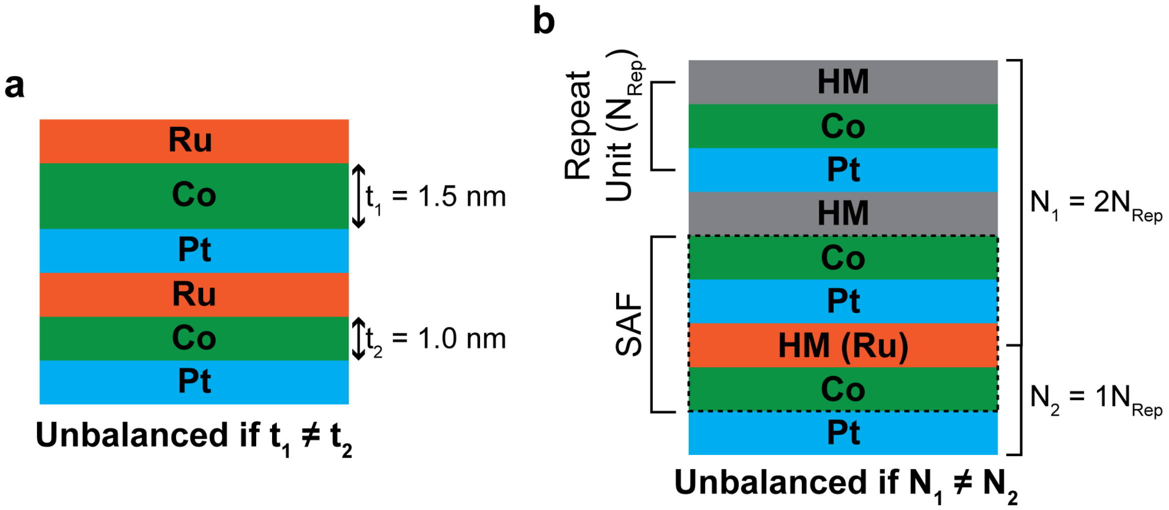

Figure 6.2: Methods for creating unbalanced SAF systems, which exhibit non-zero magnetic contrast during LTEM imaging. In these schematics, the elemental composition of the FM and HM layers are the same as defined in the previous section. **a** SAF system is unbalanced by tuning the thickness ratio of the Co layers. The SAF can be unbalanced by holding t_2 constant whilst varying t_1. **b** Introduction of individual [Pt/Co/HM] subsystem repeat units above and below the Ru layer can create an unbalanced multilayer SAF when N_1 and N_2 are different.

magnetic interactions. The example shown in Fig. 6.2b has an additional repeat unit above the Ru layer, such that $N_1 = 2N_{\mathrm{Rep}}$ and no additional repeat units below the Ru, such that $N_2 = 1N_{\mathrm{Rep}}$. This creates two distinct anti-parallel FM subsystems above and below Ru, where the SAF is unbalanced when $N_1 \neq N_2$. A benefit of this method is that the individual layer thicknesses (and therefore magnetic interactions) are consistent across the SAF system. Indeed, SAF skyrmions have recently been experimentally observed using LTEM imaging, within an unbalanced SAF consisting of [Co/Pd] multilayer repeat units [6]. However, this multilayer SAF system differs from the regular SAF system (Fig. 6.2) in that the repeat units (N_{Rep}) cannot be coupled antiferromagnetically to one another, thus limiting the choice of HM within N_{Rep} to one that does not provide AFM IEC. Thus, this multilayer design consists of a SAF region, and two distinct FM subsystems above and below the SAF region.

For the remainder of this thesis, the type of structure shown in Fig. 6.2b will henceforth be referred to as a multilayer-SAF (mSAF), and the type first shown in Fig. 6.1a will be referred to as a bilayer-SAF (bSAF), based on the number of FM layers.

6.1.2 Simulating Multilayer SAFs

Simulating the types of mSAF systems presented in Fig. 6.2b requires a micromagnetic simulation program that supports demagnetising field calculations whilst periodic boundary conditions are imposed. This is because the FM layers are spatially separated from each other, and thus will be subject to non-zero stray-field interactions that should be accounted for. Furthermore, since the thickness of the FM layers is extremely small compared to their lateral extent, periodic boundary conditions are required to reduce the simulation space to a feasible size. This is in contrast to the recent method undertaken in Ref. [6], whereby the FM subsystems were grouped together into a pair of antiferromagnetically coupled layers, for simulation purposes using OOMMF. The problem with this method is that it disregards any dipolar effects coming from the non-zero separation of each FM layer within the subsystems. As such for this thesis, MuMax3 was chosen as it supports demagnetising field calculations with periodic boundary conditions enabled [7]. A further benefit of MuMax3 is that it benefits from GPU-accelerated code, which means that computer systems with NVIDIA GPUs will benefit from significantly reduced compute times when compared to CPU-only simulation software such as OOMMF [8]. This is particularly important for the mSAF simulations presented here, which require additional custom energy terms, increasing the computational complexity of the simulations.

The first step is to convert the ‘real-world’ geometry of the mSAF, given in Fig. 6.2b, into a magnetic system that can be represented within MuMax3. Since we are only interested in explicitly simulating the magnetic layers, the mSAF structure can be simplified to alternating magnetic and NM regions. The magnetic layers represent the FM (Co) and the NM layers represent the combined HM ([Ru/Pt]) spacer layers. A schematic of the mSAF representation for simulation purposes can be seen in Fig. 6.3a, showing a two-dimensional mSAF cross-section. This structure demonstrates the two separate FM multilayer subsystems (blue and red layers), which each consist of FM layer repeat units with FM IEC between them. The two subsystems are aligned anti-parallel to each other (shown by the white arrows representing the magnetisation direction), due to the AFM IEC. This AFM IEC represents the RKKY coupling introduced by the Ru spacer layer, with a strength determined by the thickness of this layer. The FM IEC represents RKKY interactions between neighbouring FM layers within the multilayer subsystems that do not contain Ru, but instead other HM that facilitate FM coupling. This type of FM IEC has been demonstrated to exist within multilayer Co/Pt systems [9], where the strength of this effect is greatly enhanced when Pt thickness is less than 3 nm [10]. Given the desirable thickness of Pt in mSAF systems is on the order of 1 nm, it is highly likely that the subsystems will be ferromagnetically coupled in the manner described in Ref. [9].

Both the AFM and FM IEC are introduced into MuMax3 through separate custom field and energy terms. Since the magnetisation vector $\mathbf{m}$ is normalised in the simulations, we introduce the RKKY fields by first calculating an RKKY scalar factor that is subsequently multiplied by $\mathbf{m}$. The RKKY scalar factors for AFM and FM coupling,

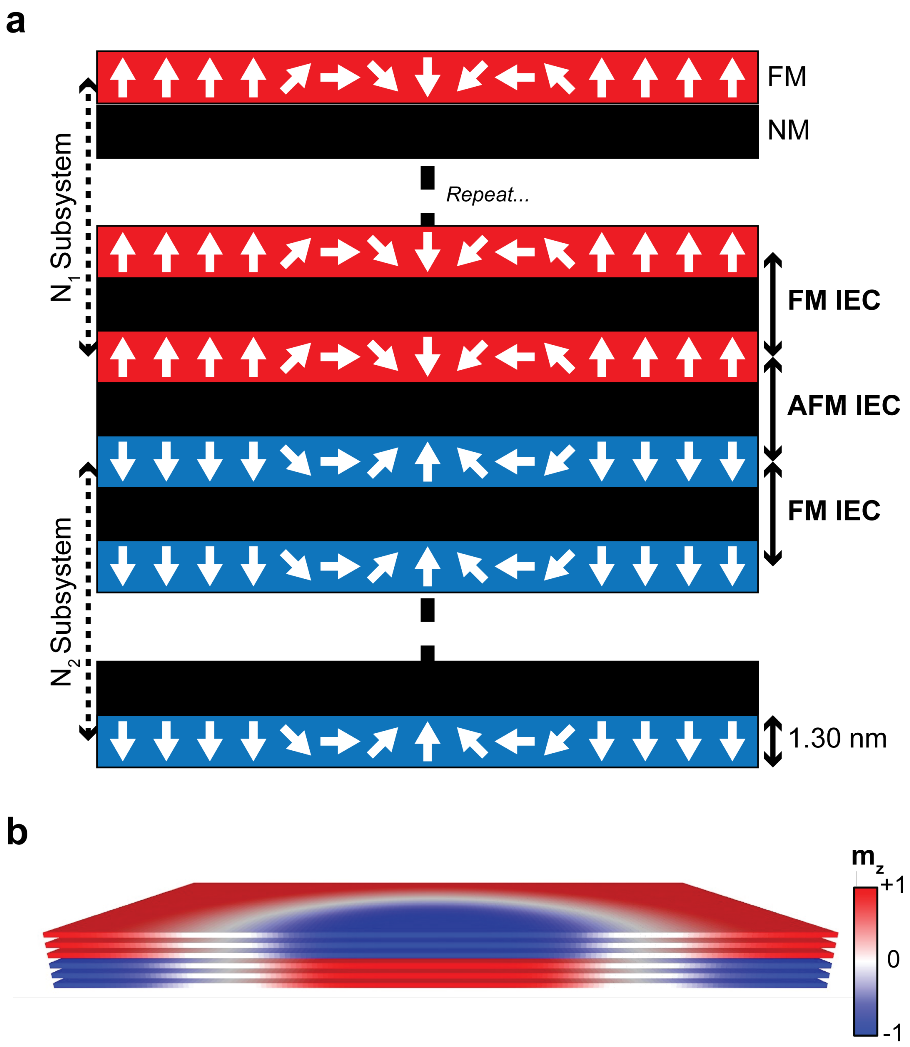

Figure 6.3: **a** Schematic demonstrating the multilayer SAF geometry simulation configuration. The structure consists of two FM subsystems (red and blue layers), which exhibit FM IEC coupling between neighbouring layers within the subsystem. However, the two innermost layers have AFM coupling between them, enabling the anti-parallel spin alignment (shown by white arrows) between the subsystems. **b** MuMax3 simulation initial state example for $N_1 = 3$, $N_2 = 3$, coloured by m_z magnetisation.

C_{AFM} and C_{FM} are calculated according to:

$$C_{AFM} = \frac{J_{RKKY\ AFM}}{\text{cell}_z \times M_s} \tag{6.1}$$

and

$$C_{FM} = \frac{J_{RKKY\ FM}}{\text{cell}_z \times M_s} \tag{6.2}$$

where cell_z is the z-axis cell size, which is a proxy for the layer thickness. For simplicity, the following explanation is in terms of C_{AFM}, however the exact same process is carried out for C_{FM}. The calculated scalar C_{AFM} is multiplied by $\mathbf{m}$ within the two layers participating in the interaction, which in the case of the AFM IEC is between the two neighbouring layers that have anti-parallel spin alignment. This generates two local fields, which are then additively combined, resulting in a net AFM field, $\mathbf{B}_{\mathrm{AFM}}$, acting between the two participating layers. The corresponding AFM energy density associated with the two interacting layers is subsequently calculated according to:

$$E_{AFM} = M_s(-\mathbf{m} \cdot \mathbf{B}_{\mathrm{AFM}}) \tag{6.3}$$

This process is repeated for the FM IEC, between all pairs of qualifying layers, such that the total energy now takes the form:

$$E_{tot} = E_{ex} + E_{demag} + E_{anis} + E_{Zeeman} + E_{FM} + E_{AFM} \tag{6.4}$$

Note that both E_{FM} and E_{AFM} will only be non-zero for simulation cells that have an associated FM or AFM IEC. In other words, only layers that are participating in FM(AFM) coupling will contribute $E_{FM}(E_{AFM})$ to the total energy during minimisation.

For all simulations in this section, the strength of AFM and FM IEC was set to $J_{RKKY\ AFM} = -0.5\ \mathrm{mJ\ m^{-3}}$ and $J_{RKKY\ FM} = +2.00\ \mathrm{mJ\ m^{-3}}$, taken from Ref. [10] and Ref. [11], respectively. The remaining simulation parameters are as follows: cell size $cell_{x,y,z} = 1.3$ nm, interfacial DM interaction strength $D_{ind} = 1.0 \times 10^{-3}$ Jm^{-2}, saturation magnetisation $M_s = 1.2 \times 10^6$ Am^{-1}, exchange stiffness $A_{ex} = 10$ pJm^{-1}, uniaxial anisotropy constant (z-axis) $K_u = 0.995 \times 10^6$ Jm^{-3}, Landau-Lifshitz damping parameter $\alpha = 0.02$. The choice of interfacial DM interaction strength is supported by previous studies involving Pt/Co/Ru systems [12]. The effect of a biasing layer (BL), to stabilise the SAF skyrmions, was introduced using a small perpendicular ($+B_z$) magnetic field of 0.08 T applied to only the top-most layer in every simulation. Note that the cell size is a proxy for the layer thickness, and as such the FM layer thickness and NM spacer are both equal to 1.3 nm in these simulations. As such, they represent physical systems in which the FM and NM sections have equal thicknesses, and systems that deviate from that restriction cannot be simulated precisely using this method. All simulations contained within this chapter have a lateral ($x - y$) simulation mesh size of 256 × 256, with the z-dimension determined by the thickness and number of layers being simulated. The total simulation size is then determined by multiplication of the mesh dimensions with the cell size used within the specific simulation.

The reason for choosing the above parameters was to determine the stability of SAF skyrmions within extended mSAF systems, particularly when unbalanced ($\mathrm{N}_1 \neq \mathrm{N}_2$). The material parameters were used to represent Pt/Co/Ru/HM multilayer systems, where HM could be chosen to fine-tune DMI and/or the IEC. A range of mSAF systems with N_1 and N_2 ranging between one and five were simulated, resulting in a total of 25 simulations. These simulations were initialised with a skyrmion of the appropriate polarity in each of the FM layers. An example of the initial state is shown in Fig. 6.3b, for the $\mathrm{N}_1 = \mathrm{N}_2 = 3$ simulation. The large SAF skyrmion can be seen in the cross-section, after initialisation this state was allowed to relax until the minimum energy configuration was obtained and the simulation ended.

6.1.3 Results

The magnetisation configurations corresponding to the minimum energy state for the 3-layer unbalanced mSAFs can be seen in Fig. 6.4, where the scalar plots are coloured by the m_z magnetisation component. In these, and all future simulations, layers will be ordered such that Layer 1 is the topmost layer with the additional $B_z = 0.08$ T, accounting for the effect of the BL. Furthermore, the simulations will be referenced within the text by a pair of numbers denoting their N_1 and N_2 values, for example 1-2 and 2-1. The annotated arrows show the type of IEC coupling that has been implemented in the simulation between each of the corresponding layers. Additionally, the skyrmion radius (given in nm) has been calculated for each layer, using the contour of $m_z = 0$.

Immediately apparent, is the fact that in both simulations a relatively small SAF skyrmion is stabilised with average radii of 12.2 nm and 14.4 nm, respectively. The smallest individual skyrmion is within Layer 1 of simulation 1-2 and this is due to the fact that the BL field is acting in this layer and its only neighbouring layer is one of anti-parallel spin alignment (Layer 2), minimising demagnetising effects. This small radius is then translated to Layer 2 through the AFM IEC, and to Layer 3 through the FM IEC. It can be seen that the skyrmion radius does increase slightly from Layer 1 to Layer 3, likely due to uncompensated stray-field interactions. A slightly different behaviour is present in simulation 2-1, where although the isolated layer (Layer 3 in this case) has the smallest skyrmion radius, the average skyrmion radius is greater. This is likely due to the lack of the compound effect found in simulation 1-2, whereby the isolated layer was also the layer affected by the BL field. However, there are still clear stray-field compensation effects in 2-1, shown by the smallest skyrmion in Layer 3. These simulations demonstrates that a simple 3-layer mSAF with appropriate magnetic interactions and a BL is capable of stabilising a small SAF skyrmion in an unbalanced system that should generate a net Lorentz deflection, and therefore magnetic contrast in LTEM imaging. A comparison between the simulated Fresnel contrast images generated by balanced and unbalanced mSAFs will be performed at the end of this section.

Next, the number of layers within the mSAF is increased to determine what effect this may have on the individual skyrmion radii, and by extension the entire SAF

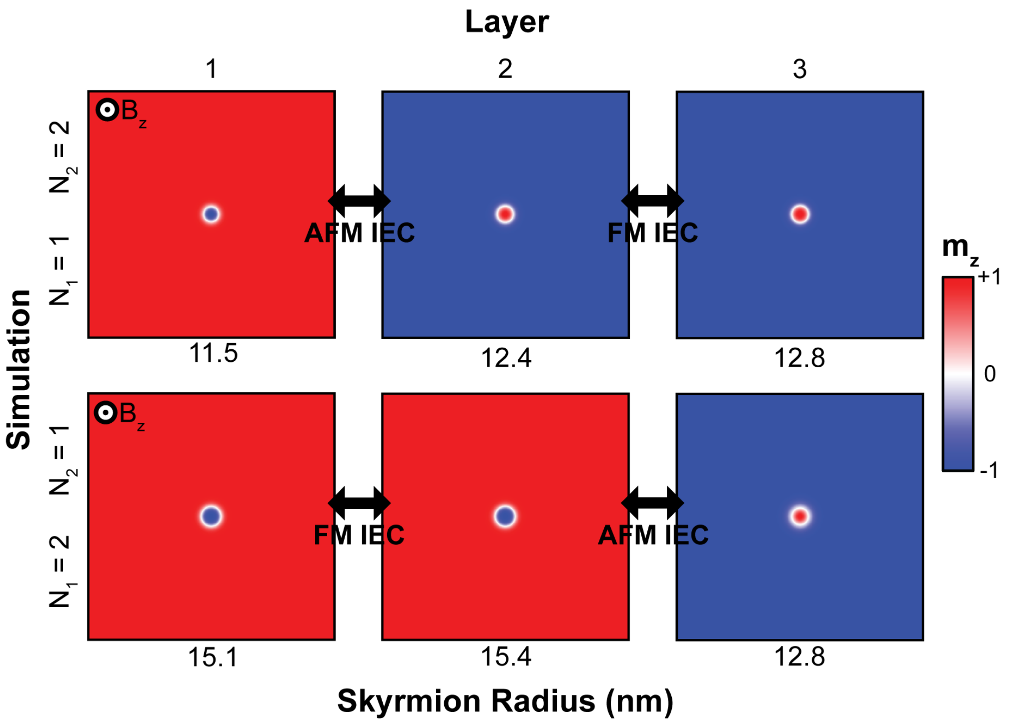

Figure 6.4: Magnetisation scalar plots coloured by m_z, given by the colour bar, for each layer within the 3-layer unbalanced mSAFs, $\mathrm{N}_1 = 1$ $\mathrm{N}_2 = 2$ and $\mathrm{N}_1 = 2$ $\mathrm{N}_2 = 1$. Skyrmion radius is calculated using the contour of $m_z = 0$ in each layer. Annotated arrows highlight the type of IEC present between the corresponding layers, as implemented in the simulation. The BL field is acting in Layer 1, out of the plane of the page.

skyrmion stability. Figure 6.5 shows the minimum energy magnetic configuration for the 4-layer mSAFs, 1-3, 2-2 and 3-1. Note that although the panel sizes differ compared to the 3-layer mSAF, the simulation size is identical and simply scaled to fit on the page. The average SAF skyrmion radius has increased in all simulations, most notably in the unbalanced mSAFs, 1-3 and 3-1, it is 30.3 nm and 37.4 nm respectively. This indicates that the increased number of uncompensated layers has led to further destabilising effects from the additive stray-fields. Again, 1-3 stabilises smaller skyrmions than 3-1 due to the BL field acting in Layer 1. However, the balanced 2-2 simulation shows quite different behaviour, with an average SAF skyrmion radius of only 15.5 nm. The fact that this system is balanced appears to have provided a stabilising effect on the skyrmions, as seen through a reduction in their radii. This is despite the fact that Layer 1 and Layer 4 are generating uncompensated stray-fields over short distances. However, the fact that there is symmetry about the AFM IEC has led to a significant reduction in skyrmion radius. This can be understood by the fact that although Layers 1 and 4 are not immediately neighbouring, there may still be significant compensation of the long range stray-fields associated with these layers due to the aforementioned symmetry. As such, the balanced mSAF (much like the bSAF) can still stabilise small SAF skyrmions, suitable for technological purposes.

Furthermore, the increased SAF skyrmion radius in the 4-layer mSAFs may provide useful for imaging purposes, especially in Fresnel LTEM imaging where spatial resolution may be a limiting factor. In addition to the increased radius, the increased net B_z magnetisation may provide additional sensitivity in DPC imaging, through larger Lorentz deflections.

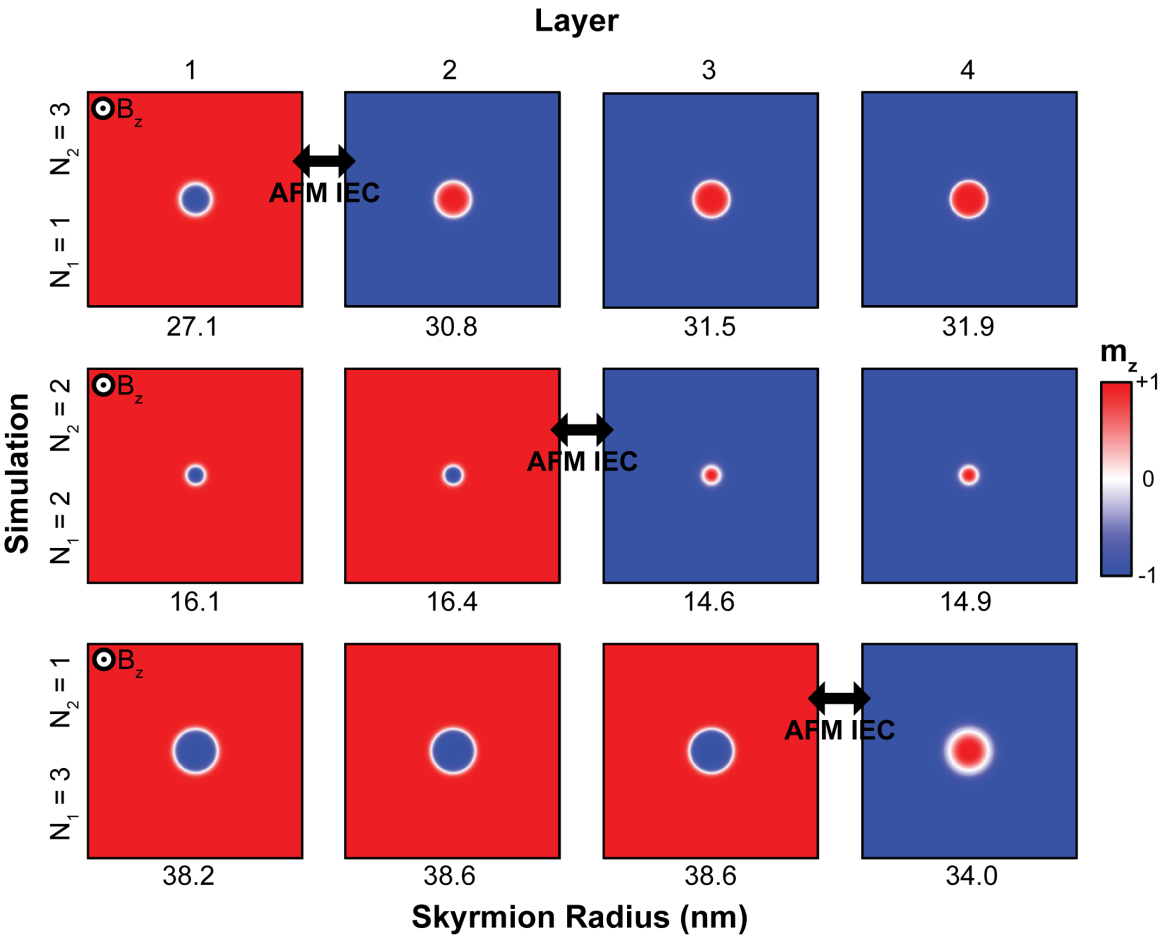

Figure 6.5: Magnetisation scalar plots coloured by m_z, given by the colour bar, for each layer within the 4-layer mSAFs, $\mathrm{N}_1 = 1\ \mathrm{N}_2 = 3$, $\mathrm{N}_1 = 2\ \mathrm{N}_2 = 2$ and $\mathrm{N}_1 = 3\ \mathrm{N}_2 = 1$. Skyrmion radius is calculated using the contour of $m_z = 0$ in each layer. Annotated arrows highlight the AFM IEC present between the corresponding layers, the FM IEC is implied between all layers with parallel spin alignment. The BL field is acting in Layer 1, out of the plane of the page.

Figure 6.6 shows the minimum energy magnetisation configurations for the 5-layer mSAF simulations, where 4-1 shows a worm-like structure, continuous in the $x - y$ plane due to the periodic boundary conditions. Finally, we reach an mSAF system in which skyrmions are unstable, namely the 4-1 simulation. However, the 1-4 simulation still hosts a SAF skyrmion with a large average radius of 86.4 nm, and this is again due to the stabilising BL field applied to Layer 1. In this case, the BL field stabilised skyrmion in Layer 1 also has stray-field compensation from Layer 2, and this stabilised structure then propagates through the mSAF as was described for simulation 1-3. However, the BL field in simulation 4-1 is not sufficient to overcome the destabilising effect of the severely unbalanced SAF structure, which relaxes to a labyrinth or worm-like magnetic configuration. Both 2-3 and 3-2 behave in predictable ways, compared to the previous simulations, namely 2-3 hosts a SAF skyrmion with a smaller radius than 3-2 due to the combination of BL field, stray-field compensation and structure propagation via IEC.

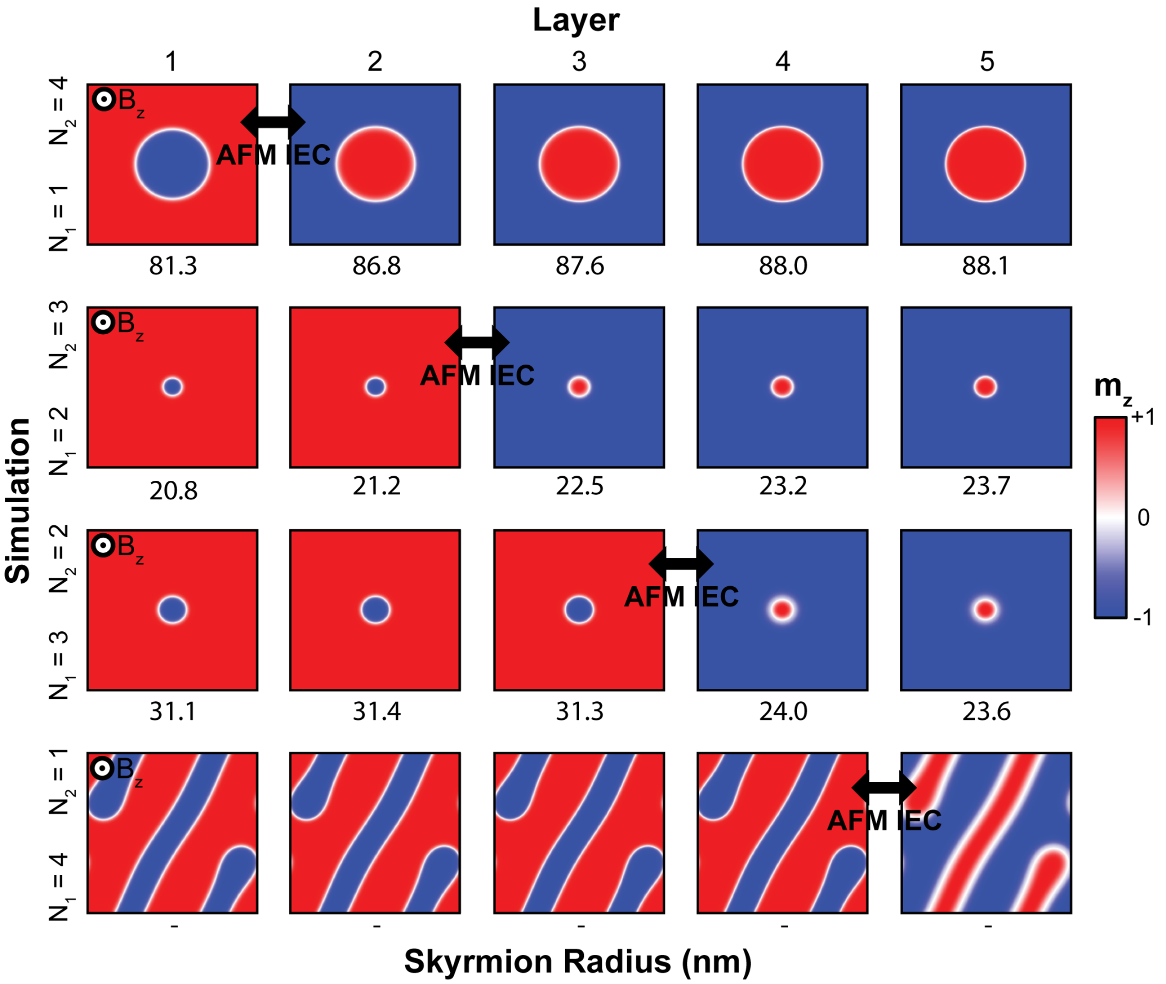

Figure 6.6: Magnetisation scalar plots coloured by m_z, given by the colour bar, for each layer within the 5-layer mSAFs, $N_1 = 1$ $N_2 = 4$, $N_1 = 2$ $N_2 = 3$, $N_1 = 3$ $N_2 = 2$ and $N_1 = 4$ $N_2 = 1$. Skyrmion radius is calculated using the contour of $m_z = 0$ in each layer. Annotated arrows highlight the AFM IEC present between the corresponding layers, the FM IEC is implied between all layers with parallel spin alignment. The BL field is acting in Layer 1, out of the plane of the page.

With simulation 4-1 in Fig. 6.6, we have reached a point of instability with the current simulation parameters, and given that the BL field appears to have a limited effect on stabilising extended mSAFs it is unlikely that just increasing this value will be sufficient to stabilise the entire SAF skyrmion. Instead we may take guidance from the stabilising effect of the IEC, in its ability to propagate or 'transfer' the skyrmion structure throughout the mSAF. To demonstrate this effect, the same BL field (0.08 T) is used to stabilise a skyrmion structure in Layer 1 and the AFM IEC constant is increased from -0.5 mJ m^{-3} to -2.0 mJ m^{-3}, where all other simulation parameters remain the same. The results of this simulation are shown in Fig. 6.7a, where the minimum energy magnetisation configuration for a 7-layer mSAF is shown. A small skyrmion is stable across the mSAF, which qualitatively has a relatively consistent size, highlighting the stabilising effect of increasing only the AFM IEC. This is in contrast to the magnetic configuration shown in Fig. 6.7b, which has extended into a labyrinthine structure when the original AFM IEC strength of -2.0 mJ m^{-3} is used. Finally, we can confirm that the destabilising effect and non-uniformity of the skyrmions within extended mSAFs is due to the stray-fields, by switching the demagnetising field off in the MuMax3 simulations. Indeed, by inspecting Fig. 6.7c we can see that an extremely small SAF skyrmion is stable in an 8-layer system with the original simulation parameters, when the stray-field effects are unaccounted for.

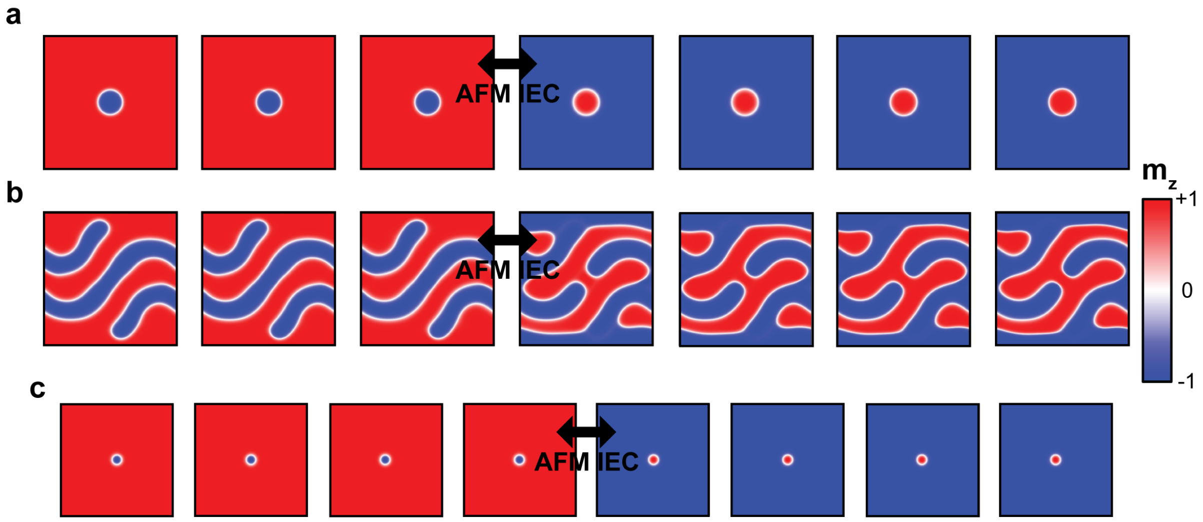

Figure 6.7: Magnetisation scalar plots coloured by m_z, given by the colour bar for mSAFs with different parameters. Although the scale is different in these figures, the simulation space is the same for all cases. **a** 7-layer mSAF with $J_{RKKY\ AFM} = -2.0\,\mathrm{mJ\,m^{-3}}$ **b** 7-layer mSAF with $J_{RKKY\ AFM} = 0.5\,\mathrm{mJ\,m^{-3}}$ **c** 8-layer mSAF with demagnetising field switched off in MuMax3.

Finally, a comparison between the simulated Fresnel images of three different mSAF systems is given in Fig. 6.8. First, the magnetisation was averaged across the thickness of each of the mSAF simulations, generating a 2D vector plot of the average magnetisation. Next, a phase image of this magnetic configuration was generated, followed by a simulated Fresnel image using the mag_tools module in the fpd python library [**fpd**]. The colour bar in each of the images gives the relative pixel intensity, with an arbitrary scale. Immediately apparent in Fig. 6.8a is the extremely low intensity compared to those in Fig. 6.8b,c. In fact, the generated Fresnel intensity is almost two orders of magntitude weaker, due to the fact that simulation 1-1 is balanced. Due to the fact that both simulation 1-2 (Fig. 6.8b) and simulation 2-3 (Fig. 6.8c) are unbalanced, means that a much higher Fresnel intensity is generated.

A characteristic feature in Fig. 6.8c is the faint halo of intensity around the central bright spot, which is likely due to the variation in skyrmion radii through the thickness.

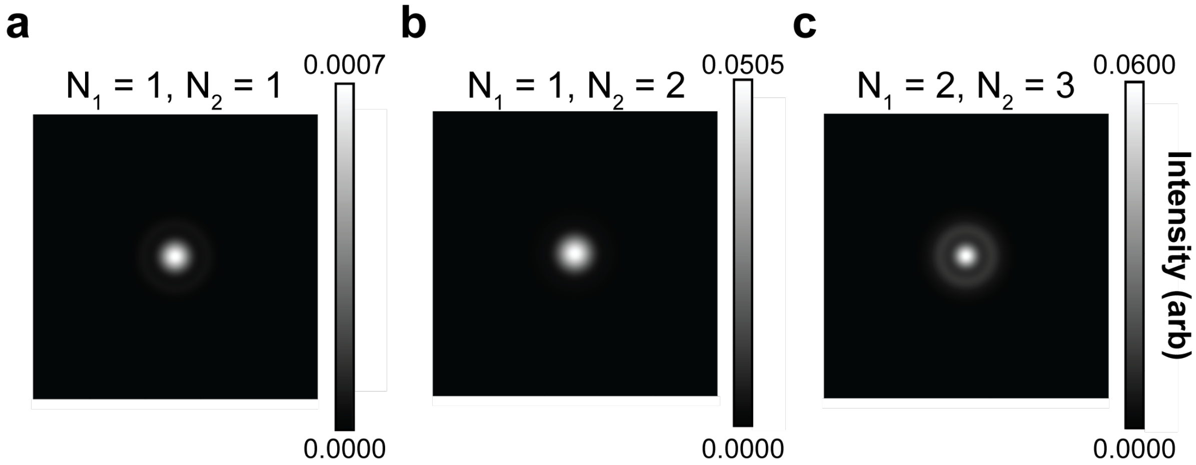

Figure 6.8: Simulated Fresnel images of the **a** 1-1, **b** 1-2 and **c** 2-3 mSAF systems. Images were simulated using the python fpd package [**fpd**], with simulation parameters: spherical aberration $C_S = 0.5$ mm, defocus $\Delta f = 500$ μm and 200 kV acceleration voltage.

Through a series of micromagnetic simulations in this section, it has been shown that SAF skyrmions can be stabilised in extended mSAF systems, including unbalanced SAFs for TEM imaging purposes. The primary factor in destabilisation appears to be due to uncompensated stray-field interactions across the multilayer, especially in severely unbalanced systems. Through multilayer engineering and use of different materials, it may be possible to extend the stability of skyrmions in mSAFs with a relatively large number of layers, particularly if the AFM IEC can be enhanced. Furthermore, intermediate mSAF systems (around four or five layers) may be able to provide increased magnetic contrast through larger skyrmion sizes and increased net B_z in more unbalanced mSAFs. However, when properly accounting for demagnetising effects, a biasing field was required to stabilise a skyrmion in all of these systems and we will now look into alternative methods for providing additional skyrmion stability in SAF systems.

6.2 Metal-Molecular Interfaces in SAF systems

Research into molecular spintronics [13], and specifically the study of "spinterfaces" has grown rapidly in recent years [14]. Spinterfaces concern the formation of magnetic metal-organic interface regions, whereby spin injection from the metal into the organic molecule takes place [15]. Importantly, at the interface between magnetic metals and fullerene molecules [16], a region of enhanced or modified magnetic properties extends into both the metal and the molecule. For example, it has recently been shown that in bilayers of C_{60} and Co, a drastic increase of in-plane anisotropy within the Co is exhibited [17]. This phenomenon is due to the in-built potential between the molecule and metal, in combination with the formation of a spin-dependent electric dipole involving $\pi - d$ hybrid orbitals, and thus named π-anisotropy. Enhancement of perpendicular magnetic anisotropy (PMA) has also been reported at Co/C_{60} interfaces in ultrathin films [18, 19]. This type of PMA enhancement has been attributed to additional interfacial anisotropy, arising from orbital hybridisation within the spinterface. Furthermore, it has been shown that C_{60} interfaced with a ferromagnet, such as Co, becomes ferromagnetic itself due to spin-polarised charge transfer from the Co. This magnetic molecular layer is coupled antiferromagnetically to the Co involved in the interface region, and acts to suppress the magnetisation of the Co film. The induced moment within C_{60} from Co charge-transfer has been measured to be 0.8 μ_B per cage in Ref. [19] and 1.2 μ_B per cage in Ref. [15], where μ_B is the Bohr magneton. Note that although C_{60} layers have been shown to enhance both PMA and in-plane anisotropy, the PMA enhancement effect is more relevant here since the magnetic layers are ultra-thin, on the order of 1 nm thickness and therefore K_u should dominate over K_v. As such, only the enhancement of PMA will be explicitly simulated here, however it should be noted that it may be possible to enhance a finite in-plane anisotropy by tuning the thickness of the magnetic layer such that K_v becomes a relevant quantity to consider.

These studies raise the possibility of modifying skyrmion stability through the modification of magnetic properties in SAF systems, through the introduction of C_{60} molecular layers. Since skyrmion size and stability has been shown to be related to PMA [20], inclusion of a Co/C_{60} interface into the SAF structure may provide stabilising effects. As such, the effect of incorporating C_{60} layers into SAF stacks will be investigated using micromagnetic simulations with custom energy terms, as in the previous section. As such, (Pt/Co/Ru)-based SAF systems will be chosen, with the inclusion of C_{60} molecular layers in contact with one of the Co layers. Two separate methods will be chosen and investigated for introducing the effects of the Co/C_{60}interface within the micromagnetic simulations. The first will involve simulating only the effects of the Co/C_{60} interface, through a reduction in the exchange stiffness and increase in PMA constant (ΔK_u) of one Co layer. These modifications to the Co layer will represent the measured magnetic effects of the Co/C_{60} interaction only. The second method will be to explicitly simulate the C_{60} magnetic layer, along with the PMA enhancing effects and reduction in exchange stiffness. This method will involve treating the molecular layer as a dilute magnet, with AFM IEC to the underlying Co layer but zero intermolecular coupling. It will be shown that both methods demonstrate qualitatively the same skyrmion stabilising effect, however the explicit simulation of C_{60} leads to some non-trivial skyrmion size behaviour. Schematics showing the first and the second simulation setups can be seen in Fig. 6.9a,b, respectively. The magnetic properties of the C_{60} layer in Fig. 6.9b have not been defined here, and will instead be discussed in Section 6.2.2. Furthermore, note that no BL field will be implemented in these simulations, since the enhancement of PMA is predicted to have a similar effect as the BL.

6.2.1 Simulating PMA Enhancement Effects

It has been shown that the metal/C_{60} interface region of modified magnetic properties extends only a few nm into the metal film. As such, within large systems, any interface effect may saturated by the bulk magnetic properties. Therefore, this type of interface behaviour is particularly well suited for thin-film multilayer systems such as SAFs, in which the thickness of the FM layers are typically on the order of 1 nm. Therefore, the magnetic enhancement effects may be assumed to be acting uniformly through the layer thickness. This drastically simplifies the SAF simulations, where the cell size is already a proxy for the layer thickness. This way, each layer in the simulation can have constant magnetic properties, in contrast to simulating a thicker (>10 nm) film, whereby magnetic properties would be inhomogeneous, changing far from the interface region.

In the following simulations, a bSAF system will be chosen with one of the Co layers having modified magnetic properties due to the interface with C_{60}. To simplify the simulation and the number of variable parameters, only the PMA enhancement effect and reduction in exchange stiffness will be explicitly simulated. However, since the C_{60} layer has been shown to modify the spin-orbit coupling at the interface [21], a modification of the interfacial DM interaction is also expected. This modification was excluded from the following simulations, since further studies on the strength of this DM interaction are required. The strength of the PMA enhancing effect was given in Ref. [18] as $\Delta K_u = +0.27$ MJ m^{-3}, and the exchange stiffness for Co in contact with C_{60} is given in Ref. [17] as $A_{ex} = 4$ pJ m^{-1}. The reduction in exchange stiffness was deduced experimentally and is due to electron transfer from the Co to the C_{60}. The bottom Co layer will remain unchanged, as it is spatially separated from the C_{60} layer and as such will not form a spinterface. All other simulation and material parameters are as follows: cell size $cell_{x,y,z} = 1.47$ nm, AFM IEC constant $J_{RKKY\ AFM} = -0.23$ mJ m^{-3}, interfacial DM strength $D_{ind} = 0.8 \times 10^{-3}$ Jm^{-2}, saturation magnetisation $M_s = 1.2 \times 10^6$ Am^{-1}, uniaxial anisotropy constant (z-axis) $K_u = 0.905 \times 10^6$ Jm^{-3}, exchange stiffness for bottom Co layer $A_{ex} = 10$ pJm^{-1}, exchange stiffness for top Co layer $A_{ex} = 4$ pJm^{-1}, Landau-Lifshitz damping parameter $\alpha = 0.02$. An additional anisotropy constant, ΔK_u, ranging between 0.00 and 0.34 MJ m^{-3} was added to the top Co layer for each simulation.

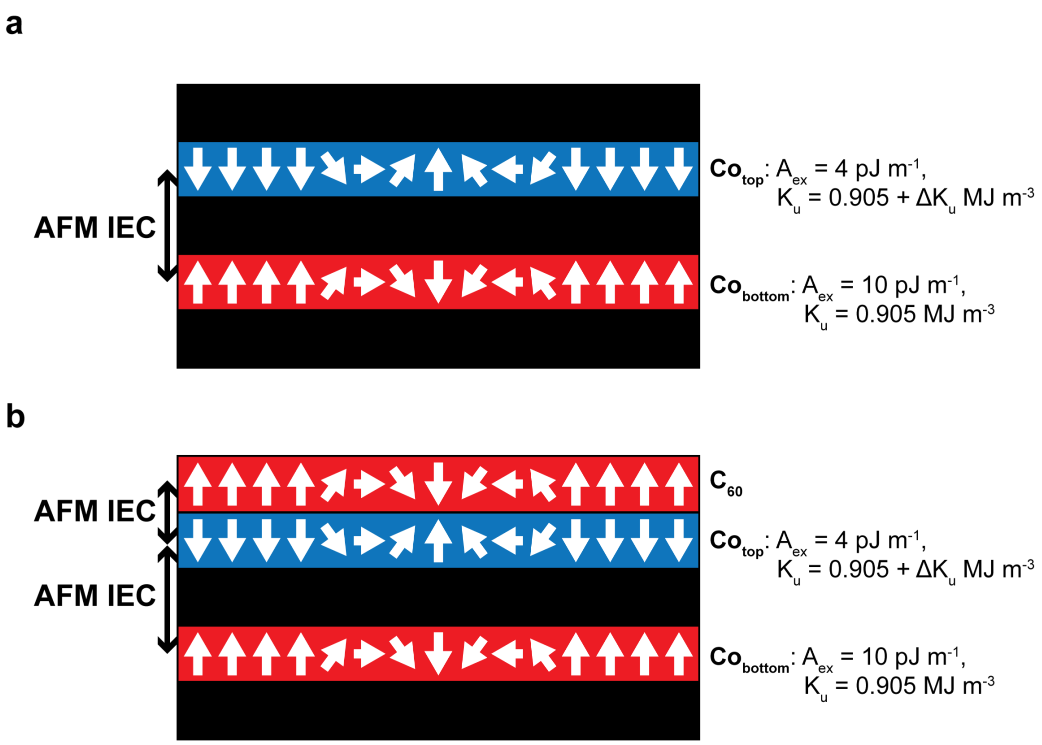
a
AFM IEC
Co$_{top}$: A$_{ex}$ = 4 pJ m^{-1},
K$_u$ = 0.905 + ΔK$_u$ MJ m^{-3}
Co$_{bottom}$: A$_{ex}$ = 10 pJ m^{-1},
K$_u$ = 0.905 MJ m^{-3}
b
AFM IEC
AFM IEC
C$_{60}$
Co$_{top}$: A$_{ex}$ = 4 pJ m^{-1},
K$_u$ = 0.905 + ΔK$_u$ MJ m^{-3}
Co$_{bottom}$: A$_{ex}$ = 10 pJ m^{-1},
K$_u$ = 0.905 MJ m^{-3}

Figure 6.9: Simulation layer setup for the different methods of investigating the enhanced PMA from a Co/C$_{60}$ within a SAF system. **a** bSAF with effect of C$_{60}$ introduced through modification of magnetic properties. The C$_{60}$ is assumed to be in contact with the top Co layer in this case. **a** bSAF with a C$_{60}$ layer explicitly simulated along with the modification of magnetic properties. The magnetic properties of the C$_{60}$ layer will be defined and discussed in Section 6.2.2.

The minimum energy magnetic configurations can be seen in the scalar plots in Fig. 6.10a, for the simulations with additional PMA ranging from $\Delta K_u = 0$ to $\Delta K_u = 0.29$ MJ m^{-3}. The panels on the left are for the top Co layer, with the modified magnetic properties due to the Co/C$_{60}$ interface, whilst the panels on the right are for the unmodified bottom Co layer. Immediately apparent is the skyrmion stabilising effect as the PMA is increased. This can be seen as the magnetic structure transitions from an extended labyrinth-type structure at $\Delta K_u = 0$ MJ m^{-3} to a circular skyrmion structure at $\Delta K_u = 0.06$ MJ m^{-3}. Further increasing the additional PMA in the top layer reduces the skyrmion radius significantly, which is reflected in both Co layers. Although the additional PMA is only added to the top Co layer, the bottom layer hosts a very similar structure due to the AFM IEC between the two layers. The black outlined panels in Fig. 6.10a highlight the skyrmion structure stabilised when $\Delta K_u = 0.27$ MJ m^{-3}, which is the measured PMA enhancing effect as measured in Ref. [18] for a Co/C$_{60}$ interface. This suggests that a sub-10 nm skyrmion may be achievable by utilising the PMA enhancing effect of the spinterface. Indeed, it has been recently experimentally demonstrated in Ref. [21] that the size of magnetic bubble domains within a Pt/Co/C$_{60}$/Pt system are drastically reduced when compared with a Pt/Co/Pt system. This behaviour has similarities to the radius reduction seen for skyrmions in the present ΔK_u simulations.

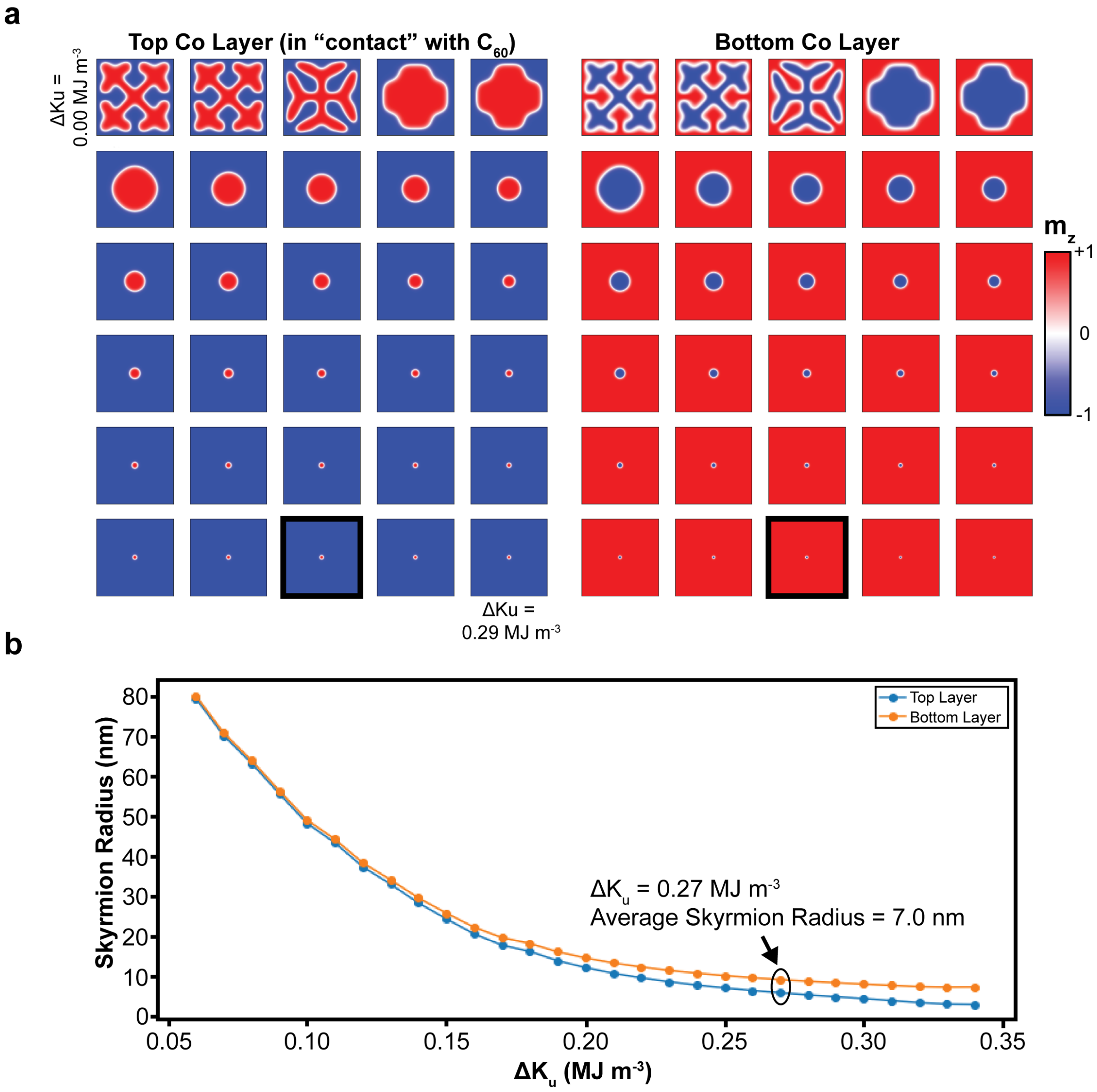

Figure 6.10: **a** 2D Scalar plots of the minimum energy magnetic configuration of the top (left) and bottom (right) Co layers in a SAF system that incorporates the effect of a Co/C$_{60}$ interface. Each image corresponds to a simulation with a different value of ΔK_u added to the top Co layer. The panel with the black outline reflects the experimentally measured value of $\Delta K_u = 0.27$ MJ m^{-3} for the PMA enhancing effect. Coloured by m_z magnetisation as given by the colour bar. **b** Plot of skyrmion radius as a function of ΔK_u. The circled data points again reflect the experimentally measured PMA enhancing effect value of $\Delta K_u = 0.27$ MJ m^{-3}.

The skyrmion size dependency over the entire range of ΔK_u can be seen in Fig. 6.10b, where an initial decrease in skyrmion radius quickly stabilises to an average value of approximately 7 nm. The circled data points again highlight the experimentally determined value of $\Delta K_u = 0.27$ MJ m^{-3}. Furthermore, it is clear that the skyrmions in the top and bottom layers have different radii. This discrepancy between the top and bottom skyrmions is due to the difference in PMA values within these layers. Within this SAF system there is essentially two separate equilibrium skyrmion radii, one for the top Co layer and one for the bottom Co layer. This effect is most obvious at ΔK_u values above 0.15 MJ m^{-3}, where the difference in the individual equilibrium skyrmion sizes becomes most apparent. It is the coupling of these two separate equilibrium sizes via the AFM IEC, which stabilises the SAF skyrmion even when the additional PMA in the top Co layer is increased by 37 % over the value in the bottom Co layer. It is important to note that these SAF skyrmion structures are only stable when the interface effect is applied to a single Co layer. In fact, if the K_u value is increased for both the top and bottom Co layers, then the skyrmions quickly collapse to zero radius and are thus annihilated.

These series of simulations provide some evidence towards the potential for implementing Co/C$_{60}$ interfaces within SAF structures to enhance skyrmion stability. Importantly, they show that a small SAF skyrmion is stabilised in these systems, without the need for a biasing layer (BL). However, since the specific spinterface effect is not well understood within SAF systems, it is important to carry out some complementary experimental observations involving SAF systems containing C$_{60}$ layers. Furthermore, since the C$_{60}$ layer breaks the symmetry within the SAF and creates a new interface region, it may have other effects on the magnetic interactions such as DM and RKKY. Investigation of these effects and implementation into the simulations were not included in this study as they were beyond the scope of the work presented in this thesis.

6.2.2 Explicit Simulation of C$_{60}$

Within a Co/C$_{60}$ interface region, the C$_{60}$ molecules in contact with the Co become magnetic, with magnetic spins aligned anti-parallel to the neighbouring Co. This is due to spin-polarised electron transfer from Co to C$_{60}$, as described in Ref. [15]. This means that the C$_{60}$ molecular layer may be simulated within MuMax3 as very weakly magnetic, with AFM IEC between itself and the Co layer. This type of setup was introduced within the schematic in Fig. 6.9b, whereby a new magnetic layer representing the C$_{60}$ is placed in contact with the top Co layer. However, in order to simulate the molecular layer, appropriate material parameters for C$_{60}$ must first be determined.

Firstly, $D_{ind} = 0$ and $K_u = 0$ are set within the C$_{60}$ layer, on the assumptions that the molecular layer will not host a DM interaction, or exhibit significant anisotropy effects. The approximate separation between C$_{60}$ cages within a molecular layer is 1 nm [22], and this means that simulation cell sizes of around 1 nm will represent individual C_{60} cages. It should be noted that this choice of discretisation may introduce errors into the simulation, since the micromagnetics framework is based upon continuously varying magnetisation vectors. In some sense, the fundamental magnetic unit within the molecular layer is the C_{60} cage (approximately 1 nm diameter), and as such its representation inside the micromagnetic simulation (with cell sizes of 1 nm) is subject to no coarse-graining. Furthermore, the relatively large (compared to atomic separation) intermolecular distance prompts the use of $A_{ex} = 0$ for the C_{60} layer, an assumption that there is essentially zero magnetic coupling between the cages. This means that neighbouring simulation cells within the C_{60} may have large angles between their magnetic moments, which is a source of error within the MuMax3 simulation code [7]. The assumption of $A_{ex} = 0$ admittedly requires more detailed theoretical or experimental work to determine whether it is appropriate, as it is possible that some exchange coupling between C_{60} cages exists. However, verifying this assumption is outwith the scope of the work in this thesis, and as such the simplifying assumption of $A_{ex} = 0$ will be used. The saturation magnetisation, M_s, may be determined from the approxiamte cage volume (1 nm^3) and the magnetic moment per cage, $1.2\ \mu_B$ as determined in Ref. [15]. This results in $M_s = 11100$ A m^{-1}, which is less than 1 % than that of the Co layer. Finally, a AFM IEC between the top Co layer and the C_{60} layer is introduced, with a strength of $J_{RKKY\ AFM} = -0.02$ mJ m^{-3}. Again, the true magnitude of this effect is uncertain, however it was found that any magnitude above approximately 0.01 mJ m^{-3} produced the same minimum energy magnetic configurations. A cell size of 1.47 nm was chosen to allow the other calculated material properties (for the Co layers) to remain the same. Again, an additional PMA constant was added to the top Co layer as in the previous simulations, and this amount was varied between 0.00 and 0.34 MJ m^{-3}.

A selection of minimum energy magnetic configurations for the C_{60}, top Co and bottom Co layers can be seen in Fig. 6.11a, where the plots are coloured by m_z as indicated by the colour bar. The values of ΔK_u for each magnetic configuration can be seen at the top of each column of panels, and these states were chosen to illustrate key differences in the skyrmion size-behaviour when including C_{60} in the simulations. Firstly, additional PMA of 0.07 MJ m^{-3} is sufficient to stabilise a circular skyrmion structure within each of the three layers, which shows a quick initial reduction in size, in line with the simulations in Section 6.2.1. However, a step-change reduction in skyrmion radii is observed between 0.25 and 0.26 MJ m^{-3} as highlighted by the corresponding magnetic configuration plots. This behaviour is elucidated further through the plot of skyrmion radius as a function of ΔK_u in Fig. 6.11b. Here, the radius of each skyrmion within the three layers is plot individually on the same axis, note that the C_{60} line exactly tracks that of the top Co layer. There is an initial rapid decrease in skyrmion radii in all three layers, which stabilises to approximately

40 nm at around 0.12 MJ m^{-3}. The skyrmion radii does not change significantly on further increase of ΔK_u until 0.26 MJ m^{-3}, when the step-change reduction occurs. At this point, the bottom Co layer stabilises a larger skyrmion than the top Co and C_{60} layers, this discrepancy is due to the additional PMA in the top Co layer.

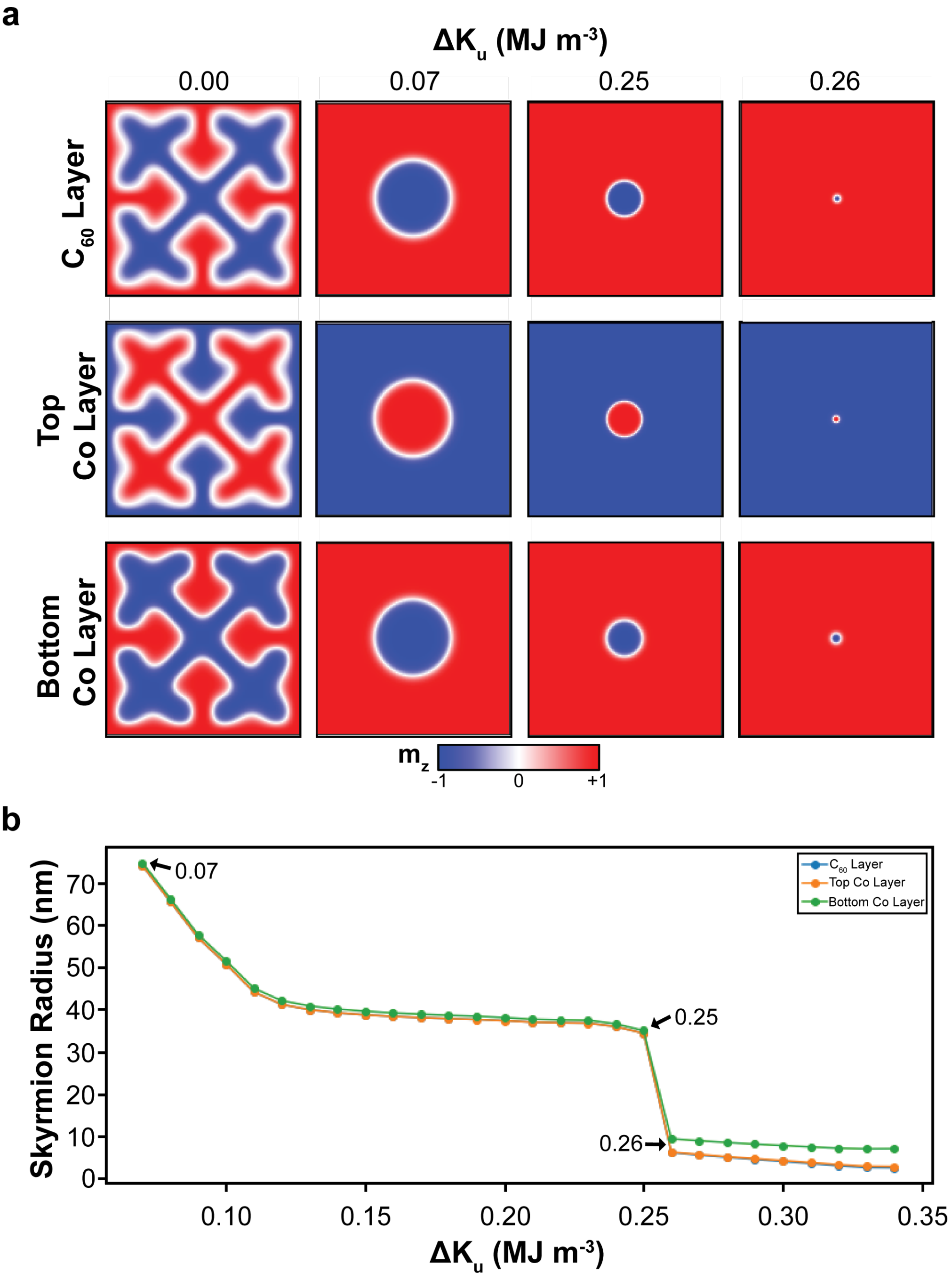

Figure 6.11: **a** 2D Scalar plots of the minimum energy magnetic configuration for C_{60} layer, top Co layer and bottom Co layer for some instructive values of ΔK_u. **b** Plot of skyrmion radius as a function of ΔK_u for each layer in the simulation.

This more complex (when compared with the simulations in Section 6.2.1) skyrmion size-behaviour is due to the fact that each of the simulated layers have different magnetic properties, and therefore each would stabilise skyrmions of different radii if simulated in isolation. However, simulated together with IEC, which provides coupling between each of these individual magnetic layers, the 3-layer SAF skyrmion reaches an average radius. This coupled system demonstrates a resilience against skyrmion radii fluctuations as PMA is increased in the top Co layers, which should initate skyrmion size reduction. Thus, the inclusion of the magnetic C_{60} layer appears to provide a mechanism by which the skyrmion radii are stabilised at some intermediate radii (in this case 40 nm), even when ΔK_u is increased. The step-change at 0.26 MJ m^{-3} indicates that this stabilising effect is overcome once a tipping-point is reached, whereby the additional PMA in the top Co layer eventually dominates the other energy contributions.

Comparison between this behaviour and that from simulations in Section 6.2.1, can be seen in Fig. 6.12, where the skyrmion radii in each layer have been averaged to a single value for each case. Immediately apparent is the existence of three separate regions (labelled A, B and C), where the simulations demonstrate similar behaviour in regions A and C, but divergent behaviour in region B. Note that the label "Cages" and "No Cages" refers to the simulations that explicitly and implicitly simulate the effects of C_{60}, respectively. In region A, the two different methods appear to qualitatively follow the same skyrmion size-reduction behaviour. However, upon reaching the boundary between regions A and B, the observed behaviours diverge. At this point, when only the Co layers are simulated (No Cages) the average skyrmion radius continues to decrease smoothly whereas when the C_{60} layer is simulated (Cages) the skyrmion radii does not decrease further as ΔK_u is increased. Finally, at the boundary between regions B and C, there is a sharp discontinuous decrease in skyrmion radius for the explicit C_{60} simulation. From this point, the two behaviours are identical and the C_{60} layer appears to have no effect on the skyrmion radius.

Although the exact reason for the stabilising effect of the C_{60} was not able to be determined here, it does provide an opportunity for experimental investigation. If the magnetic C_{60} cages are able to form long-range magnetic structure then it may be possible to access this step-change in skyrmion radius through the modification of Co thickness. Given that the unmodified PMA, K_u, is dependent on the magnetic layer thickness according to Eq. 2.12 in Section 2.2.3, tuning the top layer Co thickness may provide a means of accessing the discontinuous size behaviour either side of the B/C boundary in Fig. 6.12.

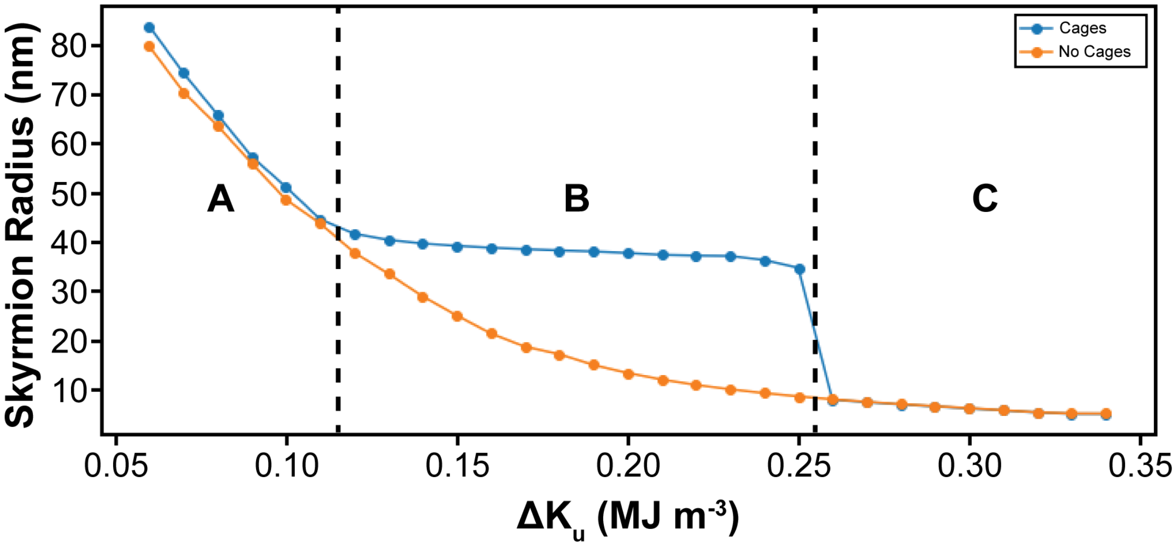

Figure 6.12: Comparison plot of skyrmion radius as a function of ΔK_u when only the Co layers are simulated (No Cages) and when the C_60 layer is explicitly simulated (Cages).

6.3 Discussion and Conclusions

The technological relevance of synthetic antiferromagnetic (SAF) systems was the motivation for much of the work contained within this chapter. Understanding the intricate balance of magnetic interactions in these multilayer systems is integral towards realising SAF-based skyrmion devices such as those proposed in Refs. [23, 24]. The presented micromagnetic simulation studies demonstrate the ability to tune magnetic interactions and thus skyrmion stability when designing such multilayer skyrmion-hosting systems. Focusing on unbalanced synthetic antiferromagnetic (SAF) systems, Section 6.1 demonstrated the limits of skyrmion stability when designing systems that may be imaged using Lorentz TEM imaging methods. In Section 6.1.1 it was shown that an unbalanced SAF may be generated by using differing numbers of multilayer repeat units above and below the central SAF region containing Ru. These systems were translated into simulation-appropriate forms and investigated using MuMax3 with custom energy terms required to account for the antiferromagnetic (AFM) interlayer exchange coupling (IEC). These studies complement those already undertaken in Ref. [6], however the present work extends the micromagnetic representation to include the effect of demagnetising interactions between ferromagnetic layers. Using this micromagnetic representation, it was then shown in Section 6.1.2 that due to the non-cancelling dipolar fields in the multilayer SAF systems, there was an upper limit on the number of constituent repeat units before skyrmion structures were no longer stable within the system. It was shown that it is possible to increase this upper limit by increasing the AFM IEC strength, so that the coupling is able to overcome the destabilising effect of the non-zero dipolar fields. Therefore, this work highlights the importance of SAF multilayer engineering and hints at the potential pitfalls associated with homogeneity during fabrication. Furthermore, it demonstrates the importance of interlayer exchange coupling in stabilising SAF skyrmions as also reported for dynamics in synthetic ferromagnetic [25], and synthetic antiferromagnetic systems [26].

In Section 6.2, simulations involving metal-molecular interfaces between Co and C_{60} were investigated. In such systems, a region of enhanced perpendicular magnetocrystalline anisotropy (PMA) is generated and the effects enhanced PMA, as reported in Ref. [19], on skyrmion stability was investigated. In Section 6.2.1 it was shown that through the enhancement of PMA in only one layer of Co, small skyrmions with an average radius under 10 nm may be stabilised without the need for a biasing layer (BL). Finally, in Section 6.2.2 the C_{60} was explicitly simulated as a weak magnetic layer, where the magnetic character was due to spin-polarised charge transfer from the Co to the C_{60} cages. This resulted in different behaviour to that when the C_{60} was not simulated, and highlighted a complexity of radius behaviour due to the coupling of three distinct magnetic layers. Both methods of simulating the metal-molecular effects resulting in a reduction in skyrmion size, a similar effect of which was reported in Ref. [21] for bubble domain size reduction in a Pt/Co/C_{60}/Pt system.

Bibliography

1. Büttner, F., Lemesh, I. & Beach, G. S. Theory of isolated magnetic skyrmions: From fundamentals to room temperature applications. *Scientific Reports* **8,** 1–12 (2018).
2. Fert, A., Reyren, N. & Cros, V. Magnetic skyrmions: Advances in physics and potential applications. *Nature Reviews Materials* **2** (2017).
3. Legrand, W. *et al.* Room-temperature stabilization of magnetic skyrmions in synthetic antiferromagnets. *Nature Materials,* 1–23 (Sept. 2018).
4. Zhang, X., Zhou, Y. & Ezawa, M. Magnetic bilayer-skyrmions without skyrmion Hall effect. *Nature Communications* **7** (2016).
5. Barker, J. & Tretiakov, O. A. Static and Dynamical Properties of Antiferromagnetic Skyrmions in the Presence of Applied Current and Temperature. *Physical Review Letters* **116,** 147203 (May 2016).
6. Chen, R. *et al.* Realization of isolated and high-density skyrmions at room temperature in uncompensated synthetic antiferromagnets. *Nano Letters* **20,** 3299–3305 (2020).
7. Vansteenkiste, A. *et al.* The design and verification of MuMax3. *AIP Advances* **4,** 107133 (2014).
8. Donahue, M. J. & Porter, D. G. OOMMF User's Guide, Version 1.0. *Interagency Report NISTIR 6376* (1999).
9. Knepper, J. W. & Yang, F. Y. Oscillatory interlayer coupling in Co Pt multilayers with perpendicular anisotropy. *Physical Review B - Condensed Matter and Materials Physics* **71** (2005).
10. Demidov, E. S. *et al.* Interlayer interaction in multilayer [Co/Pt]n/Pt/Co structures. *Journal of Applied Physics* **120,** 173901 (Nov. 2016).

11. Bloemen, P. J., Van Kesteren, H. W., Swagten, H. J. & De Jonge, W. J. Oscillatory interlayer exchange coupling in Co/Ru multilayers and bilayers. *Physical Review B* **50,** 13505–13514 (1994).

12. Khadka, D., Karayev, S. & Huang, S. X. Dzyaloshinskii-Moriya interaction in Pt/Co/Ir and Pt/Co/Ru multilayer films. *Journal of Applied Physics* **123,** 123905 (Mar. 2018).

13. Cornia, A. & Seneor, P. Spintronics: The molecular way. *Nature Materials* **16,** 505–506 (Apr. 2017).

14. Sanvito, S. Molecular spintronics: The rise of spinterface science. *Nature Physics* **6,** 562–564 (June 2010).

15. Moorsom, T. *et al.* Spin-polarized electron transfer in ferromagnet/C60 interfaces. *Physical Review B - Condensed Matter and Materials Physics* **90,** 125311 (2014).

16. Céspedes, O., Ferreira, M. S., Sanvito, S., Kociak, M. & Coey, J. M. *Contact induced magnetism in carbon nanotubes* Feb. 2004.

17. Moorsom, T. *et al.* π-anisotropy: A nanocarbon route to hard magnetism. *Physical Review B* **101** (2020).

18. Bairagi, K. *et al.* Tuning the Magnetic Anisotropy at a Molecule-Metal Interface. *Physical Review Letters* **114** (2015).

19. Mallik, S. *et al.* Enhanced anisotropy and study of magnetization reversal in Co / C 60 bilayer thin film. *Applied Physics Letters* **115,** 242405 (2019).

20. Wang, X. S., Yuan, H. Y. & Wang, X. R. A theory on skyrmion size. *Communications Physics* **1,** 1–7 (Dec. 2018).

21. Sharangi, P., Mukhopadhyaya, A., Mallik, S., Ali, M. E. & Bedanta, S. Effect of Fullerene on domain size and relaxation in a perpendicularly magnetized Pt/Co/C60/Pt system (Dec. 2020).

22. Goel, A., Howard, J. B. & Sande, J. B. Size analysis of single fullerene molecules by electron microscopy. *Carbon* **42,** 1907–1915 (2004).

23. Zhang, X., Ezawa, M. & Zhou, Y. Thermally stable magnetic skyrmions in multilayer synthetic antiferromagnetic racetracks. *Physical Review B* **94** (2016).

24. Fattouhi, M. *et al.* Logic Gates Based on Synthetic Antiferromagnetic Bilayer Skyrmions. *Physical Review Applied* **16,** 014040 (July 2021).

25. Waring, H. J., Li, Y., Moutafis, C., Vera-Marun, I. J. & Thomson, T. Magnetization dynamics in synthetic ferromagnetic thin films. *Physical Review B* **104,** 14419 (2021).

26. Qiu, L. *et al.* Interlayer coupling effect on skyrmion dynamics in synthetic antiferromagnets. *Applied Physics Letters* **118,** 082403 (Feb. 2021).

Chapter 7

Summary and Outlook

This thesis provided experimental and theoretical studies on the dynamic processes, physical and topological stability and magnetic phase transitions involving magnetic skyrmions, in a range of different material systems. This was achieved through a combination of the following three broad methodologies. First, the use of fast magnetic field pulses and Lorentz Fresnel transmission electron microscopy (TEM) to prepare and observe interesting frustrated skyrmion defect states. Second, advanced image analysis utilising machine learning on fast-frame video datasets showing skyrmion dynamics, thereby extracting key configurational states, time series and lifetime information. Third, micromagnetic simulations involving both static and dynamic magnetic systems to investigate energy landscapes, minimum energy configurations and transition pathways to supplement and inform Fresnel TEM experiments.

In Chapter 4, spontaneous skyrmion dynamics involving distinct skyrmion defect states within a skyrmion crystal lattice (SkX) were investigated. Analysis of a fast-frame (10 ms) Fresnel video dataset was analysed using image processing techniques including background subtraction, Delaunay Triangulation and visual inspection. This led to the identification of six distinct skyrmion defect states involved in the spontaneous motion, consisting of three primary states and three transition states. Further image analysis of the six states was performed, involving generating average images of each state, and this led to the discovery of the continuously deforming structure of the skyrmion at the centre of the heptagon in the 5-7 defect (SkCoH). Through image analysis in a frame-by-frame manner, it was determined that the spontaneous motion consisted of the movement of 5-7 skyrmion lattice defects and the continuous splitting and merging of skyrmions. It was found that extreme deformation of the elongated SkCoH was integral to the skyrmion splitting process, and the subsequent formation of a high skyrmion density state led to the merging of neighbouring skyrmions. This was elucidated further using micromagnetic simulations involving 5-7 defects, and it was concluded that the interplay between Zeeman and exchange energies associated with the different defect states helped to explain the observed spontaneous motion between states, facilitated by thermal energy. By using the order of occurrence data, it was possible to determine the average lifetime of the states, and model the process as a Markov chain. This resulted in the discovery that not all possible types of transitions occurred within the observed data, and that certain transitions were more likely to occur than others. This was related back to the configuration of each of the states, and justified through the fact that the more likely transitions were those that required minimal bulk lattice reorientation. Furthermore, one state was found to act as a nexus point, whereby it was observed to have transitions to and from every other observed state. Although this state had the most occurrences, it did not have the longest lifetime. It was proposed that this was due to an entropy-compensation type effect, decreasing the lifetime of the state due to the number of possible transitions. Finally, through the use of dynamic micromagnetic simulations, a series of mechanisms were proposed for the observed splitting and merging of skyrmions, resulting in skyrmion creation and annihilation. These mechanisms involved the appearance and subsequent destruction of antiskyrmions structures, that fulfilled topological conservation through the transitions. The proposed mechanism is consistent with previous work including Refs. [1–6].

This work presented distinct benefits and limitations of Fresnel TEM imaging using a direct electron detector, namely the ability to obtained high temporal resolution data at the cost of some spatial resolution, due to the defocused state of the TEM. Although the Fresnel data contained rich temporal and spatial information, the intricate details of the magnetic configurations for the transition states were not resolvable. In a recent study [7], the authors attempted to solve these problems through the use of the higher spatial resolution technique of differential phase contrast (DPC) imaging. Through slowing the skyrmion dynamics by lowering temperature, and pinning a helical line at a defect site, they were able to image the type of transition states involving antiskyrmion structures proposed at the end of Chapter 4. However, further improvements to both spatial and temporal resolution in Lorentz TEM imaging is still required to fully resolve the complexity of magnetic configurations present during fast dynamic processes. Although a direct electron detector with a faster frame rate, such as the Timepix3 [8], could help with the temporal resolution problem, there are more fundamental limitations on the spatial resolution due to Fresnel being an intrinsically out of focus imaging mode. A potential solution to the resolution problem could be to develop a method of imaging with DPC using a reduced scan area to reduce the time it takes to raster a sample. Crucially, the rastering time would need to be sufficiently less than the characteristic timescale of the dynamics under observation. However, a technique such as this may be able to provide additional spatial resolution and quantative information of dynamic magnetic processes, at the cost of temporal resolution.

In order to improve the robustness of the configurational skyrmion state identification, and to enable the use of sub-ms frame acquisition times, Chapter 5 began by introducing a series of advanced image analysis techniques. These included the implementation of denoising algorithms, frame subsampling and machine learning algorithms. Total variation (TV) denoising was combined with frame subsampling to improve the signal-to-noise (SNR) ratio of fast-frame Fresnel video datasets. This technique was then complemented by non-negative matrix factorisation (NMF) to identify key skyrmion states held within Fresnel videos containing skyrmion dynamics. Although NMF as a technique has been utilised in analysing electron microscopy data previously, see Refs. [9–12], this work demonstrates the ability to gain both spatial and temporal information on dynamic processes involving skyrmions. Specifically, it was shown that NMF is able to provide a high-throughput method for automatically identifying key features within a multi-frame image dataset, through the decomposition of the data into a number of user defined basis images. Although an arbitrary number of basis images may be chosen, it is possible to choose different sets of basis images, providing a range of information on the types of image variation associated with the dynamic processes. Therefore, it is helpful to have an idea of the number of key features held within the dataset from brief visual inspection, as a first guess, to determine whether the NMF algorithm identifies the expected states. Higher order structural variations may then be accounted for through an increased number of basis images. This process was exemplified in Section 5.1.2, whereby a dataset showing relatively slow skyrmion dynamics was treated with NMF of two, three and then finally four basis images. It is worth noting here that the use of too few basis images results in a loss of information, whereas too many may result in overfitting of the dataset. It is possible to use cross-validation to determine the ‘best’ number of components, however this is both time intensive and computationally demanding, as it involves running many iterations of NMF on the same dataset. The method chosen in this thesis may be less statistically robust, as it requires user input to determine whether the generated basis images are ‘sensible’ representations of the features in question. The use of the accompanying coefficient matrix as a means to plot the time series behaviour of the basis images provided the ability to determine order of occurrence of the key states, and also their approximate lifetimes. Non-trivial behaviour involving four basis images, together representing two skyrmion defects, was observed within this time series data. Both continuous and discontinuous, correlated and anti-correlated behaviours were observed between the four basis images, highlighting the complexity of structural variations involved in the transitions between two skyrmion defects.

The analysis work was followed by the implementation of pulsed magnetic fields within the transmission electron microscope (TEM), to induce frustrated skyrmion states using a bespoke microcoil device. Both the microcoil and current pulser devices were designed and fabricated in with the intent to supply bi-directional magnetic field pulses of nanosecond duration and magnitudes of approximately 0.15 T. The implementation of these devices led to the generation of highly disordered skyrmion states within the SkX, including high 5-7 defect density and a highly symmetric rare 5-5 defect. Furthermore, by combining the individual magnetic field pulses from the microcoil with the static field increases provided by the TEM objective lens, it was possible to easily generate highly mixed skyrmion phases and significantly frustrated, metastable regions. The kinds of magnetic state configurations found here are similar to those previously observed in Refs. [7, 13], however the images obtained offer more clarity than those presented in Ref. [13]. Additionally, this device provides a way of navigating the helimagnetic phase space in a controllable manner, whereby the speed of the magnetic field pulses may be tuned to allow or disallow large scale lattice reorientation. Furthermore, this highlights the ability to generate a wide range of magnetic states through combining pulsed magnetic fields (generated by the microcoil) with static magnetic fields (generated by the objective lens).

The work contained within this chapter provides both experimental and analysis tools for inducing and investigating skyrmion dynamic processes in detail. Unfortunately, due to instrument downtime, it was not possible to combine both the fast-frame analysis and fast magnetic field pulses within this thesis. However, it is expected that frame capture on the Merlin detector could be synced up with the magnetic field pulses, in order to acquire images of the magnetic state during the magnetic field pulse. Furthermore, calibration of the true strength of the magnetic field pulses at the sample location as a function of supplied voltage is desirable. It is expected that skyrmion lattice parameter variation may be used for this purpose, as it varies as a function of magnetic field. Combined with frame acquisition triggered by the magnetic field pulse, a series of images at different pulse voltages may be acquired, and the skyrmion lattice parameter may then be measured and compared with those acquired at known, static magnetic fields. Finally, it should be possible to combine both magnetic field pulses and magnetic patterning of magnetic structures to influence skyrmion lattice formation and dynamics.

Finally, in Chapter 6, a series of micromagnetic simulation studies were performed on synthetic antiferromagnetic (SAF) multilayer skyrmion-hosting systems. The aim of these studies was to provide insight into SAF skyrmion stability within different magnetic multilayer systems, given the technological relevance of SAF skyrmions for devices as proposed in Refs [14, 15]. Additionally, the investigation of unbalanced SAF systems, consisting of ferromagnetically coupled repeat units, was undertaken to determine the feasibility of stabilising skyrmions within unbalanced SAFs. These types of structures are important as they provide a means of generating magnetic contrast in Lorentz TEM, and thus the ability to image SAF skyrmions in TEM experiments. It was found that interlayer exchange coupling (IEC) was vitally important in stabilising SAF skyrmions in unbalanced SAFs, due to the extended destabilising effect of stray-field interactions. Furthermore, it was shown that experimentally feasible values of IEC were sufficient to stabilise skyrmions in both balanced, and unbalanced multilayer SAFs. This work adds to the studies already undertaken in Ref. [16], except that the present work takes into account the effect of demagnetising interactions between ferromagnetic layers by explicitly simulating each magnetic layer.

Next, the micromagnetic simulations of SAFs were extended to include the effects of molecular-metal interfaces. Such interfaces have been experimentally shown to provide enhanced or otherwise modified magnetic properties, and thus a potential to be included in magnetic multilayer systems. Specifically, it has been shown in Refs. [17, 18] that PMA is greatly enhanced at a Co/C_{60} interface. By introducing further custom energy terms into the micromagnetic solver, the effect of a Co/C_{60} interface was investigated. This was accomplished through both non-explicit and explicit simulation of the C_{60} layer in the micromagnetic simulations. It was found that the anisotropy enhancing effect of the Co/C_{60} interface was sufficient to stabilise SAF skyrmions without the need of exchange coupling to a separate biasing layer. Furthermore, explicit simulation of the C_{60} layer led to non-trivial skyrmion size behaviour due to the coupling between three distinct magnetic layers. The results obtained here are consistent with a similar effect reported in Ref. [19] for bubble domains in a similar magnetic system.

The importance of tuning magnetic interactions for skyrmion stability through multilayer engineering was thus demonstrated, and evidence was provided for limited SAF skyrmion stability in extended multilayers, due to demagnetising effects. These studies provide a preliminary attempt to simulate complex SAF multilayer structures, which host a wide range of magnetic interactions. Comparison with future experiments will provide a means of tuning and improving the micromagnetic models of SAF systems. Given that SAF skyrmions may only be simulated in MuMax3 using custom code, it would be valuable to compare simulations of the kind presented in this thesis with both analytical and perhaps atomistic models. Furthermore, comparison with experimental studies with help to determine the validity and inform further simulations involving complex multilayer magnetic systems. Nevertheless, the micromagnetic simulation studies presented herein demonstrate the richness of the accessible parameter space associated with skyrmion stability, through magnetic/non-magnetic/organic multilayer engineering in future skyrmion based information devices.

Bibliography

1. Koshibae, W. & Nagaosa, N. Theory of antiskyrmions in magnets. *Nature Communications* **7,** 10542 (Apr. 2016).
2. Garanin, D. A., Chudnovsky, E. M. & Zhang, X. Skyrmion clusters from Bloch lines in ferromagnetic films. *Epl* **120** (2017).
3. Pierobon, L., Moutafis, C., Li, Y., Löffler, J. F. & Charilaou, M. Collective antiskyrmion-mediated phase transition and defect-induced melting in chiral magnetic films. *Scientific Reports* **8,** 16675 (Dec. 2018).
4. Desplat, L., Suess, D., Kim, J. V. & Stamps, R. L. Thermal stability of metastable magnetic skyrmions: Entropic narrowing and significance of internal eigenmodes. *Physical Review B* **98,** 134407 (2018).
5. Müller, G. P. *et al.* Duplication, Collapse, and Escape of Magnetic Skyrmions Revealed Using a Systematic Saddle Point Search Method. *Physical Review Letters* **121** (July 2018).
6. Desplat, L., Kim, J. .-V. & Stamps, R. L. Paths to annihilation of first- and second-order (anti)skyrmions via (anti)meron nucleation on the frustrated square lattice. *Physical Review B* **99** (Feb. 2019).
7. Matsumoto, T., So, Y. G., Ikuhara, Y. & Shibata, N. Direct visualization of nucleation intermediate state of magnetic skyrmion from helical stripes assisted by artificial surface pits. *Journal of Magnetism and Magnetic Materials* **531,** 167976 (2021).
8. Frojdh, E. *et al.* Timepix3: First measurements and characterization of a hybrid-pixel detector working in event driven mode. *Journal of Instrumentation* **10** (2015).
9. Kiss, Á. K. & Lábár, J. L. Determining Projections of Grain Boundaries from Diffraction Data in Transmission Electron Microscope. *Microscopy and Microanalysis* **22,** 551–564 (Feb. 2016).

10. Shiga, M. *et al.* Sparse modeling of EELS and EDX spectral imaging data by nonnegative matrix factorization. *Ultramicroscopy* **170,** 43–59 (Nov. 2016).
11. Jany, B. R., Janas, A. & Krok, F. Automatic microscopic image analysis by moving window local Fourier Transform and Machine Learning. *Micron* **130,** 102800 (Mar. 2020).
12. Uesugi, F. *et al.* Non-negative matrix factorization for mining big data obtained using four-dimensional scanning transmission electron microscopy. *Ultramicroscopy* **221,** 113168 (Feb. 2021).
13. Müller, J. *et al.* Magnetic Skyrmions and Skyrmion Clusters in the Helical Phase of Cu2OSeO3. *Physical Review Letters* **119,** 137201 (2017).
14. Zhang, X., Ezawa, M. & Zhou, Y. Thermally stable magnetic skyrmions in multilayer synthetic antiferromagnetic racetracks. *Physical Review B* **94** (2016).
15. Fattouhi, M. *et al.* Logic Gates Based on Synthetic Antiferromagnetic Bilayer Skyrmions. *Physical Review Applied* **16,** 014040 (July 2021).
16. Chen, R. *et al.* Realization of isolated and high-density skyrmions at room temperature in uncompensated synthetic antiferromagnets. *Nano Letters* **20,** 3299–3305 (2020).
17. Bairagi, K. *et al.* Tuning the Magnetic Anisotropy at a Molecule-Metal Interface. *Physical Review Letters* **114** (2015).
18. Mallik, S. *et al.* Enhanced anisotropy and study of magnetization reversal in Co / C 60 bilayer thin film. *Applied Physics Letters* **115,** 242405 (2019).
19. Sharangi, P., Mukhopadhyaya, A., Mallik, S., Ali, M. E. & Bedanta, S. Effect of Fullerene on domain size and relaxation in a perpendicularly magnetized Pt/Co/C60/Pt system (Dec. 2020).